Flinders UNIVERSITY
ADELAIDE · SOUTH AUSTRALIA

The Replacement of Chalcopyrite by Copper Sulphides and Its Application in Cu Extraction

By

Zhen He

Master of Science (Chemistry)

Thesis
Submitted to Flinders University
for the degree of

Doctor of Philosophy

College of Science and Engineering

Approved by 28th Oct 2022

TABLE OF CONTENTS

ABSTRACT

Mineral replacement reactions occur widely in Nature and result in the formation of a range of sulphide minerals in the presence of hydrothermal fluids. These mineral replacement reactions under hydrothermal conditions have been intensively studied over past two decades, but only a few studies have focused on the replacement of chalcopyrite by copper sulphides. In Nature, chalcopyrite is replaced by covellite, and digenite in the supergene zone of ore deposits, but the mechanism and kinetics of these reactions are not fully understood. Moreover, the dissolution of chalcopyrite at low temperature is one of biggest challenges in the copper mining sector and previous studies suggest that covellite and digenite more readily dissolve at low temperatures. The purpose of this project was to investigate the mechanisms and kinetics of the replacement of chalcopyrite by covellite and digenite and assess potential applications in *in-situ* covellite dissolution at low temperature. In this project, the replacement reaction of chalcopyrite by covellite or digenite were investigated in detail under hydrothermal conditions and the kinetic data were extrapolated to lower temperatures. An environmentally friendly chemical reagent (glycine) was chosen for the covellite dissolution study at low temperature.

Chalcopyrite was successfully replaced by covellite in the temperature range of 140-200 °C under acidic condition (pH 0.7-3) via a coupled dissolution-reprecipitation reaction mechanism. Covellite was identified by X-ray powder diffraction (XRD), scanning electron microscopy (SEM) and energy dispersive analysis (EDAX). The replacement reaction rate was controlled by solution chemistry (pH values), temperature, availability of dissolved oxygen and the surface area of chalcopyrite grains. Covellite precipitation is the rate-determining step of the overall mineral replacement reaction at temperatures above 140 °C, with elemental sulphur found to be an intermediate product in initial stage of the replacement reaction. At 120 °C, only elemental sulphur was formed after reaction of 18 days without covellite. X-ray photoelectron spectroscopy (XPS) was used to assist in the identification of the reaction mechanism during the chalcopyrite dissolution step. The results show 89±5% of chalcopyrite was replaced by covellite at pH 0.7 and 200 °C after 16 h in the presence of 0.44 mmol H_2O_2. The average activation energies of replacement reaction at pH 0.7, 1 and 1.5 are 90±21 kJ/mol, 86±17 kJ/mol and 27±7 kJ/mol respectively.

Covellite precipitated as the dominant product in the replacement of chalcopyrite by copper sulphides in the presence of added Cu^{2+}. Digenite was formed by replacing

chalcopyrite only at or above 180 °C in pH 2 and pH 2.5 solutions with 0.22 mmol $CuCl_2$ and 0.44 mmol H_2O_2. At pH 3, chalcopyrite was replaced by digenite and covellite at temperatures between 140-180 °C with same added amount of Cu (II) ions and oxidants. The replacement reaction proceeds via dissolution of chalcopyrite and reprecipitation of digenite and covellite. The surface morphology of digenite was imaged by SEM. The fraction of digenite in the final solid residues of replacement reaction was found to increase with: increasing concentration of $CuCl_2$ (up to 0.66 mmol), increasing temperature (up to 200 °C); decreasing acidic condition (pH 1-pH 2.5) or increasing specific surface area. The activation energies of chalcopyrite dissolution during the replacement reactions at pH 2 and 2.5 are 44±6 kJ/mol and 46±14 kJ/mol respectively.

The dissolution of covellite was investigated by using alkaline glycine solution at low temperatures (25-55 °C). The Cu concentration in the solution was measured by inductively coupled plasma optical emission spectrometry (ICP-OES). The results revealed that 57±5% of covellite, 38-75 μm size fraction was dissolved and Cu-glycinate complexes were formed at 55 °C in pH 11 solutions with 0.5 M glycine after 107 h of reaction. The dissolution rate of covellite was influenced by OH^- concentration, availability of dissolved oxygen and the glycine concentration. The shrinking core model was used to determine the dissolution rate and controlled by diffusion through product layer. The activation energy of covellite dissolution is 33±7 kJ/mol.

DECLARATION

I certify that this thesis does not incorporate without acknowledgment any material previously submitted for a degree or diploma in any university; and that to the best of my knowledge and belief it does not contain any material previously published or written by another person except where due reference is made in the text.

Signed.....Zhen He.....

Date.....28/10/2022.....

ACKNOWLEDGEMENTS

First of all, I would like to thank my principal supervisor Professor Sarah Harmer for her excellent supervision, guidance and support throughout my PhD candidature. She has provided excellent opportunities for data collection with advanced techniques, and professional data analysis in XPS. It is my great pleasure to have the opportunity to work and learn in this project. I wish to also acknowledge and thank my co-supervisor Professor Allan Pring for his professional knowledge in mineral replacement field, and his support for my wonderful scientific communication experiences in Goldschmidt conference. I am very thankful for the professional experimental demonstration of my co-supervisor Dr. Gujie Qian, and his helpful advice on the experimental design and setup. I wish to particularly thank the hard work and comments of my all three supervisors on my writing during the drafting process. All three of my supervisors made an excellent team, I would not be able to complete the work of this project without their continuing advice and knowledge.

I wish to thank Christopher Bassell at University of South Australia for his assistance of XPS data collection. I gratefully acknowledge the training and assistance on ICP-OES analysis of Helena Anderson at Flinders Analytical. I would like to acknowledge Dr. Alex Sibley and Dr. Jing Zhao for their assistance of carbon-coating for better SEM imaging quality. Sincere thanks to the past and present members of Harmer research group for their support and contributions to my PhD candidature.

My deepest gratitude to my girlfriend Helen, who supports me with her love and patience through the hardest time of my candidature. Most importantly, I would like to thank my parents for their financial and mental supporting through my candidature, especially when my candidature is significantly affected by COVID. This work would not be completed without their support.

I acknowledge Flinders University for providing me the tuition fee waiver scholarship. The financial support of BHP Olympic Dam Operations and the Australian Research Council Linkage project LP160101497 is gratefully acknowledged.

LIST OF PUBLICATIONS

Poster Presentation

Z. He, G. Qian, A. Pring, S.L. Harmer, *The replacement reaction of chalcopyrite by covellite under hydrothermal conditions,* Flinders University Institute for Nanoscale Science & Technology 8th Annual Conference, 2018.

Z. He, G. Qian, A. Pring, S.L. Harmer, *The replacement reaction of chalcopyrite by covellite under hydrothermal conditions,* Goldschmidt Conference, Barcelona, Spain 2019.

Z. He, G. Qian, A. Pring, S.L. Harmer, *The replacement reaction of chalcopyrite by covellite under hydrothermal conditions,* Flinders University Molecular Science and Technology HDR student Conference 2019.

Z. He, G. Qian, A. Pring, S.L. Harmer, *Covellite dissolution with glycine under alkaline conditions,* Flinders University Institute for Nanoscale Science & Technology 10th Annual Conference, 2020.

Oral Presentation

Z. He, G. Qian, A. Pring, S.L. Harmer, *The replacement reaction of chalcopyrite by covellite under hydrothermal conditions,* GSA Earth Sciences Student Symposium, 2019

Z. He, *New approach of copper extraction: the replacement reaction of chalcopyrite by covellite and chalcocite*, 3 Minute Thesis, Flinders University, 2020,

LIST OF FIGURES

LIST OF TABLES

CHAPTER 1 INTRODUCTION

1.1 Project Background

Copper is one of Earth's primary base metals and its widespread use in electronic, batteries, chemicals alloys make it essential and of great economic importance in our modern world. However, these is an imbalance between the copper production and the world demanding. Most copper is extracted from the copper sulphide minerals by first concentrating the ore by froth flotation, followed by smelting, and refining (Watling, 2013). There has been a decline in the average grade of copper of in major copper mines over the last 75 years and it often recognised as a potential challenge to the mining industry in the future (Watling, 2013, Northey et al., 2014).

Chalcopyrite ($CuFeS_2$), covellite (CuS), digenite ($Cu_{1.8}S$) and chalcocite (Cu_2S), together with bornite (Cu_5FeS_4) are the principal economically important copper minerals which are commonly found in the Earth's crust. Deep below the earth's surface, hypogene processes may to occur and create primary minerals, such as chalcopyrite and pyrite (FeS_2). In comparison, supergene enrichment processes take place at or near the Earth's surface where the secondary minerals such as covellite, digenite and chalcocite are generally found (Rakovan, 2003).

Covellite, digenite and chalcocite are all containing higher copper content than chalcopyrite, but chalcopyrite is much more abundant and widespread and thus economically important. Chalcopyrite, however, is refractory because of its crystal structure, which makes copper extraction difficult compared to covellite and chalcocite (Fuentes-Aceituno et al., 2008, Veloso et al., 2016). Chalcopyrite has also been found challenging to be dissolved in heap leaching at low temperature (Qian et al., 2021). In the supergene zone, the chalcocite and covellite have been reported to form via the supergene enrichment process, a process similar to a mineral replacement reaction (Vasconcelos et al., 2015). Digenite is often intergrown with chalcocite, covellite, chalcopyrite and pyrite. Therefore, the replacement processes of chalcopyrite by covellite/chalcocite have attracted attention from the mining industry and scientific community. The purpose of this work was to investigate the optimal conditions and reaction rate for the replacement of chalcopyrite by covellite and by digenite at conditions similar to those found in supergene environment. However, the rate of transformation of

chalcopyrite into digenite or covellite is extremely slow under supergene environment due to the low temperature conditions (15°C), which may take centuries or even longer to complete in Nature. Thus, the experiments in this project were performed under mild hydrothermal conditions (≤ 200°C) and results can be extrapolated to low temperature conditions relevant to supergene environments. If chalcopyrite is able to be converted to covellite or digenite at low temperature on a laboratory time scale, the ultimate goal of this project was to extract copper from covellite/digenite *in situ* with environmental-friendly chemical reagents.

1.2 Minerals

1.2.1 Chalcopyrite, covellite and chalcocite

Chalcopyrite is known as one of the most abundant copper sulphides in the earth's crust and is commonly found with other sulphide minerals including pyrite, bornite (Cu_5FeS_4), chalcocite and covellite. It is one of the most well-studied sulphide minerals and has a chemical formula, $Cu^{I}Fe^{III}S^{-II}_2$. The Fe(III) state in chalcopyrite has been identified using Mossbauer spectroscopy (Raj and Chandra, 1968, Mussel et al., 2007). Based on X-ray photoelectron spectroscopy (XPS) and X-ray absorption spectroscopy (XAS), the copper atoms were found to be most considered monovalent (Nakai et al., 1978, Goh et al., 2006, Petiau et al., 1988). Chalcopyrite has a tetragonal unit cell. Each metal atom is tetrahedrally coordinated to four sulphur atoms and each sulphur atom is tetrahedrally coordinated to four metal atoms (Vaughan, 2006) as illustrated in Figure 1.

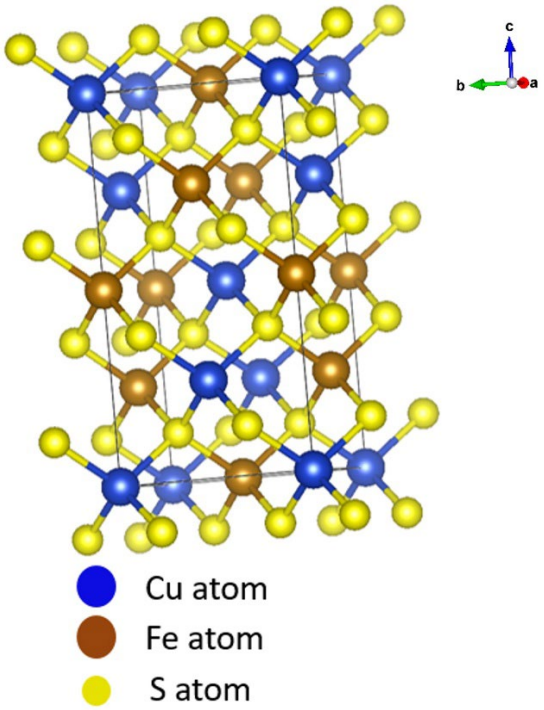

Figure 1 : the crystal structure of chalcopyrite.

Chalcocite ($Cu^{I}_2S^{-II}$) is a copper sulphide mineral, generally found in supergene enriched zones of sulphide deposits. It has a very high copper content (66.6 at.%) which makes it one of the most profitable copper resources (Evans, 1979, Reddy et al., 2007). This cuprous sulphide mineral has two different crystal structures low chalcocite (below 103.5°C) or high chalcocite (above 103.5°C). In high chalcocite, S^{2-} anions are arranged hexagonally with highly mobile copper mainly in trigonal coordination (Buerger and Wuensch, 1963, Cava et al., 1981). The high chalcocite belongs to $P6_3/mmc$ space group and hexagonal cell of contains 2 formula units. Below the transition point, the Cu atom in low chalcocite become immobilized and are mainly in triangularly coordinated with S. The monoclinic unit cell of low chalcocite has 24 independent fully occupied Cu sites and independent 12 S in space group $P2_1/c$ and contains 48 formula units in each unit cell. The low chalcocite unit cell is a $3a \times 4b \times 2c$ supercell of the high chalcocite orthohexagonal cell i(Evans and Konnert, 1976).

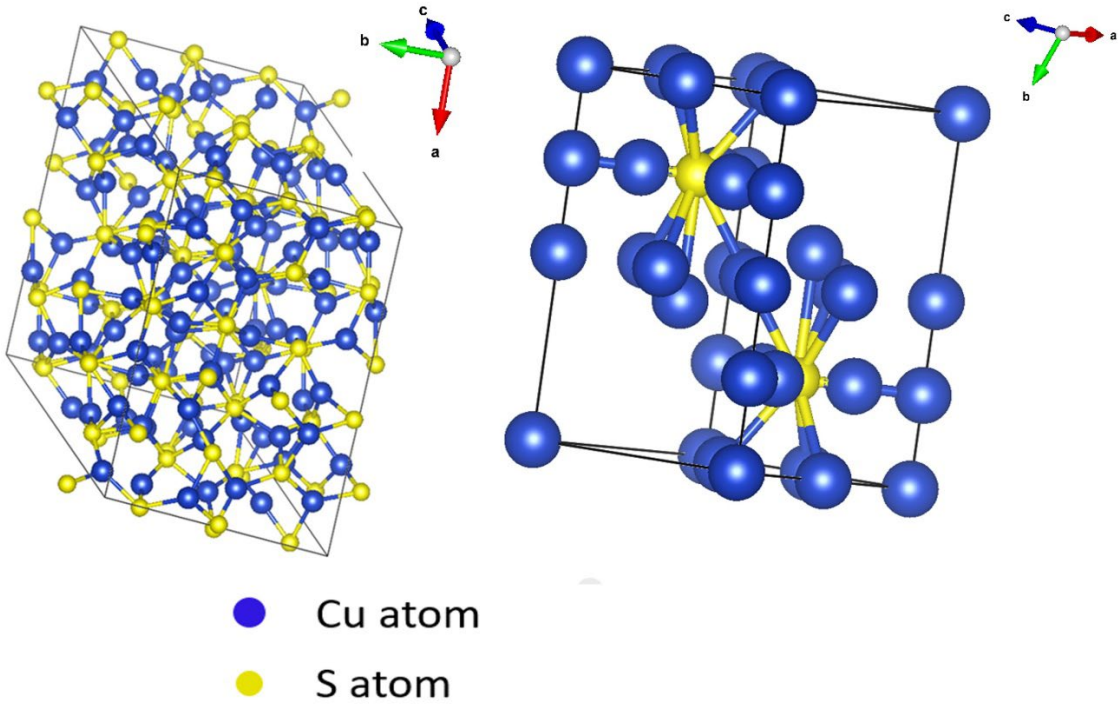

Figure 2: Schematic diagrams showing the crystal structure of low chalcocite (left) and high chalcocite (right).

Covellite (CuS) is commonly found along with chalcocite in supergene zone. Its crystal structure consists of alternating layers tetrahedrally coordinated Cu and trigonally coordinated Cu that linked by di-sulphide ions (Vaughan, 2006). The crystal structure has hexagonal symmetry at room temperature, which will transform to an orthorhombic symmetry when cooled below 55 K (Evans and Konnert, 1976). The electronic structure of covellite was reported to be similar to that of cupric (Cu^{2+}) sulphide, i.e. $(Cu^{+})_3(S^{2-})(S_2)^{-}$ (Liang and Whangbo 1993). However, a study by Kumar et al. (2013) showed that CuS contains Cu(I) at its trigonal sites and Cu(II) at the tetrahedral sites. Therefore, the appropriate ionic model of CuS is most likely to be $(Cu^{4/3+})_3(S_2^{2-})(S^{2-})$ (Mazin, 2012).

Digenite is an unusual Cu-bearing sulphide mineral found in both hypogene and supergene zones of copper deposits. It is deep blue to black in colour with a metallic lustre and is usually massive, with distinct crystals being rare. Digenite exists in three polymorphs including a high-temperature form, a low-temperature form and a transitional metastable form. Low digenite exists below 73°C, high digenite exists above 90°C and a transitional metastable phase forms between 73°C and 90°C (Morimoto and Kullerud, 1963, Will et al., 2002). Low digenite is a cubic in space group *Fd3m.* Morimoto and

Kullerud (1963) suggested that sulphur atoms likely form a cubic close-packed structure in the face-centred lattice, but the distribution of copper atoms was not discovered. High digenite belongs to the space group *Fm3m* with mobile Cu atoms (Morimoto and Kullerud, 1963).

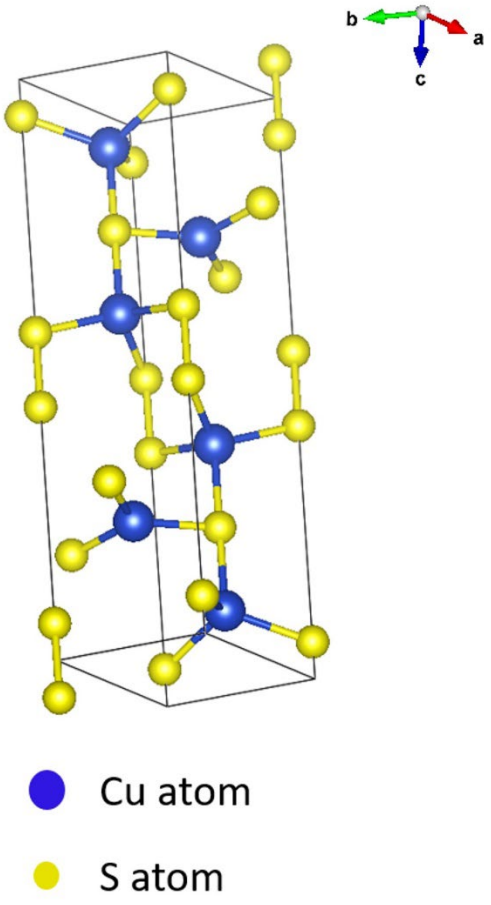

Figure 3 The crystal structure of covellite.

Roseboom (1966) constructed a phase diagram of Cu-S system and illustrated the stability of each copper sulphides phases across a range of at temperatures. Covellite was found to be stable at temperature up to 700°C, while digenite was found to have two different phases above and below 76°C, commonly known as digenite-low or digenite-high. Chalcocite has two different phases (low and high) above or below 103.5°C.

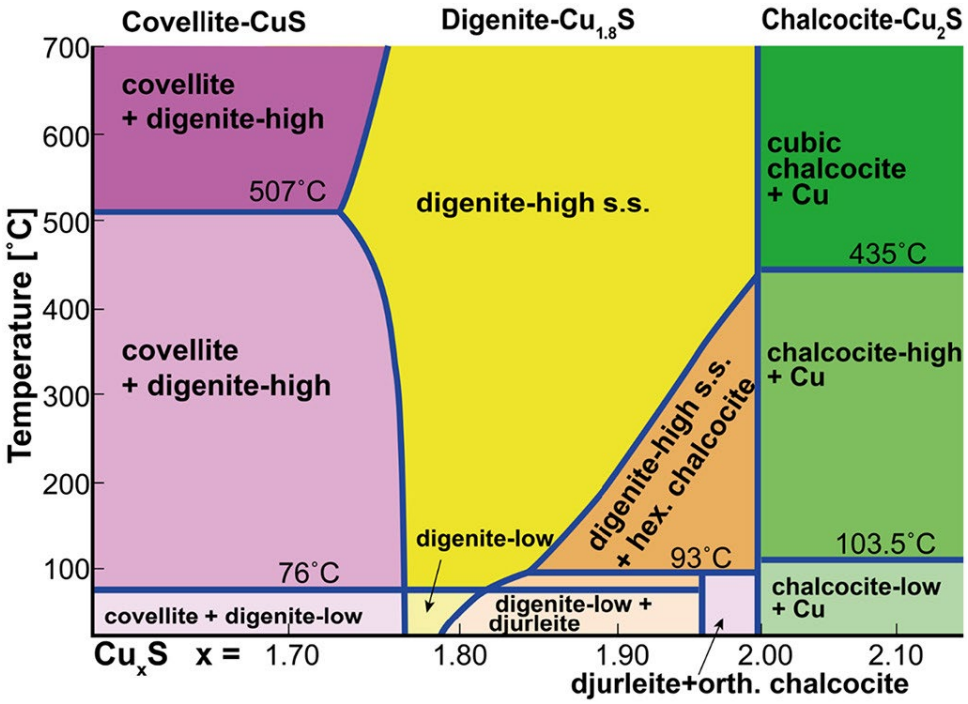

Figure 4 A phase diagram of the Cu-S system illustrating the stability of each copper sulphide mineral at different temperatures and Cu contents (Roseboom 1966).

1.3 Supergene Copper Deposits

The copper deposits general has supergene zone which intersects the water table and is below the oxidized zone. The supergene zones generally have a diversity in mineralogy. The metal deposits in supergene zone are generally have high grade of the ore, and it is relatively close to the Earth's surface makes it easy to access. Those two advantages make supergene mineral deposits have gained increasing attention. Supergene deposits are formed by processes that oxidize, dissolve and reconcentrate the metals buried beneath (Vasconcelos et al., 2015).

Supergene enrichment is a phenomenon that results in accumulation or concentration of metals *in situ*. Generally, it consists of three principal processes: 1) the electrochemical oxidation or dissolution of primary sulphides (e.g. $CuFeS_2$ to Cu^{2+}), oxides (e.g. CuO to Cu^{2+}) or native metals (e.g. native copper Cu(0) to Cu^{2+}) ; 2) the movement of the water-soluble metal species, such as $CuSO_4$ and $AuCl_4^-$; 3) the re-precipitation of the metals and supergene mineral deposits via reduction (e.g. Cu^{2+} to native copper Cu(0)), via supersaturation (e.g. formation of magnesite deposits by Mg^{2+}), or via cation-exchange (e.g. formation of smectite- or serpentine-group minerals by Ni^{2+} exchange for Mg^{2+})

(Vasconcelos et al., 2015, Reich et al., 2009, Sillitoe, 2005, Taylor, 2011). The Fe- and S-oxidizing bacteria commonly act as catalyst in the oxidation or leaching processes occurring in Nature. Leaching processes are influenced by various physicochemical properties, such as the pH of descending aqueous solutions, the partial pressure of oxygen (pO_2) and the redox potential (Eh) of the solution (Vasconcelos et al., 2015, Taylor, 2011).

1.3.1 Copper Oxidation and Enrichment in Supergene

Below the Earth's surface, the primary pyrite-bearing assemblages are hydrolysed and oxidised releasing hydrogen and sulphate ions, resulting in a decrease in the pH of in the descending ground water. Chalcopyrite are simultaneously breakdown releasing and oxidizing Cu^{+} to Cu^{2+} and SO_4^{2-} and transport downwards into the earth's crust encountering more reducing conditions. Equation 1 describes the breakdown (oxidation dissolution) of chalcopyrite in the earth's crust. The leaching process is accompanied by the precipitation of iron oxyhydroxides ($Fe(OH)_3$) in the leached zone with aqueous Cu^{2+} released from chalcopyrite oxidation dissolution. The leached zone of porphyry Cu deposits can reach several hundred meters in thickness, with deep enough water table for the supergene oxidation and enrichment processes (Taylor, 2011).

$$4CuFeS_{2(s)} + 17O_{2(g)} + 10H_2O_{(aq)} \rightarrow 4Fe(OH)_{3(s)} + 4Cu^{2+}{}_{(aq)} + 8SO_{4(aq)}^{2-} + 8H^{+}{}_{(aq)} \quad (1)$$

In the subjacent oxide zone, the concentration of copper is very high, and a variety of copper oxides can be found in this layer including cuprite (Cu_2O) and tenorite (CuO).. Those copper oxides are known as 'green oxides' due to the colour of mineral surface. In the 'green oxides' zone, mineral assemblages are precipitated, which are controlled by the different enclosing rock types and pH (Figure 6). The oxides layers are 200-300 m in thickness, with more than 1% wt% Cu grade (Vasconcelos et al., 2015). When the environment becomes more reduced, the secondary sulphides are formed with the remaining Cu and the metal- and sulphate- rich solution via oxidation dissolution of the hypogene sulphides (including pyrite, chalcopyrite and bornite). The free oxygen almost disappears in this process. Under the high Cu^{2+}/HS^{-} condition, secondary chalcocite can be formed in the top layers as illustrated in Figure 5. Under the lower Cu^{2+}/HS^{-} condition, the precipitation of covellite may occur (Vasconcelos et al., 2015).

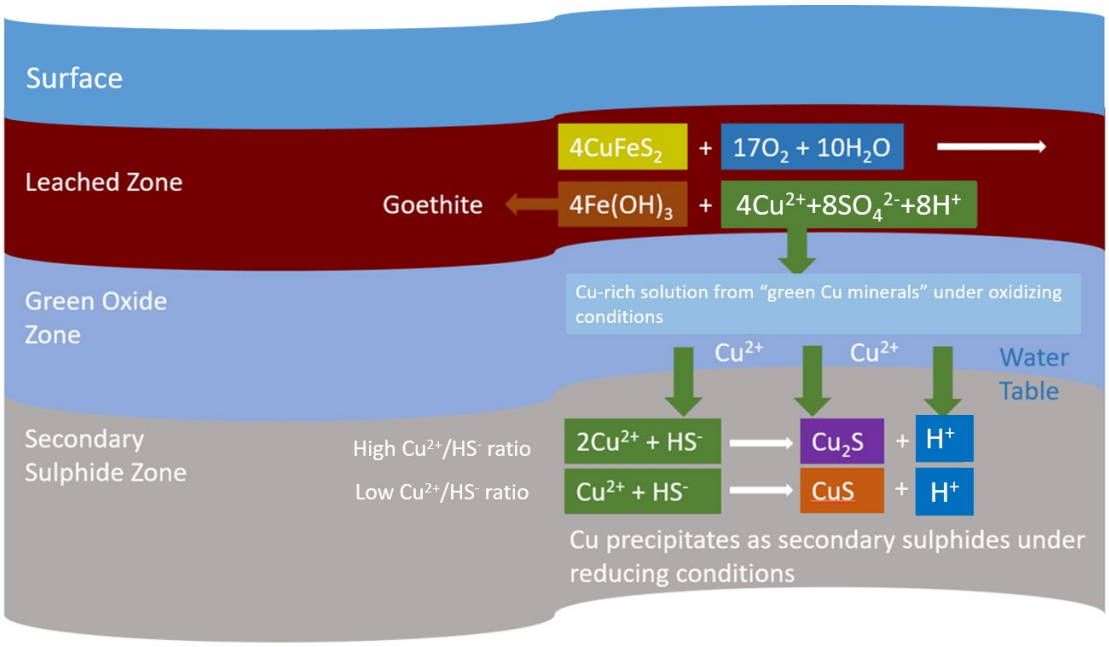

Figure 5: The schematic diagram of supergene oxidation and enrichment process of Cu (after Reich and Vasconcelos 2015).

Anderson (1982), Sillitoe (2005), Vasconcelos et al. (2015) have demonstrated the possible stable phases of supergene copper sulphide minerals in an Eh-pH phase diagram (Figure 6). In the saturated zone, chalcocite is relatively stable within pH 0-14, but covellite precipitate in the pH range of 0-9. The copper sulphide minerals are the dominant product in the enriched zone. The replacement of chalcopyrite by chalcocite or covellite has been reported in the Kuferschiefer ore in Poland (Oszczepalski, 1999, Chaudhari et al. 2021).

The thickness of enriched Cu sulphide zones in porphyry Cu deposits are generally tens to hundreds of meters which can contribute more than 1.5 gigatons of ore with 0.4-1.7 wt% Cu. In 2008, median Cu grade of 422 porphyry copper deposits is 0.44% (Singer et al., 2008). The Cu grades in the supergene metal deposits are relatively higher than in the hypogene sulphide minerals due to the Cu enrichment (Ayuso et al., 2010).

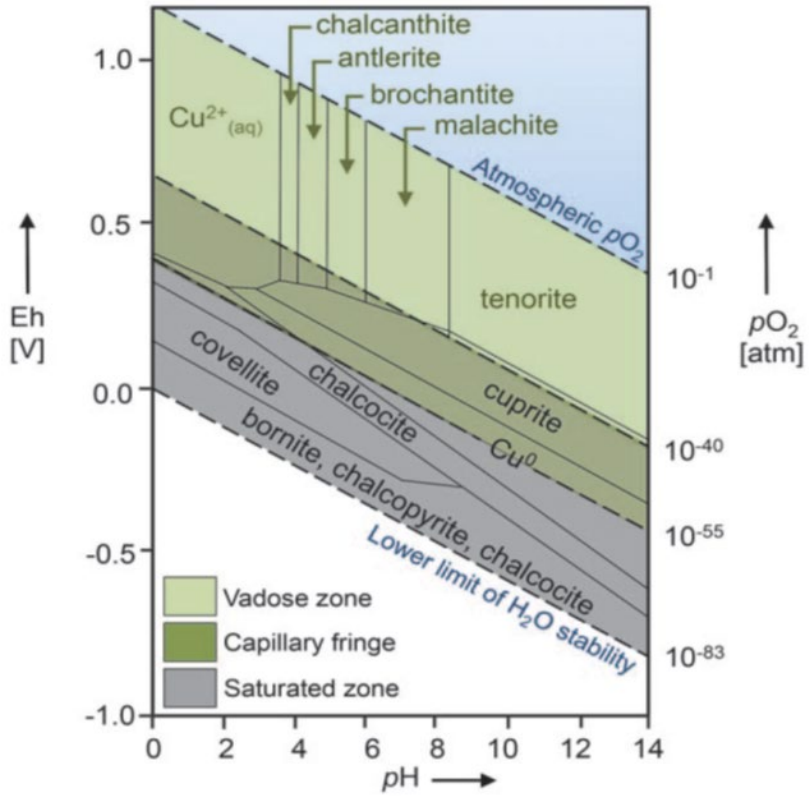

Figure 6 The phase diagram of redox potential (Eh) and partial oxygen pressure (pO_2) against the pH representing the stability of the supergene dissolved copper species and copper minerals (after Reich and Vasconcelos 2015). **Conditions assumed: 25°C and 1 atm.**

1.4 Mineral Replacement Reactions

Mineral replacement reactions generally take place when a mineral or mineral assemblage interact with a fluid. This is because the system will tend to re-equilibrate to reduce the free energy of the entire system. The dissolution of a mineral or mineral assemblage and the precipitation of a product are the principal mechanisms of the mineral replacement reaction. In Nature, mineral replacement reactions occur frequently, including chemical weathering, metasomatism, metamorphism, and leaching. The common characteristics and textural features of a fluid-mediated mineral replacement reaction has been reviewed by Putnis (2009) as follows: a) The preservation of the external dimension and internal details of the parent mineral by product phase; b) There is a sharp reaction front between the parent and product minerals; c) The product mineral contains numerous pores and/or cracks which allows the reaction front to consistently interact with the fluid; d) The parent and product minerals have an epitaxic relationship when they have the same crystal

structure; e) When the replacement reaction is associated with significant changes in volume between the parent and product minerals, pores and fractures will be generated at the reaction front. Table 1 summarised the previous studies on mineral replacement reactions.

Table 1 Some examples of studies into the Nature of mineral replacement reactions.

Mineral Replacement Reaction Studies	Reference
Quartz → Gibbsite	Nahon and Merino (1997)
Calcite → Fluorite	Putnis (2009), Sippel and Glover (1965)
Aragonite, Calcite → Hydroxyapatite	Kasioptas et al. (2008)
KBr → KCl	Putnis and Mezger (2004), Putnis et al. (2005)
Leucite → Analcime	Putnis et al. (1994), Putnis et al. (2007)
Bone → Calcite	Pewkliang et al. (2008)
Calcite → Opal	Pewkliang et al. (2008)
Magnetite → Pyrite	Qian et al. (2010)
Pyrrhotite → Pyrite/Marcasite	Qian et al. (2011)
$SrSO_4$ → SrF_2/$Sr(OH)_2$	Rendón-Angeles et al. (2006)
Pentlandite → Violarite	Tenailleau et al. (2006), Xia et al. (2009)
Calaverite → Gold	Zhao et al. (2009)
Chalcopyrite → Bornite	Zhao et al. (2014b)
Hematite → Chalcopyrite/Bornite	Zhao et al. (2014a)
Magnetite → Hematite	Zhao et al. (2019)
Bornite and Chalcocite → Digenite	Hidalgo et al. (2019)
Chalcopyrite → Covellite/Digenite	Chaudhari et al. (2021)
Bornite → Chalcopyrite/Copper Sulphides	Adegoke et al. (2022)

Figure 7 has illustrated the mineral replacement reaction of magnetite (Fe_3O_4) by pyrite (FeS_2) at 125°C and pH 4 for 504 hours (Qian et al., 2010). In the first stage, magnetite is dissolved by H^+ and H_2S and is released Fe^{2+} in the solution at reaction front. Once the concentration of aqueous Fe^{2+} becomes supersaturated, precipitation of pyrite will occur on the surface of magnetite. The replacement reaction initiates at the surface of magnetite and then proceeds towards the core of magnetite until all magnetite has dissolved. For pyrite, numerous pores and cracks have been observed which enables the hydrothermal fluid to continuously interacts with the interface between magnetite and pyrite.

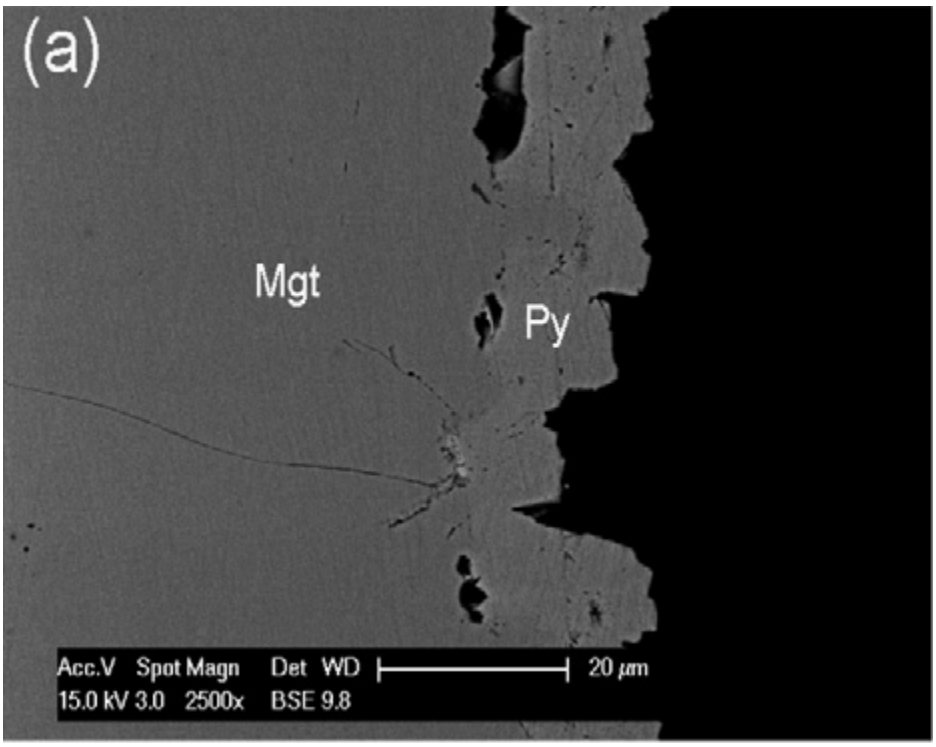

Figure 7 The backscatter image of the mineral replacement reaction of magnetite by pyrite at 125°C and pH 4 for 504 hours (Qian et al. 2010)

1.4.1 Pseudomorphic Replacement

The key feature of a pseudomorphic replacement reactions is the preservation of external shape of primary minerals by secondary minerals. The degree of spatial pseudomorph of the coupling mineral replacement reactions has been reported to vary from the nanometre scale to the millimetre scale depending on cases (Xia et al. 2009). Rendón-Angeles et al. (2006) carried out the replacement reaction of $SrSO_4$ by $SrF_2/Sr(OH)_2$ under hydrothermal conditions. SrF_2 has preserved the very fine textural features of $SrSO_4$ in the nanometre scale, but $Sr(OH)_2$ only preserves the external features at the large scale. Tenailleau et al. (2006) and Xia et al. (2009) investigated the replacement of pentlandite $(Fe, Ni)_9S_8$ by violarite $(Ni, Fe)_3S_4$ and the roles of temperature and fluid composition in the mineral replacement reaction. In the studies of Xia et al. (2009), the concept of the scale of pseudomorphism was proposed to describe the degree of spatial coupling between the dissolution and precipitation process. They reported that in this case the change of the coupling between the primary mineral and the secondary mineral depends on the pH of the reaction solution. When the reaction solutions are between pH 1-6, the rate-limiting step is the dissolution of pentlandite and the nanometre scale preservation of the

morphology and internal details of the parent phase by the product has been observed. The precipitation of violarite appears to be rate-limiting under strong acidic condition (pH<1) and the product only roughly preserved the morphology of pentlandite with a length scale of 10's of microns rather than nanometre. Figure 8 illustrates the importance of the coupling between the dissolution rate of the parent and the precipitation rate of the daughter product. When the precipitation rate is slower than the dissolution rate, a fluid gap between the parent mineral and product phase will be formed at reaction front. The fluid gap is widened if precipitation is slower than dissolution as illustrated in Figure 8a. On the other hand, the fluid gap could not be formed when the precipitation rate is equal to, or faster than the dissolution rate, resulting in preservation as illustrated in Figure 8b. Therefore, the degree of coupling between the dissolution and precipitation rate determines the scale of morphological preservation of the reaction (Putnis, 2002, Putnis, 2009, Altree-Williams et al., 2015).

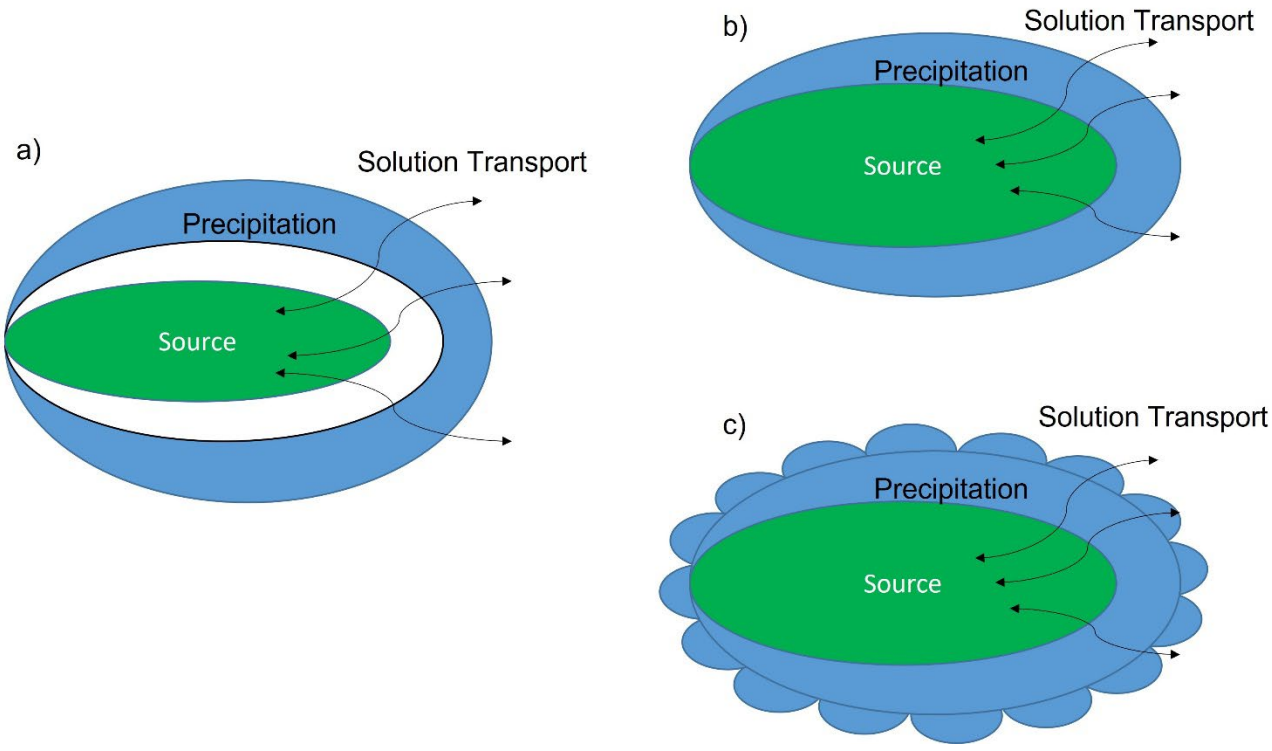

Figure 8 The schematic diagram of the effect of the coupling degree between dissolution and precipitation on the gap generation at the reaction front between the parent and product minerals. a) loose coupling when dissolution rate is greater than precipitation rate; b) coupled parent mineral dissolution and product mineral precipitation; c) overgrowth

because of the overall external dimension of the product phase is larger than the parent grain.

1.4.2 Porosity and Cracks

The generation of pores and cracks is very important feature of mineral replacement reactions in that they strongly affect the rate of the replacement of the parent minerals by the product minerals. The porosity is also interacting with fluid pathways, which affects the patterns of replacement. However, the relationship between the pre-existing fluid flow paths and reaction-induced porosity affects fluid flow are poorly understood. Four different mechanisms of porosity generation in mineral replacement reaction are proposed as follows: 1) formation 'homogeneous' reaction-induced porosity in the product; 2) formation of reaction-induced microfracturing at the reaction front; 3) generation of grain boundaries; 4) formation of cleavage planes and twin boundaries (Altree-Williams et al., 2015).

Reaction-induced pores enables the fluid is constantly contact with the replacement reaction front, with mass transport between the bulk solution and the reaction interface. In the replacement of leucite ($KAlSi_2O_6$) by analcime ($NaAlSi_2O_6 \cdot H_2O$), Xia et al. (2009b) reported a typical reaction-induced porosity in the product textures, which is controlled by the nucleation rate and growth mechanism of the daughter phase. The overall volume change in the replacement reaction is also affects the textures. A highly ordered pore network is observed in the product texture, which provides a pathway of species transport between reaction front and bulk solution. The product nucleation mechanism controls the nature of the porosity in the non-pseudomorphic replacement, when the rate-limiting step is the precipitation (Altree-Williams et al., 2015).

Reaction-induced fractures are reported to be an important factor in the enhancement of mineral replacement reactions (Janssen et al., 2010, Plümper et al., 2012, Jamtveit et al., 2009). The formation of fractures is related to the deformation and deviatoric stresses affiliated with tectonic processes (Iyer et al., 2008, Putnis and Austrheim, 2010). Many studies reported ICDR replacement reactions have influenced on fracture propagation (Putnis et al., 2007, Jamtveit et al., 2009, Plümper et al., 2012). Plümper et al. (2012) suggested the fracture propagation is initialized by stress accumulation in a ICDR replacement with defected surface on parent phase.

The formation of fractures is also associated with the volume changes between the parent phase and product phase in a mineral replacement reaction. During the replacement reaction, both tensile and compressional stresses are generated at the reaction front between parent and product phase. Fractures are formed by the accumulated stresses, which is more than the tensile strength of the parent phase or product phase. The patterns of fractures formed are depends on the volume change (Altree-Williams et al., 2015). In the replacement of pyrrhotite by pyrite/marcasite, Qian et al. (2011) has found the volume of parent mineral (pyrrhotite) is reduced by 31% and 29% respectively, and large number of fractures are formed in the final product (pyrite and marcasite). However, a 60% increased volume was found in the replacement reaction of magnetite to pyrite or marcasite (Qian et al., 2010). A significant number of pores and fractures has been produced in the final product phase in order to preserve the external morphology from parent phase.

In a relative dry system, the mass transport in mineral replacements is associated with the fluid-saturated grain boundaries as it provides a pathway for diffusion (Altree-Williams et al., 2015). The mass transport associated with grain boundaries is found an order of magnitude faster than with reaction-induced porosity (Jonas et al., 2014).

Twin boundaries and cleavage planes are found in the mineral replacement with irregularly shaped reaction front formation, which are important roles in the mass transport. In the replacement of calcite (CaCO3) by siderite (FeCO3) and dolomite (CaMg(CO3)2), Pearce et al. (2013) reported the products nucleate along the twin boundaries of parent phase. Zhao et al. (2014b) found that bornite is continuing replace chalcopyrite along the cleavage planes of chalcopyrite after the reaction-induced porosity is disappeared as the reaction progresses.

1.5 Formation of Copper Sulphides

The processes of supergene enrichment of copper sulphide have been investigated by Mcgauley et al. (1956) and used for metallurgical purposes. They mixed chalcopyrite with cupric sulphate solution and heated up to 160-230 °C. The following reaction equation (2) has been proposed. Chalcopyrite was treated with cupric sulphate solution under 180-200 °C as the equation (3) (Johnson and Coltrinari 1976).

$$CuFeS_{2(s)} + CuSO_{4(aq)} \rightarrow 2CuS_{(S)} + FeSO_{4(aq)} \quad (2)$$

$$3CuFeS_{2(aq)} + 6CuSO_{4(aq)} + 4H_2O_{(aq)} \rightarrow 5Cu_{1.8}S_{(s)} + 3FeSO_{4(aq)} + 4H_2SO_{4(aq)} \quad (3)$$

This reaction was reported by Sohn (1981) in the temperature range of 55-90 °C. The replacement rate was found to be very slow under these low temperature conditions. Sohn (1981) suggested that covellite is an intermediate product in the reaction (equation 2). A further enrichment of covellite has been observed which converted to digenite as equation (4).

$$6CuS_{(s)} + 3CuSO_{4(aq)} + 4H_2O_{(aq)} \rightarrow 5Cu_{1.8}S_{(s)} + 4H_2SO_{4(aq)} \quad (4)$$

Chalcopyrite can also undergo the oxidation enrichment without adding cupric sulphate as represented by equation (5). Jones (1974) observed covellite and elemental sulphur as the final product above 140 °C (equation 5). In the study of the solubility of chalcopyrite conducted by Icikuni (1960), they found reaction (6) is very slow and only Fe^{2+} ions were solubilized.

$$CuFeS_{2(s)} + 2H^+{}_{(aq)} + O_{2(g)} \rightarrow CuS_{(s)} + Fe^{2+}{}_{(aq)} + S^0{}_{(s)} + H_2O_{(aq)} \quad (5)$$

$$CuFeS_{2(s)} + 2H^+{}_{(aq)} \rightarrow CuS_{(s)} + Fe^{2+}{}_{(aq)} + H_2S_{(aq)} \quad (6)$$

1.6 Mineral Replacement Reaction of Chalcopyrite

Jang (1992) has reported experiments on the hydrothermal conversion of chalcopyrite to copper sulphides under 170-200 °C with 0.5 M sulphuric acid. The formation of covellite and defected chalcocite (digenite) were found. They proposed chalcopyrite is converted to covellite and then defected chalcocite (digenite) as represented by the anodic half-cell electrochemical reaction (7), (8) and (9).

$$CuFeS_{2(s)} + 4H_2O_{(aq)} \rightarrow CuS_{(s)} + Fe^{2+}{}_{(aq)} + SO^{2-}_{4(aq)} + 8H^+{}_{(aq)} + 8e^- \quad (7)$$

$$CuS_{(s)} + 4H_2O_{(aq)} \rightarrow Cu^{2+}{}_{(aq)} + SO^{2-}_{4(aq)} + 8H^+{}_{(aq)} + 8e^- \quad (8)$$

$$2CuS_{(aq)} + Cu^{2+}{}_{(aq)} + 2e^- \rightarrow Cu_2S_{(aq)} \quad (9)$$

Zhao et al. (2014a) reported the replacement reaction of hematite by both chalcopyrite and bornite via sulfidation at temperatures 200-300 °C in solutions containing Cu(I) and

hydrogen sulphide. The replacement reaction proceeds via coupled dissolution-reprecipitation with an increase of volume (230%) from the primary mineral (hematite) to the product mineral (chalcopyrite). Adegoke et al. (2022) investigated the replacement reaction of bornite by copper sulphides at temperatures 160-200 °C via fluid-induced solid-state diffusion and coupled dissolution-reprecipitation. Chalcopyrite lamellae coated by digenite was formed homogenously in the whole bornite grains by removing Fe^{3+}. Chalcopyrite was successfully replaced by bornite in solutions containing Cu(I) and hydrosulphides in the temperature range of 200-320 °C. Digenite was found as a by-product of the replacement reaction and the fraction is decreased as the temperature increased from 200 °C (53%) to 320°C (10%) (Zhao et al., 2014b). The replacement reaction of chalcopyrite by copper sulphides in $CuCl_2$ and H_2SO_4 solutions at temperatures in the range (180 to 300 °C) was investigated using an *in situ* cell in synchrotron powder X-ray diffraction. Chalcopyrite was replaced by digenite-high at or above 200 °C or above via interfacial dissolution-reprecipitation mechanism (Chaudhari et al., 2021).

Overall, five factors can affect the reaction of hydrothermal replacement of chalcopyrite by covellite or chalcocite according to the previous studies of the enrichment of chalcopyrite. The first one is the addition of cupric ions solution and both covellite and defect chalcocite (digenite $Cu_{1.8}S$) can be formed. The addition of oxygen is the second factor and the covellite is most likely to be formed. Temperature is the third factor which has the influence on the reaction rate. The other two factors are the pH of the solution (Xia et al., 2009) and the particle size of chalcopyrite (Kimball et al., 2010, Tester et al., 1994).

1.7 Dissolution of Covellite

Covellite dissolution under acidic conditions has been extensively studied. Thomas and Ingraham (1967) investigated the leach kinetics of synthetic covellite using 0.1 M sulfuric acid and 0.25 M ferric sulphate at temperature from 25 to80 °C. The leaching reaction of covellite is predominated by Equation (10). Ferric ions are the active agent in the leaching process. Dutrizac and MacDonald (1974) also studied the dissolution of covellite in acidic sulphate solution from 55-95 °C. They found elemental sulphur formed as the principal sulfuric species during the leaching process as Equation (11).

$$CuS_{(S)} + 4H_2O_{(aq)} + 8{Fe^{3+}}_{(aq)} \rightarrow {Cu^{2+}}_{(aq)} + 8{H^{+}}_{(aq)} + SO^{2-}_{4(aq)} + 8{Fe^{2+}}_{(aq)} \quad (10)$$

$$CuS_{(s)} + 2{Fe^{3+}}_{(aq)} \rightarrow {Cu^{2+}}_{(aq)} + 2{Fe^{2+}}_{(aq)} + {S^{0}}_{(s)} \quad (11)$$

$$2CuS_{(s)} + O_{2(aq)} + 4H^{+}{}_{(aq)} + 2Cl^{-}{}_{(aq)} \rightarrow 2CuCl^{+}{}_{(aq)} + 2H_2O_{(aq)} + S^{0}{}_{(s)} \quad (12)$$

Covellite dissolution in oxygenated alkaline solutions were also conducted with complex forming agents, ethylene diamine tetra-acetic acid (EDTA) and ethylene diamine (EDA). The dissolution rate is dependent on the reagent concentration and pH value of solutions (Tomásek and Neumann, 1982). Baba et al. (2017) studied the natural covellite dissolution in alkaline ammonia solutions over the temperature range of 25-75 °C. They found stable $Cu(NH_3)_4^{2+}$ complexes when covellite dissolves in $NH_4OH/(NH_4)_2SO_4$ solutions as Equation (13).

$$CuS_{(s)} + 4NH_4OH_{(aq)} + 2(NH_4)_2SO_{4(aq)} \rightarrow Cu[(NH_3)_4]^{2+}{}_{(aq)} + 3SO^{2-}_{4(aq)} + 4NH^{+}_{4(aq)} + 4H_{2(g)} \quad (13)$$

1.8 Glycine

Glycine is an α-amino acid consisting of a carboxylic acid group and an amine group (Figure 9A). It is an environmentally friendly reagent and can be easily digested in most living organisms. In aqueous solutions, glycine can exist as three different forms which are cation, zwitterion and anion. The equilibrium equation can be expressed as shown in Figure 9B (Turner and Johnson, 1962). Another advantage of glycine is that it can enhance the Cu ions solubility in aqueous solution by chelating copper (Aksu and Doyle, 2002). The stoichiometric equation of the formation of Cu-glycinate complex in alkaline solution can be described by Equation (14).

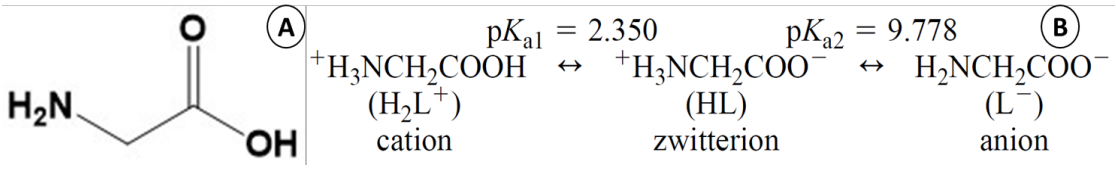

Figure 9 A) The chemical structure of glycine. **B)** The equilibrium equation of glycine three aqueous forms cation, zwitterion and anion.

$$Cu^{2+}{}_{(aq)} + 2NH_2CH_2COOH_{(aq)} + 2OH^{-}{}_{(aq)} \rightarrow Cu(NH_2CH_2COO)_{2(aq)} + 2H_2O_{(aq)} \quad (14)$$

Oraby and Eksteen (2014) used glycine as lixiviant agent to leach Cu selectively from a gold-copper concentrate. They reported 98% of copper dissolved within 48 h under

ambient conditions at pH 11, indicating that glycine might be able to leach Cu from copper-bearing minerals. Tanda et al. (2017) studied the copper extraction from copper oxide minerals in aqueous alkaline glycine solutions. They found the dissolution of malachite, azurite and cuprite is very fast when the glycine to copper molar ratio is 4:1. A few studies focused on Cu leaching from chalcopyrite in alkaline glycine solutions (Eksteen et al., 2017, Tanda et al., 2019, Khezri et al., 2021, Shin et al., 2019b). Eksteen et al. (2017) proposed a conceptual process to collect Cu from chalcopyrite in alkaline glycine solution. They proposed that chalcopyrite dissolution in alkaline glycine solution occurs via Equation (15). Tanda et al. (2019) investigated the kinetics and surface analysis and found iron oxyhydroxide(s) on the leach residue surface. Tanda et al. (2018) investigated the kinetics and mechanism of chalcocite leaching in alkaline glycine solutions. They proposed the chalcocite leaching consists of two stages of chemical reactions as presented in Equation (16) and (17). They reported the formation of covellite on the residue surface and confirmed this by SEM-EDX and XPS during the first stage of leaching process. Covellite are further dissolved by glycine and hydroxide ions and form cupric ions and sulphate ions.

$$CuFeS_{2(s)} + 2NH_2CH_2COOH_{(aq)} + 3OH^-{}_{(aq)} + 4.5O_{2(g)} \rightarrow Cu(NH_2CH_2COOH)_{2(aq)} + FeO(OH)_{(s)} + 2SO_{4(aq)}^{2-} + 2H_2O_{(aq)} \quad (15)$$

$$Cu_2S_{(s)} + 2NH_2CH_2COOH_{(aq)} + 0.5O_{2(g)} \rightarrow Cu(NH_2CH_2COOH)_{2(aq)} + CuS_{(s)} + H_2O_{(aq)} \quad (16)$$

$$CuS_{(s)} + 2NH_2CH_2COOH_{(aq)} + 2OH^-{}_{(aq)} + 2O_{2(g)} \rightarrow Cu(NH_2CH_2COOH)_{2(aq)} + SO_{4(aq)}^{2-} + 2H_2O_{(aq)} \quad (17)$$

Covellite dissolution in alkaline glycine solution is not fully understood yet. Glycine is selected as a chemical reagent as it is environmentally friendly and biodegradable. It also has the potential be able to apply in *in-situ* covellite leaching. Chapter 5 is focused on the covellite dissolution with glycine under alkaline conditions.

1.9 Research Objective

The goal of this research project is investigate the mechanism and kinetics of transformation chalcopyrite to covellite or digenite *in-situ* and extract Cu through *in-situ* copper sulphides dissolution at relatively low temperature conditions. Chapter 2 describes the methodology and techniques used to achieve this goal. Chapter 3 is focused on the

understanding of mechanism and kinetics for the replacement of chalcopyrite to covellite. Experiments were conducted under hydrothermal conditions (120-200 °C) and various pH conditions to investigate the optimal condition for the replacement reaction. Kinetic data was fitted using the *Avrami* equation. The rate constant and the 'modified time to a given fraction' methods were used to calculate the activation energy of replacement reactions and covellite dissolution. The replacement reaction rate at room temperature was estimated using extrapolate kinetic data.

Chapter 4 is focus on the replacement of chalcopyrite to digenite or covellite under hydrothermal condition (140-200 °C) in acidic solution (pH 1-3). $CuSO_4$ or $CuCl_2$ was added to achieve the Cu enrichment of chalcopyrite and form digenite. Activation energy of chalcopyrite dissolution was determined by the rate constant method and the 'modified time to a given fraction' method.

Chapter 5 presents a study on the covellite dissolution using an environmentally friendly chemical reagent. Glycine in alkaline solutions were selected to investigate the dissolution rate at low temperatures (25-55 °C). Shrinking core model was used to determine the reaction rate constant. Activation energy was calculated by *Arrhenius* equation.

A conclusion of the overall experiment results and findings is presented in Chapter 6. The future work and implication of this research project are discussed in Chapter 6.

1.10 Reference List

ADEGOKE, I. A., XIA, F., DEDITIUS, A. P., PEARCE, M. A., ROBERTS, M. P. & BRUGGER, J. 2022. A new mode of mineral replacement reactions involving the synergy between fluid-induced solid-state diffusion and dissolution-reprecipitation: A case study of the replacement of bornite by copper sulfides. Geochimica et Cosmochimica Acta.

AKSU, S. & DOYLE, F. M. 2002. The role of glycine in the chemical mechanical planarization of copper. Journal of the Electrochemical Society, 149, G352.

ALIYU, H. & NA'ALIYA, J. 2012. Potentiometric studies on essential metal (II) amino acid complexes. International Research Journal of Pharmacy Pharmacology 2, 76-80.

ALTREE-WILLIAMS, A., PRING, A., NGOTHAI, Y. & BRUGGER, J. 2015. Textural and compositional complexities resulting from coupled dissolution–reprecipitation reactions in geomaterials. Earth-Science Reviews, 150, 628-651.

ANDERSON, J., A, 1982. Characteristics of Leached Capping and Techniques of Appraisal. In: TITLEY, S. R. (ed.) Advances in Geology of the Porphyry Copper Deposits, Southwestern North America: Tuson. USA: University of Arizona Press.

AYUSO, R. A., BARTON, M. D., BLAKELY, R. J., BODNAR, R. J., DILLES, J. H., GRAY, F., GRAYBEAL, F. T., MARS, J. L., MCPHEE, D. K. & SEAL II, R. R. 2010. Porphyry copper deposit model: Chapter B in Mineral deposit models for resource assessment. US Geological Survey.

BABA, A. A., BALOGUN, A. F., BALE, R. B., ADEKOLA, F. A. & ALABI, A. G. 2017. Treatment of a Nigerian covellite ore. Part I: Dissolution kinetics study by ammonia solution. Russian Journal of Non-Ferrous Metals, 58, 1-7.

BUERGER, M. & WUENSCH, B. 1963. Distribution of atoms in high chalcocite, Cu2S. Science, 141, 276-277.

CAVA, R., REIDINGER, F. & WUENSCH, B. 1981. Mobile ion distribution and anharmonic thermal motion in fast ion conducting Cu2S. Solid State Ionics, 5, 501-504.

CHAUDHARI, A., WEBSTER, N. A., XIA, F., FRIERDICH, A., RAM, R., ETSCHMANN, B., LIU, W., WYKES, J., BRAND, H. E. & BRUGGER, J. 2021. Anatomy of a complex mineral replacement reaction: role of aqueous redox, mineral nucleation, and ion transport properties revealed by an in-situ study of the replacement of chalcopyrite by copper sulfides. Chemical Geology, 581, 120390.

CHENG, C. Y. & LAWSON, F. 1991. The kinetics of leaching covellite in acidic oxygenated sulphate-chloride solutions. Hydrometallurgy, 27, 269-284.

DUTRIZAC, J. & MACDONALD, R. 1974. The kinetics of dissolution of covellite in acidified ferric sulphate solutions. Canadian metallurgical quarterly, 13, 423-433.

EKSTEEN, J., ORABY, E. & TANDA, B. 2017. A conceptual process for copper extraction from chalcopyrite in alkaline glycinate solutions. Minerals Engineering, 108, 53-66.

EVANS, H. & KONNERT, J. 1976. Crystal structure refinement of covellite. American Mineralogist, 61, 996-1000.

EVANS, H. T. 1979. The crystal structures of low chalcocite and djurleite. Zeitschrift für Kristallographie-Crystalline Materials, 150, 299-320.

FUENTES-ACEITUNO, J., LAPIDUS-LAVINE, G. & GONZÁLEZ-MARTÍNEZ, I. 2008. Electrochemical characterization of the solid products formed in the electro-assisted reduction of chalcopyrite. Hydrometallurgy 2008. Society for Mining, Metallurgy and Exploration, Inc.(SME) Littleton ….

GOH, S. W., BUCKLEY, A. N., LAMB, R. N., ROSENBERG, R. A. & MORAN, D. 2006. The oxidation states of copper and iron in mineral sulfides, and the oxides formed on initial exposure of chalcopyrite and bornite to air. Geochimica et Cosmochimica Acta, 70, 2210-2228.

HIDALGO, T., KUHAR, L., BEINLICH, A. & PUTNIS, A. 2019. Kinetics and mineralogical analysis of copper dissolution from a bornite/chalcopyrite composite sample in ferric-chloride and methanesulfonic-acid solutions. Hydrometallurgy, 188, 140-156.

ICIKUNI, M. 1960. On the Dissolution of the Mineral Sulfides in Various Media II: Dissolution of Pyrite and Chalcopyrite. Bull. Chem. Soc. Japan, 33(3), 1052-1057.

IYER, K., JAMTVEIT, B., MATHIESEN, J., MALTHE-SØRENSSEN, A. & FEDER, J. 2008. Reaction-assisted hierarchical fracturing during serpentinization. Earth Planetary Science Letters, 267, 503-516.

IZATT, R., OSCARSON, J., GILLESPIE, S., GRIMSRUD, H., RENUNCIO, J. & PANDO, C. 1992. Effect of temperature and pressure on the protonation of glycine. Biophysical journal, 61, 1394-1401.

JAMTVEIT, B., PUTNIS, C. V. & MALTHE-SØRENSSEN, A. 2009. Reaction induced fracturing during replacement processes. Contributions to Mineralogy Petrology, 157, 127-133.

JANG, J. H. 1992. Hydrothermal Conversion of Chalcopyrite to Copper Sulfide. Doctor of Philosophy in Metallurgy PhD Thesis, University of Utah.

JANSSEN, A., PUTNIS, A., GEISLER, T. & PUTNIS, C. 2010. The experimental replacement of ilmenite by rutile in HCl solutions. Mineralogical Magazine, 74, 633-644.

JOHNSON, R. K. & COLTRINARI, E. L. 1976. Recovery of copper from chalcopyrite utilizing copper sulfate leach. U.S.A patent application.

JONAS, L., JOHN, T., KING, H. E., GEISLER, T. & PUTNIS, A. 2014. The role of grain boundaries and transient porosity in rocks as fluid pathways for reaction front propagation. Earth Planetary Science Letters, 386, 64-74.

JONES, D. L. 1974. The leaching of chalcopyrite. Doctor of Philosophy in Metallurgy, University of British Columbia.

KASIOPTAS, A., PERDIKOURI, C., PUTNIS, C. & PUTNIS, A. 2008. Pseudomorphic replacement of single calcium carbonate crystals by polycrystalline apatite. Mineralogical Magazine, 72, 77-80.

KHEZRI, M., REZAI, B., ABDOLLAHZADEH, A. A., WILSON, B. P., MOLAEINASAB, M. & LUNDSTRÖM, M. 2021. Investigation into the effect of mechanical activation on the leaching of chalcopyrite in a glycine medium. Hydrometallurgy, 203, 105492.

KIMBALL, B. E., RIMSTIDT, J. D. & BRANTLEY, S. L. 2010. Chalcopyrite dissolution rate laws. Journal of Applied Geochemistry, 25, 972-983.

KUMAR, P., NAGARAJAN, R. & SARANGI, R. 2013. Quantitative X-ray absorption and emission spectroscopies: electronic structure elucidation of Cu 2 S and CuS. Journal of Materials Chemistry C, 1, 2448-2454.

LIANG, W. & WHANGBO, M.-H. 1993. Conductivity anisotropy and structural phase transition in covellite CuS. Solid State Communications, 85, 405-408.

MAZIN, I. Structural and Electronic properties of the 2D Superconductor CuS covellite with 113-valent Copper. APS March Meeting Abstracts, 2012. Q21. 008.

MCGAULEY, P. J., SCHAUFELBERGER, F. A. & ROHERTS, E. S. 1956. Selective replacement of metal sulfides. U.S. patent application.

MORIMOTO, N. & KULLERUD, G. 1963. Polymorphism in digenite. American Mineralogist: Journal of Earth Planetary Materials 48, 110-123.

MUSSEL, W., MURAD, E., FABRIS, J., MOREIRA, W., BARBOSA, J., MURTA, C., ABRAHÃO, W., DE MELLO, J. & GARG, V. 2007. Characterization of a chalcopyrite from Brazil by Mössbauer spectroscopy and other physicochemical techniques. Physics and Chemistry of Minerals, 34, 383-387.

NAHON, D. & MERINO, E. 1997. Pseudomorphic replacement in tropical weathering; evidence, geochemical consequences, and kinetic-rheological origin. American Journal of Science, 297, 393-417.

NAKAI, I., SUGITANI, Y., NAGASHIMA, K. & NIWA, Y. 1978. X-ray photoelectron spectroscopic study of copper minerals. Journal of Inorganic Nuclear Chemistry, 40, 789-791.

NAKAMURA, M. & WATSON, E. 2001. Experimental study of aqueous fluid infiltration into quartzite: implications for the kinetics of fluid redistribution and grain growth driven by interfacial energy reduction. Geofluids, 1, 73-89.

NORTHEY, S., MOHR, S., MUDD, G. M., WENG, Z. & GIURCO, D. 2014. Modelling future copper ore grade decline based on a detailed assessment of copper resources and mining. Resources, Conservation Recycling, 83, 190-201.

ORABY, E. & EKSTEEN, J. 2014. The selective leaching of copper from a gold–copper concentrate in glycine solutions. Hydrometallurgy, 150, 14-19.

OSZCZEPALSKI, S. 1999. Origin of the Kupferschiefer polymetallic mineralization in Poland. Mineralium Deposita, 34, 599-613.

PEARCE, M. A., TIMMS, N. E., HOUGH, R. M. & CLEVERLEY, J. S. 2013. Reaction mechanism for the replacement of calcite by dolomite and siderite: implications for geochemistry, microstructure and porosity evolution during hydrothermal mineralisation. Contributions to Mineralogy Petrology, 166, 995-1009.

PETIAU, J., SAINCTAVIT, P. & CALAS, G. 1988. K X-ray absorption spectra and electronic structure of chalcopyrite CuFeS2. Materials Science Engineering: B, 1, 237-249.

PEWKLIANG, B., PRING, A. & BRUGGER, J. 2008. The formation of precious opal: clues from the opalization of bone. The Canadian Mineralogist, 46, 139-149.

PLÜMPER, O., RØYNE, A., MAGRASÓ, A. & JAMTVEIT, B. 2012. The interface-scale mechanism of reaction-induced fracturing during serpentinization. Geology, 40, 1103-1106.

PUTNIS, A. 1992. An introduction to mineral sciences, Cambridge University Press.

PUTNIS, A. 2009. Mineral replacement reactions. Reviews in mineralogy and geochemistry, 70, 87-124.

PUTNIS, A. & AUSTRHEIM, H. 2010. Fluid-induced processes: metasomatism and metamorphism. Geofluids, 10, 254-269.

PUTNIS, A., PUTNIS, C. V. & GIAMPAOLO, C. 1994. The Microstructure of Analcime Phenocrysts in Igneous Rocks. European Journal of Mineralogy, 66, 689-708.

PUTNIS, C. V., GEISLER, T., SCHMID-BEURMANN, P., STEPHAN, T. & GIAMPAOLO, C. 2007. An experimental study of the replacement of leucite by analcime. American Mineralogist, 92, 19-26.

PUTNIS, C. V. & MEZGER, K. 2004. A mechanism of mineral replacement: isotope tracing in the model system KCl-KBr-H2O. Geochimica et Cosmochimica Acta, 68, 2839-2848.

PUTNIS, C. V., TSUKAMOTO, K. & NISHIMURA, Y. 2005. Direct observations of pseudomorphism: compositional and textural evolution at a fluid-solid interface. American Mineralogist, 90, 1909-1912.

QIAN, G., FAN, R., HUANG, J., PRING, A., HARMER, S. L., ZHANG, H., REA, M. A. D., BRUGGER, J., TEASDALE, P. R. & GIBSON, C. T. 2021. Oxidative dissolution of sulfide minerals in single and mixed sulfide systems under simulated acid and metalliferous drainage conditions. Environmental Science Technology, 55, 2369-2380.

QIAN, G., BRUGGER, J., SKINNER, W. M., CHEN, G. & PRING, A. 2010. An experimental study of the mechanism of the replacement of magnetite by pyrite up to 300 C. Geochimica et Cosmochimica Acta, 74, 5610-5630.

QIAN, G., XIA, F., BRUGGER, J., SKINNER, W. M., BEI, J., CHEN, G. & PRING, A. 2011. Replacement of pyrrhotite by pyrite and marcasite under hydrothermal conditions up to 220 C: An experimental study of reaction textures and mechanisms. American Mineralogist, 96, 1878-1893.

RAJ, D. & CHANDRA, K. 1968. Mössbauer studies of chalcopyrite. Journal of the Physical Society of Japan, 24, 39-41.

RAKOVAN, J. 2003. A Word to the Wise: Hypogene & Supergene. Rocks & Minerals, 78, 419.

REDDY, S. L., FAYAZUDDIN, M., FROST, R. L. & ENDO, T. 2007. Electron paramagnetic resonance and optical absorption spectral studies on chalcocite. Spectrochimica Acta Part A: Molecular Biomolecular Spectroscopy, 68, 420-423.

RENDÓN-ANGELES, J., PECH-CANUL, M., LÓPEZ-CUEVAS, J., MATAMOROS-VELOZA, Z. & YANAGISAWA, K. 2006. Differences on the conversion of celestite in solutions bearing monovalent ions under hydrothermal conditions. Journal of Solid State Chemistry, 179, 3645-3652.

ROSEBOOM, E. H. 1966. An investigation of the system Cu-S and some natural copper sulfides between 25 degrees and 700 degrees C. Economic Geology, 61, 641-672.

SHIN, D., AHN, J. & LEE, J. J. H. 2019. Kinetic study of copper leaching from chalcopyrite concentrate in alkaline glycine solution. 183, 71-78.

SILLITOE, R. H. 2005. Supergene Oxidized and Enriched Porphyry Copper and Related Deposits

SINGER, D. A., BERGER, V. I. & MORING, B. C. 2008. Porphyry copper deposits of the world: Database and grade and tonnage models: USGS Open-File Report 2008-1155. *USGS: Reston, VA, USA*.

One Hundredth Anniversary Volume. In: HEDENQUIST, J. W., THOMPSON, J. F. H., GOLDFARB, R. J. & RICHARDS, J. P. (eds.). Society of Economic Geologists.

SIPPEL, R. F. & GLOVER, E. D. 1965. Structures in carbonate rocks made visible by luminescence petrography. Science, 150, 1283-1287.

SOHN, H. 1981. Chemical and Electrochemical Conversion of Chalcopyrite to Copper Sulfide. Ph. D. , The University of Utah.

TANDA, B., EKSTEEN, J. & ORABY, E. 2017. An investigation into the leaching behaviour of copper oxide minerals in aqueous alkaline glycine solutions. Hydrometallurgy, 167, 153-162.

TANDA, B., EKSTEEN, J. & ORABY, E. 2018. Kinetics of chalcocite leaching in oxygenated alkaline glycine solutions. Hydrometallurgy, 178, 264-273.

TANDA, B., EKSTEEN, J., ORABY, E. & O'CONNOR, G. 2019. The kinetics of chalcopyrite leaching in alkaline glycine/glycinate solutions. Minerals Engineering, 135, 118-128.

TESTER, J. W., WORLEY, W. G., ROBINSON, B. A., GRIGSBY, C. O. & FEERER, J. L. 1994. Correlating quartz dissolution kinetics in pure water from 25 to 625 C. Geochimica et Cosmochimica Acta, 58, 2407-2420.

TENAILLEAU, C., PRING, A., ETSCHMANN, B., BRUGGER, J., GRGURIC, B. & PUTNIS, A. 2006. Transformation of pentlandite to violarite under mild hydrothermal conditions. American Mineralogist, 91, 706-709.

THOMAS, G. & INGRAHAM, T. 1967. Kinetics of dissolution of synthetic covellite in aqueous acidic ferric sulphate solutions. Canadian Metallurgical Quarterly, 6, 153-165.

TOMÁSEK, J. & NEUMANN, L. 1982. Dissolution of secondary copper sulphides using complex-forming agents (EDTA, EDA). Part I: Covellite dissolution in EDTA and EDA. International Journal of Mineral Processing, 9, 23-40.

TURNER, D. & JOHNSON, G. 1962. The effect of some addition agents on the kinetics of copper electrodeposition from a sulfate solution: I. Cathode potential-current density relation. Journal of the Electrochemical Society, 109, 798.

VASCONCELOS, P. M., REICH, M. & SHUSTER, D. L. J. E. 2015. The paleoclimatic signatures of supergene metal deposits. Elements, 11, 317-322.

VAUGHAN, D. J. 2006. Sulfide mineralogy and geochemistry, Mineralogical Society of America.

VELOSO, T. C., PAIVA, P. R. P., SILVA, C. A. & LEÃO, V. A. 2016. Leaching of Bornite Produced from the Sulfurization of Chalcopyrite. Metallurgical Materials Transactions B, 47, 2005-2014.

WATLING, H. 2013. Chalcopyrite hydrometallurgy at atmospheric pressure: 1. Review of acidic sulfate, sulfate–chloride and sulfate–nitrate process options. Hydrometallurgy, 140, 163-180.

WILL, G., HINZE, E. & ABDELRAHMAN, A. R. M. 2002. Crystal structure analysis and refinement of digenite, Cu1. 8S, in the temperature range 20 to 500 C under controlled sulfur partial pressure. European Journal of Mineralogy, 14, 591-598.

XIA, F., BRUGGER, J., CHEN, G., NGOTHAI, Y., O'NEILL, B., PUTNIS, A. & PRING, A. 2009. Mechanism and kinetics of pseudomorphic mineral replacement reactions: A case study of the replacement of pentlandite by violarite. Geochimica et Cosmochimica Acta, 73, 1945-1969.

ZHAO, J., BRUGGER, J., CHEN, G., NGOTHAI, Y. & PRING, A. 2014b. Experimental study of the formation of chalcopyrite and bornite via the sulfidation of hematite: Mineral replacements with a large volume increase. American Mineralogist, 99, 343-354.

ZHAO, J., BRUGGER, J., GRUNDLER, P. V., XIA, F., CHEN, G. & PRING, A. 2009. Mechanism and kinetics of a mineral transformation under hydrothermal conditions: Calaverite to metallic gold. American Mineralogist, 94, 1541-1555.

ZHAO, J., BRUGGER, J., NGOTHAI, Y. & PRING, A. 2014a. The replacement of chalcopyrite by bornite under hydrothermal conditions. American Mineralogist, 99, 2389-2397.

ZHAO, J., BRUGGER, J. & PRING, A. 2019. Mechanism and kinetics of hydrothermal replacement of magnetite by hematite. Geoscience Frontiers, 10, 29-41.

CHAPTER 2 METHODOLOGY

The research reported in this thesis has involved the use of a number of experimental methods and analytical techniques. These methods included sample characterization and crushing, preparation of buffer solution, powder X-ray diffraction, scanning electron microscopy, inductively coupled plasma optical emission spectroscopy and X-ray photoemission spectroscopy. These methods and techniques together with the instrumentation used are briefly described below.

2.1 Chalcopyrite and Covellite Sample

The natural mineral chalcopyrite sample used in mineral replacement reaction experiments is sourced from multiple mining sites of China and mixed homogeneously after grinding. Covellite used in leaching experiments is sourced from Montana, USA. The identifications and purity of chalcopyrite and covellite were established using a powder X-ray diffractometer (Bruker D8 Advance Eco) at Flinders University. XRD analysis indicates that the natural chalcopyrite sample (Figure 10) contains 97±5 wt% chalcopyrite and 3±1.5 wt% quartz, and the natural covellite sample (Figure 11) contains 3±1.5 wt% pyrite, 14±2.5 wt% chalcopyrite and 83±4.7 wt% covellite. Chalcopyrite and covellite were crushed with a jaw crusher and a rolling mill, then wet-sieved into four different size fractions of 38-75 μm, 75-150 μm, 150-425 μm and 425-1020 μm.

All mineral particles were washed in an ultrasonic bath with distilled water to remove the fine particles on the surface. 3 M hydrochloric acid solution was used to dissolve the oxidised layer on the mineral particle surface. The sample was washed with 50%, 70% and 100% ethanol one by one from lowest to highest concentration to remove the water and left under vacuum for drying. All washed mineral samples were stored in a freezer below -80 °C prior to use in experiments.

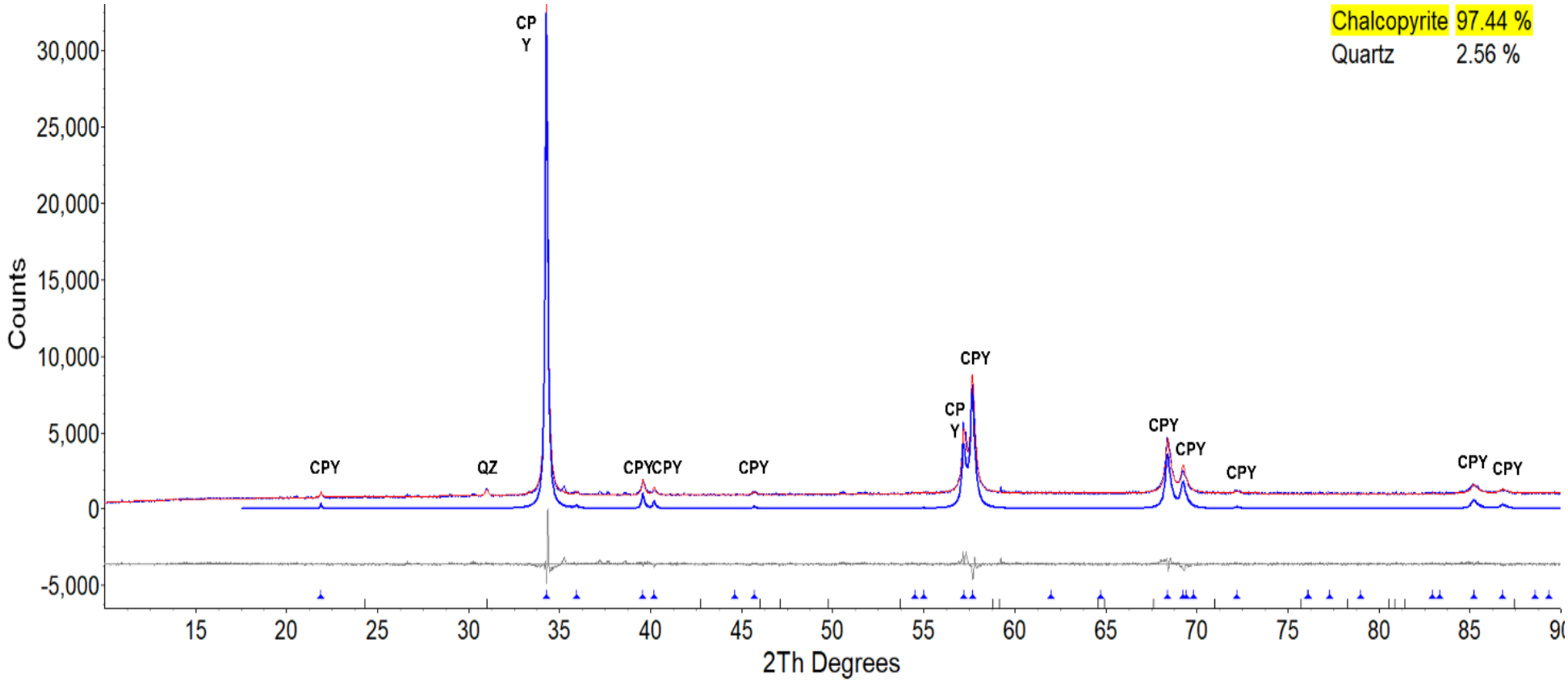

Figure 10 The XRD patterns of the unreacted chalcopyrite sample sourced from multiple minting of China. The blue marker reflects the position of chalcopyrite.

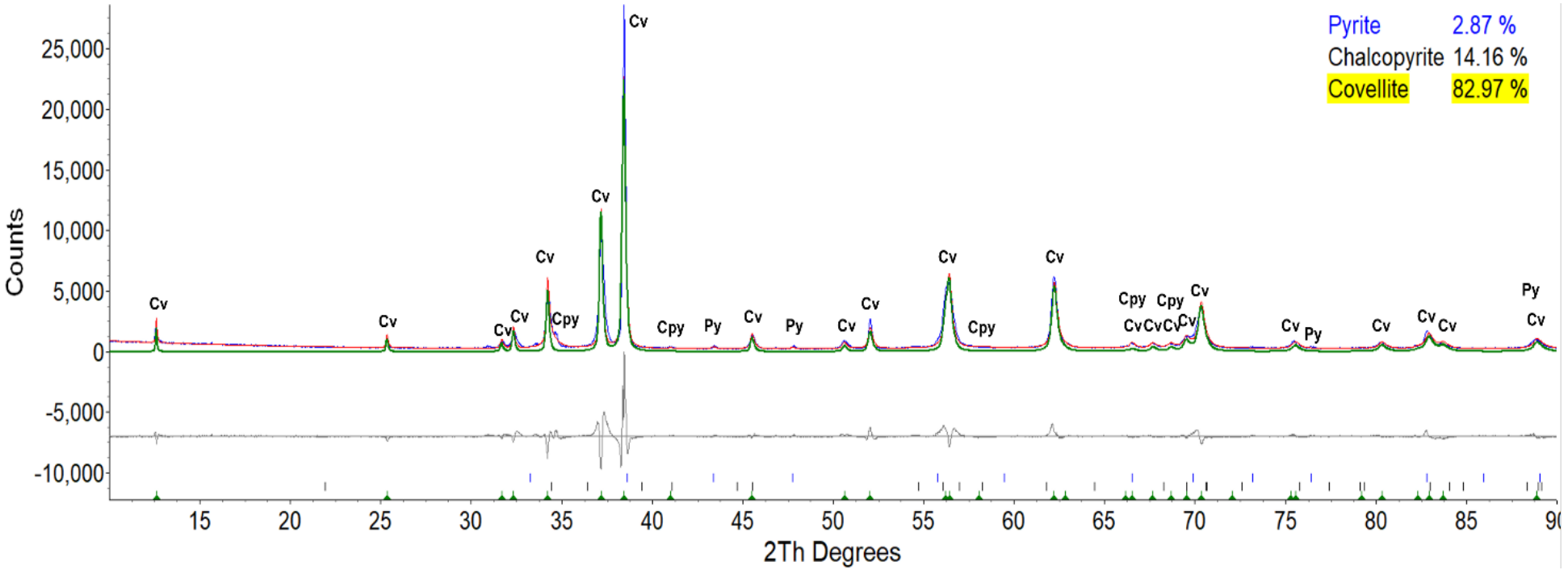

Figure 11 The XRD patterns of the unreacted covellite sample sourced from Montana, USA. The green marker reflects the position of covellite.

The elemental composition of natural chalcopyrite was measured using ICP-MS. 0.25 g of mineral sample was dissolved in 5 ml Aqua regia in an Anton Parr ECO microwave. Samples were made up to 50 ml and diluted as necessary for analysis. Each elemental composition analysis was performed in triplicate. The natural chalcopyrite sample was found to consist of 29.16 ± 0.53% Fe, 34.93 ± 1.09% Cu, 0.12 ± 0.003% Pb, 0.02 ± 0.0003% Zn, 0.005 ± 0.0006% Ni and 35.76 ± 0.52% S.

Two natural covellite sample (250 mg) were digested in two separate Teflon digestion tubes containing Aqua Regia (5 ml) and heated up in an Anton Parr microwave (175 °C) prior to analysis. After the samples were cooled to room temperature and diluted up to 50 ml with Milli-Q water. Each sample were analysed in duplicated for ICP-OES to determine the concentration of Cu, Fe and S, ICP-MS for As, Pb, Zn, Ni and Mn. The elemental composition of covellite sample is summarised in Table 3, consisted of 31.11 ± 3.03% S, 67.48 ± 1.08% Cu, 1.41 ± 0.09% Fe and trace amount of As, Pb, Zn, Ni and Mn (0.001%).

Table 2 The elemental composition of natural chalcopyrite used in mineral replacement reaction experiments determined by ICP-MS.

Elemental Composition	Fe	Cu	Pb	Zn	Ni	S
Concentration (mg/g)	288	345	1.2	0.2	0.05	354
wt%	29.16	34.93	0.12	0.02	0.005	35.76

Table 3 The elemental composition of natural covellite used in covellite dissolution in alkaline glycine solution determined by ICP-MS.

Elemental Composition	Fe	Cu	Pb	As	Zn	Ni	Mn	S
Concentration (mg/g)	12.4	635	0.01	0.01	0.01	0.01	0.01	315
wt%	1.41	67.48	0.001	0.001	0.001	0.001	0.001	31.11

2.2 Preparation of Buffer Solutions

Buffer solutions were prepared at pH 0.7, 1, 1.5, 3, 4, 5, 6, 7, 9 and 11 for the mineral replacement reaction experiments. Each buffer solution was prepared using Milli-Q water. The components of the buffer solutions are summarized in Table 4. Hydrochloric acid and potassium chloride solutions were used for pH 1 and 2 buffer solutions as per previous

mineral replacement reaction studies (Xia et al., 2009, Qian et al., 2010, Qian et al., 2011). Acetic acid and sodium acetate solutions were used for pH 3, 4 and 5 buffer solutions (Xia et al., 2009, Zhao et al., 2009, Qian et al., 2011, Zhao et al., 2014).. The pathways used to synthesize covellite by replacing chalcopyrite aerobically and anaerobically were proposed as equations (18) and (19) respectively. Therefore, those acids and conjugated bases are selected to prepare the buffer solutions in this research.

$$CuFeS_{2(s)} + 2H^{+}{}_{(aq)} + O_{2(aq)} \rightarrow CuS_{(s)} + Fe^{2+}{}_{(aq)} + S^{0}{}_{(s)} + H_2O_{(aq)} \quad (18)$$

$$CuFeS_{2(aq)} + 2H^{+}{}_{(aq)} \rightarrow CuS_{(s)} + Fe^{2+}{}_{(aq)} + H_2S_{(aq)} \quad (19)$$

In order to form digenite, additional $CuCl_2$ solutions were added to complete the Cu enrichment on chalcopyrite as the following reaction equation (20).

$$3CuFeS_{2(aq)} + 6CuCl_{2(aq)} + 2H^{+}{}_{(aq)} + 2O_{2(g)} \rightarrow 5Cu_{1.8}S_{(s)} + 3FeCl_{2(aq)} + H_2SO_{4(aq)} + 6Cl^{-}{}_{(aq)} \quad (20)$$

Solutions used in covellite leaching experiments were prepared by dissolving specific amounts of glycine (0.5 M) in Milli-Q water, followed by pH adjustment to 11 with addition of NaOH pellets.

The initial pH of each buffer solution was measured at room temperature using a temperature-corrected pH/Ion/mV Meter (Thermo Electron Corporation, model Orion 720A+) with an Ag/AgCl pH probe. Probe calibrations were performed daily using QUASPEX standard buffer solutions including KH-phthalate buffer ($pH_{25°C}$ 4.01), phosphate ($pH_{25°C}$ 7.00), and carbonate buffer ($pH_{25°C}$ 10.01).

Table 4 The buffer solutions and their composition.

Buffer Solutions	Initial $pH_{20°C}$	Component
pH 0.5	0.70	0.316 M HCl
pH 1	1.01	0.111 M HCl + 0.05 M KCl
pH 1.5	1.52	0.035 M HCl + 0.05 M KCl
pH 2	2.01	0.011 M HCl + 0.05 M KCl
pH 2.5	2.52	0.004 M HCl + 0.05 M KCl
pH 3	3.09	0.098 M CH_3COOH + 0.018 M CH_3COONa
pH 4	4.66	0.033 M CH_3COOH + 0.036 M CH_3COONa
pH 5	5.75	0.012 M CH3 COOH + 0.140 M CH3COONa
pH 6	6.02	0.006 M NaOH + 0.05 M KH2PO4
pH 7	7.13	0.029 M NaOH + 0.05 M KH2PO4

pH 9	9.47	0.00046 M HCl + 0.125 M Na2[B4O5(OH)4]·8H2O
pH 11	11.67	0.0041 M NaOH + 0.025 M Na2HPO4

2.3 Apparatus

The hydrothermal replacement reactions of chalcopyrite to covellite or digenite were conducted using the 25 mL polytetrafluoroethylene-lined (PTFE) jackets (Figure 12) The maximum working temperature for the PTFE cells is approximately 220 °C, and therefore it is safe to be used in the hydrothermal experiments in this research project (120-200 °C). Reactors were heated up in ovens set at specific temperature as shown in Figure 14. The stainless-steel jacketed PTFE cells were quenched by cold water after reaction. Solutions were collected for pH measurement and ICP-OES analysis, and solid products were obtained for SEM and XRD analyse.

Covellite dissolution experiments were conducted in 1 L glass reactor vessels with magnetic stirrers applied for stirring on a hot plate. The temperature was checked twice a day by a thermometer to ensure it is stable. Each reactor was equipped with a lid that contained 5 ports and each port was sealed by parafilm to avoid the solution loss from except when one of the ports was required for N_2 or compressed air purging required. The solid-weight to liquid-volume ratio of all covellite leaching experiments was set up to 4 g/L. pH of the solution were regularly checked with the same pH meter used in mineral replacement reactions. Solutions were collected and filtered using Millipore syringe filter of 0.45 μm for ICP-OES analysis. The leaching residue was collected for SEM imaging and EDAX and qualitative XRD analysis to identify the formed solid product.

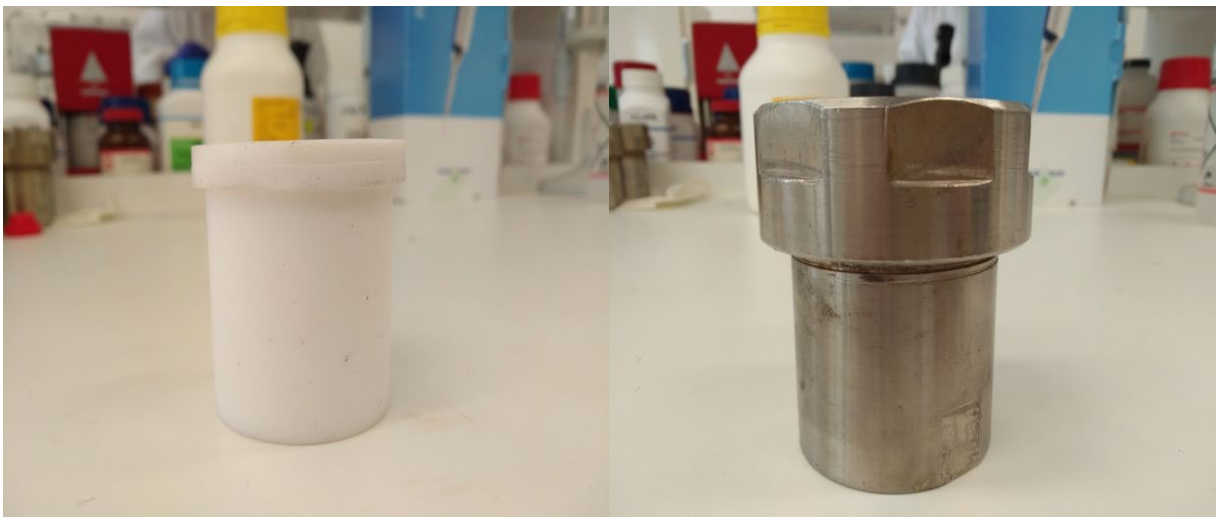

Figure 12 The PTFE cell (Left) and stainless-steel jacket (Right) used in hydrothermal replacement reaction of chalcopyrite to covellite or digenite.

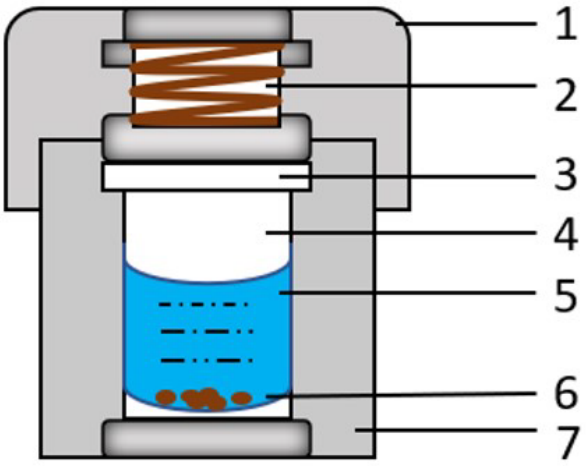

Figure 13 Schematic diagram of PTFE cells equipped with stainless-steel jacket. 1 stainless steel cap, 2 stainless steel spring, 3 PTFE cap, 4 PTFE body, 5 buffer solution, 6 mineral particles, 7 stainless steel body.

Figure 14 The ovens used in this research project to heat up. The maximum temperature of ovens is 500°C.

Figure 15 The reactor used in covellite leaching experiments equipped with condenser.

2.4 Powder X-ray Diffraction

Powder X-ray diffraction (XRD) is a commonly used technique to both qualitatively and quantitatively analyse crystalline powdered samples. The principal theory of XRD is based on the Bragg's law written as equation (21)

$$n\lambda = 2d \sin\theta \qquad (21)$$

In equation (21), *n* is an integer determined by the order given (±1, ±2, etc.) λ represents the wavelength of incident X-ray, *d* is the distance of crystal {hkl} planes, and θ is the diffraction angle. The constructive interference occurs at a specific angle when *2dsinθ* equal to an integer multiple of the X-ray wavelength. Pecharsky and Zavalij (2008) has given more detailed principles of XRD.

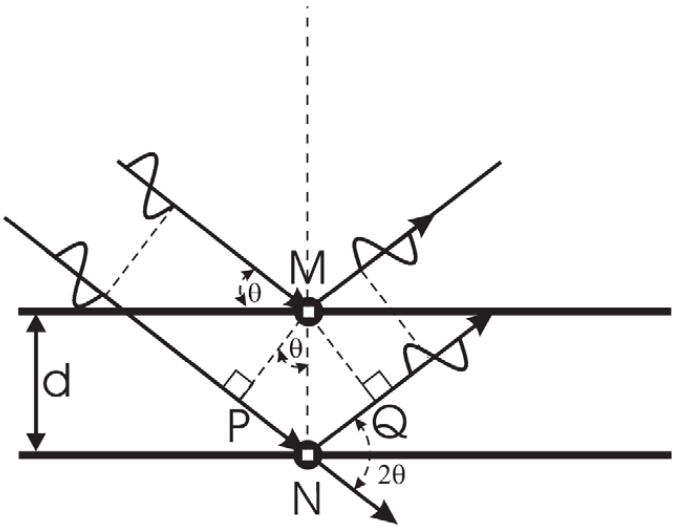

Figure 16 The illustration of Bragg's law. (Dinnebier and Billing, 2008)

In this project, XRD in Flinders Microscopy and Microanalysis (FMMA) was used to identify the composition of the primary mineral and final solid products from the hydrothermal reactions and covellite leaching experiments. Samples were ground with acetone before loaded onto the rotatory stage. Co $K\alpha_1$ X-radiation (λ = 1.790 Å) generated at 35 kV and 28 mA was used to collect the mineral phase information of sample with 2θ angel ranging from 10° to 90° with 0.0195° increment. Each spectrum was collected with 4106 steps with 0.6 seconds per step. A strong preferred orientation was observed on the XRD patterns of the synthetic covellite from the {0 0 6} planes (Figure 17). Capillary tube stage was then

used to quantify the synthetic covellite collected from the mineral replacement reaction in order to minimize the preferred orientation from the {0 0 6} planes (Figure 18). The quenched product was grounded with acetone and loaded into a silica glass capillary tube (0.7 mm in diameter). The XRD patterns were collected with 2θ angle from 30° to 90°, due to the poor background from 10° to 30°, with the same increment and rotation speed The mineral phase identification was conducted using Bruker Diffrac Eva V4.1.1 program with PDF-4 2020 database.

The XRD data of chalcopyrite and covellite were summarized in the following tables (Table 5, 6 and 7). The XRD patterns of natural chalcopyrite sample have strong diffractions from {1 1 2}, {2 2 0}, {0 2 4}, {3 1 2} and {0 3 3} planes. The synthetic covellite showed {0 1 2}, {0 1 3}, {0 0 6}, {0 1 7}, {1 1 0}, {0 1 8} and {1 1 6} diffractions. Chalcopyrite {1 1 2} diffraction and covellite {0 1 2} diffraction at 34° of 2θ angle, overlapped significantly. Therefore, chalcopyrite residue was identified using two typical {*hkl*} diffractions at 58° and 59° after the mineral replacement reaction. Digenite can be identified based on diffractions from {*hkl*} planes of {1 1 1}, {0 0 2}, {0 2 2}, {3 1 0}, {3 1 1} and {0 0 4}.

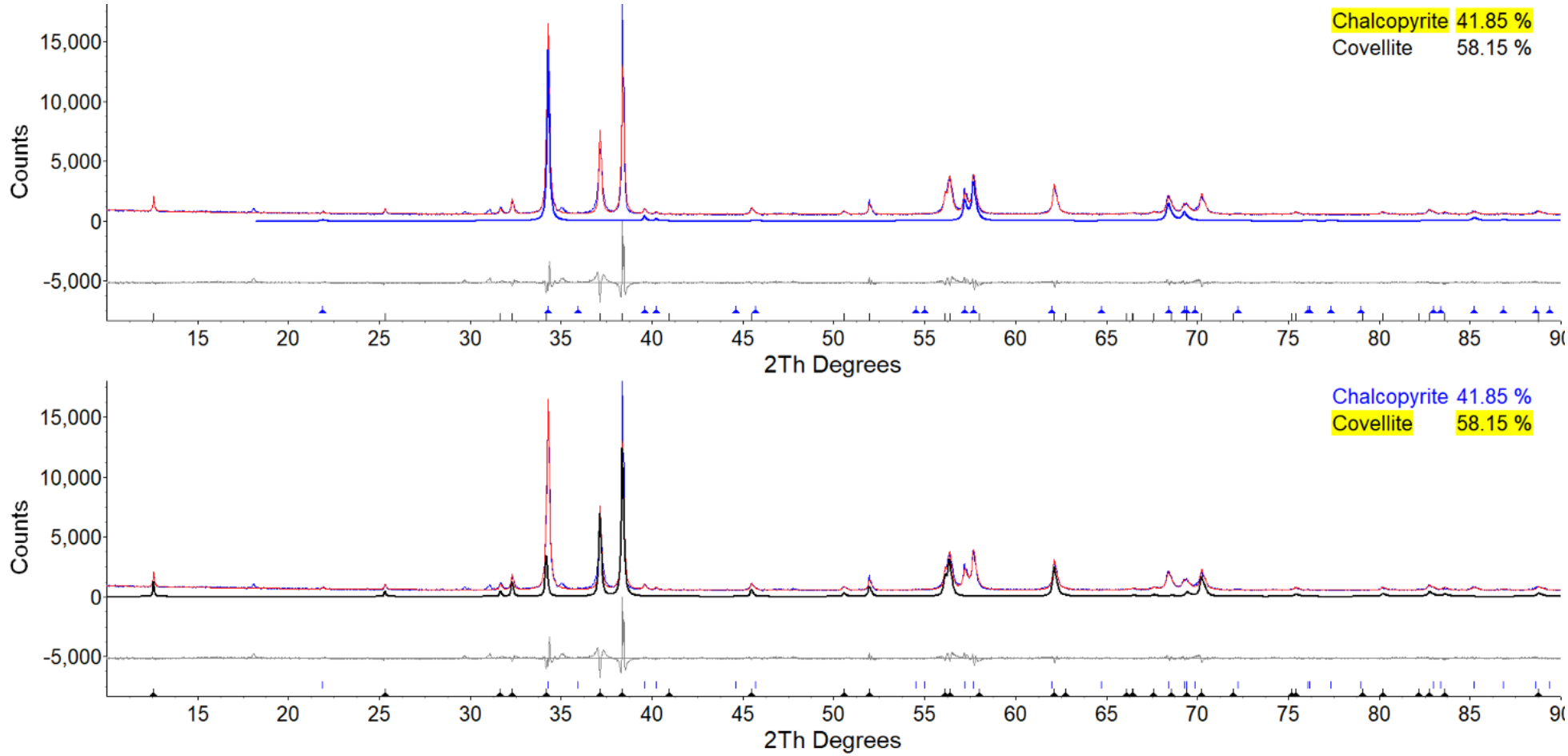

Figure 17 X-ray powder diffraction patterns of natural chalcopyrite and synthetic covellite in mineral replacement reaction. Sample loaded on the zero-background silicon substrate rotary stage.

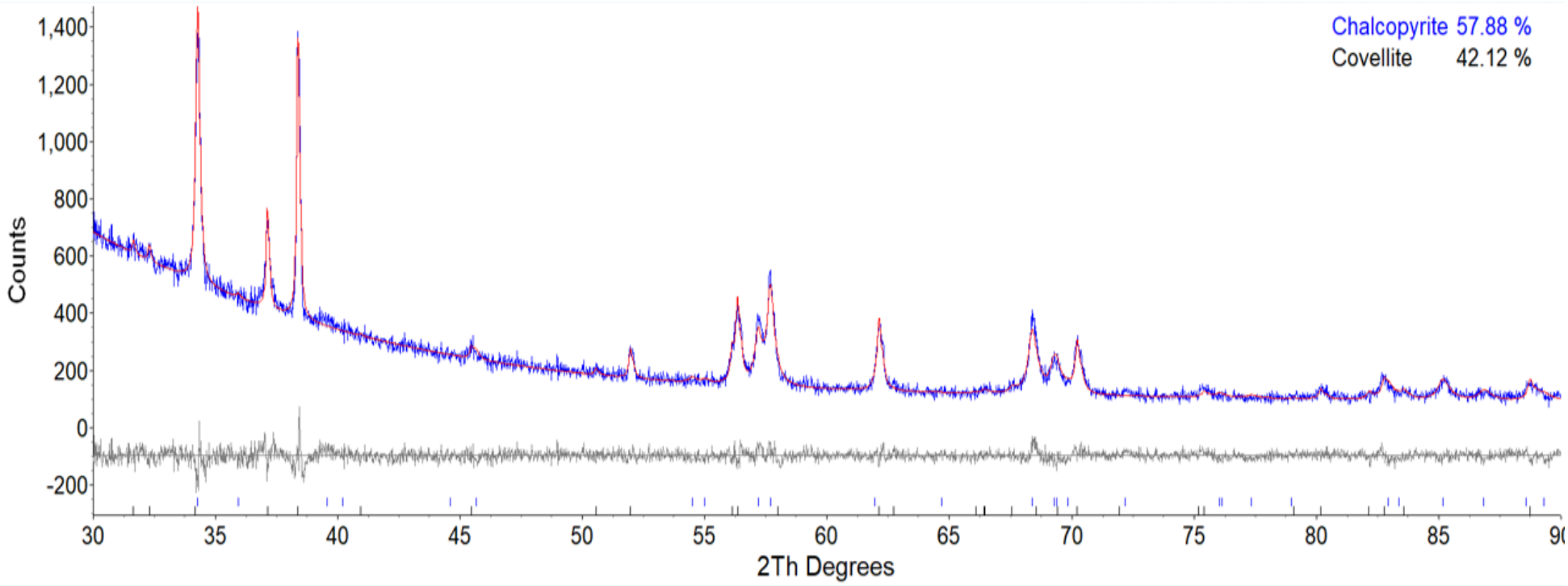

Figure 18 X-ray powder diffraction patterns of natural chalcopyrite and synthetic covellite in mineral replacement reaction. Sample loaded into the 0.7 mm diameter quartz capillary tube with capillary stage.

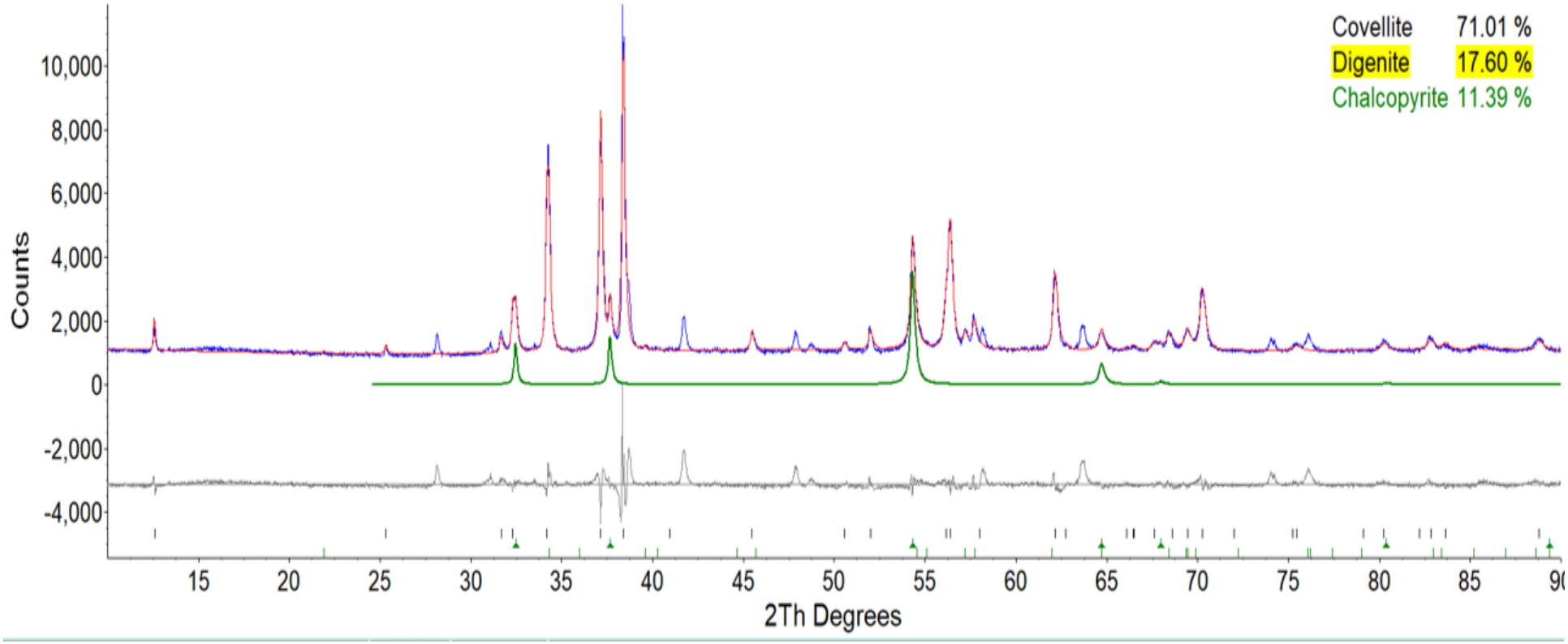

Figure 19 X-ray powder diffraction patterns of digenite synthesized by mineral replacement reaction of chalcopyrite with rotary stage.

Table 5 X-ray powder diffraction data of synthetic covellite.

hkl Planes	d	*hkl* Planes	d
{0 0 2}	8.16840	{0 2 0}	1.64040
{0 0 4}	4.08420	{0 0 10}	1.63368
{0 1 0}	3.28079	{0 2 2}	1.60829
{0 1 1}	3.21657	{0 1 9}	1.58830
{0 1 2}	3.04441	{0 2 3}	1.57068
{0 1 3}	2.81019	{1 1 6}	1.55492
{0 0 6}	2.72280	{0 2 5}	1.46601
{0 1 4}	2.55776	{0 1 10}	1.46240
{0 1 5}	2.31511	{0 2 6}	1.40510
{0 1 6}	2.09522	{1 1 8}	1.38873
{0 0 8}	2.04210	{0 0 12}	1.36140
{0 1 7}	1.90174	{0 1 11}	1.35299
{1 1 0}	1.89417	{0 2 7}	1.34205
{1 1 2}	1.84520	{0 2 8}	1.27888
{0 1 8}	1.73369	{0 2 0}	1.64040

Table 6 X-ray powder diffraction data of natural chalcopyrite.

hkl Planes	d	*hkl* Planes	d
{0 1 1}	4.71255	{0 2 4}	1.85431
{1 1 2}	3.03575	{3 1 2}	1.59126
{0 2 0}	2.64250	{1 1 6}	1.57378
{0 0 4}	2.60272	{0 2 6}	1.45041
{2 2 0}	1.86853	{0 1 7}	1.43166
{0 4 0}	1.32125	{0 0 8}	1.30136

Table 7 X-ray powder diffraction data of synthetic digenite.

*hkl P*lanes	d
{1 1 1}	3.19997
{0 0 2}	2.77125
{0 2 2}	1.95957
{3 1 1}	1.67113
{2 2 2}	1.59998

{0 0 4}	1.38563

The Rietveld quantitative phase analysis method (QPA) was used in this research project to quantify the reaction extent of the replacement reaction product. The program of TOPAS (Bruker, 2009) was mainly used to quantify the reaction extent of chalcopyrite, covellite and digenite in the solid product collected from mineral replacement reaction. The quality of the refinement can be determined by goodness-of-fit parameter (R_p, R_{wp}, GOF). Each parameter can be defined as following equation:

R-pattern: $$R_p = \left[\frac{\sum|y_{o,m}-y_{c,m}|}{\sum y_{o,m}}\right]^{\frac{1}{2}} \quad (22)$$

R-weighted pattern: $$R_{wp} = \left[\frac{\sum w_m(y_{o,m}-y_{c,m})^2}{\sum w_m {y_{o,m}}^2}\right]^{\frac{1}{2}} \quad (23)$$

R-expected: $$R_{exp} = \left[\frac{M-P}{\sum w_m {y_{o,m}}^2}\right]^{\frac{1}{2}} \quad (24)$$

Goodness of fit: $$GOF = X^2 = \left[\frac{{R_{wp}}^2}{{R_{exp}}^2}\right] = \left[\frac{\sum w_m(y_{o,m}-y_{c,m})^2}{M-P}\right]^{\frac{1}{2}} \quad (25)$$

in which $y_{o,m}$ and $y_{c,m}$ are the observed and calculated diffraction intensities respectively collected at data point m, M is the number of data observed, P is the number of parameters being estimated, w_m is the weighting given to each data point m. GOF value is expected to be close to 1 with a good refinement. The weight percentages of the involved mineral phases are determined by the following equation:

$$W_p = \frac{(SZMV)_p}{\sum_i (SZMV)_i} \quad (26)$$

where S is represents the scale factor, Z is the number of formula units of each unit cell, M is the molar mass of the formula unit, V is the total volume of unit cell and i is an index running over all mineral phases. Young (1993) provides more details of Rietveld refinement method. The RAW format files obtained using XRD were loaded as scan file

using TOPAS 4.2 program by left-click ‘file’ at the top-left corner as illustrated in Figure 20A. A Chebychev polynomial background function was used to refine the background. Goniometer radii were set at 250° (Figure 20B). *CoKα3.lam* file was selected as emission profile, but *CoKα3* was deleted as only *CoKα1* and *CoKα*2 were used as X-ray source in this project with the areas were set at 0.666:0.333 (Figure 20C). Interested mineral CIF files were loaded to quantify each mineral phase with PV_MOD peak type. All mineral CIF files used in mineral phase quantification were sourced from the American Mineralogist Crystal Structure Database website. The chalcopyrite CIF file is originally from Knight et al. (2011), quartz file is from Levien et al. (1980), covellite file is from Berry (1954), digenite file is from Will et al. (2002) and hematite is from Blake et al. (1966). In each mineral phase of sites section, the numbers in x, y and z column were converted to a fraction number if possible. Corresponding element with correct oxidation state in the mineral phase were selected and run the refinement. This method tends to underestimate the errors as those solid products dissolved in solution or adhered to the surface of PTFE reactors were not counted. Those reaction extent quantification errors are the main reasons for the declining reaction extent observed at longer experimental durations for some experiments.

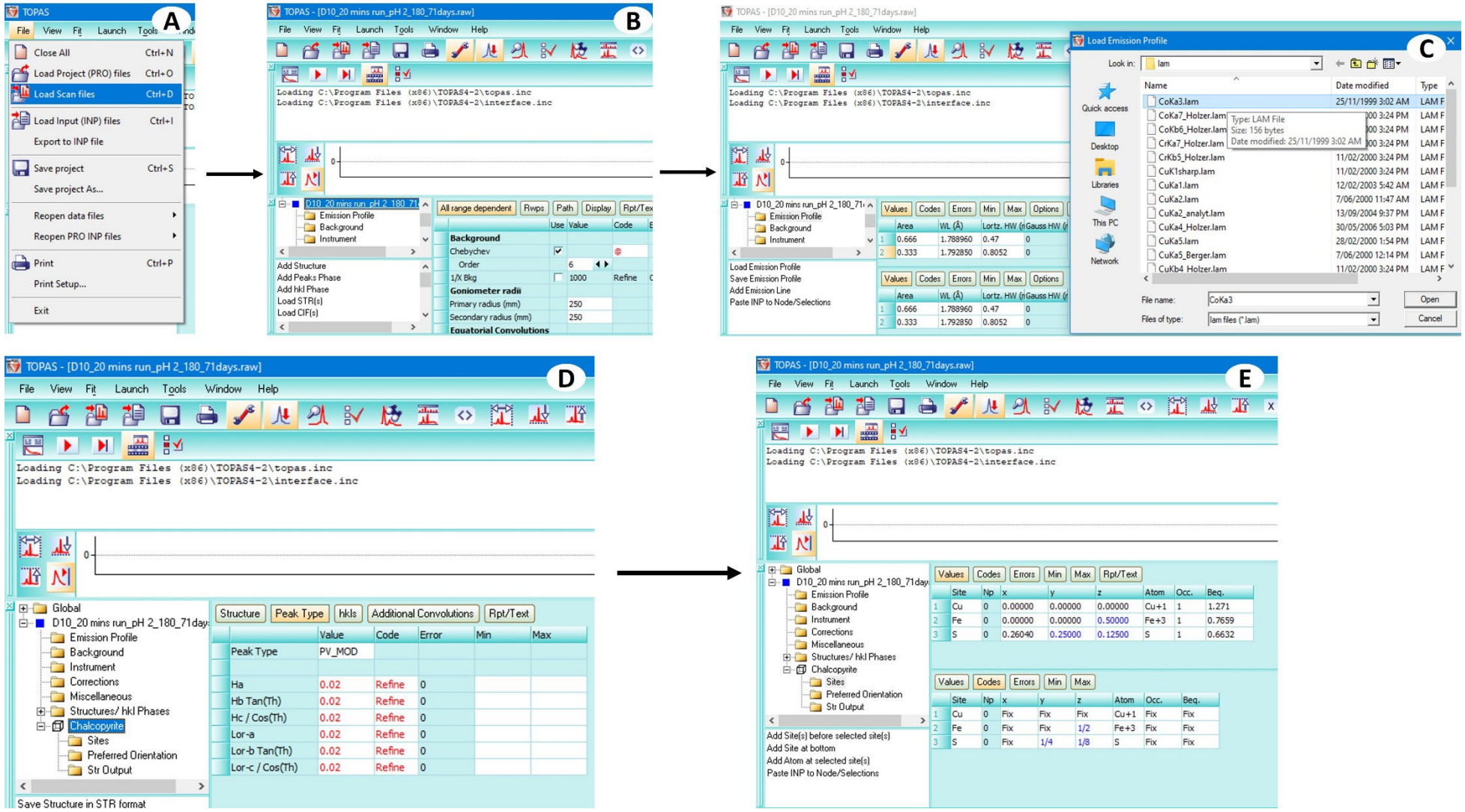

Figure 20 The flow chart of the refinement using TOPAS program. A) Loading XRD scan RAW file; B) Background of refinement set up; C) Loading emission profile; C) Select the peak type to refine each mineral phase; D) Converting the values of *xyz* into fraction and select the corresponding atom with correct oxidation state.

Figure 21 X-ray diffractometer in Flinders Microscopy and Microanalysis (FMMA) (Bruker, Eco D8 Advance).

2.5 Scanning Electron Microscopy (SEM)

Scanning electron microscope (SEM) imaging is one of the common techniques used to obtain the surface image of samples in the nanometre to centimetre scale. In this research, the morphological information of the product surface was obtained from SEM in FMMA. After a focused beam of electrons interacts with the surface of the sample, various processes including secondary electrons, backscattered electrons and characteristic X-ray will be produced after the electrons interact with the sample. The morphological information is detected by the secondary electrons emitted by the excitation of atoms by the electron beam (McMullan, 1995).

Backscattered electrons are the scattered primary electrons after the electron beam introduce the surface of sample and reflect. Those elements with higher atomic number tend to have more BSE and resulting a brighter image. Thus, BSE imaging is used to collect compositional variations in the sample.

In energy dispersive analysis of X-rays (EDAX), the inner electrons of the atoms on the sample are excited and ionized. After the inner electrons being excited and ionized, the

gap will be filled by outer electrons. A characteristic X-ray will be generated after this process due to the releasing of excess energy. These characteristic X-rays will be collected and used to characterize the elemental composition of the sample (Goldstein et al., 2017). In this project, this technique was used to qualitative the chemical composition of the final product from the hydrothermal reactions.

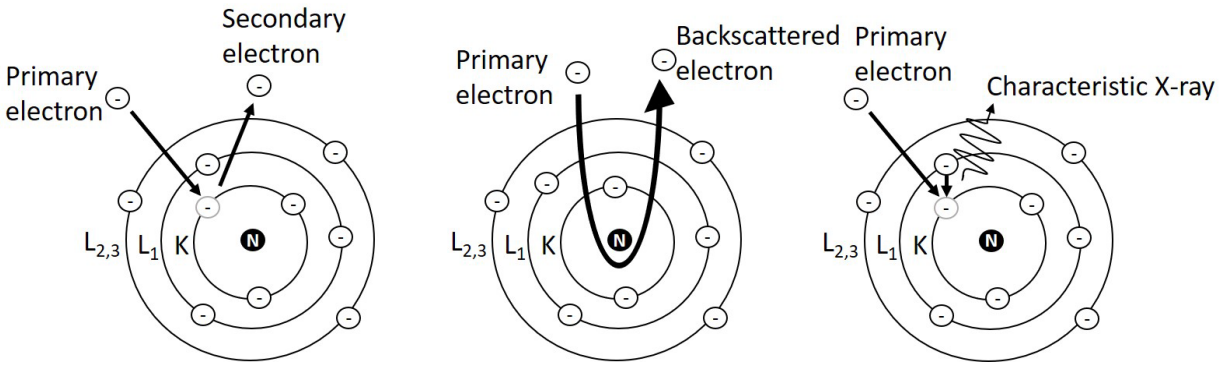

Figure 22 Formation of different electrons from incident X-rays or electrons. Secondary electrons are emitted from inelastic collisions with electrons in the valence shell. Backscattered electrons are formed from elastically scattering events with larger atoms. Characteristic X-rays are formed by the ejection of inner shell electron and fill in by an electron from higher orbital.

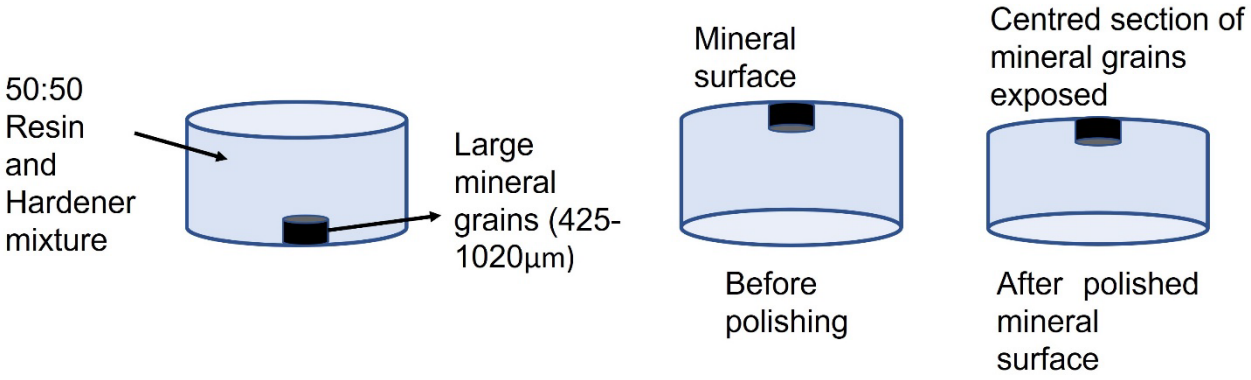

Figure 23 Schematic diagram of the preparation of epoxy resin coated chalcopyrite SEM sample used to observing the cross section of reacted grains.

Figure 24 Field Emission Scanning electron microscope in FMMA equipped with EDAX, BSE and SE detector. (Inspect F50)

All samples were mounted on carbon tape and carbon coated using a spin coater to investigate the surface morphology. Large particle size (425-1025 μm) of chalcopyrite grains were selected to imaging the cross sections of partially reacted chalcopyrite. It was embedded in epoxy resin made by 50:50 resin and hardener, and then evacuated under vacuum to remove air bubbles. After the epoxy resins were cured, they were polished by sandpapers (P120-P1200) and diamond paste (3μm and 1μm). It was carbon coated (5-10 nm in thickness) prior to SEM and BSE imaging and EDAX analysis.

2.6 Inductively Coupled Plasma Optical Emission Spectrometry (ICP-OES)

ICP-OES is one of common analytical techniques used to quantify certain elements contains in a sample. When atoms or ions absorb energy from inductively coupled plasma, the electrons will move from the ground state to an excited state. A light at specific wavelengths is released when the excited atoms or ions transits to a lower energy level, usually the ground state. The ICP-OES uses the emitted light at a specific wavelength to determine which element it is. The amount of emitted light at a specific wavelength is increasing as the number of atoms or ions making the transition increase. A calibration graph is established from a series of specific element standard solutions. The concentration of specific element is calculated by using the calibration graph.

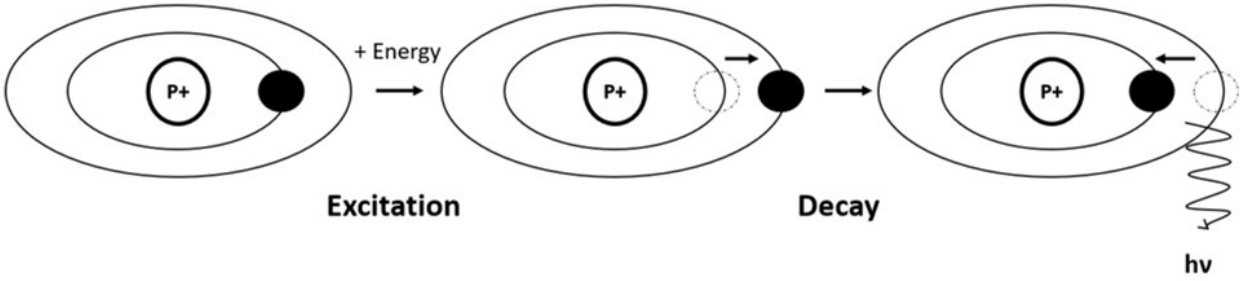

Figure 25 After an atom is excited by absorbing energy, an electron transits to higher energy level orbital. The atom may transfer to a lower energy state by releasing a photon.

In this research project, ICP-OES in Flinders Analytical was used to determine the concentration of S, Cu and Fe in the solution collected from mineral replacement reaction experiments and measure the concentration of Cu in the alkaline glycine solution from covellite leaching experiments. Each sample was filtered through a 0.5 μm syringe filter and diluted with 2% HNO_3 solution either 100x or 1000x. A 10 ppm Mn solution and a 1 ppm Mn solution were used for daily torch axial and radial alignment respectively. Yttrium solution was used as an internal standard. Cu metal solution digested by 2% HNO_3 solution was used to prepared Cu standard solution. 1000ppm Cu copper metal solution was used as stock solution to prepare 10 ppm Cu solution by 100x dilution. The standard solutions were prepared as showed in Table 8. Pure 2% HNO_3 solution was used as a blank solution.

Table 8 Preparation of Cu standard solutions for ICP-OES analysis using 10ppm Cu stock solution.

Standard Solution	**2% HNO_3 (mL)**	**Stock Solution (mL)**
5ppm	5	5
2ppm	2	8
1ppm	1	9
500ppb	0.5	9.5
250ppb	0.25	9.75
100ppb	0.1	9.9
75ppb	0.075	9.925
50ppb	0.05	9.95
25ppb	0.025	9.975
10ppb	0.01	9.99

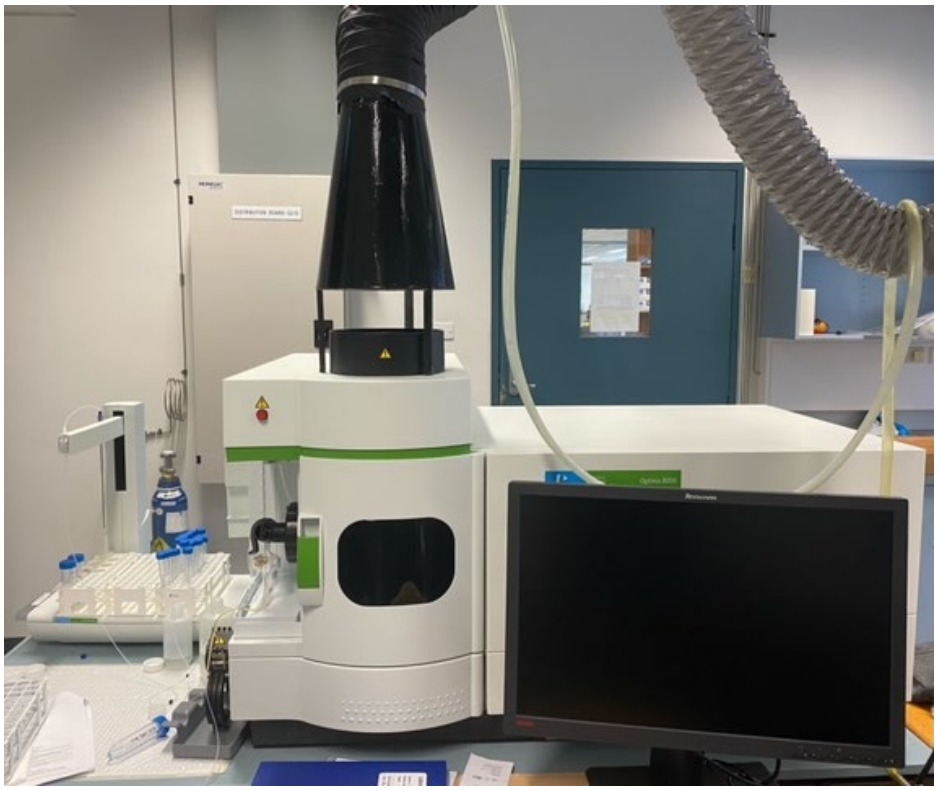

Figure 26 Inductively Coupled Plasma Optical Emission Spectrometry in Flinders Analytical (PerkinElmer Optima 8000).

2.7 X-ray Photoemission Spectroscopy

XPS is one of widely used techniques for mineral surface studies. Mg Kα (1253.6 eV) and Al Kα (1486.6 eV) are two most commonly used X-ray sources. A monochromator is generally used to reduce peak width of the X-ray source. X-ray's bombard the sample under an ultra-high vacuum and cause electron ejection form the core level of an atom. The hole in the core level will be filled by electron from higher energy level orbital. XPS measures the kinetic energy (E_K) of the emitted electrons, and the binding energy (E_B) is given by Equation (27). hv represents the incident radiation energy, and φ is the work function of minimum energy required to cause electron ejection. The binding energy can be used to determine the element and its chemical state.

$$E_K = hv - E_B - \varphi \quad (27)$$

A Kratos Axis Ultra XPS (Monochromatized AlKα X-ray; 1487eV) from University of South Australia was used to determine the chemical state of elements on the surface of chalcopyrite partially replaced by covellite. The XPS analysis was performed in a cold stage at temperature of -168°C and under ultra-high vacuum (≈10^{-8} Torr). The unreacted chalcopyrite XPS samples were stored in a freezer at -80°C after surface cleaning (see section 2.2). Reacted chalcopyrite XPS samples were prepared by exposes chalcopyrite to buffer solutions (pH 0.5, 1 and 1.5 were used) at 180°C for 2 hours. After quenching, samples were collected in a N_2-purged glove box and rinsed by fresh N_2-purged buffer solutions. All samples were snap frozen by liquid nitrogen and stored in a -80°C freezer until analysis. Survey scan spectra of all samples were collected with 20 eV pass energy, and it can identify the chemical composition onto the surface. S *2p* spectra were collected with 10 eV pass energy and they were used to identify the sulfur species formed on the surface of chalcopyrite after reaction for 2 h.

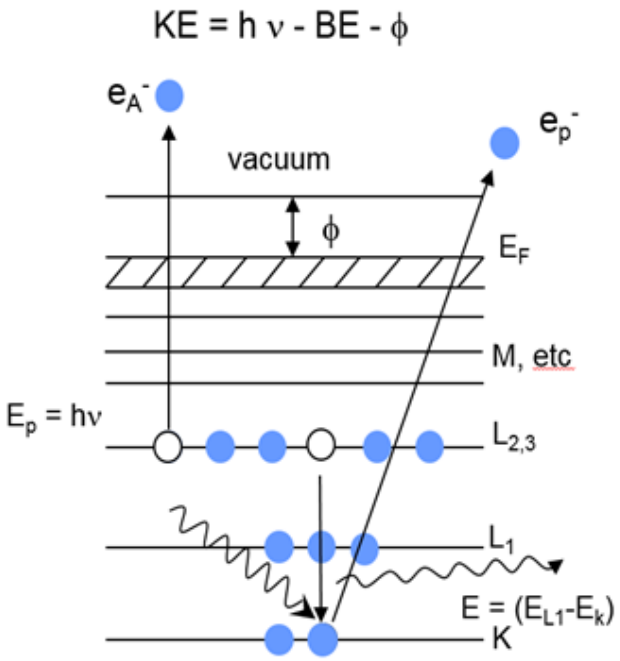

Figure 27: Illustration of photoemission effect.

CasaXPS software (Fairley, 2009) was used in this project to analyse the collected XPS spectra. The calibration of all spectra was performed by aligning C *1s* peak to 284.8 eV (Metson, 1999). Shirley background was applied in all survey scan spectra and sulphur *2p* spectra (Shirley, 1972). 50:50 Gaussian and Lorentzian function was used to fit all sulphur *2p* spectra. S *2p* peaks generally combined with two peaks (S $2p_{3/2}$ and S $2p_{1/2}$) because of the spin orbit splitting. The S $2p_{3/2}$ peak has 1.19 eV higher binding energy than that of S $2p_{1/2}$. The intensity of S $2p_{3/2}$ peak is twice of S $2p_{1/2}$ (Nesbitt and Muir, 1998, Schaufuß et al., 1998, Yang et al., 2015).

The fracture surface of chalcopyrite has been reported a number of sulphur species contribute to the S *2p* spectrum, which including fully coordinated bulk S atoms (S $2p_{3/2}$ binding energy of 161.33 eV), surface monosulphide (S $2p_{3/2}$ binding energy of 160.84 eV) and surface polysulphide species ($2p_{3/2}$ binding energy of 161.88 eV) (Harmer et al., 2004). An elemental sulphur found on the leached chalcopyrite surface and has a S $2p_{3/2}$ binding energy of 164.1 eV (Nesbitt and Muir, 1998, Harmer et al., 2006).

Table 9 The binding energy of each sulphur specie in chalcopyrite used to fit XPS S 2*p* spectrum.

Sulphur Species	Binding energy ($2p_{3/2}$)
Fully coordinated bulk S	161.33eV (Nesbitt and Muir, 1998, Harmer et al., 2004, Harmer et al, 2006, Yang et al., 2015)
Surface monosulphides	160.84eV (Nesbitt and Muir, 1998, Harmer et al., 2004, Harmer et al, 2006, Yang et al., 2015)
Surface polysulfides	163.3eV (Nesbitt and Muir, 1998, Harmer et al., 2004, Harmer et al, 2006, Yang et al., 2015)
Elemental sulphur	164.1eV (Nesbitt and Muir, 1998, Harmer et al., 2004, Harmer et al, 2006, Yang et al., 2015)
Sulphate	167.5eV (Harmer et al., 2006)
Energy loss feature	163.8eV (Fujisawa et al., 1994, Harmer et al., 2004, Yang et al., 2015)

Table 10 The binding energy of each Cu and Fe species found in chalcopyrite XPS spectrum.

Cu and Fe Species in Chalcopyrite	Binding energy
Cu (I)-S	931.8eV (Sarah L. Harmer, 2006, Pearce et al., 2006, Goh et al., 2006)
Fe(III)-S	708.2eV (McIntyre and Zetaruk, 1977, Sarah L. Harmer, 2006, Yang et al., 2015)
Fe(III)-O-OH	711.0eV (McIntyre and Zetaruk, 1977, Sarah L. Harmer, 2006, Yang et al., 2015)

2.8 Reference

BERRY, L. 1954. The crystal structure of covellite, cuse and klockmannite, cuse. American Mineralogist: Journal of Earth Planetary Materials, 39, 504-509.

BLAKE, R., HESSEVICK, R., ZOLTAI, T. & FINGER, L. W. 1966. Refinement of the hematite structure. American Mineralogist: Journal of Earth Planetary Materials, 51, 123-129.

BRUKER, A. X. S. 2009. Topas V4. 2: General profile and structure analysis software for powder diffraction data. Karlsruhe, Germany: Bruker AXS.

FAIRLEY, N. 2009. CasaXPS Mannual, Version 2.3.15. Casa Software Ltd.

FUJISAWA, M., SUGA, S., MIZOKAWA, T., FUJIMORI, A. & SATO, K. 1994. Electronic structures of CuFeS 2 and CuAl 0.9 Fe 0.1 S 2 studied by electron and optical spectroscopies. Physical Review B, 49, 7155.

GOH, S. W., BUCKLEY, A. N., LAMB, R. N., ROSENBERG, R. A. & MORAN, D. 2006. The oxidation states of copper and iron in mineral sulfides, and the oxides formed on initial exposure of chalcopyrite and bornite to air. Geochimica et Cosmochimica Acta, 70, 2210-2228.

GOLDSTEIN, J. I., NEWBURY, D. E., MICHAEL, J. R., RITCHIE, N. W., SCOTT, J. H. J. & JOY, D. C. 2017. Scanning electron microscopy and X-ray microanalysis, Springer.

HARMER, S. L., PRATT, A. R., NESBITT, W. H. & FLEET, M. E. 2004. Sulfur species at chalcopyrite (CuFeS2) fracture surfaces. American Mineralogist, 89, 1026-1032.

HARMER, S. L., THOMAS, J. E., FORNASIERO, D. & GERSON, A. R. 2006. The evolution of surface layers formed during chalcopyrite leaching. Geochimica et Cosmochimica Acta, 70, 4392-4402.

KNIGHT, K. S., MARSHALL, W. G. & ZOCHOWSKI, S. W. 2011. The low-temperature and high-pressure thermoelastic and structural properties of chalcopyrite, CuFeS2. The Canadian Mineralogist, 49, 1015-1034.

LEVIEN, L., PREWITT, C. T. & WEIDNER, D. J. 1980. Structure and elastic properties of quartz at pressure. American Mineralogist, 65, 920-930.

MCINTYRE, N. & ZETARUK, D. 1977. X-ray photoelectron spectroscopic studies of iron oxides. Analytical Chemistry, 49, 1521-1529.

MCMULLAN, D. 1995. Scanning electron microscopy 1928–1965. Scanning, 17, 175-185.

METSON, J. 1999. Charge compensation and binding energy referencing in XPS analysis. Surface Interface Analysis: An International Journal devoted to the development application of techniques for the analysis of surfaces, interfaces thin films, 27, 1069-1072.

NESBITT, H. & MUIR, I. 1998. Oxidation states and speciation of secondary products on pyrite and arsenopyrite reacted with mine waste waters and air. Mineralogy Petrology, 62, 123-144.

PEARCE, C., PATTRICK, R., VAUGHAN, D., HENDERSON, C. & VAN DER LAAN 2006. Copper oxidation state in chalcopyrite: Mixed Cu d9 and d10 characteristics. Geochimica et Cosmochimica Acta, 70, 4635-4642.

PECHARSKY, V. & ZAVALIJ, P. 2008. Fundamentals of powder diffraction and structural characterization of materials, Springer Science & Business Media.

QIAN, G., BRUGGER, J., SKINNER, W. M., CHEN, G. & PRING, A. 2010. An experimental study of the mechanism of the replacement of magnetite by pyrite up to 300 C. Geochimica et Cosmochimica Acta, 74, 5610-5630.

QIAN, G., XIA, F., BRUGGER, J., SKINNER, W. M., BEI, J., CHEN, G. & PRING, A. 2011. Replacement of pyrrhotite by pyrite and marcasite under hydrothermal conditions up to 220 C: An experimental study of reaction textures and mechanisms. American Mineralogist, 96, 1878-1893.

SCHAUFUß, A. G., NESBITT, H. W., KARTIO, I., LAAJALEHTO, K., BANCROFT, G. M. & SZARGAN, R. 1998. Reactivity of surface chemical states on fractured pyrite. Surface Science, 411, 321-328.

SHIRLEY, D. A. 1972. High-resolution X-ray photoemission spectrum of the valence bands of gold. Physical Review B, 5, 4709.

WILL, G., HINZE, E. & ABDELRAHMAN, A. R. M. 2002. Crystal structure analysis and refinement of digenite, Cu1. 8S, in the temperature range 20 to 500 C under controlled sulfur partial pressure. European Journal of Mineralogy, 14, 591-598.

XIA, F., BRUGGER, J., CHEN, G., NGOTHAI, Y., O'NEILL, B., PUTNIS, A. & PRING, A. 2009. Mechanism and kinetics of pseudomorphic mineral replacement reactions: A case study of the replacement of pentlandite by violarite. Geochimica et Cosmochimica Acta, 73, 1945-1969.

YANG, Y., HARMER, S. & CHEN, M. 2015. Synchrotron-based XPS and NEXAFS study of surface chemical species during electrochemical oxidation of chalcopyrite. Hydrometallurgy, 156, 89-98.

YOUNG, R. 1993. The rietveld method.

ZHAO, J., BRUGGER, J., GRUNDLER, P. V., XIA, F., CHEN, G. & PRING, A. 2009. Mechanism and kinetics of a mineral transformation under hydrothermal conditions: Calaverite to metallic gold. American Mineralogist, 94, 1541-1555.

ZHAO, J., BRUGGER, J., NGOTHAI, Y. & PRING, A. 2014. The replacement of chalcopyrite by bornite under hydrothermal conditions. American Mineralogist, 99, 2389-2397.

CHAPTER 3 THE REPLACEMENT REACTION OF CHALCOPYRITE BY COVELLITE UNDER HYDROTHERMAL CONDITION

3.1 Introduction

Mineral replacement reactions involving hydrothermal fluids occur widely in Nature. Previous studies of mineral replacement reaction suggested they are more likely to proceeds via an interfacial coupled dissolution and reprecipitation (ICDR) reaction mechanism (Putnis, 2002, Putnis, 2009, Xia et al., 2009, Qian et al., 2010, Qian et al., 2011, Zhao et al., 2014a, Zhao et al., 2014b). Chalcopyrite ($CuFeS_2$) is well-known as the most economically important and widespread Cu-bearing mineral (Córdoba et al., 2008). The formation of chalcopyrite is generally associated with Cu-rich saline hydrothermal fluids in the hypogene zone of ore deposits. Chalcopyrite will also react with hydrothermal fluids, often undergoing altered or replaced reaction, forming other copper sulphides including covellite (CuS), digenite ($Cu_{1.8}S$), chalcocite (Cu_2S) and bornite (Cu_5FeS_4) (Zhao et al., 2014b, Li et al., 2018, Chaudhari et al., 2021). In supergene deposits, covellite is found as a replacement reaction product on the surface of chalcopyrite at Butte, Montana, and Summitville. Colorado, U.S.A and other localities (Anthony, 1995). It suggests that the alteration of chalcopyrite to covellite in supergene mineral deposits proceeds via ICDR mechanism. Xia et al. (2009) first reported the effect of dissolution and precipitation kinetics in decoupling of the replacement of pentlandite by violarite by a ICDR reaction. The kinetic controls on the replacement reaction of chalcopyrite by covellite have not been studied in detail, but it is very important in the understanding of reaction mechanism and determination of rate-limiting step of the replacement reaction. In this chapter, the mechanism and kinetics of replacement reaction of chalcopyrite by covellite were systematically investigated across a range of different parameters to establish their effect on the reaction rates. The parameters investigated in this set of experiments including pH of solution, oxidant concentration, temperature, specific surface area and Fe and Cu ions concentration in solution.

3.2 Methodology

3.2.1 Hydrothermal Reaction Experiments

PTFE-lined (25 mLs) stainless-steel autoclaves were used as container for all mineral replacement reaction experiments. The source and composition of natural chalcopyrite sample is described in Section 2.1. All chalcopyrite grains used in this Chapter were

washed and sonicated as Section 2.1, resulting a clean surface (Figure 28A) and free of fine particles on the surface. Buffer solutions and its composition were included in section 2.2. pH 0.7-11 buffer solutions were used in the experiments in this chapter. A grain size of 75-150 μm for the chalcopyrite was used in all experiments in a temperature range of 120-200 °C in all runs except the experiments were probing the effect of specific surface area. The solid mass to fluid volume (S/F) ratio was set at 2 g/L in all experiments except the experiments on the effect of S/F ratio. Table 11 was summarized all of the experiments performed in this chapter under different conditions. All experiments were quenched in cold water upon removal from the ovens, solutions were filtered by 0.5 μm syringe filter and measure the concentration of Cu, Fe and S were determined by inductively coupled plasma optical emission spectrometry (ICP-OES). Solid residues were collected and ground with acetone for mineral product identification by X-ray powder diffraction (XRD). All scanning electron microscopy (SEM) sample was carbon coated (5-10 nm thick) prior to secondary electron (SE) and backscattered (BSE) imaging. Quantitative phase analysis of reaction extent in solid residue was carried out using PXRD data analysed using TOPAS. Mineral CIF files used in TOPAS (Bruker, 2009) was downloaded from American Mineralogist Crystal Structure Database website and sourced from Knight et al. (2011) (chalcopyrite) and Berry (1954) (covellite). $X^{0.35}$ where X is the reaction extent of mineral was used to determine the errors of uncertainties in Rietveld refinement method at 95% confidence level (Geelhoed et al., 2002, Qian et al., 2017). The Rietveld phase quantification methods does not consider all errors and uncertainties in the reactions. Some mineral particles may dissolved in solution or stuck to the surface of PTFE autoclaves. Those errors are the reasons why some reactions appear run backwards.

Table 11 Summary of experimental conditions for chalcopyrite replaced by covellite under hydrothermal conditions.

Experiments[a]	T(°C)	Measured	S/F	Time	Filling	H_2O_2	Particle	wt% of product[b]

		pH	(g/L)	(h)	gas	(mmol)	size (μm)	
A73	180	0.7	2	24	Air	0.44	75-150	Cpy(29), Cv(71)
A53	180	1	2	24	Air	0.44	75-150	Cpy(60), Cv(40)
A93	180	1.5	2	24	Air	0.44	75-150	Cpy(75), Cv(25)
D1	180	2.04	2	24	Air	0.44	75-150	Cpy(90), Cv(10)
A1	180	3.05	2	24	Air	0.44	75-150	Cpy(100), Cv(0)
A2	180	4.61	2	24	Air	0.44	75-150	Cpy(100), Cv(0)
A3	180	5.67	2	24	Air	0.44	75-150	Cpy(100), Cv(0)
A4	180	5.98	2	24	Air	0.44	75-150	Cpy(100), Cv(0)
A5	180	7.01	2	24	Air	0.44	75-150	Cpy(100), Cv(0)
A6	180	9.13	2	24	Air	0.44	75-150	Cpy(100), Cv(0)
A7	180	11.11	2	24	Air	0.44	75-150	Cpy(100), Cv(0)
D9	180	2.04	2	1464	Air	0.44	75-150	Cpy(36), Cv(64)
A11	180	3.05	2	1464	Air	0.44	75-150	Cpy(64), Cv(36)
A12	180	4.61	2	1464	Air	0.44	75-150	Cpy(70), Cv(30)
A13	180	5.67	2	1464	Air	0.44	75-150	Cpy(100), Cv(0)
A14	180	5.98	2	1464	Air	0.44	75-150	Cpy(100), Cv(0)
A15	180	7.01	2	1464	Air	0.44	75-150	Cpy(100), Cv(0)
A16	180	9.13	2	1464	Air	0.44	75-150	Cpy(100), Cv(0)
A17	180	11.11	2	1464	Air	0.44	75-150	Cpy(100), Cv(0)
A21	180	1	2	24	Air	0.44	38-75	Cpy(68), Cv(32)
A22	180	1	2	24	Air	0.44	150-425	Cpy(80), Cv(20)
A23	180	1	2	24	Air	0.44	425-1020	Cpy(90), Cv(10)
A28	180	1	2	24	N_2	0	75-150	Cpy(92), Cv(8)
A30	180	1	2	24	Air	0.88	75-150	Cpy(18), Cv(82)
A31	180	1	2	24	Air	1.76	75-150	Cpy(19), Cv(81)
A41	180	1	1	24	Air	0.88	75-150	Cpy(4), Cv(96)
A42	180	1	4	24	Air	0.88	75-150	Cpy(18), Cv(82)
A43	180	1	8	24	Air	0.88	75-150	Cpy(10), Cv(90)
A44	160	1	1	24	Air	0.88	75-150	Cpy(91), Cv(7)
A45	160	1	2	24	Air	0.88	75-150	Cpy(33), Cv(67)
A46	160	1	4	24	Air	0.88	75-150	Cpy(45), Cv(55)
A47	160	1	8	24	Air	0.88	75-150	Cpy(49), Cv(51)
A44A	140	1	1	24	Air	0.88	75-150	Cpy(0), S(100), Cv(0)
A45A	140	1	2	24	Air	0.88	75-150	Cpy(0), S(100), Cv(0)
A46A	140	1	4	24	Air	0.88	75-150	Cpy(2), S(96), Cv(2)
A47A	140	1	8	24	Air	0.88	75-150	Cpy(14), S(60), Cv(26)
A48	200	1	1	24	Air	0.88	75-150	Cpy(0), Cv(100)
A48A	200	1	2	24	Air	0.88	75-150	Cpy(0), Cv(100)
A49	200	1	4	24	Air	0.88	75-150	Cpy(0), Cv(100)
A49A	200	1	8	24	Air	0.88	75-150	Cpy(49), Cv(51)
A108[c]	180	1	2	24	N_2	0	75-150	Cpy(62), Cv(38)
A109[c]	180	1	2	24	N_2	0	75-150	Cpy(35), Cv(65)
A110[c]	180	1	2	24	N_2	0	75-150	Cpy(42), Cv(49), Dg (7)
A111[d]	180	1	2	24	N_2	0	75-150	Cpy(78), Cv(22)
A112[d]	180	1	2	24	N_2	0	75-150	Cpy(84), Cv(16)
A113[d]	180	1	2	24	N_2	0	75-150	Cpy(86), Cv(14)
A114[e]	180	1	2	24	N_2	0	75-150	Cpy(76), Cv(24)
A115[e]	180	1	2	24	N_2	0	75-150	Cpy(66), Cv(34)
A116[e]	180	1	2	24	N_2	0	75-150	Cpy(62), Cv(38)
A117[f]	180	1	2	24	N_2	0	75-150	Cpy(88), Cv(12)
A118[f]	180	1	2	24	N_2	0	75-150	Cpy(88), Cv(12)
A119[f]	180	1	2	24	N_2	0	75-150	Cpy(86), Cv(14)
A51-A62	180	1	2	2-234	Air	0.44	75-150	See kinetic study result
A71-A82	180	0.7	2	2-39	Air	0.44	75-150	
A91-A102	180	1.5	2	2-820	Air	0.44	75-150	
B1-B12	140	1.5	2	24-408	Air	0.44	75-150	
B21-B32	140	1	2	48-696	Air	0.44	75-150	
B41-B52	140	0.7	2	48-552	Air	0.44	75-150	
B71-B82	200	1	2	4-65	Air	0.44	75-150	
B91-B102	160	1	2	12-552	Air	0.44	75-150	
C1-C12	160	0.7	2	12-408	Air	0.44	75-150	
C21-C32	160	1.5	2	47.5-792	Air	0.44	75-150	
C41-C52	200	0.7	2	2-20	Air	0.44	75-150	

C71-C82	200	1.5	2	24-382	Air	0.44	75-150

[a] 40 mg (0.22 mmol) of chalcopyrite grains (China) were used in most of experiments.

[b] Cpy = Chalcopyrite, Cv = Covellite, S = Elemental Sulphur, Dg = Digenite.

[c] Different amount of $CuCl_2$ were added to each run (0.22, 0.44 and 0.88 mmol).

[d] Different amount of Fe^{2+} were added to each run (0.22, 0.44 and 0.88 mmol)

[e] Different amount of Fe^{3+} were added to each run (0.22, 0.44 and 0.88 mmol).

[f] Different amount of acetamide were added to each run (0.22, 0.44 and 0.88 mmol)

3.2.2 Activation Energy Calculation

The rate constant method is widely applied in mineral replacement reaction to quantify the kinetics and determine the average activation energy (E_a) of the reaction. Empirical *Avrami* equation (28) is commonly used, where *k* is a rate constant, *t* is the duration of reaction, *y* is the product fraction formed and *n* is a constant that depends on the mechanism. All kinetic data of each temperature (140-200 °C) was fitted using the empirical *Avrami* equation.

$$y = 1 - exp(-(kt)^n) \tag{28}$$

$$y = \frac{Y_t - Y_0}{Y_e - Y_0} \times 100\% = \frac{Y_t}{Y_e} \times 100\% \; Y_0 = 0 \tag{29}$$

The fraction replaced *y* is determined by the equation (29), where Y_t, Y_0 and Y_e are the fraction of covellite formed at a specific time *t*, *t* = 0 initially and *t* = ∞ when reaches equilibrium is reached (Zhao et al., 2019, Putnis, 1992, Yund and Hall, 1970, Wang et al., 2005, Xia et al., 2009). The linearization of equation (28), gives formula:

$$\ln\left[ln\left(\frac{1}{1-y}\right)\right] = nlnk + nlnt \tag{30}$$

The *Arrhenius* plot of ln*k* against 1/*T* is commonly used to determine the activation energy of reactions (Putnis, 1992, Xia et al., 2009). As the equation (37) shown, it is linear, and the slope is equal to $-E_a/R$. *A* is a pre-exponential factor, *R* is the gas constant (equivalent to 8.314J mol^{-1} K^{-1}), and *T* is temperature in Kelvin.

$$k = Aexp\left(\frac{-E_a}{RT}\right) \quad (31)$$

However, the value of *k* is based on the selection of the empirical equation *f(y),* where y is the reaction extent, in equation (31). Thus, the selection of rate equation can change the empirical activation energy E_a calculated this way. This is a significant disadvantage of this method because the data can be fitted equally well by numerous different forms of rate equations, and possibly resulting in different E_a (Putnis, 1992). This method has another disadvantage that E_a may changes during the reactions, and this may not be readily ascertained.

$$\frac{dy}{dt} = k \times f(y) \quad (32)$$

The 'time to a given fraction' method can be used to obtain a series of E_a as a function of reaction progression. The activation energy E_a obtained by this method is independent of *f(y)* in the rate equation. With this method it is possible to ascertain whether E_a changes during the replacement reaction by collect the E_a for different time intervals of the reaction (Putnis, 1992, Qian et al., 2017).

$$dt = k^{-1} \times f^{-1}(y)dy \quad (33)$$

In this method, the functional relationship between the fraction extent *y* and the time *ty* is the principal of the theory. Therefore, equation (33) is transformed from Eq. (32) once the time *t* becomes a dependent variable. Thus, Eq. (33) can be further transformed to Eq. (34) to calculate the specific time t_Y for a given fraction extent $y = Y$ (Putnis, 1992).

$$t_Y = k^{-1} \int_{y=0}^{y=Y} f^{-1}(y)dy \quad (34)$$

The integral of equation (34) has a constant numerical value, if the function *f(y)* does not change over the temperature range studied. Therefore,

$$t_Y \propto k^{-1} \quad (35)$$

$$t_Y \propto A^{-1}e^{(\frac{E_a}{RT})} \quad (36)$$

The equation (36) can be transformed into equation (37). An average E_a from the start of dissolution to a specific extent t_Y can be obtained from this equation.

$$lnt_Y = const - lnk_0 + \frac{E_a}{RT} \quad (37)$$

A specific range of reaction extent (Y_p to Y_q) can be selected and substituted into equation (34), which given equation (38). Therefore, equation (37) can be written as equation (39), where t_{Y_q} and t_{Y_p} are the times until the specific reaction fractions, Y_q *and* Y_p respectively. The average activation energy between the reaction range of t_{Y_q} to t_{Y_p} is represented by $E_a(Y_q)$ (Qian et al., 2017).

$$t_{Y_q} - t_{Y_p} = k^{-1} \int_{y=Y_p}^{y=Y_q} f^{-1}(y)dy \quad (38)$$

$$\ln\left(t_{Y_q} - t_{Y_p}\right) = const - lnk_0 + \frac{E_a(Y_q)}{RT} \quad (39)$$

After modification of the time to a given fraction methods, equation (39) can be used to calculate E_a at a certain reaction period of time rather than an average E_a obtained from (37). Both of rate constant method and modified time to a given method were used in this study to determine the activation energies.

3.3 Results

3.3.1 Morphology and Texture

SEM images showed that hexagonal, euhedral covellites were formed on the chalcopyrite surface at pH 0.7-1.5 and 180 °C (Figure 28B and 28C). Covellite crystals formed on the chalcopyrite surface at pH 1.5 (approximately 10 μm, Figure 28C) are much smaller than those formed at pH 0.7 and 1 (approximately 50 μm, Figure 28B). Some *ex-situ* synthetic covellite crystals were also observed, with sharp edges, perfect hexagonal structure and very thin layer (Figure 28D). After reaction of 2 h at pH 1 and 180 °C, round blobs of elemental sulphur were observed randomly distributed on the chalcopyrite surface and identified by EDAX (Figure 28E). Under same condition, covellite was also formed on the chalcopyrite surface, as spider-web like crusts with holes in the centre (Figure 28F).

Energy dispersive X-ray analyss mapping of the cross-section shows the presences of two minerals with red (atomic percentage: 49% S, 27% Fe and 24% Cu) and blue pixels (51% S, 1% Fe and 48% Cu) (Figure 29C). Blue pixels mineral only presented on S (Figure 29E) and Cu (Figure 29F) spectra, identified as covellite. Red pixels mineral presented on Fe (Figure 29D), Cu and S spectra, identified as chalcopyrite. As shown on S spectra, chalcopyrite presented brighter signals than covellite due to higher S content in chalcopyrite. On the contrary, covellite presented brighter signals than chalcopyrite as shown on Cu spectra due to higher Cu content in covellite. Backscattered images show that covellite crystals nucleate on the surface of chalcopyrite grains or along with cracks at pH 1 and 180 °C. Figure 29A shows that the precipitated covellite exists as an outer rim on the chalcopyrite grains. This rim was made up of numerous individual microscale covellite crystals, rather than a large grain. A sharp reaction front was observed between the secondary covellite and chalcopyrite grains, indicative of dissolution-reprecipitation reaction mechanism. Numerous pores and cracks were formed on the chalcopyrite grains. A visible gap (about 5 μm, Figure 29B) between the chalcopyrite and covellite suggests that the dissolution of chalcopyrite and the precipitation of covellite are not tightly coupled.

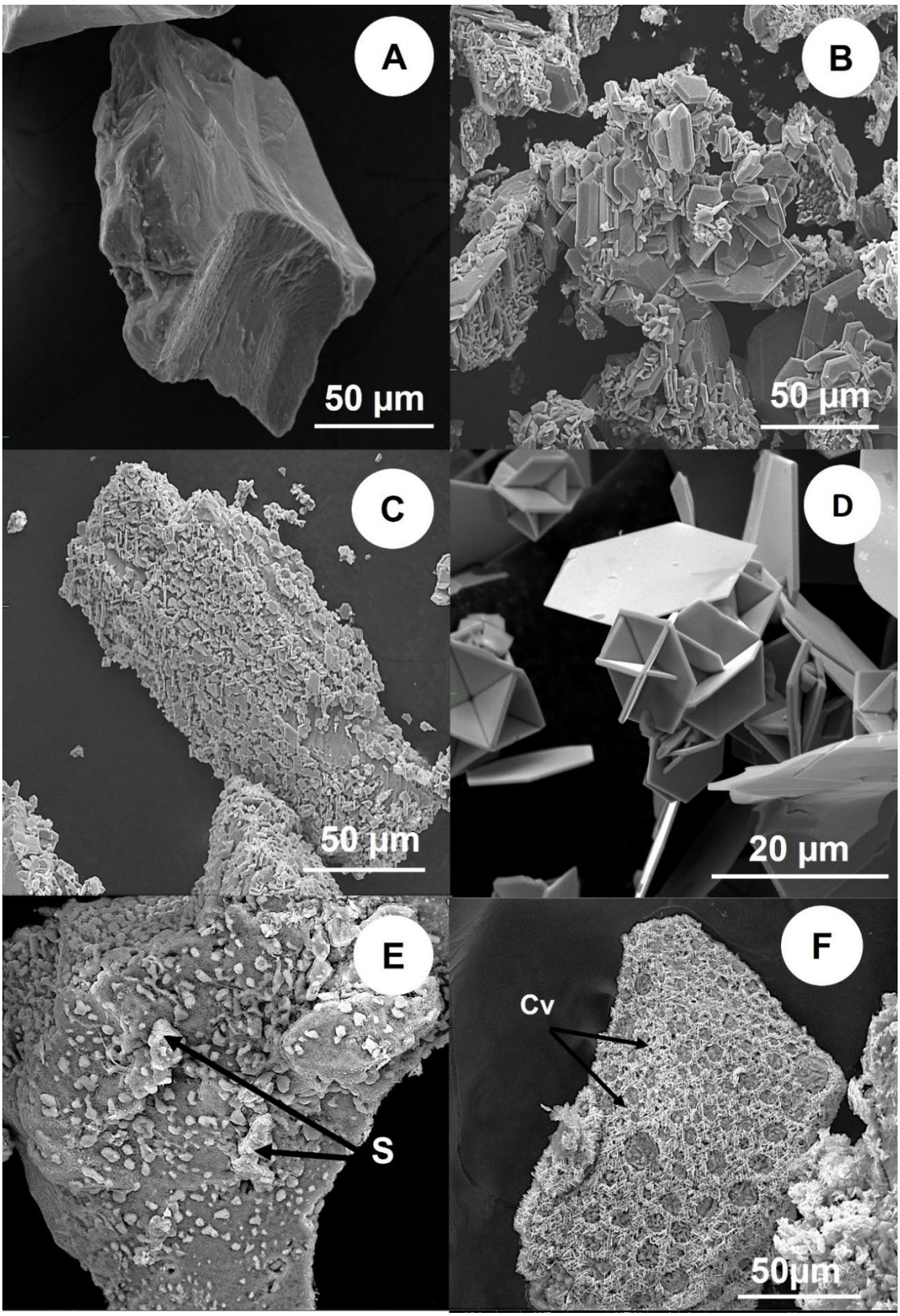

Figure 28 SEM secondary electron images of (A) unreacted chalcopyrite grain (75-150 µm) after acid wash and ultrasonic cleaning showing smooth surface, (B) partially reacted chalcopyrite (75-150 µm) at pH 1 and 180°C for 24 h, showing covellite on the surface, (C) partially reacted chalcopyrite (75-150 µm) at pH 1.5 and 180°C for 24 h, showing smaller covellite on the surface, (D) *ex-situ* covellite formed from the solution at pH 1 and 180°C,

sulphur (E) and covellite (F) formed on the chalcopyrite surface reacted at pH 1 and 180 °C for 2 h.

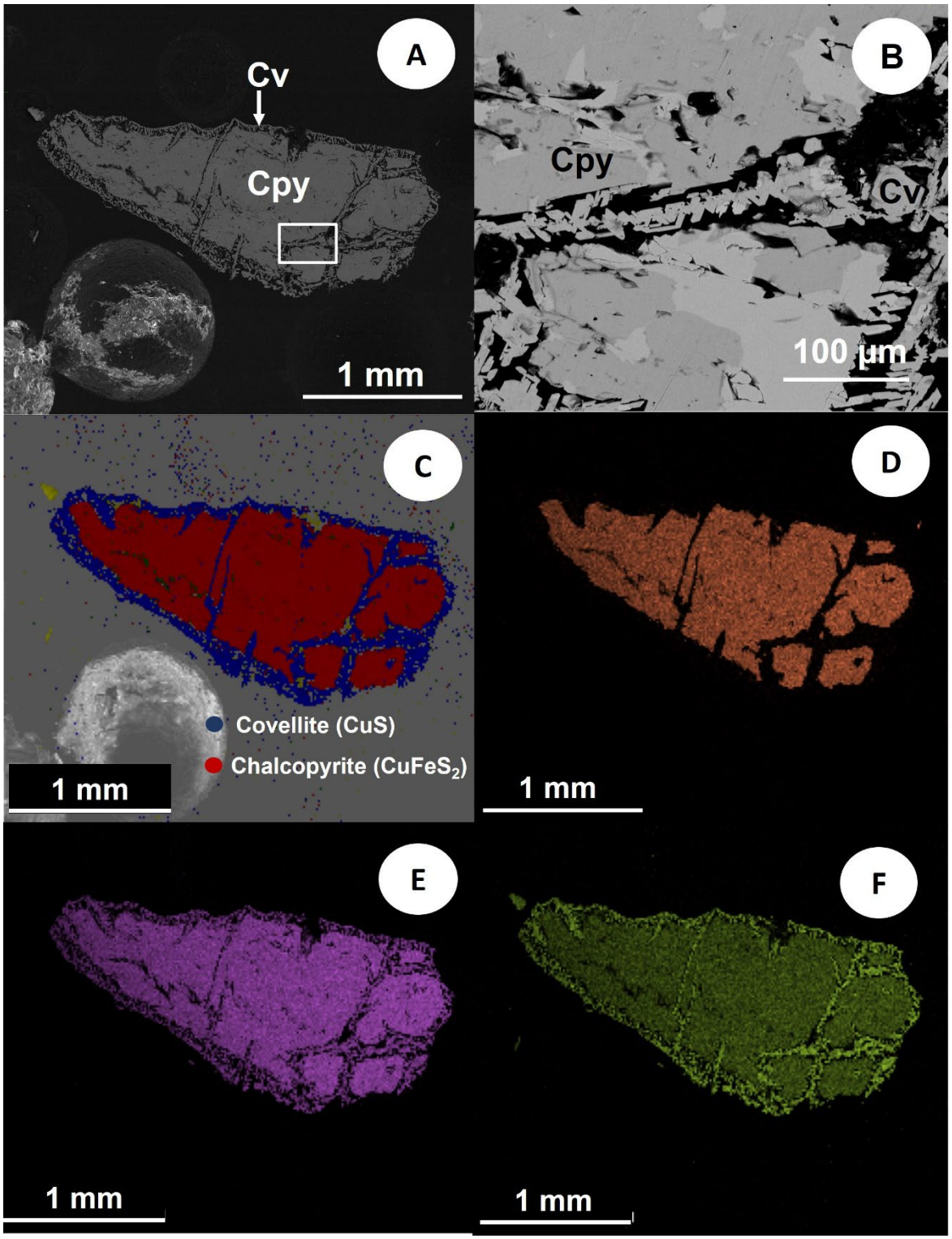

Figure 29 Backscattered images of the cross section of chalcopyrite partially replaced by covellite (A) at pH 1 and 180°C for 10 days, B) zoomed-in images of (A), C) EDAX mapping of (A) made by chalcopyrite (Blue pixels) and covellite (Red pixels), D) Fe spectra of (A), E) S spectra of (A), F) Cu spectra of (A).

3.3.2 Effect of pH

The effect of pH on the transformation rate was investigated through two sets of experiments: one with the reaction time fixed at 24 h; and the other at 68 days. In all these experiments, the temperature was fixed at 180 °C with 0.44 mmol H_2O_2, the solid-weight-to-fluid-volume ratio of 2 g/L. At or above pH 3, no covellite was observed after 24 h of reaction. The quantitative XRD analysis indicates the transformation rate declines gradually when pH increases from 0.7 to 2. After 24 h of reaction, 71±4% of chalcopyrite transformed to covellite at pH 0.7, decreasing to 40±4% at pH 1, 25±3% at pH 1.5 and 10±2% at pH 2. After 68 days, only 71±4% of chalcopyrite converted to covellite at pH 2, 18±3% at pH 3, 15±3% at pH 4 and no covellite formed when pH≥5 (Figure 30). The covellite formed at pH 0.7 and 1 were small metallic blue crystals in the centre or attached to the wall of PTFE-liners (Figure 31a and 31b). Red hematite (Fe_2O_3) was formed at pH 3-5 and detected by XRD after 68 days of reaction.

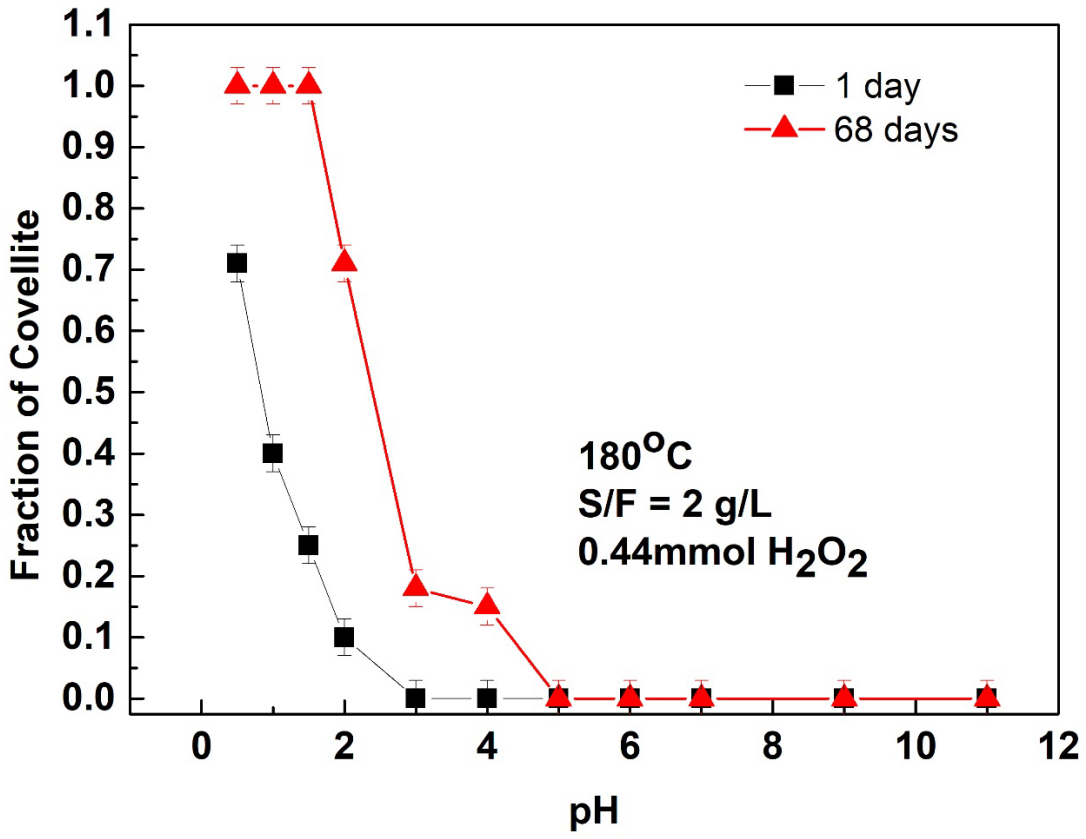

Figure 30 Graphs illustrating the effect of pH on the reaction faction of covellite in final product using 0.44 mmol H_2O_2 as oxidant at 180 °C.

3.3.3 Effect of Temperature

The effect of temperature on the chalcopyrite to covellite conversion was studied under the conditions of pH 0.7-1.5, the S/F ratio of 2 g/L and 140-200 °C. The XRD quantitative analysis showed that the reaction rate increases with increasing temperature under all pH conditions. The covellite was found on the walls of the PTFE cell at pH 0.7-1.5 in the temperature range of 160-200 °C. A significant amount of H_2S were detected and confirmed using acetic acid-soaked pH stripes. The experiments conducted at pH 1 and 120°C gave limited amounts of covellite in the early stage of reactions (prior to 18 days). Between 24-93 days, no covellite and chalcopyrite were detectable by XRD. Elemental sulphur and small amounts of hematite (<4±1 wt%) were present as the solid products with pale blue solutions (Figure 31d). These results suggest complete chalcopyrite dissolution.

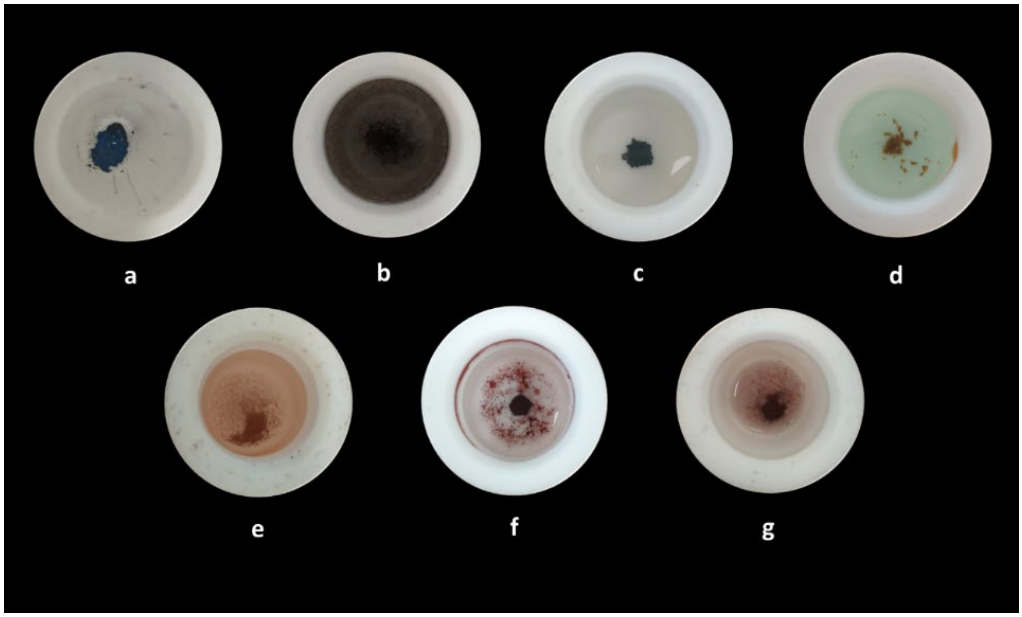

Figure 31 Products formed under various conditions. (a) pH 0.7, 180 °C and 0.44 mmol H_2O_2, after 24 h, (b) pH 1, 180 °C and 0.44 mmol H_2O_2, after 24 h, (c) pH 1, 140 °C and 0.44 mmol H_2O_2, after 360 h, (d) pH 1, 120 °C and 0.44 mmol H_2O_2, after 68 days, (e) pH 3, (f) 4 and (g) 5 180 °C and 0.44 mmol H_2O_2, after 68 days.

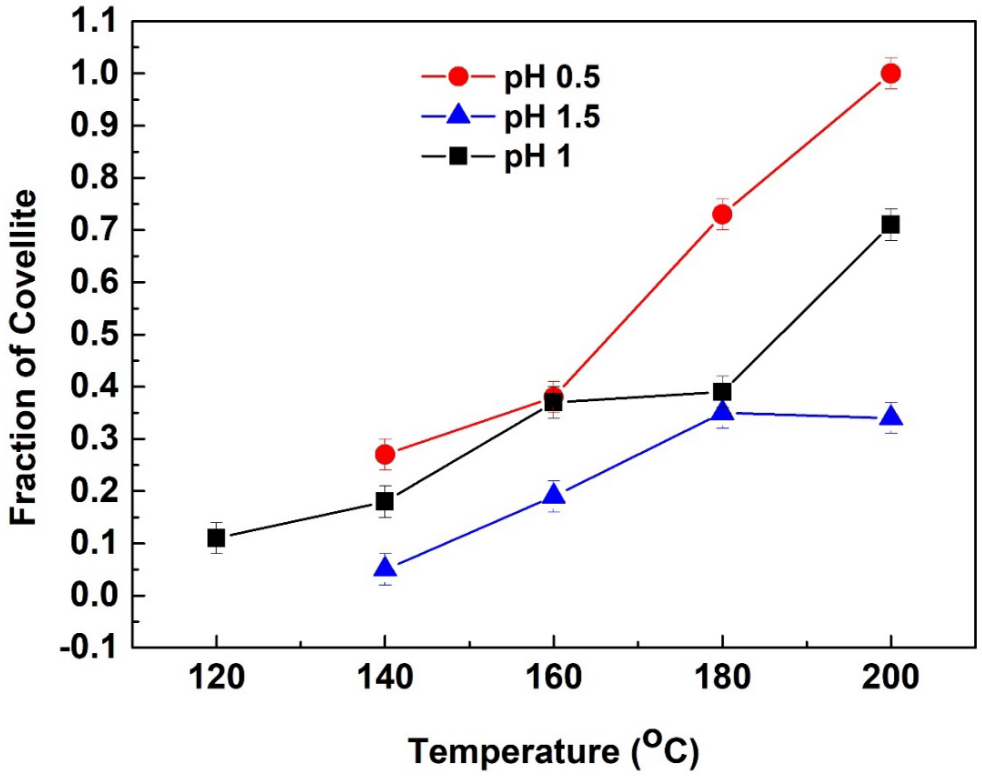

Figure 32 Graphs illustrating the effect of temperature on the fraction of covellite in final product. All these experiments were carried out at pH 0.7, 1 and 1.5 with 0.44 mmol H_2O_2 for 24 h.

3.3.4 Effect of the Availability of Oxygen

The transformation of chalcopyrite to covellite can undergoes oxidation reaction, and therefore, the addition of oxidants is expected to affect the reaction rate. Hydrogen peroxide was used to investigate the effect of the concentration of O_2 on the replacement rate. The effect of the availability of O_2 on the replacement rate was studied using pure N_2, air, and H_2O_2. The experiments were conducted at pH 1 and 180 °C, and a fixed S/F (2 g/L). The quantitative analysis results of the fraction of covellite indicates that the replacement rate rapidly increases with increasing H_2O_2 concentration, but there is no significant difference in the reaction rate between doubled (0.44 mmol) and quadrupled (0.88 mmol) within 24 hours reaction. The reaction at N_2 atmosphere (0 mmol H_2O_2) shows that the replacement of chalcopyrite by covellite is able to proceed without O_2 but with very sluggish rate (Hidalgo et al., 2019).

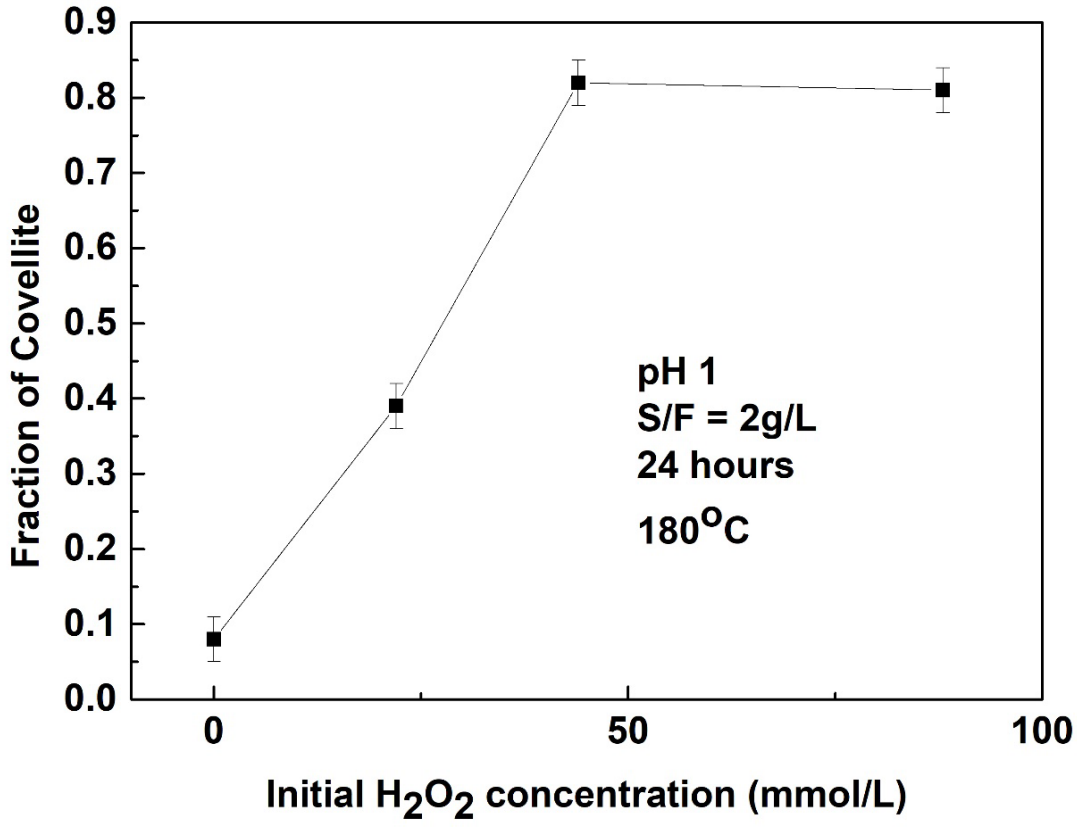

Figure 33 Graphs illustrating the effect of availability and H_2O_2 concentration on the fraction of covellite in final product. All experiments were carried out at pH 1, 180 °C, *S/F* = 2 g/L for 24 h.

3.3.6 Effect of Particle Sizes

Four particle sizes (38-75, 75-150, 150-425 and 425-1020 μm) were selected to determine the influence of specific surface area on the transformation rate. All of the experiments were maintained at 180 °C, pH 1 and fixed *S/F* ratio of 2 g/L. Assuming all of the particles are spherical, the geometric specific surface areas of each particle size are calculated by following equation (40). The A_{geo} is the total surface areas of different particle sizes for a given sample mass. ρ is the density of chalcopyrite and d_e is the effective grain diameter of chalcopyrite particles in a given sieved size fraction (cm). d_{max} is the maximum particle size and d_{min} is the minimum particle size. The calculated specific surface areas are 21.07 cm^2/g for 425-1020 μm, 54.23 cm^2/g for 150-425 μm, 132.34 cm^2/g for 75-150 μm and 294.96 cm^2/g for 38-75 μm. The fraction of covellite in the product indicated the linear relationship between the reaction rate and specific surface area of starting chalcopyrite. At the range of 20-80% reaction extent, the covellite increases 10% with every 50 cm^2/g of increasing specific surface area of chalcopyrite grains.

$$A_{geo} = \frac{6}{\rho_{chalcopyrite} \times d_e} \quad (40)$$

$$d_e = \frac{d_{max} - d_{min}}{\ln(\frac{d_{max}}{d_{min}})} \quad (41)$$

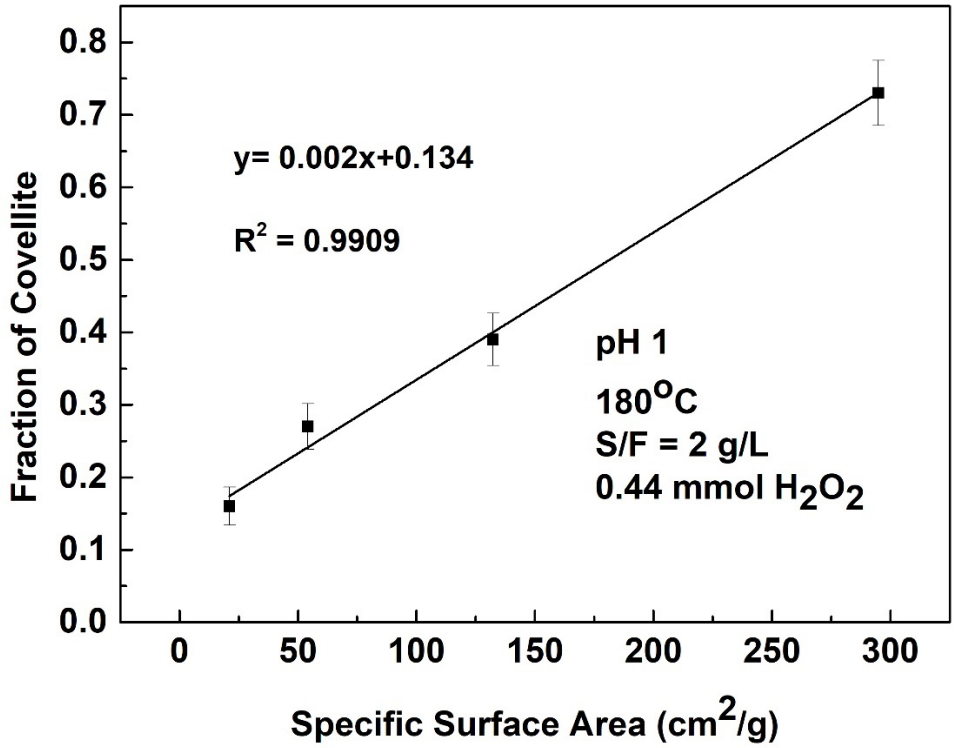

Figure 34 Graphs illustrating the effect of specific surface area on the fraction of covellite in final product. All of the experiments were conducted at pH 1 for 24 h of reaction and maintaining the other reaction parameters constant as included in the labels.

3.3.7 Effect of Cu^{2+}

Previous studies suggest that cupric chloride accelerates the dissolution rate of chalcopyrite in ferric ion media (Duterizac 1978). The effect of the addition of Cu^{2+} on the kinetics was investigated by introducing three different amounts of initial $CuCl_2$ (0.22 mmol, 0.44 mmol and 0.88 mmol) into 20 mL pH 1 buffer solution. All experiments were carried out at fixed temperature (180 °C), *S/F* (2 g/L), and reaction time (24 h) under N_2 atmosphere. The results show that the weight percentage of chalcopyrite in product decreases with the increasing initial Cu^{2+} concentration. With no addition of $CuCl_2$, only 10±2% of chalcopyrite replaced by covellite, 37±4% with 0.22 mmol addition of $CuCl_2$, 60±4% with 0.44 mmol and 56±4% with 0.88 mmol. These results suggest that chalcopyrite dissolution was maximised when the ratio between $CuCl_2$ addition and

amount of chalcopyrite is 3:1 (0.66 mmol: 0.22 mmol). Digenite ($Cu_{1.8}S$) was observed on the experiment with addition of 0.88 mmol $CuCl_2$ after 24 h.

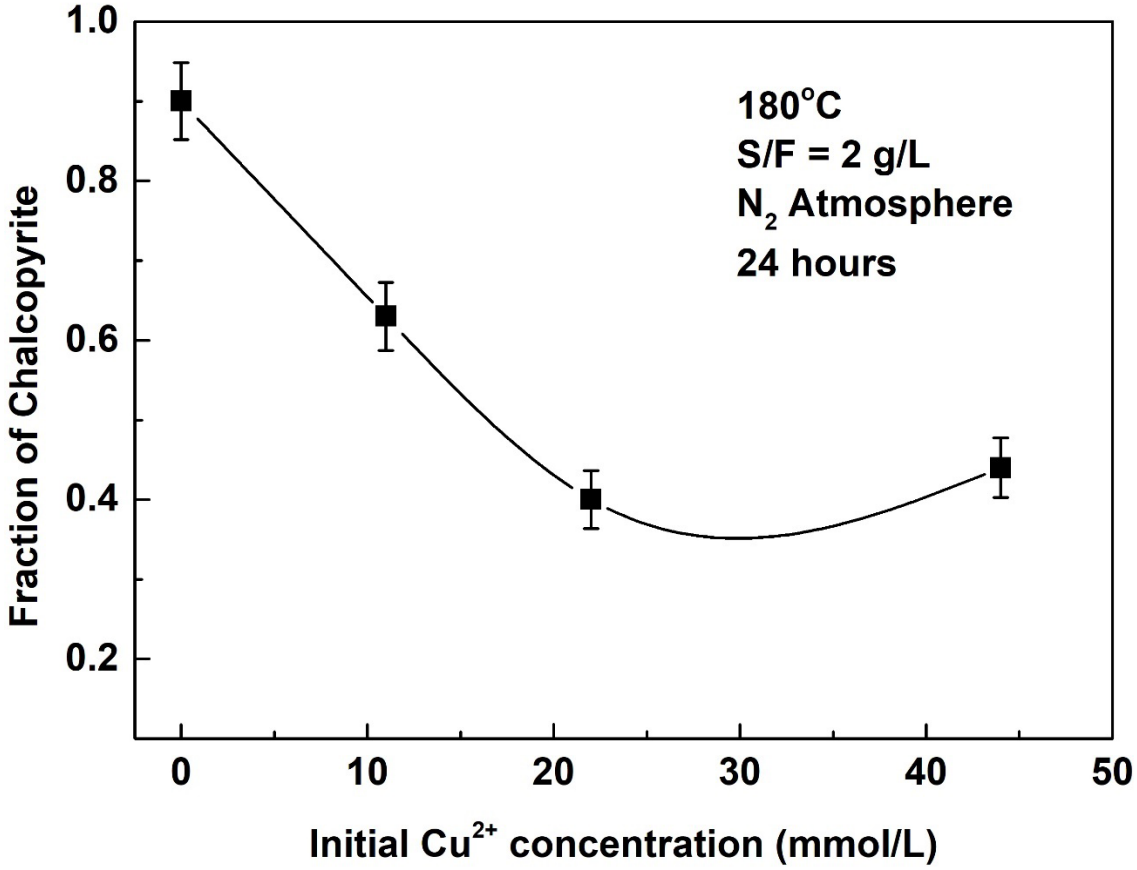

Figure 35 Graph illustrating the effect of the initial concentration of Cu^{2+} on the fraction of chalcopyrite in final product. All of the experiments were conducted under N_2 atmosphere at pH 1 and 180 °C for 24 h of reaction.

3.3.8 Effect of Fe^{2+} and Fe^{3+}

Previous studies reported that the chalcopyrite dissolution rate is influenced by the concentration of Fe^{3+} (Dutrizac and MacDonald, 1974, Dutrizac, 1981, Hirato et al., 1987, Hiroyoshi et al., 2001, Dixon et al., 2008, Watling, 2013, Li et al., 2015). The effect of the addition of Fe^{2+} and Fe^{3+} on the transformation rate was studied by adding $FeCl_3$ and $FeSO_4$ respectively. Three different amounts (0.22 mmol, 0.44 mmol and 0.88 mmol) were added to modify the initial Fe^{2+} and Fe^{3+} concentrations. PXRD quantitative analysis indicate the reaction rate of chalcopyrite replacement by covellite increases with increasing concentrations of the initial Fe^{3+}. 10±2% of chalcopyrite replaced by covellite at pH 1 and 180 °C under N_2 atmosphere after 24 h of reaction with no added Fe^{3+}. The reaction extent of covellite increased to 24±3% with the addition of 0.22 mmol Fe^{3+}, 34±3% with 0.44

mmol Fe^{3+} and 38±4% with 0.88 mmol Fe^{3+}. However, the change of covellite fraction in Fe^{2+} bearing experimental product indicates the replacement rate is slightly increased at 11 mmol/L Fe^{2+} and constantly decreases as initial concentration of Fe^{2+} increases.

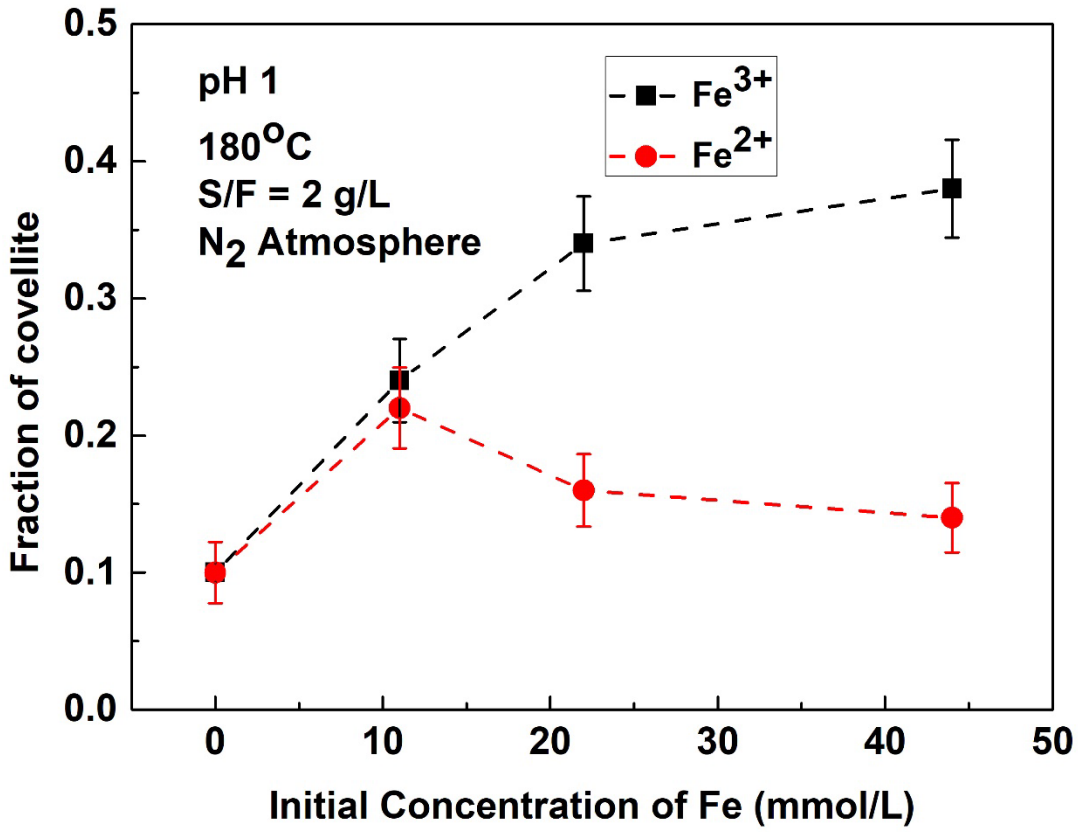

Figure 36 Graph illustrating the effect of the addition of Fe^{2+} and Fe^{3+} on the formation of covellite. All of the experiments were conducted under N_2 atmosphere at pH 1 and 180 °C for 24 h of reaction.

3.3.9 Effect of H_2S

Covellite formed by the precipitation reaction between Cu^{2+} and H_2S (Rickard, 1972). Therefore, the addition of H_2S might have influences on the overall replacement reaction rate. Thioacetamide was used to investigate the effect of H_2S on the transformation rate of chalcopyrite by covellite. Heating thioacetamide to above 105 °C causes it to breakdown to H_2S (Qian et al., 2010, Qian et al., 2011, Zhao et al., 2014a). All experiments are conducted under N_2 atmosphere to avoid the oxidation of H_2S. The results show that the addition of H_2S had no significant impact on the replacement rate of chalcopyrite by covellite. Covellite fractions increased from 10±2% to 12±2% with 11 and 22 mmol/L initial H_2S concentration, and 14±3% with 44 mmol/L.

$$CH_3CSNH_{2(s)} + H_2O_{(aq)} \xrightarrow{\Delta} CH_3CONH_{2(aq)} + H_2S_{(aq)} \quad (42)$$

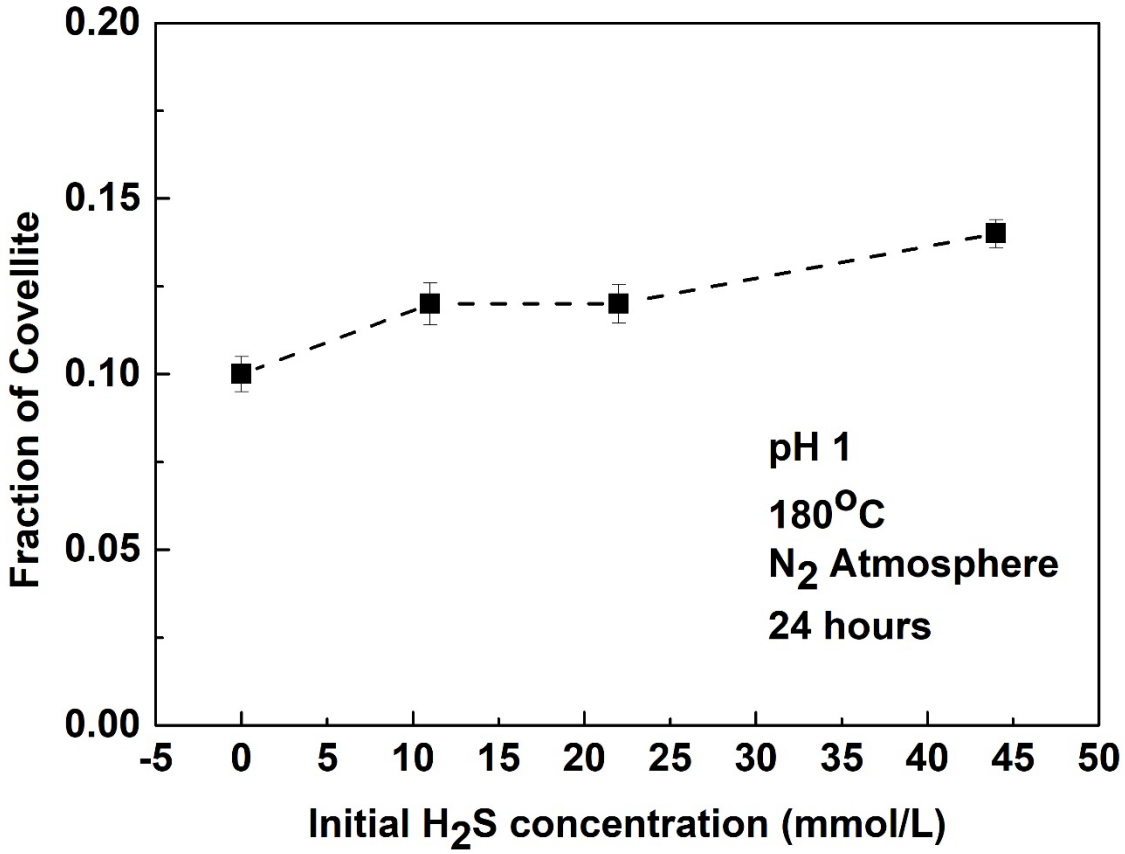

Figure 37 Graph illustrating the effects of the initial concentration of H_2S on the fraction of covellite. All of the experiments were conducted under N_2 atmosphere at pH 1 and 180 °C for 24 h.

3.3.10 Quantitative Kinetic Study

A series of experiments were conducted to investigate the overall reaction rate for the replacement of chalcopyrite by covellite. All experimental conditions were at pH 1, with 0.44 mmol H_2O_2, *S/F* = 2 g/L. At 140 °C, the rate constant *k* is 1.99±0.27 × 10^{-3} h^{-1}, at 160 °C, 5.12±0.66 × 10^{-3} h^{-1}, at 180 °C, 8.57±0.88 × 10^{-3} h^{-1} and at 200 °C, *k* is 5.77±0.25 × 10^{-2} h^{-1}. The values of *n* for the four temperatures are 0.81±0.18, 0.44±0.06, 0.59±0.08 and 0.53±0.03, respectively.

All experimental conditions were at pH 0.5, with 0.44 mmol H_2O_2, *S/F* = 2 g/L The replacement rate was found to be dependent on the temperature. The rate constant *k* is calculated to be 3.79±0.22 × 10^{-3} h^{-1} at 140 °C, 11.8±0.92 × 10^{-3} h^{-1} at 160 °C, 4.7±0.26 × 10^{-2} h^{-1} at 180 °C and 9.7±0.54 × 10^{-2} h^{-1} at 200 °C. The values of *n* for the four temperatures are 1.51±0.21, 0.85±0.09, 1.51±0.18 and 1.9±0.3, respectively.

The experimental conditions are pH 1.5, with 0.44 mmol H_2O_2, *S/F* = 2 g/L. At 140 °C, the rate constant *k* is 2.39±0.26×10^{-3} h^{-1}, at 160 °C, 1.18±0.2×10^{-3} h^{-1}, at 180 °C, 1.9±0.46×10^{-3} h^{-1} and at 200 °C, 3.74±0.56×10^{-3} h^{-1}. The values of *n* for the four temperatures are 0.59±0.07, 0.36±0.05, 0.36±0.05 and 0.42±0.06, respectively.

Table 12 Summary of kinetic data and fitted *Avrami* curve parameters (*k* and *n*) for the replacement of chalcopyrite by covellite at pH 1.

pH 1, 140°C		**pH 1, 160°C**		**pH 1, 180°C**		**pH 1, 200°C**	
Time (h)	**Cv[1] (wt%)**	**Time (h)**	**Cv[1] (wt%)**	**Time (h)**	**Cv[1] (wt%)**	**Time (h)**	**Cv[1] (wt%)**
0	0	0	0	0	0	0	0
48	10	12	21	2	8	4	38
96	37	25	39	9	5	16	63
192	32	73	51	19	32	20	63
264	47	146.5	57	24	41	24	70
432	46	243	65	48	39	28	72
504	54	294	63	72	48	34	74
550	65	340	66	99	58	47	82
600	70	412	78	122	60	65	90
696	92	552	92	144	68		
				174	70		
				234	88		
R^2 = 0.87		R^2 = 0.96		R^2 = 0.94		R^2 = 0.99	
k = 1.99±0.27E-3 h^{-1}		*k* = 5.12±0.66E-3 h^{-1}		*k* = 8.57±0.88E-3 h^{-1}		*k* = 5.77±0.25E-2 h^{-1}	
n = 0.81±0.18		*n* = 0.44±0.06		*n* = 0.59±0.08		*n* = 0.53±0.03	

[1] Cv stands for covellite precipitated.

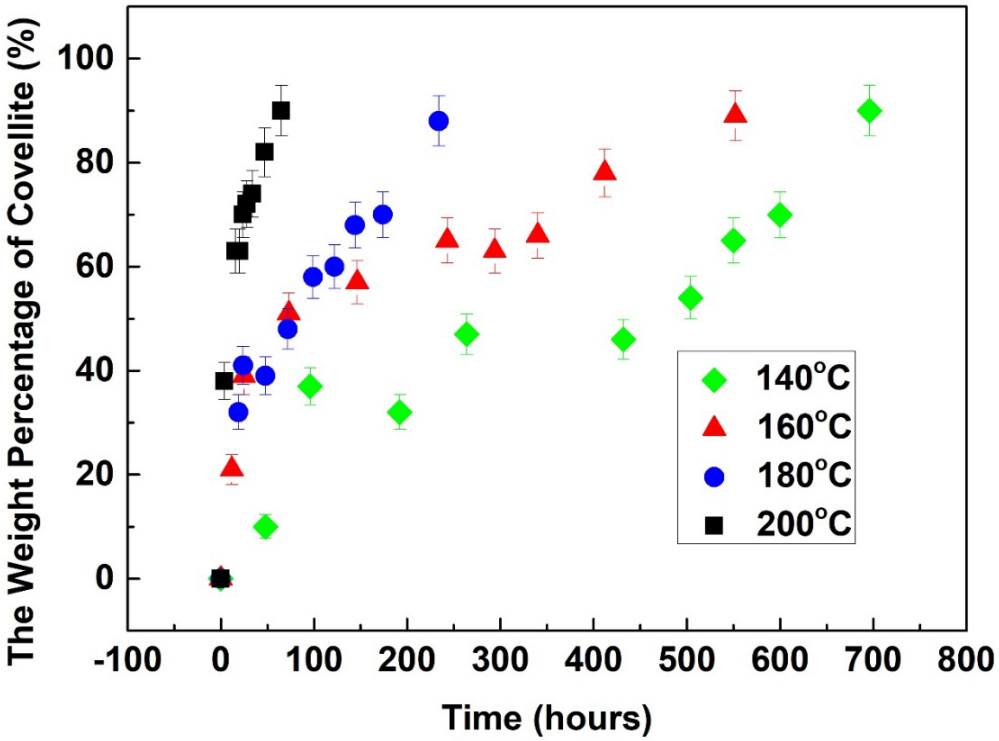

Figure 38 The fraction of covellite in final product against time of experiments at pH 1 with 0.44 mmol H_2O_2 in the 25 mL static Teflon reactor.

Table 13 Summary of kinetic data and fitted *Avrami* curve parameters (*k* and *n*) for the replacement of chalcopyrite by covellite at pH 0.5.

pH 0.5, 140°C		**pH 0.5, 160°C**		**pH 0.5, 180°C**		**pH 0.5, 200°C**	
Time (h)	**Cv[1] (wt%)**	**Time (h)**	**Cv[1] (wt%)**	**Time (h)**	**Cv[1] (wt%)**	**Time (h)**	**Cv[1] (wt%)**
0	0	0	0	0	0	0	0
48	14	12	15	2	5	2	10
120	16	19	18	4	8	4	25
144	34	29	42	6	10	6	32
240	62	41	42	8	29	8	32
288	73	53	62	10.5	29	11	65
336	74	79	63	13	31	13	89
552	89	102	60	16	50	14	85
		144	71	21	60	16	89
				24	73		
R^2 = 0.96		R^2 = 0.96		R^2 = 0.96		R^2 = 0.95	
k = 3.79±0.2E-3 h^{-1}		k = 11.8±0.9E-3 h^{-1}		k = 4.7±0.3E-2 h^{-1}		k = 9.71±0.5E-2 h^{-1}	
n = 1.51±0.21		n = 0.85±0.08		n = 1.51±0.18		n = 1.9±0.3	

[1] Cv stands for covellite precipitated.

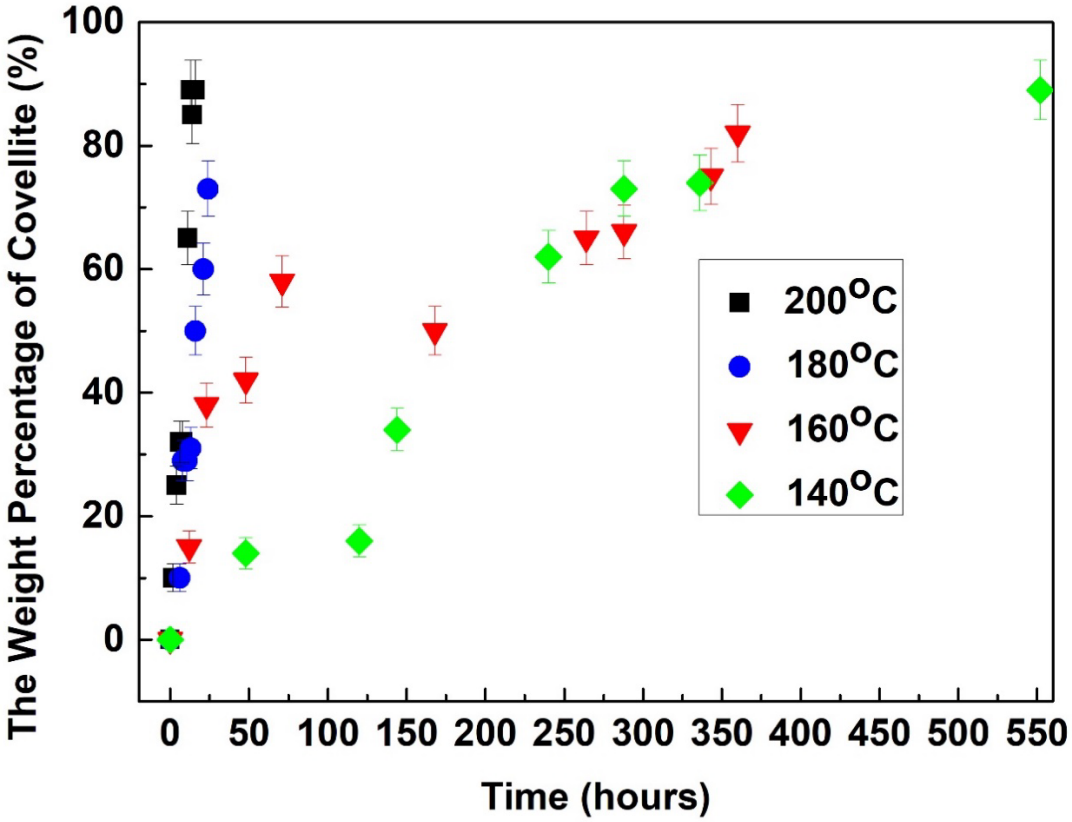

Figure 39 The weight percentage of covellite in final product against time of experiments at pH 0.5 with 0.44 mmol H_2O_2 in the 25 mL static Teflon reactor.

Table 14 Summary of kinetic data and fitted *Avrami* curve parameters (*k* and *n*) for the replacement of chalcopyrite by covellite at pH 1.5.

pH 1, 140°C		**pH 1, 160°C**		**pH 1, 180°C**		**pH 1, 200°C**	
Time (h)	**Cv[1] (wt%)**	**Time (h)**	**Cv[1] (wt%)**	**Time (h)**	**Cv[1] (wt%)**	**Time (h)**	**Cv[1] (wt%)**
0	0	0	0	0	0	0	0
24	12	47.5	26	9	26	24	34
48	25	95	42	24	35	48	41
120	40	120	41	48	40	72	43
168	48	145	43	72	40	101	41
216	46	192	42	148	43	120	47
240	53	264	49	264	48	164	58
336	62	360	48	368	49	215	62
408	57	435	49	600	70	310	68
		648	60	820	76	382	65
		792	67				
R^2 = 0.96		R^2 = 0.95		R^2 = 0.92		R^2 = 0.96	
k = 2.39±0.26E-3 h^{-1}		k = 1.18±0.2E-3 h^{-1}		k = 1.9±0.46E-3 h^{-1}		k = 3.74±0.56E-3 h^{-1}	
n = 0.59±0.07		n = 0.36±0.05		n = 0.35±0.05		n = 0.42±0.06	

[1] Cv stands for covellite precipitated.

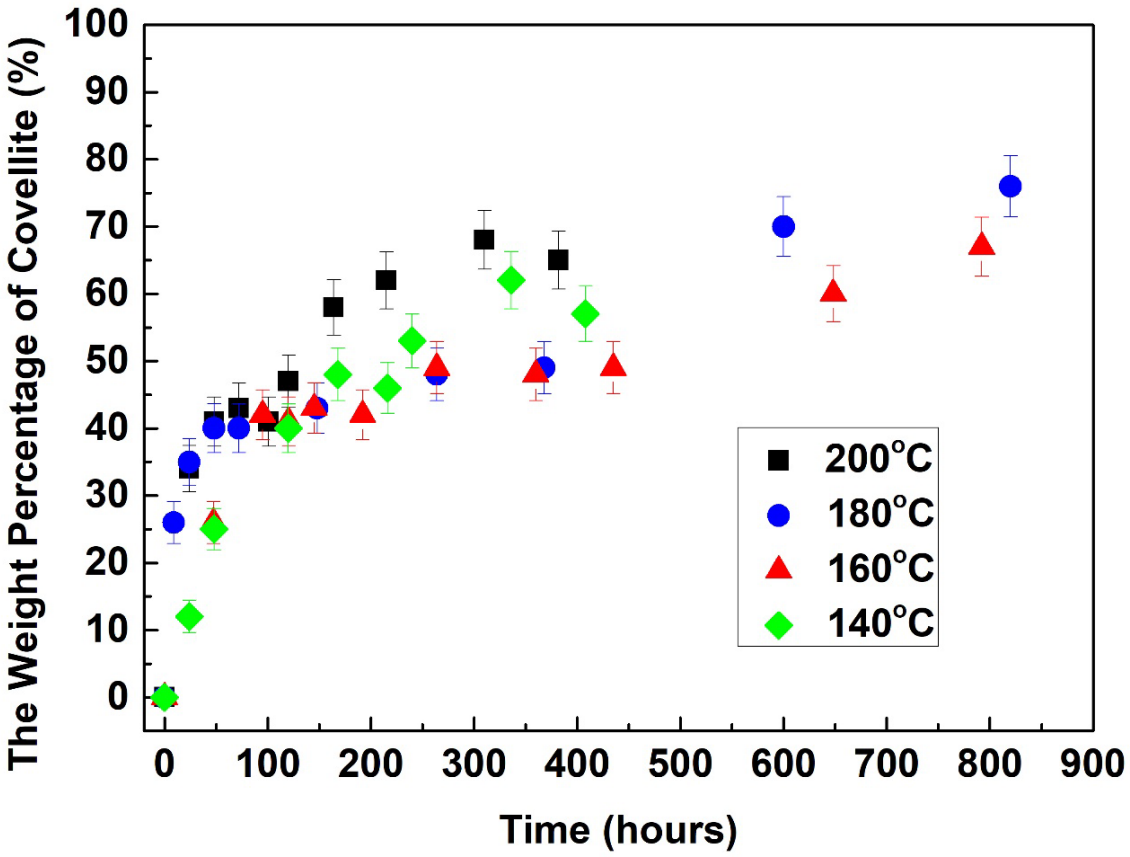

Figure 40 The fraction of covellite in final product against time of experiments at pH 1.5 with 0.44mmol H_2O_2 in the 25 mL static Teflon reactor.

3.3.11 XPS

3.3.11.1 Surface chemical composition

According to the results on effect of pH on chalcopyrite replacement, pH 0.5, pH 1 and pH 1.5 are the three fastest pH conditions under which complete replacement chalcopyrite occurs within time frame. The replacement rate is very fast (within days) at 180 °C. To understand the mechanism of the replacement reaction of chalcopyrite by covellite, three samples at the early stage (2 h) with limited amounts chalcopyrite replaced by covellite were selected. The surface elemental compositions are listed in Table 12. Carbon is the most abundant element which contributed to 29 -43% atomic percentage at surface and was most likely from exposure to atmosphere. The second most abundant element is oxygen, potentially from oxides, hydroxides, and attached and absorbed water (Harmer et al, 2006). S/(Cu + Fe) ratio increased from 0.82 for the original chalcopyrite to 1.37, 1.4 and 1.21 for the chalcopyrite exposed at 180 °C in solution with pH 0.5, pH 1 and pH 1.5 respectively after 2 h.

Table 15 Atomic concentration (%) of elements of unreacted chalcopyrite, chalcopyrite exposed in solution of pH 0.5, pH 1 and pH 1.5 at 180 °C for reaction of 2 h (*hv* = 1487 eV).

	C	O	S	Fe	Cu
Original Chalcopyrite	42.9	36.2	9.4	4.5	6.9
pH 0.5	34.3	16.6	28.4	15.8	4.9
pH 1	42.9	22.0	20.5	3.5	11.1
pH 1.5	29.4	19.4	28.0	5.5	17.7

3.3.11.2 S 2p Spectra

The S *2p* spectra were fitted using computer program CasaXPS (N. Fairley, 2009). The spectra were calibrated by aligning C *1s* peak to 284.8eV prior to fitting. Due to the spin orbit splitting, S *2p* peaks generally occur as doublets (S $2p_{3/2}$ and S $2p_{1/2}$). The binding energy of S $2p_{3/2}$ is 1.19eV higher than that S $2p_{1/2}$ (Nesbitt et al., 1998; Schaufuß et al., 1998; Yang et al., 2015). The Shirley background was used to subtract the S *2p* spectra background (Shirley, 1972), 50% Gaussian and 50% Lorentzian was used to fit the S *2p* spectra. The parameters used for fitting were based on previous publications (Harmer et al, 2006; Yang et al., 2015). Polysulfide on chalcopyrite surface contains multiple chain length and it is difficult to resolve (Smart, 1991). There is also an overlap between elemental sulphur and polysulfide at 164.0 eV (Harmer et al, 2006; Smart, 1991; Yang et al., 2015), so a broad peak was used to represent both of the sum of the two sulphur species in this study. An energy loss feature was applied to resolve the charge transfer to S *3p*-Fe *3d* overlapping states (Fujisawa et al., 1994; Harmer et al., 2004).

There are five sulphur species found on the chalcopyrite surface, which are bulk monosulphide (161.2eV), surface disulphide (162.2eV), polysulphide (163.3eV), elemental sulphur (164.0eV) and energy loss feature (163.8eV) (Nesbitt and Muir, 1998, Fujisawa et al., 1994, Harmer et al., 2004, Harmer et al., 2006, Yang et al., 2015). Under the ambient condition S *2p* spectra (0.3%, Figure 41B), the elemental sulphur on the surface is significantly less than those collected cold stage (6.4%, Figure 41A). It indicates that elemental sulphur is highly volatile at ambient temperature. Increased amount of elemental sulphur and disulphide were observed after chalcopyrite was reacted in acidic solutions with 0.44 mmol H_2O_2 added. More elemental sulphur and less disulphide were observed on the surface as the pH decreases.

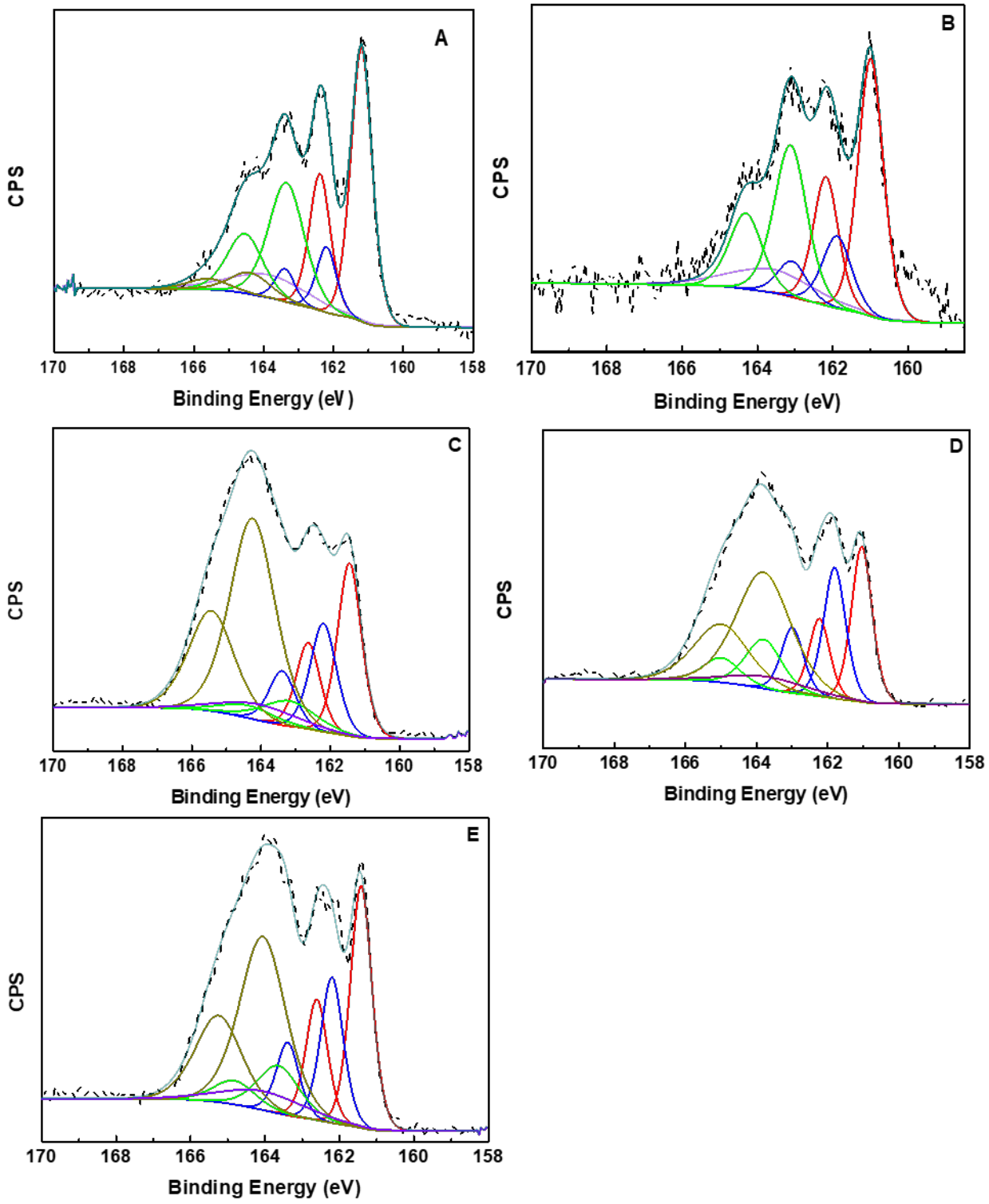

Figure 41 S *2p* XPS spectra of original chalcopyrite collected at temperature colder than room temperature (A), room temperature (B), chalcopyrite reacted at 180 °C in solutions with pH 0.5 (C), pH 1 (D) and pH 1.5 (E) for 2 h collected at -168 °C (Collected by *Al* K_α X-ray source (1487 eV), data analysed using Casa XPS).

Table 16 Composition of sulphur species on the surface of unreacted chalcopyrite, chalcopyrite reacted at 180 °C pH 0.5, pH 1 and pH 1.5 for 2 h (*hv* = 1487 eV).

	Bulk Monosulphide (161.2 eV) (%)	**Surface Disulphide (162.2eV) (%)**	**Polysulphide (163.3eV) (%)**	**Elemental Sulphur (164.0eV) (%)**	**Energy Loss Feature (163.8eV) (%)**
Unreacted Chalcopyrite (Cold)	43.4	9.7	31.8	6.4	8.7
Unreacted Chalcopyrite (Ambient)	43.7	14.0	33.2	0.3	8.8
pH 0.5	22.7	15.7	7.3	49.7	4.6
pH 1	25.4	16.1	9.5	44.0	5.1
pH 1.5	26.7	16.8	10.1	41.0	5.3

3.3.11.3 Cu *2p* and Fe *2p* spectra

Figure 38 showed the Cu *2p* spectra collected at pH 0.5, 1 and 1.5. Cu (I) was the only Cu species (931.8 eV) observed (Goh et al., 2006) on the unreacted chalcopyrite surface because of the Cu $2p_{3/2}$ peak. After the chalcopyrite was exposed to acidic solutions, the Cu $2p_{3/2}$ shifted to higher binding energies, suggesting the formation of Cu oxide on the surface. (Pearce et al., 2006). Copper remained in the +1 oxidation state after reaction for 2 h as no satellite lines between 940-950 eV due to Cu(II) were present.

The Fe *2p* spectra of unreacted and reacted chalcopyrite are shown in Figure 43. The peak from original chalcopyrite at 708.2 eV was possibly from Fe(III)-S (McIntyre and Zetaruk, 1977). All the three reacted chalcopyrite samples showed a feature at 711.0 eV, which is likely from to iron(III)-O-OH species such as iron (III) oxyhydroxides (McIntyre and Zetaruk, 1977).

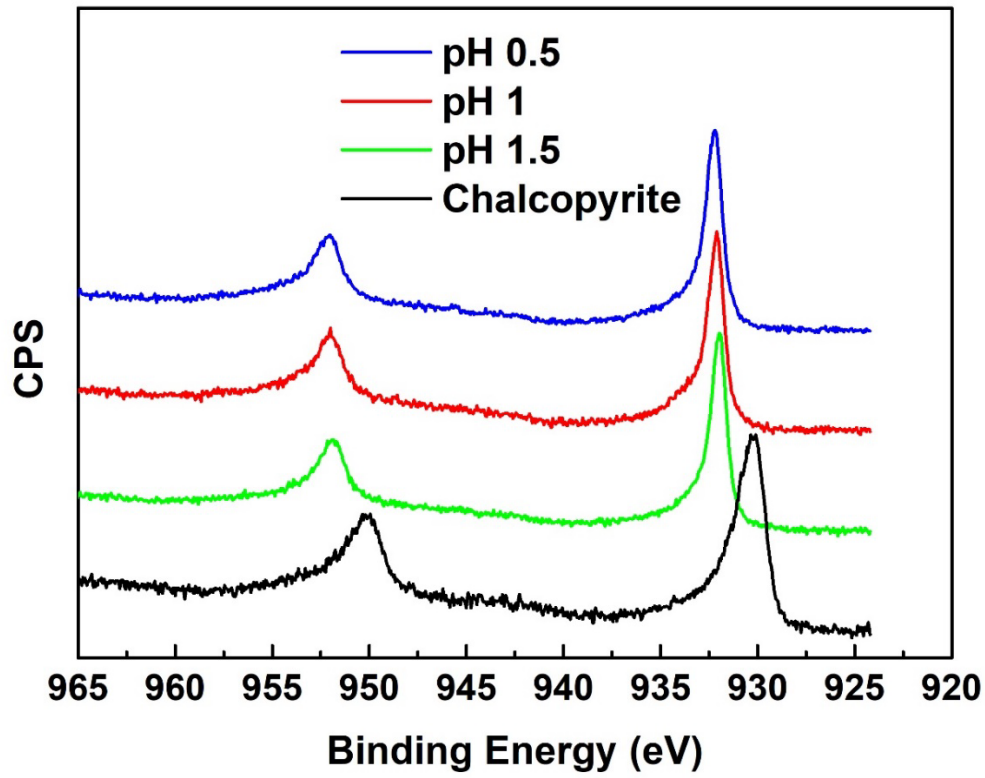

Figure 42 Cu *2p* XPS spectra of unreacted chalcopyrite (Black), chalcopyrite reacted at 180°C in solution with pH 0.5 (Blue), pH 1 (Red) and pH 1.5 (Green) for 2 h.

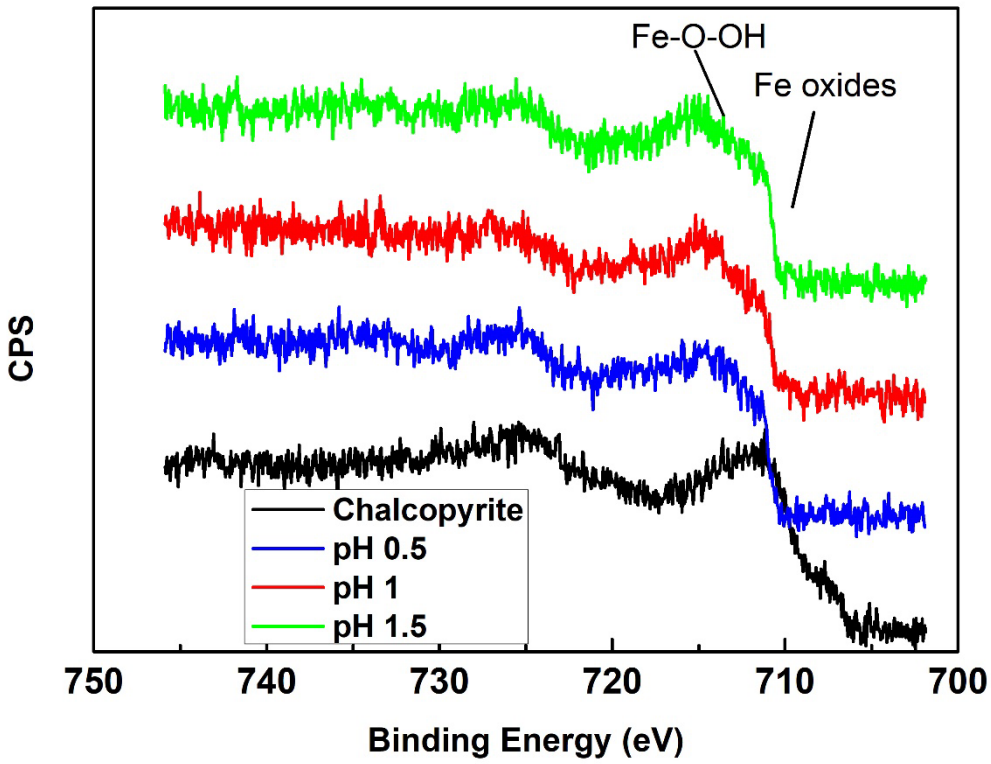

Figure 43 Fe *2p* XPS spectra of unreacted chalcopyrite (Black), chalcopyrite reacted at 180°C in solution with pH 0.5 (Blue), pH 1 (Red) and pH 1.5 (Green) for 2 h.

3.4 Discussion

3.4.1 Reaction Mechanism

The textural characteristics for an interfacial coupled dissolution-reprecipitation (ICDR) mechanism include a sharp reaction front and the visible gaps between chalcopyrite and covellite at pH 1 (Putnis, 2002, Putnis, 2009, Xia et al., 2009, Qian et al., 2010, Zhao et al., 2014b). It indicates the dissolution of chalcopyrite is faster than re-precipitation of covellite. Xia et al. (2009) performed a pseudo-morphic replacement on the nm scale where the tightly coupled reaction has faster precipitation of violarite than dissolution of pentlandite, but also a decoupling at acidic conditions with a gap between the violarite and pentlandite. Solid-state diffusion (SSD) is dependent on the availability of defection sites of the crystal structure, and the density of intrinsic vacancies of crystals increases exponentially with increasing temperature (Putnis, 1992, Altree-Williams et al., 2015). At high temperatures, the activation energy barriers might be overcome by increased kinetic energy and crystal defects induced atomic diffusion within crystals, which is the dominant mechanism for re-establishing the equilibrium process of mineral assemblages. The number of crystal defects is relatively low at low temperature (<500 °C) in most of materials which causes the retarding of SSD. On the other hand, the ICDR mechanism is kinetically favourable at low temperature for the re-equilibration process (Rubie, 1986, Putnis, 2002, Zhao et al., 2013, Altree-Williams et al., 2015). Adegoke et al. (2022) reported a fluid-induced solid-state diffusion reaction mechanism in the replacement of bornite by chalcopyrite and digenite at 160-200 °C with textural evidence of grain boundaries formation. They found the growth of chalcopyrite and digenite lamellae were hindered at the grain boundaries. Textural evidence clearly shows that the replacement reaction to convert chalcopyrite to covellite consists of chalcopyrite dissolution and covellite re-precipitation, rather than solid-state diffusion.

The molar volume change of chalcopyrite replaced by covellite was determined by equation (43), where n_p and n_d represents the number of moles of dissolved mineral (chalcopyrite) and precipitated mineral (covellite). $V_{m,p}$ and $V_{m,d}$ are the molar volumes of precipitated phased and dissolved phase (Pollok et al., 2011, Altree-Williams et al., 2015). A decrease of molar volume (ΔV = -53.3%) was found in the replacement reaction of chalcopyrite by covellite associated with the formation of fractures and pores. Zhao et al. (2009) also reported a negative molar volume change in the replacement reaction of calaverite by gold with generation of pores in the product phase. In this research, covellite was formed along with the fractures and pores, suggesting fluids remains contact with

chalcopyrite assemblages through the formed fractures and pores (Putnis, 2009, Altree-Williams et al., 2015).

$$\Delta V = 100\% \times \left(\frac{n_p V_{m,p} - n_d V_{m,d}}{n_d V_{m,d}}\right) \quad (43)$$

Porous secondary covellite with numerous cracks is also one of the characteristics for interfacial dissolution-reprecipitation reaction (Putnis, 2009, Xia et al., 2009, Adegoke et al., 2022, Altree-Williams et al., 2015, Zhao et al., 2014b, Zhao et al., 2014a). The formation of the outer rim of covellite and chalcopyrite core at pH 1 is also a strong indication of dissolution and reprecipitation processes. Natural samples from the Chuquicamata open pit copper mine also contain covellite existing as outer rims (Marie-Caroline Pinget, 2011). It indicates the replacement of chalcopyrite by covellite in the supergene layer have a similar morphology as the synthetic covellite in this study. The direct relationship between replacement rate and specific surface area of starting chalcopyrite is against a solid-state diffusion mechanism, since the solid-state nucleation of covellite are more difficult at smaller particle size, and then would expect to decrease the reaction rate (Cardew et al. 1984).

3.4.2 XPS Results

As the XPS S 2*p* spectra presented (Figure 37 A), bulk monosulphide (43.4%) is the dominant sulphur specie on the unreacted chalcopyrite surface, following by polysulphide (31.8%), disulphide (9.7%) and elemental sulphur (6.4%). A large amount of elemental sulphur was observed on the surface of chalcopyrite at 164.0 eV of binding energy. An elemental sulphur loss was observed at room temperature under ultra-high vacuum condition by comparing the XPS S 2*p* spectra collected at cold stage (colder than room temperature, 6.4% elemental sulphur) (Figure 41A) and room temperature (0.3% elemental sulphur) (Figure 41B). Therefore, all XPS S 2*p* spectra were collected using a cold stage to investigate the weight percentage of each sulphur specie formed on chalcopyrite surface.

Under acidic conditions, the S/(Cu + Fe) ratio on the surface of chalcopyrite increased after 2 h of reaction at 180 °C with oxidants (0.44 mmol H_2O_2), suggesting chalcopyrite becomes metal-deficient after reaction. Elemental sulphur was formed as dominant sulphur species, which increases with decreasing pH of solution (Figure 41 C, D and E). At pH 0.7, 49.7% of elemental sulphur was found on chalcopyrite surface, decreases to 44% at pH 1 and 41% at pH 1.5. On contrary, the bulk monosulphide and polysulphide species

were significantly decreased on chalcopyrite surface. 43.4% of bulk monosulphide specie was observed on the unreacted chalcopyrite, and decreased to 22.7%, 25.4% and 26.7% after 2 h reactions at pH 0.7, 1 and 1.5 respectively. Polysulphide specie changed from 31.8% to 7.3%, 9.5% and 10.1% respectively after the reaction. No sulphate specie was observed on chalcopyrite surface after reaction. It is suggesting the dissolution chalcopyrite with oxidants under acidic condition is likely to takes the form indicated by equation 44 and form elemental sulphur (Holliday and Richmond, 1990, Hiroyoshi et al., 2001, Hiroyoshi et al., 1997, Hiroyoshi et al., 2000).

$$CuFeS_{2(s)} + O_{2(g)} + 4H^{+}_{(aq)} \rightarrow Cu^{2+}_{(aq)} + Fe^{2+}_{(aq)} + 2S^{0}_{(s)} + 2H_2O_{(aq)} \quad (44)$$

3.4.3 Proposed Reaction Pathway

After 2 h of reaction at 180 °C under acidic conditions (pH 0.7, 1 and 1.5) with oxidants (0.44 mmol), chalcopyrite was firstly dissolved by reacting with protons and oxygen, forming sulphur and covellite on the surface and Cu^{2+} and Fe^{2+} ions in solution via equation (44). Elemental sulphur was observed on chalcopyrite surface using XRD (Figure 90, 91 and 92 in APPENDIX I), SEM and XPS. ICP-MS results indicate that water soluble Cu and Fe ions formed in the solution after reaction, and the concentration of both ions decreased with increasing pH of solution. Previous studies on chalcopyrite oxidation proposed reaction equations (44) and (45) in sulphuric acid with dissolved oxygen as the oxidants (Hiroyoshi et al., 1997, Hiroyoshi et al., 2000, Hiroyoshi et al., 2001, Holliday and Richmond, 1990). Fe^{2+} ions can be oxidized by H^{+} and dissolved oxygen but is very sluggish compared to the dissolved oxygen consumption by chalcopyrite dissolution (Hiroyoshi et al., 1997). Replacement reaction experimental results indicate that chalcopyrite dissolution can be enhanced by the addition of Fe^{3+} (Figure 36). Chalcopyrite dissolution can also follow equation (46) with Fe^{3+} from Fe^{2+} oxidation under acidic condition with dissolved oxygen. The redox potential of each solution is 712 mV at pH 0.7, 730 mV at pH 1 and 727 mV (SHE). Koleini et al. (2011) found that Cu extraction from chalcopyrite is most rapid in the redox potential range of 610-640 mV (SHE). Other studies also reported the most rapid copper leaching from chalcopyrite at a high redox potential (Córdoba et al., 2009, Kametani and Aoki, 1985, Sandström et al., 2005, Viramontes-Gamboa et al., 2007).

$$4Fe^{2+}_{(aq)} + 4H^{+}_{(aq)} + O_{2(aq)} \rightarrow 4Fe^{3+}_{(aq)} + 2H_2O_{(aq)} \quad (45)$$

$$CuFeS_{2(s)} + 4Fe^{3+}_{(aq)} \rightarrow Cu^{2+}_{(aq)} + 5Fe^{2+}_{(aq)} + 2S^{0}_{(s)} \quad (46)$$

A three-step reaction pathway was proposed by Harmer et al. (2006) to describe the formation of surface layers during chalcopyrite leaching by using XPS, SEM and time of flight secondary ion mass spectrometry (ToF-SIMS). After the underlying Cu rich layer on chalcopyrite surface was oxidized through the first step (Equation 47), S_n^{2-} layer formed and release Cu^+ and Fe^{2+} ions into solution. Cu^+ was oxidized to Cu^{2+} immediately in the solution. A reduction step (Equation 48) occurs afterwards, which converts S_n^{2-} to S^{2-} or other short chain S_n^{2-} with oxidation of Fe^{2+} to Fe^{3+}. H^+ ions from solution is adsorbed on the surface during the second step to balance the overall surface charge. Crystalline S^0 produced from short chain S_n^{2-} on the surface by the structural rearrangement via the second oxidation step (Equation 49). Both oxidation and reduction steps are involved in the proposed reaction mechanism, resulting regeneration of Fe^{3+} during the chalcopyrite leaching process.

$$3nCuFeS_{2(s)} + (12n-12)Fe^{3+}{}_{(aq)} \rightarrow [4(CuFe)^{4+}6(S_n^{2-})]_{(s)} + (3n-4)Cu^{2+}{}_{(aq)} + (15n-16)Fe^{2+}{}_{(aq)}\ where\ n \geq 2 \quad (47)$$

$$[4(CuFe)^{4+}6(S_n^{2-})]_{(s)} + (12n-12)Fe^{2+}{}_{(aq)} + (12n-12)H^+{}_{(aq)} \rightarrow [3(CuFe)^{4+}(12n-12)H^+6(S_n^{2-})]_{(s)} + (12n-12)Fe^{3+}{}_{(aq)} \quad (48)$$

$$[3(CuFe)^{4+}(12n-12)H^+6(S_n^{2-})]_{(s)} + 12nFe^{3+}{}_{(aq)} \rightarrow 6S^0_{n(s)} + 3Cu^{2+}{}_{(aq)} + (12n-12)H^+{}_{(aq)} \quad (49)$$

A small amount of covellite (6-8%) was also found on the chalcopyrite surface under the same conditions, identified by SEM (Figure 28B) and XRD. ICP-OES also detected a limited amount of S in the solution, which is extremely lower than Fe and Cu concentration. Hence, chalcopyrite dissolution also occurs in the presence of water, giving covellite as a reaction product (Equation 50) (Gardner and Woods, 1979).

$$CuFeS_{2(s)} + 3H_2O_{(aq)} \rightarrow CuS_{(s)} + Fe(OH)_{3(s)} + S^0_{(s)} + 3H^+ + 3e^- \qquad (\Delta V_{solid} = -53.3\%) \quad (50)$$

Table 17 Concentration of S, Fe and Cu in the solutions collected at pH 0.7, pH 1 and pH 1.5 after 2 h reaction at 180 °C with oxidants (0.44 mmol H_2O_2). Measured by ICP-OES.

	S (ppm)	Fe (ppm)	Cu (ppm)
pH 0.7	28	368	402
pH 1	13	188	192
pH 1.5	13	87	78

Table 18 Reaction extent of chalcopyrite, covellite and sulphur in solid residues after 2 h reaction at pH 0.7, pH 1 and pH 1.5 and 180 °C with oxidants (0.44 mmol H_2O_2). Quantified by TOPAS.

	Chalcopyrite (%)	Covellite (%)	Sulphur (%)
pH 0.7	39	6	50
pH 1	64	8	24
pH 1.5	77	6	13

At elevated temperatures (140 °C or above), elemental sulphur (melting point: 112 °C) produced from chalcopyrite dissolution (Equation 44 and 46) reacts with H_2O and produce H_2S. The experimental results at pH 1 and 120 °C indicate that the sulfur reaction with water vapor does not occur at 120 °C. At 180 °C and 200 °C, sulphur was observed after heating for 2 h, but no sulfur detected after 6 h of reaction at 200 °C or after 19 h at 180 °C. This suggests that elemental sulphur is an intermediate reaction product in the replacement of chalcopyrite by covellite. When the temperature reaches 140 °C or above, the reaction between sulphur and water vapor takes place rapidly and forms H_2S, as confirmed by the detection of H_2S and the reduction of elemental sulphur after 3 days of reaction. The production of hydrogen sulfide through reaction between water and sulphur under high temperature conditions was reported in previous studies (Fang et al., 2011; Randall and Bichowsky, 1918).

$$3S_{(s)} + 2H_2O_{(g)} \rightarrow 2H_2S_{(aq)} + SO_{2(g)} \quad (51)$$

$$H_2S_{(aq)} \leftrightarrow H^+_{(aq)} + HS^-_{(aq)} \quad (52)$$

After S converts to H_2S, H_2S reacts with Cu^{2+} in the solution and precipitate either on the surface or on the reactor wall. Rickard (1972) have proposed the following mechanism in copper sulfide precipitation in Na_2S solutions reacted with copper sulfate at 25°C.

$$Cu^{2+}_{(aq)} + HS^-_{(aq)} \rightarrow CuS_{(s)} + H^+_{(aq)} \quad (53)$$

The overall replacement reaction of chalcopyrite by covellite can be written as:

$$2CuFeS_{2(s)} + 3O_2 + 6H^+ \rightarrow 2CuS_{(s)} + 2Fe^{2+} + H_2S_{(g)} + 2H_2O + SO_4^{2-} \ (\Delta V_{solid} = -53.3\%) \quad (54)$$

The replacement reaction of chalcopyrite by covellite can also be achieved under acidic conditions without dissolved oxygen, producing Cu^{2+}, Fe^{2+} and H_2S via equation (55) (Lu et al., 2016, Hidalgo et al., 2018). The oxidation state of S remains unchanged and no net transfer of electrons to solution species. The oxidation state of Cu and Fe in chalcopyrite are +1 and +3 respectively (Boekema et al., Goh et al., 2006 and Wincott and Vaughan, 2006). Cu^{2+} interacts with H_2S to form covellite as Equation (53). The fraction of covellite (10% after 24 h reaction at 180°C) indicates the reaction rate is slower than the experiments with oxidants (Figure 33).

$$CuFeS_{2(s)} + 4H^{+}_{(aq)} \rightarrow Cu^{2+}_{(aq)} + Fe^{2+}_{(aq)} + 2H_2S_{(aq)} \quad (55)$$

$$Cu^{+}_{(aq)} + Fe^{3+}_{(aq)} \rightarrow Cu^{2+}_{(aq)} + Fe^{2+}_{(aq)} \quad (56)$$

3.4.4 Activation Energy

Average activation energy at different pH values were calculated using the *Arrhenius* equation. At pH 0.7 and pH 1, the average E_a are calculated to be 90±21 kJ/mol and 86±17 kJ/mol respectively, suggesting that the replacement reaction is an interface-controlled reaction with E_a typically being ≥60 kJ/mol. The average E_a decreases to 27±7 kJ/mol at pH 1.5, implying that the reaction becomes transport controlled. For transport-controlled reactions the activation energies are typically E_a of ≈ 20 kJ/mol (Brantley, 2008).

At pH 1 with 0.22 mmol H_2O_2, the modified 'time-to-a-given-fraction' method gave a decreased E_a in the temperature range of 140-200 °C at each 10% of covellite reaction extent. The initial E_a at 0-10% of covellite reaction extent is 110 kJ/mol and end up with 69 kJ/mol at 80-90% reaction extent. It is suggesting that the replacement reaction mechanism at pH 1 is an interface-controlled reaction (typical E_a ≈ 60 kJ/mol). In comparison, the replacement reaction at pH 0.7 resulted in a decrease in the initial E_a to approximately 62 kJ/mol which progressively increased with increasing extent of reaction. This indicates that the transformation of chalcopyrite to covellite at pH 0.7 also follows an interfaced-controlled reaction mechanism (Brantley, 2008). In contrast, replacement reaction at pH 1.5 showed a constantly decreasing E_a with increasing reaction extent, starting from 56 kJ/mol to 9 kJ/mol. This suggests that the reaction mechanism possibly changes from the interface to transport-controlled mechanism (E_a ≈ 20 kJ/mol) after 40% reaction.

The SEM images of covellite surface morphology (Figure 28) indicated that larger size of covellite grains formed on chalcopyrite at pH 0.7 (Figure 28B) than pH 1 (Figure 28C). The formed covellite grains have no pores and cracks, so it is not permeable to allow the solution through and reacts with remaining chalcopyrite. Solutions can only diffuse though the gap between covellite grains after entire chalcopyrite grain coated by covellite. As the replacement reactions progress, increasing amount of large covellite grains formed on the chalcopyrite surface at pH 0.7 which may inhibit the transport of solution towards chalcopyrite grains and increase the difficulty of further reaction. Thus, the E_a are increasing as the reaction progress. On the other hand, the particle size of covellite grains formed at pH 1 is relatively smaller with numerous particles formed. The gap between each covellite particle at pH 1 is expected to be more than pH 0.7, which causes the formed covellite layer more permeable at pH 1, allows the fluids constantly contact with remained chalcopyrite. Thus, a decreasing E_a was estimated at pH 1 as reaction progress.

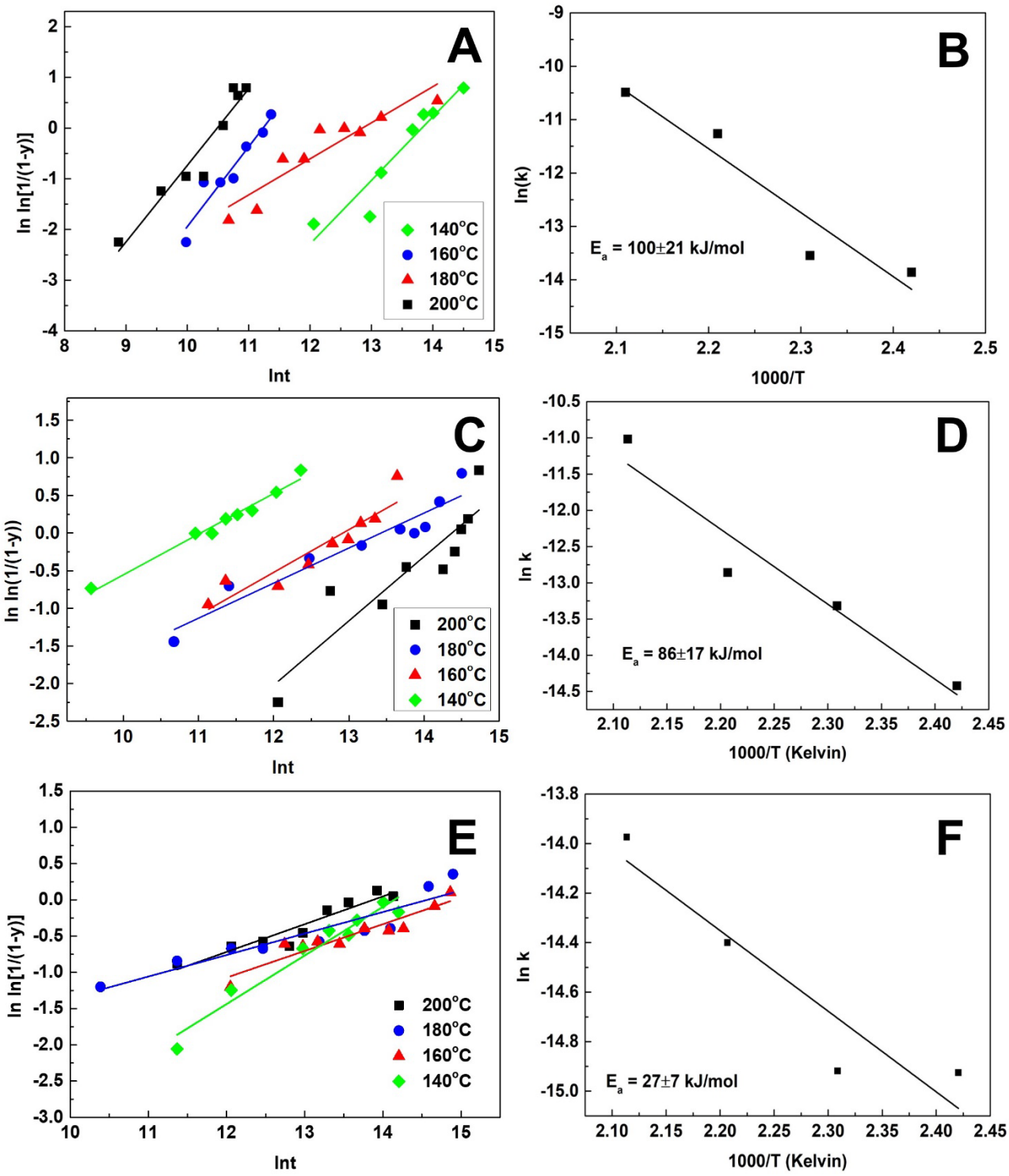

Figure 44 The lineal regression of *Avrami* plots (left) and the corresponding *Arrhenius* plots (right) within 140°C-200°C. pH 0.7 A and B, pH 1: C and D and pH 1.5: E and F.

Table 19 Activation energy calculated by *Avrami-Arrhenius* methods within 140-200°C in different pH value solutions.

	140	***160***	***180***	***200***	**Average E_a (kJ/mol)**
pH 0.7	n = 1.51	n = 0.85	n = 1.51	n = 1.9	90±21
	k = *3.79*×10^{-3} h^{-1}	k = *11.8*×10^{-3} h^{-1}	k = 4.7×10^{-3} h^{-1}	k = 9.71×10^{-3} h^{-1}	
pH 1	n = 0.81	n = *0.44*	n = 0.59	n = 0.53	86±17
	k = 1.99×10^{-3} h^{-1}	k = 5.12×10^{-3} h^{-1}	k = 8.57×10^{-3} h^{-1}	k = 5.77×10^{-3} h^{-1}	
pH 1.5	n = 0.6	n = 0.368	n = 0.3	n = 0.8	27±7
	k = *1.37*E-07	k = 3.32E-07	k = 5.57E-07	k = 8.54E-07	

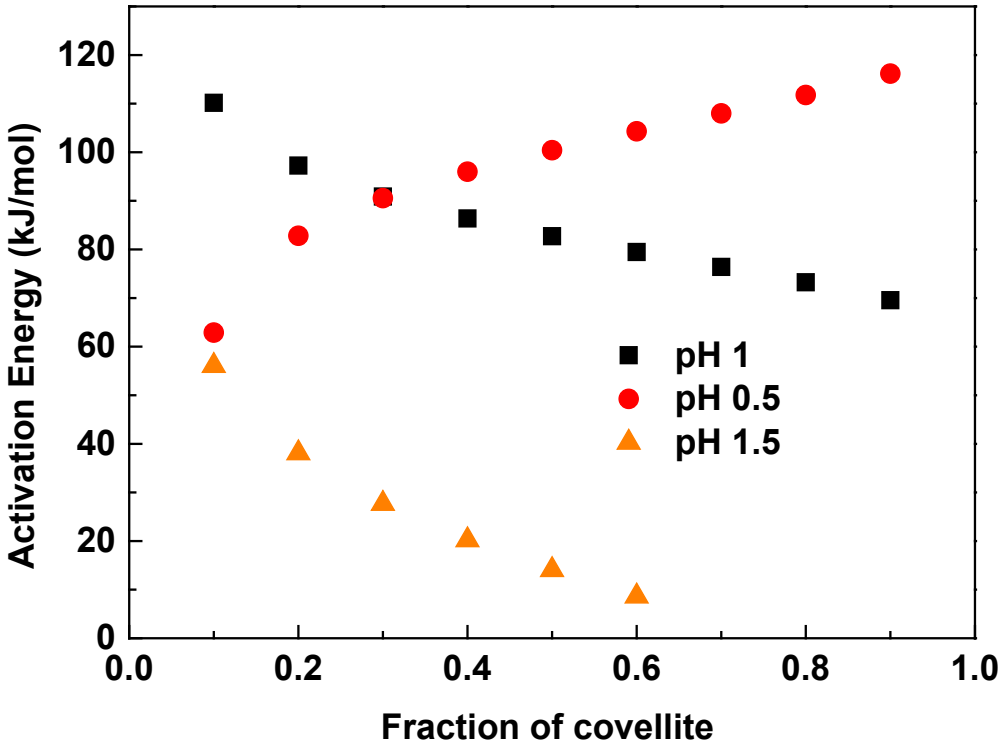

Figure 45: Activation energy fraction against the fraction of covellite, calculated by the modified 'time-to-a-given-fraction' method for the replacement reaction of chalcopyrite by covellite. Four temperatures including 140°C, 160°C, 180°C and 200°C were used for the determination of E_a.

3.4.5 Rate-determining Step

Our results suggest that the dissolution of chalcopyrite is likely to be rate-determining rather than the formation of covellite with oxidants when temperature is 140°C and above. This conjecture is supported by the following observations: (1) the solution pH tends to control the replacement rate of chalcopyrite by covellite according to the PXRD results, and pH have more influences on the chalcopyrite dissolution than on covellite precipitation;

(2) the overall reaction rate increased with the increasing initial concentration of Fe^{3+}, which only affects chalcopyrite dissolution; (3) the initial H_2O_2 concentration is strongly influenced by the transformation rate, but the covellite precipitation is not affected by O_2. (4), H_2S is one of the key factors in covellite precipitation; however, the overall replacement rate is independent of the initial H_2S concentration.

At 120°C or below, the sulphur (melting point of sulphur is 115 °C) reaction with water vapor is the rate-determining step, as chalcopyrite dissolution was completed after 18 days, but no covellite observed even after 68 days due to the lack of H_2S. This is the only pathway of H_2S production in the replacement reaction of chalcopyrite by covellite experiments. Covellite can be formed at room temperature and pressure in the solutions containing 0.001 mol $CuSO_4$ and 0.03 Na_2S (Rickard, 1972). After chalcopyrite was completely dissolved at 120 °C, the Cu concentration in the solution is much higher than Rickard (1972) study, suggesting covellite can be formed with H_2S at this temperature. Previous studies suggests that the reaction between water and sulfur can only occur at temperatures above the melting point of sulfur (Randall and Bichowsky, 1918, Fang et al., 2011).

3.4.6 The Replacement of Chalcopyrite by Covellite in Nature

The replacement reaction rate of chalcopyrite by covellite at low temperature (25 °C) can be calculated by extrapolating the data with modified time to given fraction (Eqs. (41). At 25 °C, 10% of 75-150 μm chalcopyrite would be replaced by covellite after 2.8 years of reaction in pH 0.5 solution with 0.22 mmol H_2O_2, and more than 25,000 years are required for 90% of chalcopyrite reacted. At pH 1, the first 10% of chalcopyrite is predicted to be replaced by covellite after 500 years, but 90% of reaction extent are expected after 2,000 years. These extrapolations of results suggesting that the formation of covellite in supergene deposits by replacing chalcopyrite would take centuries. However, the reaction between elemental sulphur and water was not occurs at 120 °C to produce H_2S, which is one of key reactants to form covellite. In Nature, some sulphur-reducing bacteria including *Desulfuromonas, Desulfurella* and *Sulfospirillum* species use elemental sulphur and sulfate as terminal electron acceptor for the anaerobic respiration and release H_2S (Camacho, 2009). Thus, the formation of covellite in Nature may be promoted with sulphur-reducing bacteria.

$$H_2SO_{4(aq)} + 2CH_2O \rightarrow 2CO_{2(g)} + 2H_2O_{(aq)} + H_2S_{(aq)} \quad (57)$$

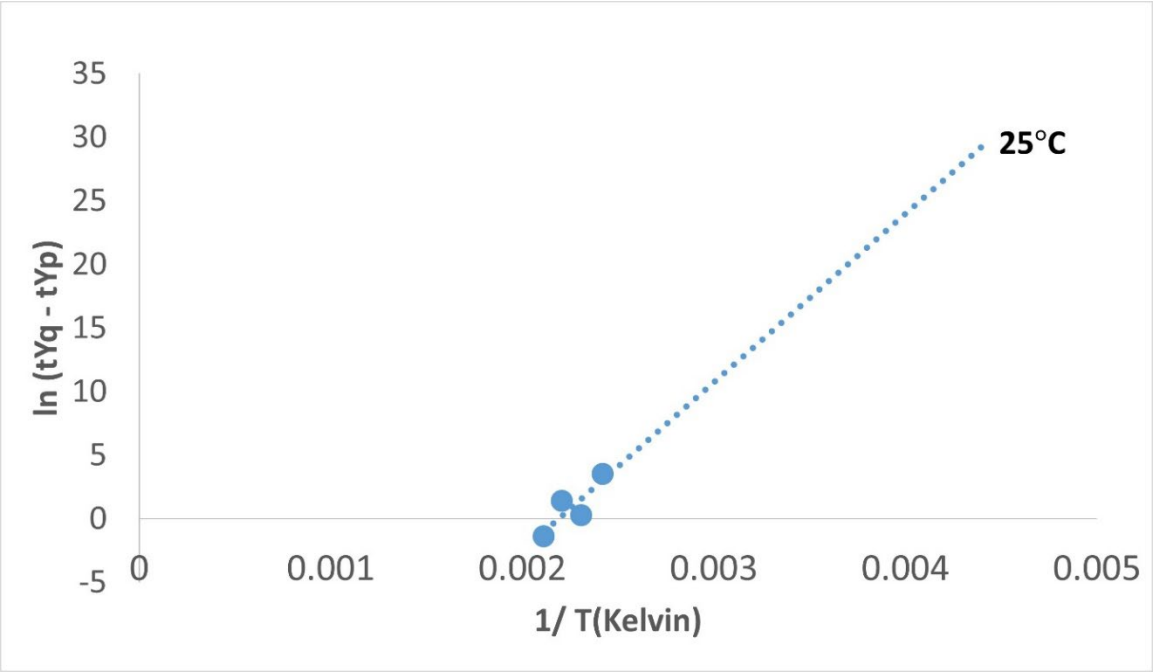

Figure 46 The estimation of reaction time needed for 10% chalcopyrite by covellite at pH 1 and 25 °C by extrapolation.

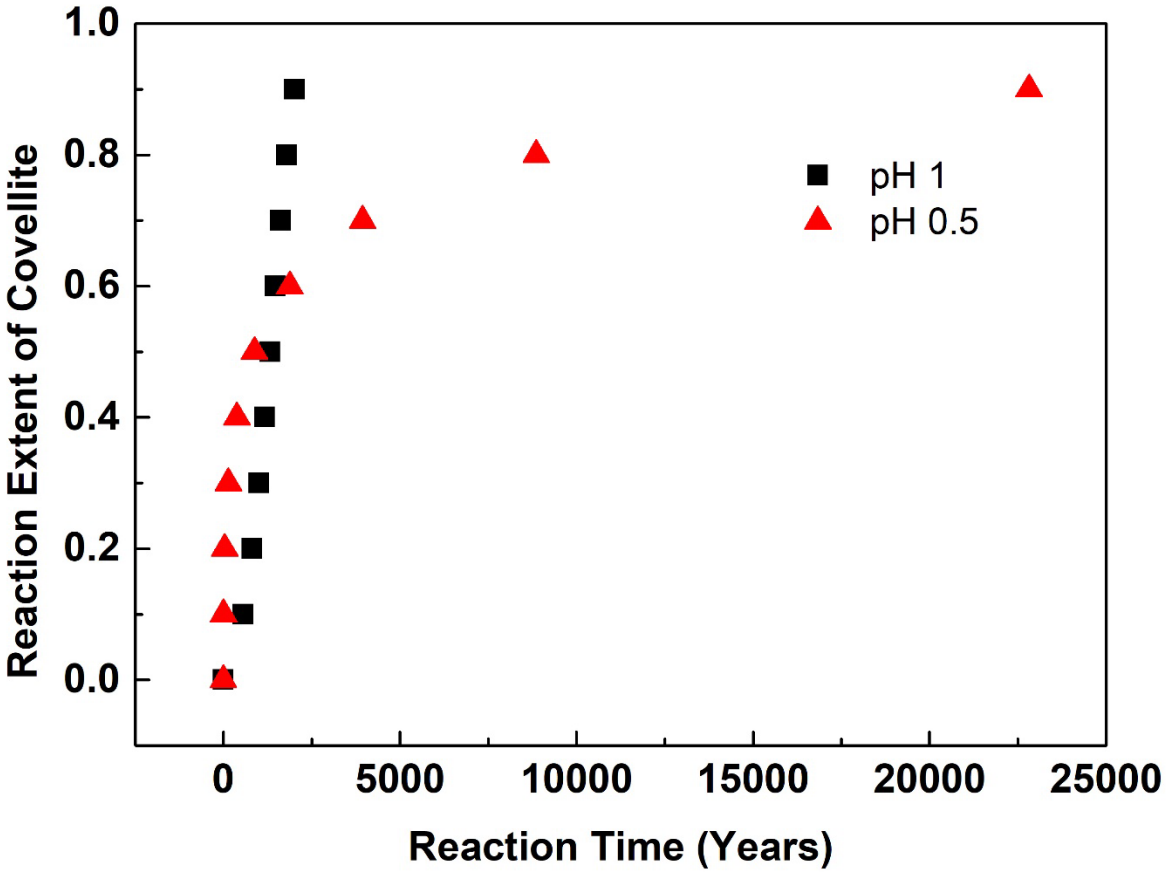

Figure 47 The estimation reaction time needed for the replacement reaction of chalcopyrite by covellite in Nature at pH 0.5 (red) and pH 1 (black).

3.5 Conclusion

In conclusion, chalcopyrite was successfully replaced by covellite under acidic condition at temperature 140-200 °C though a coupled dissolution and reprecipitation mechanism, which is proved by the textural evidence, including formation of reaction front between chalcopyrite and covellite, a gap formed in product phase and formation of pores and cracks. The replacement reaction is a three-step reaction mechanism: 1) chalcopyrite dissolution with H^+, dissolved O_2 and Fe^{3+}, which releasing Cu^{2+} and Fe^{2+} in solution and forming elemental sulphur; 2) the production of H_2S by the reaction between elemental sulphur and water; 3) covellite precipitation between Cu^{2+} and HS^-. The overall replacement reaction rate was controlled by the pH of solution, concentration of oxidants (both H_2O_2 and Fe^{3+}), temperature and specific surface area. Chalcopyrite dissolution is the rate-limiting step of overall replacement reaction, rather than covellite precipitation. *Avrami-Arrhenius* model suggested that it is an interface-controlled reaction at pH 0.7 and pH 1 with average activation energies of 90±21 kJ/mol and 86±17 kJ/mol respectively. It was changed to transport-controlled reaction at pH 1.5 with activation energy of 27±7 kJ/mol.

3.6 Reference List

ADEGOKE, I. A., XIA, F., DEDITIUS, A. P., PEARCE, M. A., ROBERTS, M. P. & BRUGGER, J. 2022. A new mode of mineral replacement reactions involving the synergy between fluid-induced solid-state diffusion and dissolution-reprecipitation: A case study of the replacement of bornite by copper sulfides. Geochimica et Cosmochimica Acta.

ALTREE-WILLIAMS, A., PRING, A., NGOTHAI, Y. & BRUGGER, J. 2015. Textural and compositional complexities resulting from coupled dissolution–reprecipitation reactions in geomaterials. Earth-Science Reviews, 150, 628-651.

ANTHONY, J. W. 1995. Mineralogy of Arizona, University of Arizona Press.

BERRY, L. 1954. The crystal structure of covellite, cuse and klockmannite, cuse. American Mineralogist: Journal of Earth Planetary Materials, 39, 504-509.

BRANTLEY, S. L. 2008. Kinetics of mineral dissolution. Kinetics of water-rock interaction. Springer.

BRUKER, A. X. S. 2009. Topas V4. 2: General profile and structure analysis software for powder diffraction data. Karlsruhe, Germany: Bruker AXS.

CHAUDHARI, A., WEBSTER, N. A., XIA, F., FRIERDICH, A., RAM, R., ETSCHMANN, B., LIU, W., WYKES, J., BRAND, H. E. & BRUGGER, J. 2021. Anatomy of a complex mineral replacement reaction: role of aqueous redox, mineral nucleation, and ion transport properties revealed by an in-situ study of the replacement of chalcopyrite by copper sulfides. Chemical Geology, 581, 120390.

CÓRDOBA, E., MUÑOZ, J., BLÁZQUEZ, M., GONZÁLEZ, F. & BALLESTER, A. 2008. Leaching of chalcopyrite with ferric ion. Part I: General aspects. Hydrometallurgy, 93, 81-87.

CÓRDOBA, E., MUÑOZ, J., BLÁZQUEZ, M., GONZÁLEZ, F. & BALLESTER, A. 2009. Passivation of chalcopyrite during its chemical leaching with ferric ion at 68 C. Minerals Engineering, 22, 229-235.

DIXON, D., MAYNE, D. & BAXTER, K. 2008. Galvanox™–a novel galvanically-assisted atmospheric leaching technology for copper concentrates. Canadian Metallurgical Quarterly, 47, 327-336.

DUTRIZAC, J. 1981. The dissolution of chalcopyrite in ferric sulfate and ferric chloride media. Metallurgical Transactions B, 12, 371-378.

DUTRIZAC, J. & MACDONALD, R. 1974. The kinetics of dissolution of covellite in acidified ferric sulphate solutions. Canadian metallurgical quarterly, 13, 423-433.

FAIRLEY, N. 2009. CasaXPS Mannual, Version 2.3.15. Casa Soft ware Ltd.

FANG, H., BROWN, B., YOUNG, D. & NEŠIĆ, S. 2011. Investigation of elemental sulfur corrosion mechanisms. CORROSION.

FUJISAWA, M., SUGA, S., MIZOKAWA, T., FUJIMORI, A. & SATO, K. 1994. Electronic structures of CuFeS 2 and CuAl 0.9 Fe 0.1 S 2 studied by electron and optical spectroscopies. Physical Review B, 49, 7155.

GEELHOED, J. S., MEEUSSEN, J. C., HILLIER, S., LUMSDON, D. G., THOMAS, R. P., FARMER, J. G. & PATERSON, E. 2002. Identification and geochemical modeling of processes controlling leaching of Cr (VI) and other major elements from chromite ore processing residue. Geochimica et Cosmochimica Acta, 66, 3927-3942.

GOH, S. W., BUCKLEY, A. N., LAMB, R. N., ROSENBERG, R. A. & MORAN, D. 2006. The oxidation states of copper and iron in mineral sulfides, and the oxides formed on initial exposure of chalcopyrite and bornite to air. Geochimica et Cosmochimica Acta, 70, 2210-2228.

HARMER, S. L., PRATT, A. R., NESBITT, W. H. & FLEET, M. E. 2004. Sulfur species at chalcopyrite (CuFeS2) fracture surfaces. American Mineralogist, 89, 1026-1032.

HARMER, S. L., THOMAS, J. E., FORNASIERO, D. & GERSON, A. R. 2006. The evolution of surface layers formed during chalcopyrite leaching. Geochimica et Cosmochimica Acta, 70, 4392-4402.

HIDALGO, T., KUHAR, L., BEINLICH, A. & PUTNIS, A. 2018. Kinetic study of chalcopyrite dissolution with iron (III) chloride in methanesulfonic acid. Minerals Engineering, 125, 66-74.

HIRATO, T., MAJIMA, H. & AWAKURA, Y. 1987. The leaching of chalcopyrite with ferric sulfate. Metallurgical Transactions B, 18, 489-496.

HIROYOSHI, N., HIROTA, M., HIRAJIMA, T. & TSUNEKAWA, M. 1997. A case of ferrous sulfate addition enhancing chalcopyrite leaching. Hydrometallurgy, 47, 37-45.

HIROYOSHI, N., MIKI, H., HIRAJIMA, T. & TSUNEKAWA, M. 2000. A model for ferrous-promoted chalcopyrite leaching. Hydrometallurgy, 57, 31-38.

HIROYOSHI, N., MIKI, H., HIRAJIMA, T. & TSUNEKAWA, M. 2001. Enhancement of chalcopyrite leaching by ferrous ions in acidic ferric sulfate solutions. Hydrometallurgy, 60, 185-197.

HOLLIDAY, R. & RICHMOND, W. 1990. An electrochemical study of the oxidation of chalcopyrite in acidic solution. Journal of electroanalytical chemistry interfacial electrochemistry, 288, 83-98.

KNIGHT, K. S., MARSHALL, W. G. & ZOCHOWSKI, S. W. 2011. The low-temperature and high-pressure thermoelastic and structural properties of chalcopyrite, CuFeS2. The Canadian Mineralogist, 49, 1015-1034.

KOLEINI, S. J., AGHAZADEH, V. & SANDSTRÖM, Å. 2011. Acidic sulphate leaching of chalcopyrite concentrates in presence of pyrite. Minerals Engineering, 24, 381-386.

LI, K., BRUGGER, J. & PRING, A. 2018. Exsolution of chalcopyrite from bornite-digenite solid solution: an example of a fluid-driven back-replacement reaction. Mineralium Deposita, 53, 903-908.

LI, Y., QIAN, G., LI, J. & GERSON, A. R. 2015. Kinetics and roles of solution and surface species of chalcopyrite dissolution at 650 mV. Geochimica et Cosmochimica Acta, 161, 188-202.

LU, D., WANG, W., CHANG, Y., XIE, F. & JIANG, K. 2016. Thermodynamic analysis of possible chalcopyrite dissolution mechanism in sulfuric acidic aqueous solution. Metals, 6, 303.

MARIE-CAROLINE PINGET, L. F. 2011. The Supergene Enrichment at Chuquicamata revisited. Proceedings 11th SGA Biennal Meeting, Antofagasta, 823-825.

MCINTYRE, N. & ZETARUK, D. 1977. X-ray photoelectron spectroscopic studies of iron oxides. Analytical Chemistry, 49, 1521-1529.

NESBITT, H. & MUIR, I. 1998. Oxidation states and speciation of secondary products on pyrite and arsenopyrite reacted with mine waste waters and air. Mineralogy Petrology, 62, 123-144.

NICOL, M., MIKI, H. & VELÁSQUEZ-YÉVENES, L. 2010. The dissolution of chalcopyrite in chloride solutions: Part 3. Mechanisms. Hydrometallurgy, 103, 86-95.

PEARCE, C., PATTRICK, R., VAUGHAN, D., HENDERSON, C. & VAN DER LAAN 2006. Copper oxidation state in chalcopyrite: Mixed Cu d9 and d10 characteristics. Geochimica et Cosmochimica Acta, 70, 4635-4642.

POLLOK, K., PUTNIS, C. V. & PUTNIS, A. 2011. Mineral replacement reactions in solid solution-aqueous solution systems: Volume changes, reactions paths and end-points using the example of model salt systems. American Journal of Science, 311, 211-236.

PUTNIS, A. 1992. An introduction to mineral sciences, Cambridge University Press.

PUTNIS, A. 2002. Mineral replacement reactions: from macroscopic observations to microscopic mechanisms. Mineralogical Magazine, 66, 689-708.

PUTNIS, A. 2009. Mineral replacement reactions. Reviews in mineralogy geochemistry, 70, 87-124.

QIAN, G., BRUGGER, J., SKINNER, W. M., CHEN, G. & PRING, A. 2010. An experimental study of the mechanism of the replacement of magnetite by pyrite up to 300 C. Geochimica et Cosmochimica Acta, 74, 5610-5630.

QIAN, G., XIA, F., BRUGGER, J., SKINNER, W. M., BEI, J., CHEN, G. & PRING, A. 2011. Replacement of pyrrhotite by pyrite and marcasite under hydrothermal conditions up to 220 C: An experimental study of reaction textures and mechanisms. American Mineralogist, 96, 1878-1893.

QIAN, G., LI, Y., LI, J. & GERSON, A. R. 2017. Consideration of enthalpic and entropic energy contributions to the relative rates of chalcopyrite dissolution in the presence of aqueous cationic impurities. International Journal of Mineral Processing, 159, 42-50.

RANDALL, M. & BICHOWSKY, F. R. V. 1918. EQUILIBRIUM IN THE REACTION BETWEEN WATER AND SULFUR AT HIGH TEMPERATURES. THE DISSOCIATION OF HYDROGEN SULFIDE. Journal of the American Chemical Society, 40, 368-375.

RICKARD, D. 1972. Covellite formation in low temperature aqueous solutions. Mineralium Deposita, 7, 180-188.

RUBIE, D. C. 1986. The catalysis of mineral reactions by water and restrictions on the presence of aqueous fluid during metamorphism. Mineralogical Magazine, 50, 399-415.

SCHAUFUß, A. G., NESBITT, H. W., KARTIO, I., LAAJALEHTO, K., BANCROFT, G. M. & SZARGAN, R. 1998. Reactivity of surface chemical states on fractured pyrite. Surface Science, 411, 321-328.

SHIRLEY, D. A. 1972. High-resolution X-ray photoemission spectrum of the valence bands of gold. Physical Review B, 5, 4709.

SMART, R. S. C. 1991. Surface layers in base metal sulphide flotation. Minerals Engineering, 4, 891-909.

VIRAMONTES-GAMBOA, G., RIVERA-VASQUEZ, B. F. & DIXON, D. G. 2007. The active-passive behavior of chalcopyrite: Comparative study between electrochemical and leaching responses. Journal of the Electrochemical Society, 154, C299.

WANG, H., PRING, A., NGOTHAI, Y. & O'NEILL, B. 2005. A low-temperature kinetic study of the exsolution of pentlandite from the monosulfide solid solution using a refined Avrami method. Geochimica et Cosmochimica Acta, 69, 415-425.

WATLING, H. 2013. Chalcopyrite hydrometallurgy at atmospheric pressure: 1. Review of acidic sulfate, sulfate–chloride and sulfate–nitrate process options. Hydrometallurgy, 140, 163-180.

XIA, F., BRUGGER, J., CHEN, G., NGOTHAI, Y., O'NEILL, B., PUTNIS, A. & PRING, A. 2009. Mechanism and kinetics of pseudomorphic mineral replacement reactions: A case study of the replacement of pentlandite by violarite. Geochimica et Cosmochimica Acta, 73, 1945-1969.

YANG, Y., HARMER, S. & CHEN, M. 2015. Synchrotron-based XPS and NEXAFS study of surface chemical species during electrochemical oxidation of chalcopyrite. Hydrometallurgy, 156, 89-98.

YUND, R. A. & HALL, H. T. 1970. Kinetics and mechanism of pyrite exsolution from pyrrhotite. Journal of Petrology 11, 381-404.

ZHAO, J., BRUGGER, J., XIA, F., NGOTHAI, Y., CHEN, G. & PRING, A. 2013. Dissolution-reprecipitation vs. solid-state diffusion: Mechanism of mineral transformations in sylvanite, (AuAg) 2Te4, under hydrothermal conditions. American Mineralogist, 98, 19-32.

ZHAO, J., BRUGGER, J., CHEN, G., NGOTHAI, Y. & PRING, A. 2014a. Experimental study of the formation of chalcopyrite and bornite via the sulfidation of hematite: Mineral replacements with a large volume increase. American Mineralogist, 99, 343-354.

ZHAO, J., BRUGGER, J., NGOTHAI, Y. & PRING, A. 2014b. The replacement of chalcopyrite by bornite under hydrothermal conditions. American Mineralogist, 99, 2389-2397.

ZHAO, J., BRUGGER, J. & PRING, A. 2019. Mechanism and kinetics of hydrothermal replacement of magnetite by hematite. Geoscience Frontiers, 10, 29-41.

CHAPTER 4: THE REPLACEMENT OF CHALCOPYRITE BY DIGENITE UNDER HYDROTHERMAL CONDITIONS

4.1 Introduction

Chalcopyrite ($CuFeS_2$) often undergoes hydrothermal replacement reactions in both hypogene and supergene zone, resulting in the formation of copper sulphides such as covellite (CuS), chalcocite (Cu_2S) and digenite ($Cu_{1.8}S$) (Zhao et al., 2014a, Rakovan, 2003, Reich and Vasconcelos, 2015). These copper-containing sulphides are all valuable minerals due to the high copper content. Hence, the scientific and mining industry sectors may gain benefits from understanding the kinetics and mechanisms of these mineral replacement reactions.

The replacement reactions of chalcopyrite by other copper sulphides have been widely studied (Jang, 1992, Zhao et al., 2014b, Chaudhari et al., 2021, Adegoke et al., 2022). Jang (1992) reported that chalcopyrite converted to digenite and covellite under hydrothermal condition in a 0.5 M H_2SO_4 in the temperature range of 170-200 °C. Chalcopyrite is converted to covellite and then forms defected chalcocite (digenite). Digenite is found in the replacement of chalcopyrite by bornite at pH 3-7 and 200-260 °C (Zhao et al., 2014b). Chaudhari et al. (2021) have recently studied the replacement reaction of chalcopyrite by digenite and covellite at 200-260 °C in H_2SO_4 solution media using *in-situ* synchrotron powder X-ray diffraction (PXRD) analysis. They reported digenite is only formed at or above 200 °C with addition of $CuCl_2$.

Chapter 3 shows that in the replacement of chalcopyrite by covellite, no digenite was formed at 140-200 °C without added Cu. Therefore, $CuCl_2$ was added in part of this study (Chapter 4) in order to achieve the Cu enrichment of chalcopyrite by the formation of digenite. The mechanisms and kinetics were investigated as a function of temperature (140-200 °C), particle sizes, the amount of added $CuCl_2$ and solution pH. In the phase diagram of Cu-S system, digenite-low is formed at or below 76 °C and digenite-high is formed at or above 90 °C (Morimoto and Kullerud, 1963, Will et al., 2002). Digenite-high is the only digenite phase formed in this study.

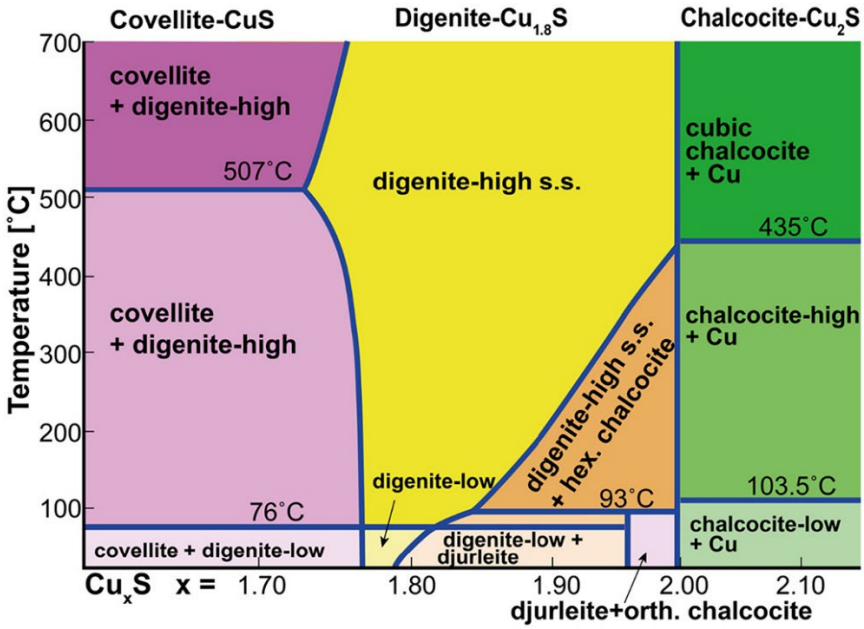

Figure 48 Phase diagram illustrated the copper sulphides stability at different temperature in the Cu-S system. Sourced from Roseboom (1966).

4.2 Methodology

4.2.1 Hydrothermal Reaction Experiments

All experiments were conducted using PTFE-lined (25 mL) stainless-steel autoclaves (Section 2.3). Natural chalcopyrite sample was sourced from multiple mining sites of China and the elemental composition was determined by ICP-OES which is described in detail in Section 2.1. All four particle sizes (38-75 µm, 75-150 µm, 150-425 µm and 425-1020 µm) of chalcopyrite were used in these experiments to investigate the effect of specific surface are on the replacement reaction rate of chalcopyrite by copper sulphides. All sizes of chalcopyrite grains were surface rinsed and cleaned as described in Section 2.1 to ensure no fine particles or oxidative layers on the chalcopyrite surface. The buffer solutions (pH 1, 1.5, 2, 2.5 and 3) used in this chapter were prepared as per Section 2.2. 0.1, 0.2 and 0.3 M sulfuric acid solutions were also used to investigate the effect of the concentration of acid on the replacement reaction mechanism. Experiments were carried out in the presence of 2 M $CuCl_2$ solution, except for experiments with sulphuric acid were 1 M $CuSO_4$ was used (as 2 M $CuSO_4$ were not completely dissolved in room temperature). Kinetic studies were carried out at four different temperatures (140 °C, 160 °C, 180 °C and 200 °C) with three different buffer solutions (pH 2, pH 2.5 and pH 3). All experimental conditions conducted in this Chapter were summarised in Table 21.

Table 20 The composition of buffer solutions used in the replacement reaction of chalcopyrite by digenite.

$pH_{25°C}$		Composition
Calculated	**Measured**	
1	1.12	0.111 M HCl + 0.05 M KCl
1.5	1.51	0.056 M HCl + 0.05 M KCl
2	2.11	0.011 M HCl + 0.05 M KCl
2.5	2.52	0.006 M HCl + 0.05 M KCl
3	3.09	0.098 M CH_3COOH + 0.018 M CH_3COONa

The replacement reaction of 75-150 µm chalcopyrite is very sluggish at or above pH 2, similar to the replacement of chalcopyrite by covellite as shown in Chapter 3. Chalcopyrite particles in the size fraction 38-75 µm were mainly used in the kinetic study of the replacement reaction experiments in this chapter. The solid-weight to liquid-volume (S/F) ratio of all experiments was kept at 2 g/L by mixing 40 mg (0.22 mmol) chalcopyrite with 20 mL of buffer solution at room temperature. 0.44 mmol of H_2O_2 were added as an oxidant to understand the effect of oxygen on the mechanism and reaction rate. Buffer solutions were collected after quenching in cold water prior to pH measurement. Solid residues were collected for XRD analysis to quantitatively determine the mineral compositions using TOPAS. Chalcopyrite CIF file used to for quantitative X-ray diffraction (QXRD) analysis was sourced from Knight et al. (2011). Covellite CIF file was sourced from Berry (1954) and digenite file was sourced from Will et al. (2002). Cross-sectional EDAX and SE/BSE imaging analyses were conducted using 425-1020 µm reacted chalcopyrite grains embedded in epoxy resins. All SEM samples were carbon coated (5-10 nm thick) prior to SEM analysis.

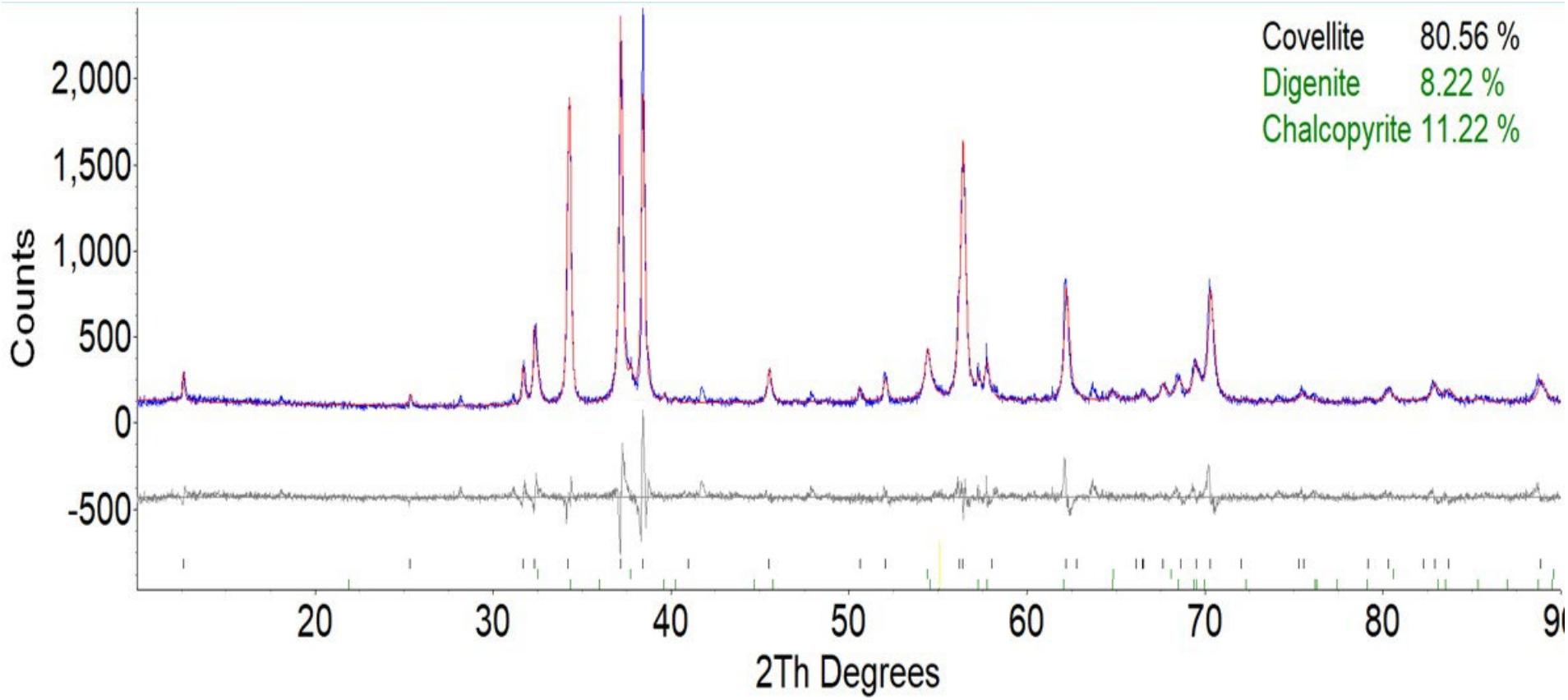

Figure 49 XRD patterns of experiment at pH 2 and 180 °C, quantitatively analysed by using TOPAS program. Original XRD data were shown with blue colour and refined with red colour.

Table 21 Summary of experimental conditions for experiments replacing chalcopyrite by covellite or digenite with addition of $CuCl_2$ under hydrothermal conditions.

Experimental number	T(°C)	Measured pH	Time (h)	$CuCl_2$ (mmol)	H_2O_2 (mmol)	Particle size (µm)	Product
T1-T3	180	1	48-144	0.22	0.44	75-150	Cpy and Cv
T4-T6	180	1	48-144	0.44	0.44	75-150	Cpy and Cv
T7-T9	180	1	264-1536	0.22	0	75-150	Cpy and Cv
T10-T12	180	1	264-1536	0.44	0	75-150	Cpy and Cv
T13-15	180	0.5	264-1536	0.22	0	75-150	Cpy and Cv
T16-T18	180	0.5	264-1536	0.44	0	75-150	Cpy and Cv
T21-T23	200	1	24-96	0.22	0.44	75-150	Cpy and Cv
T24-T26	200	1	24-96	0.44	0.44	75-150	Cpy and Cv
D1	180	1	24	0.11	0.44	75-150	Cpy and Cv
D2	180	1	24	0.22	0.44	75-150	Cpy and Cv
D3	180	1	24	0.44	0.44	75-150	Cpy and Cv, Dg
D4	180	1	24	0.88	0.44	75-150	Cpy, Cv, Dg and $CuCl_2$
D5	180	1	24	0	0.44	75-150	Cpy and Cv
D6	180	1	24	0.22	0	75-150	Cpy and Cv
D7	180	1	24	0.22	0.22	75-150	Cpy and Cv
D8	180	1	24	0.22	0.88	75-150	Cpy and Cv
D9	180	2	624	0.22	0.44	75-150	Cpy and Cv, Dg
D9A	180	2	1608	0.22	0.44	75-150	Cpy and Cv
D10	180	3	624	0.22	0.44	75-150	Cpy and Cv
D10A	180	3	1608	0.22	0.44	75-150	Cpy and Cv
D11	180	1	24	0.22	0.44	425-1020	Cpy and Cv
D12	180	1	24	0.22	0.44	150-425	Cpy and Cv
D13	180	1	24	0.22	0.44	38-75	Cpy and Cv
D15	180	1	216	0.22	0.44	425-1020	Cpy and Cv
D19	180	2	70	0.22	0	38-75	Cpy and Cv, Dg
D20	180	2	70	0.44	0	38-75	Cpy and Cv, Dg
D21	180	2	70	0.66	0	38-75	Cpy and Cv, Dg
D22	180	2	70	0.88	0	38-75	Cpy and Cv, Dg
D23	180	2	70	0.22	0.44	38-75	Cpy and Cv, Dg
D24	180	2	70	0.44	0.44	38-75	Cpy and Cv, Dg
D25	180	2	70	0.66	0.44	38-75	Cpy and Cv, Dg, $CuCl_2$
D26	180	2	70	0.88	0.44	38-75	Cpy and Cv, Dg, $CuCl_2$
D27	180	2	70	0.22	0.44	425-1020	Cpy and Cv, Dg
D28	180	2	70	0.22	0.44	150-425	Cpy and Cv, Dg
D29	180	2	70	0.22	0.44	38-75	Cpy and Cv, Dg
D30	180	2	360	0.22	0.44	425-1020	Cpy and Cv, Dg
D31	200	2	120	0.22	0.44	425-1020	Cpy and Cv, Dg
H1-H12	180	2	5-48	0.22	0.22	38-75	Cpy and Cv, Dg
H21-H25	180	3	48-1056	0.22	0.22	38-75	Cpy and Cv, Dg
H101-110	180	2.5	4-97	0.22	0.22	38-75	Cpy and Cv, Dg
H81-H93	140	2	4-119	0.22	0.22	38-75	Cpy and Cv, Dg
H41-H49	140	2.5	4-82	0.22	0.22	38-75	Cpy and Cv, Dg

H61-H74	140	3	192-1368	0.22	0.22	38-75	Cpy and Cv, Dg
I1-I10	160	2	5-72	0.22	0.22	38-75	Cpy and Cv, Dg
I21-I30	160	2.5	5-72	0.22	0.22	38-75	Cpy and Cv, Dg
I41-I50	160	3	24-264	0.22	0.22	38-75	Cpy and Cv, Dg
I61-I70	200	3	24-384	0.22	0.22	38-75	Cpy and Cv, Dg
I81-I90	200	2.5	2-22	0.22	0.22	38-75	Cpy and Cv, Dg
I101-I110	200	2	2-22	0.22	0.22	38-75	Cpy and Cv, Dg

4.2.2 Kinetic Study

The empirical *Avrami* equation was used as a kinetic model to fit the replacement reaction rate of chalcopyrite by digenite or covellite. This method has been widely used to model the kinetics of mineral replacement reactions (Putnis, 1992, Xia et al., 2009, Zhao et al., 2014b, Zhao et al., 2014a, Zhao et al., 2019). In equation (58), *k* is the rate constant, *t* is the reaction time, *y* is the phase fraction of chalcopyrite after the replacement reaction and *n* is the constant dependent on reaction mechanism. A linear equation can be obtained by rearranging equation (58), which is also known as Hancock-Sharp plot (Hancock and Sharp, 1972, Lasaga, 1998). A straight line of $\ln\left[\ln\left(\frac{1}{1-y}\right)\right]$ versus $\ln t$ plots can be resulted, with a slope of *n* and intercept of *nlnk*, if reaction mechanism does not change during the reaction.

$$y = 1 - exp(-k \times (t^n)) \tag{58}$$

$$\ln\left[\ln\left(\frac{1}{1-y}\right)\right] = n\ln k + n\ln t \tag{59}$$

If the mineral replacement reaction rate is dependent on temperature, it can be applied to the *Arrhenius* equation:

$$k = Aexp\left(\frac{-E_a}{RT}\right) \tag{60}$$

where *A* is a pre-exponential factor (s^{-1}), *T* is the absolute temperature in Kelvin, *R* is the ideal gas constant with value of 8.314 $Jmol^{-1}K^{-1}$, and E_a ($kJmol^{-1}$) is the activation energy of the reaction. Rearrange equation (60) to gives a formula:

$$\ln k = \ln A - \frac{E_a}{RT} \tag{61}$$

The activation energy of the mineral replacement reaction can be obtained by plotting *lnk* versus 1/*T*. The slope of the linear best-fit line ($\frac{-E_a}{R}$) can be used to calculated E_a. The *Avrami-Arrehenius* method is not possible to ascertain whether the activation energy and the *Avrami* rate constant change during the mineral replacement reaction (Putnis, 1992).

However, the activation energy may vary during the reaction if the reaction mechanism changes. It commonly happens in complex solid-fluid reactions, as encountered in this study (Qian et al., 2017, Nikkhou et al., 2019). The 'time to a given fraction' method is able to determine whether E_a changes during the reaction, and it is independent of rate constants calculated by kinetic models. This method was firstly proposed by Putnis (1992) and gives equation (62), and was recently modified by Qian et al. (2017) (Equation 63).

$$\ln t_Y = const - lnA + \frac{E_a}{RT} \quad (62)$$

$$\ln (t_{Y_q} - t_{Y_p}) = const - lnk_0 + \frac{E_a(Y_q)}{RT} \quad (63)$$

t_{Y_q} and t_{Y_p} are the time required to reaches reaction extent Y_q and Y_p respectively. The best-fit of the plots of $\ln (t_{Y_q} - t_{Y_p})$ against 1/*T* is linear if E_a is independent of reaction temperature. The slope of the linear best-fit line of was used to calculate the average activation energy between Y_q and Y_p.

Both the *Avrami-Arrhenius* and modified 'time to a given fraction' methods were used to in this study to determine the variations of activation energy of the replacement reaction at different reaction extent. The errors of uncertainties of the Rietveld refinement of reaction extent at 95% confidence level was estimated to be $X^{0.35}$ where X is the weight percentage of each mineral phase (Qian et al., 2017, Geelhoed et al., 2002).

4.3 Results

4.3.1 Surface Morphology and Texture

Chalcopyrite grains were cleaned and sonicated to remove the oxidized surface layers and fine particles left from crushing as described in section 2.1 described, resulting in a clean and smooth surface (Figure 50A). Euhedral and plate-like covellite crystals were developed on the surface of chalcopyrite after 216 h of reactions under conditions of 180 °C, pH 1 and 0.22 mmol $CuCl_2$ with 0.44 mmol H_2O_2 added, forming a bird nest-like structure (Figure 50B-50D). No digenite was observed at pH 1 and 180 °C. At pH 2 and 180 °C, digenite were found on the surface of chalcopyrite with a porous and worm-like structure (Figure 50E and 50F).

The atomic percentage of all mineral phases measured using EDAX (Figure 51B) are included in Table 22. The S and Cu ratio represented by blue pixels is close to 1:1, indicate that a covellite outer rim formed. Each orange pixel in the middle layer consists of 59.5% Cu and 38% S (Cu/S = 1.56:1), suggesting the formation of digenite layer. Yellow pixels in the core phase of reacted mineral grain has a S: Fe: Cu ratio of 2:1:1, consistent with the presence of unreacted chalcopyrite.

Three layers were observed in the backscattered images of the cross-section of the sample reacted at pH 2 and 180 °C with $CuCl_2$ and H_2O_2 for 216 h. The outmost layer, represented by blue pixels in the EDAX map, is covellite. A gap was found in the middle of covellite layer. Digenite formed in the middle of grains and no gaps were observed at the adjacent sites between digenite and covellite. The middle digenite layer was found to be brighter than the outermost rim and core under the backscattered electron mode. The core of the mineral grain was unreacted chalcopyrite that was coated by digenite with no gaps observed between the two minerals (Figure 51A and 51B). SEM images showed numerous pores and cracks were presented in all three mineral phases. The digenite layer has fewer purple pixels in the EDAX S spectra than the other two mineral phases (Figure 51C). Covellite and digenite did not show the presence of Fe in the corresponding EDAX map (Figure 51D). In the EDAX Cu elemental map, the chalcopyrite core is the darkest while the digenite middle layer is the brightest (Figure 51E).

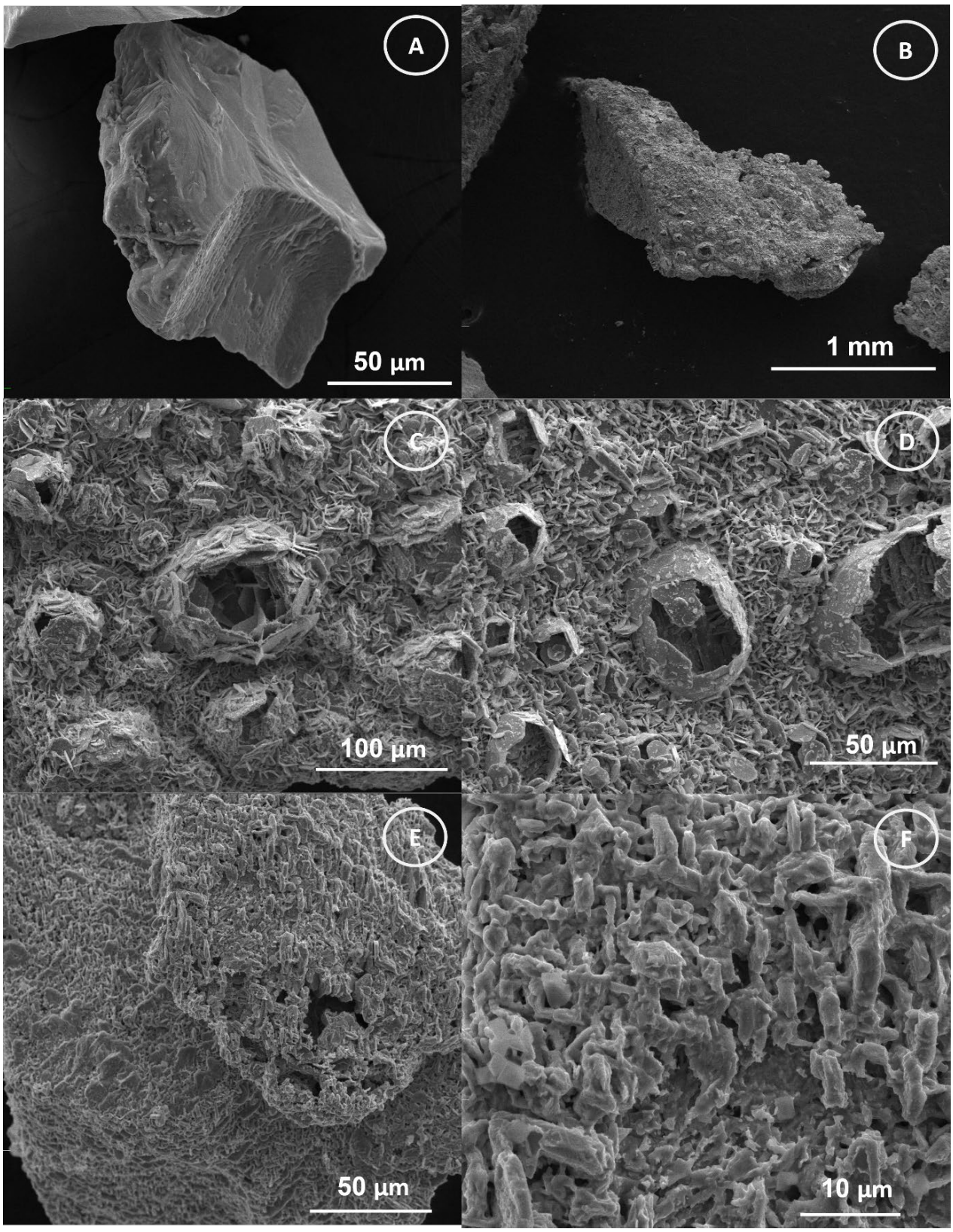

Figure 50 Secondary electron images of surface morphology collected by A) unreacted chalcopyrite; B) 425-1020 µm chalcopyrite grains reacted at 180 °C and pH 1 with 0.44 mmol H_2O_2 and 0.22 mmol $CuCl_2$ after 216 h; C) and D) zoomed-in image of B; E) 425-1020 µm chalcopyrite grains reacted at 180 °C and pH 2 with 0.44 mmol H_2O_2 and 0.22 mmol $CuCl_2$ after 216 h; F) zoomed-in image of E.

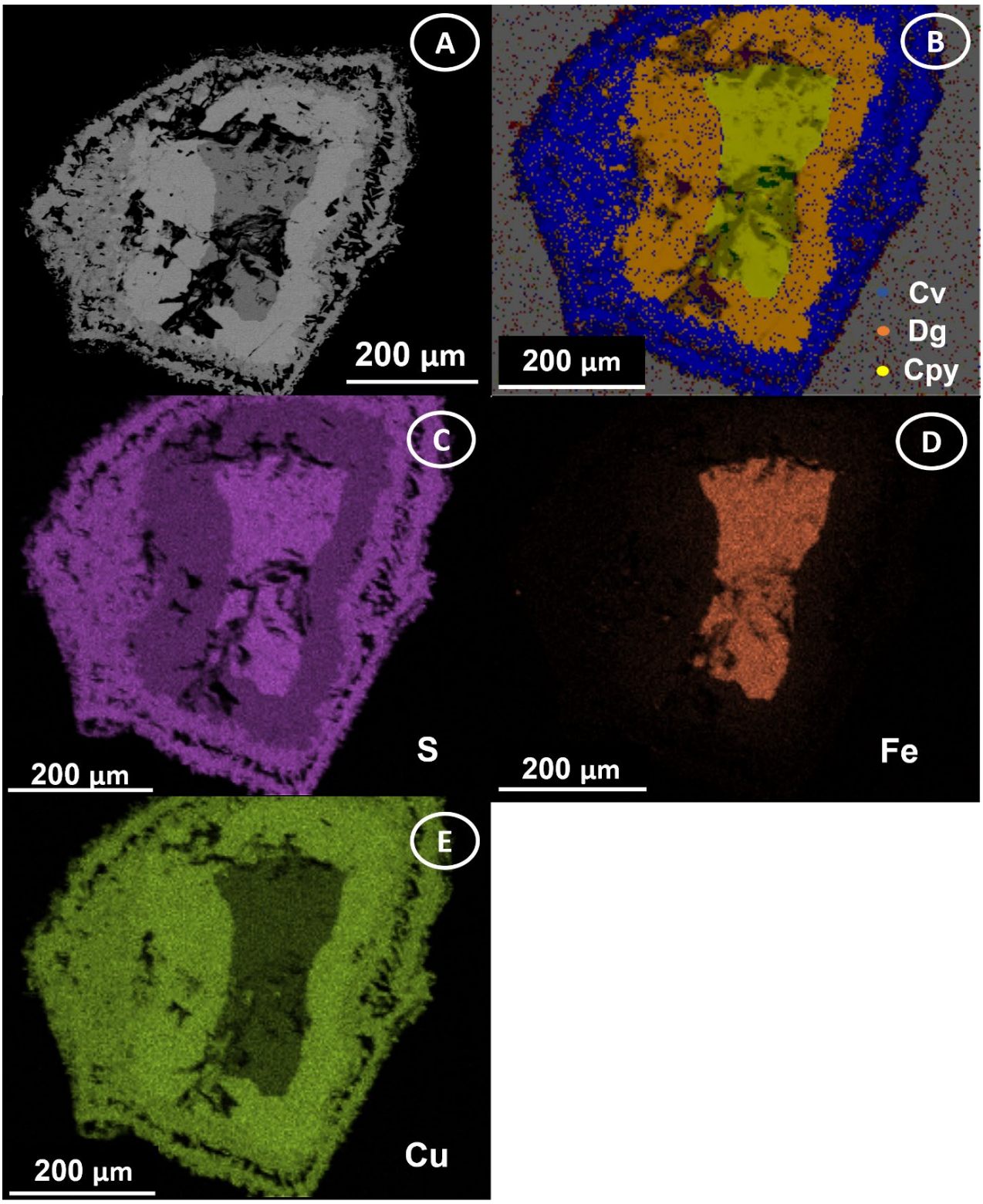

Figure 51 A) Backscattered image of cross section of 425-1020 µm chalcopyrite reacted at pH 2 and 200 °C with 0.22 mmol $CuCl_2$ and 0.44 mmol H_2O_2 after 120 h. B) Energy dispersive X-ray analysis spectra of A consists of covellite (blue pixels), digenite (orange pixels) and chalcopyrite (yellow pixels). C) EDAX sulphur spectra of A. D) EDAX Fe spectra of A. E) EDAX Cu spectra of A.

Table 22 At% of elements for each sulphide mineral resulting from EDAX analysis.

At. (%)	S	Fe	Cu
Covellite	50.5	0.5	49
Digenite	38	2.5	59.5
Chalcopyrite	48.5	25.5	26

At pH 3 and 200 °C, two mineral layers were observed in the backscattered image (Figure 52A). Copper sulphide (covellite) formed on the chalcopyrite surface as an outer rim, with no obvious gap observed (Figure 52A and 52B). Each mineral layer can be identified by examining elemental compositions. EDAX showed the presence of covellite (green pixels), residual chalcopyrite (yellow pixels) and hematite (blue pixels). Green pixel layer consists of 42% S and 54% Cu (Table 23) with no Fe (Figure 52F), suggesting that this is a covellite layer. Yellow pixel layer consists of 48% S, 25.5% Fe and 24% Cu (Table 23), corresponding to the unreacted chalcopyrite. A very thin iron oxide layer was observed as blue pixels in Figure 52B with 50% Fe and 36.5% O.

Table 23 Atomic percentage of each mineral in EDAX spectra.

At. (%)	S	Fe	Cu	O
Covellite	42	2	54	2
Hematite	4.5	50	9	36.5
Chalcopyrite	48	25.5	24	2.5

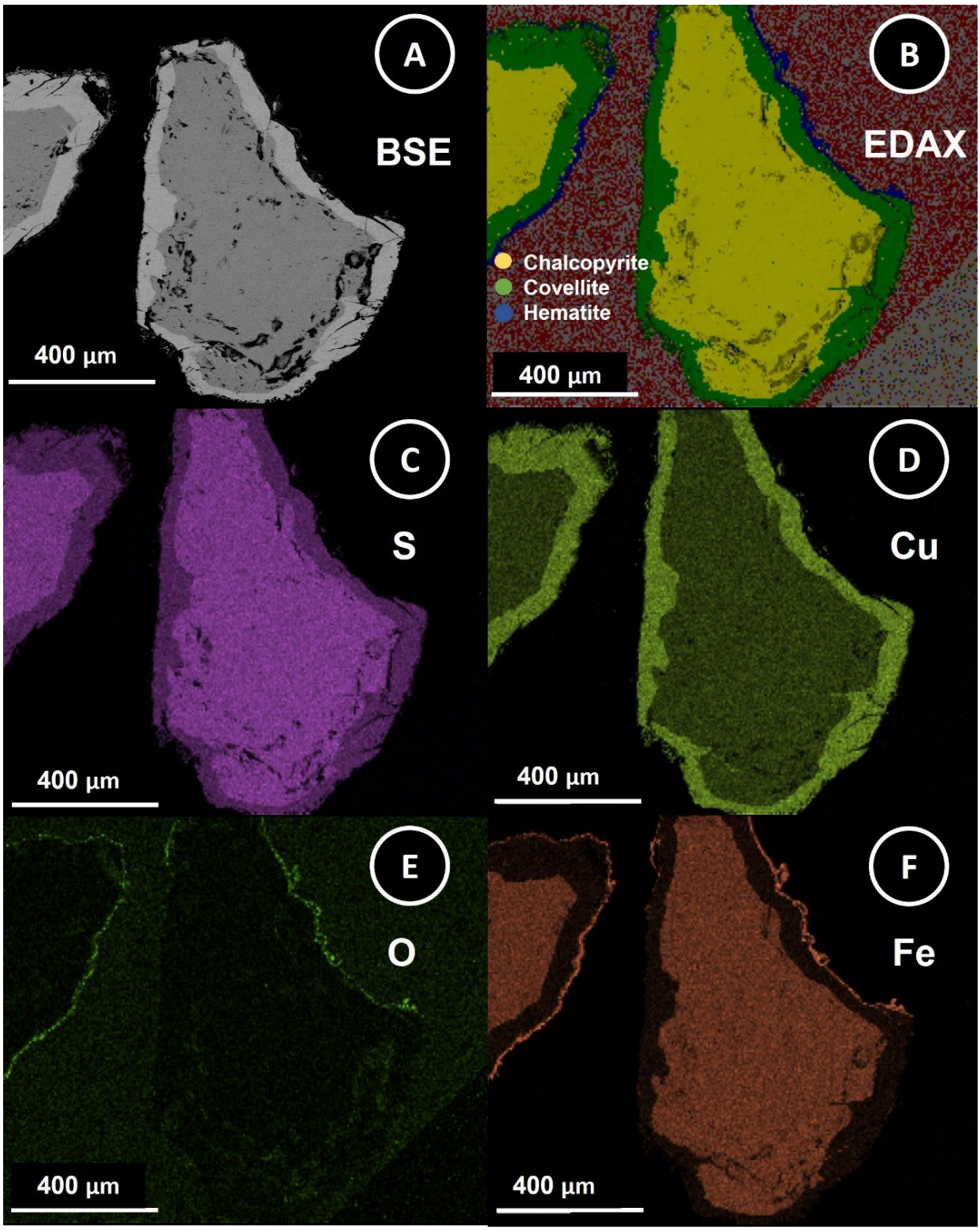

Figure 52 A) Backscattered image of C-section made by 425-1020 µm chalcopyrite reacted at pH 3 and 200 °C with 0.22 mmol $CuCl_2$ and 0.44 mmol H_2O_2 after 216 h. B) Energy dispersive X-ray analysis spectra of A consists of covellite (green pixels), hematite (blue pixels) and chalcopyrite (yellow pixels). C) EDAX sulphur spectra of A. D) EDAX Cu spectra of A. E) EDAX O spectra of A. F) EDAX Fe spectra of A.

4.3.2 Hydrothermal Mineral Replacement Reaction

Chalcopyrite was only replaced by covellite from pH 0.5-3 with no addition of Cu ions as described in Chapter 3. Therefore, the replacement reaction of chalcopyrite by digenite requires sufficient amounts of added Cu ions. pH 1, 2, 2.5 and 3 buffer solutions were selected to investigate how pH changes the mechanism and reaction rate of the replacement reaction of chalcopyrite by other copper sulphides. At pH 1, chalcopyrite was only replaced by covellite with addition of 0.11 mmol to 0.44 mmol of $CuCl_2$ (Figures 53 and 56). The reaction extent of chalcopyrite decreased with increasing amount of $CuCl_2$ addition after 24 h (Figure 56). When the addition of $CuCl_2$ increased to 0.88 mmol, 7±2% of digenite was found in the solid residues, along with the formation of $CuCl_2$ crystalline precipitates (eriochalcite; $CuCl_2 \cdot 2H_2O$) (Figure 54).

At pH 2, both covellite and digenite were formed after 70 h by the replacement reaction of chalcopyrite with addition of $CuCl_2$ (Figure 55). At 70 h, the reaction extent of covellite decreased from 68±4% to 45±4% when the amount of added $CuCl_2$ increased from 0.22 mmol to 0.88 mmol, while the weight percentage of digenite increased from 16±3% to 52±4% (Figure 57). When the amount of added $CuCl_2$ is at least 0.66 mmol, $CuCl_2$ crystals also precipitated in the solid residues.

The rate of the replacement reaction of chalcopyrite by covellite or digenite is slower when the solution pH increased. At pH 2, 9±2% of chalcopyrite was remained after reaction for 24 h in the presence of 0.22 mmol $CuCl_2$ and 0.44 mmol H_2O_2. The weight percentage of chalcopyrite increased to 22±3% at pH 2, and 81±5% at pH 3 under otherwise identical conditions. Covellite was found as the main product at pH 1-3 and the reaction extent is decrease with increasing pH of the solution. At pH 2-3, the wt% of digenite in the solid residues was all 6±2% approximately (Figure 57). A small amount of hematite (2-5 wt%) formed at pH 2-3, confirmed by PXRD analysis (Figure 55).

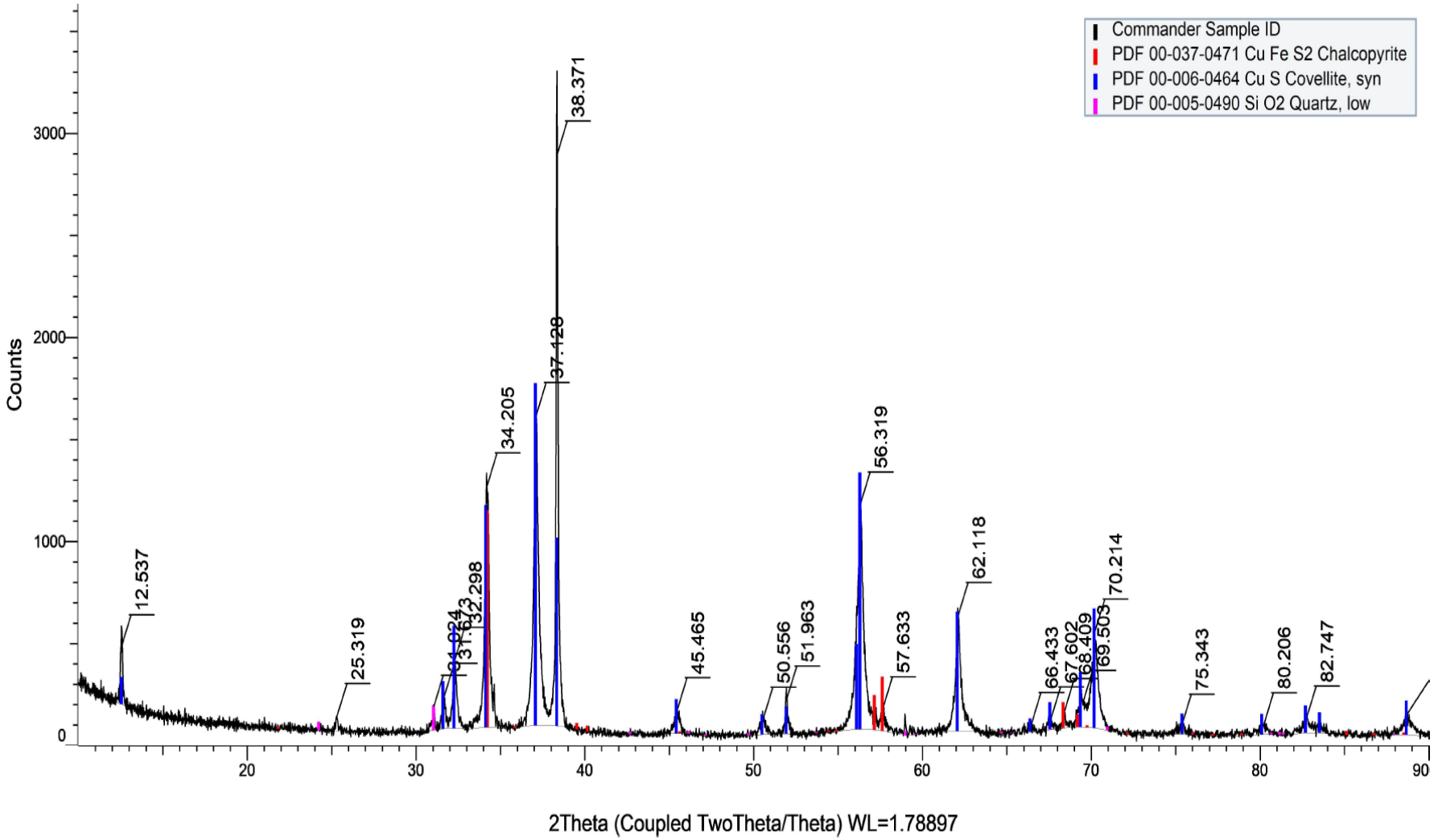

Figure 53 Powder X-ray diffraction data of the solid residue collected by the replacement reaction of chalcopyrite at pH 1 and 180 °C with 0.44 mmol $CuCl_2$ and 0.44 mmol H_2O_2 after 24 h.

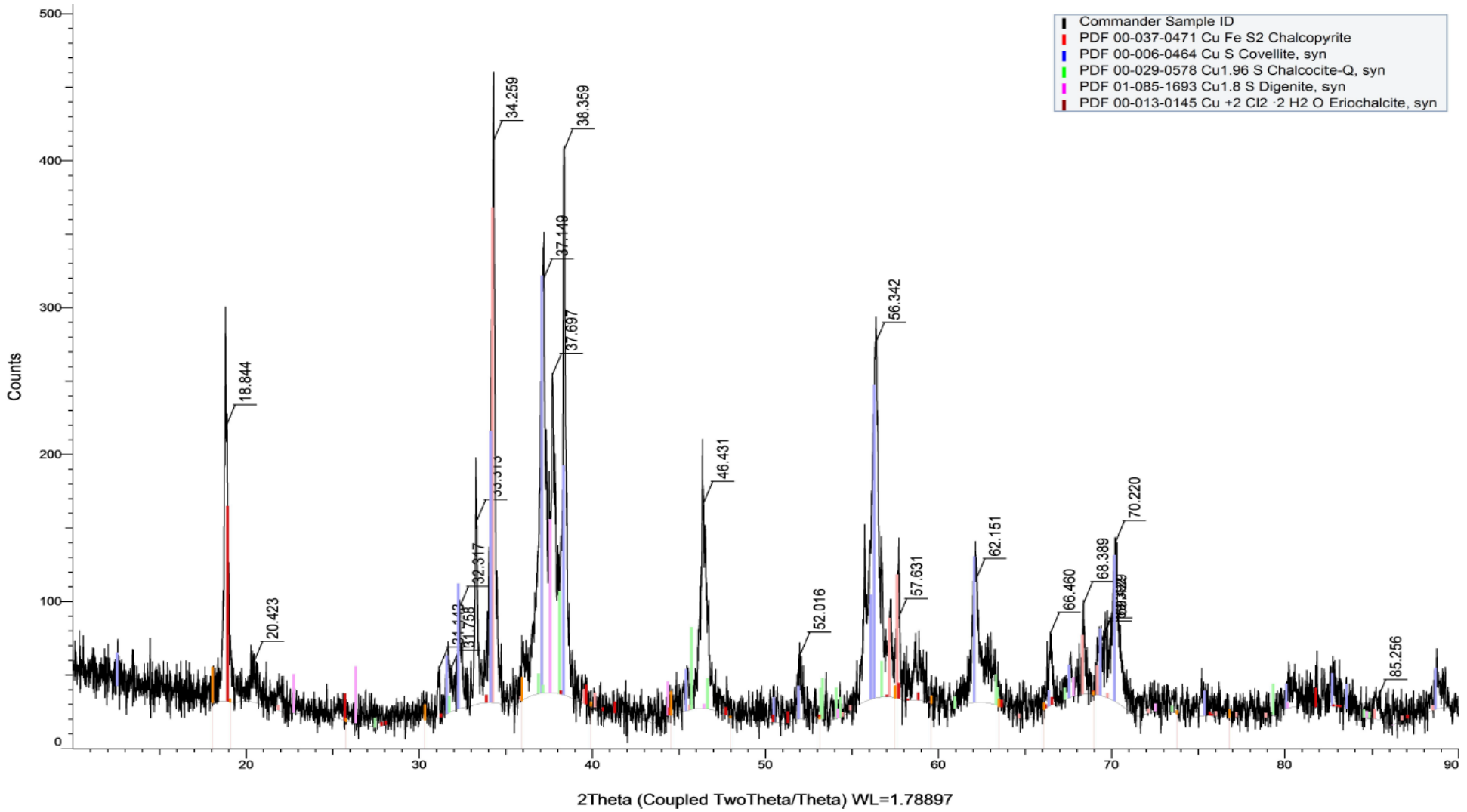

Figure 54 Powder X-ray diffraction data of the solid residue collected by the replacement reaction of chalcopyrite at pH 1 and 180 °C with 0.88 mmol $CuCl_2$ and 0.44 mmol H_2O_2 after 24 h.

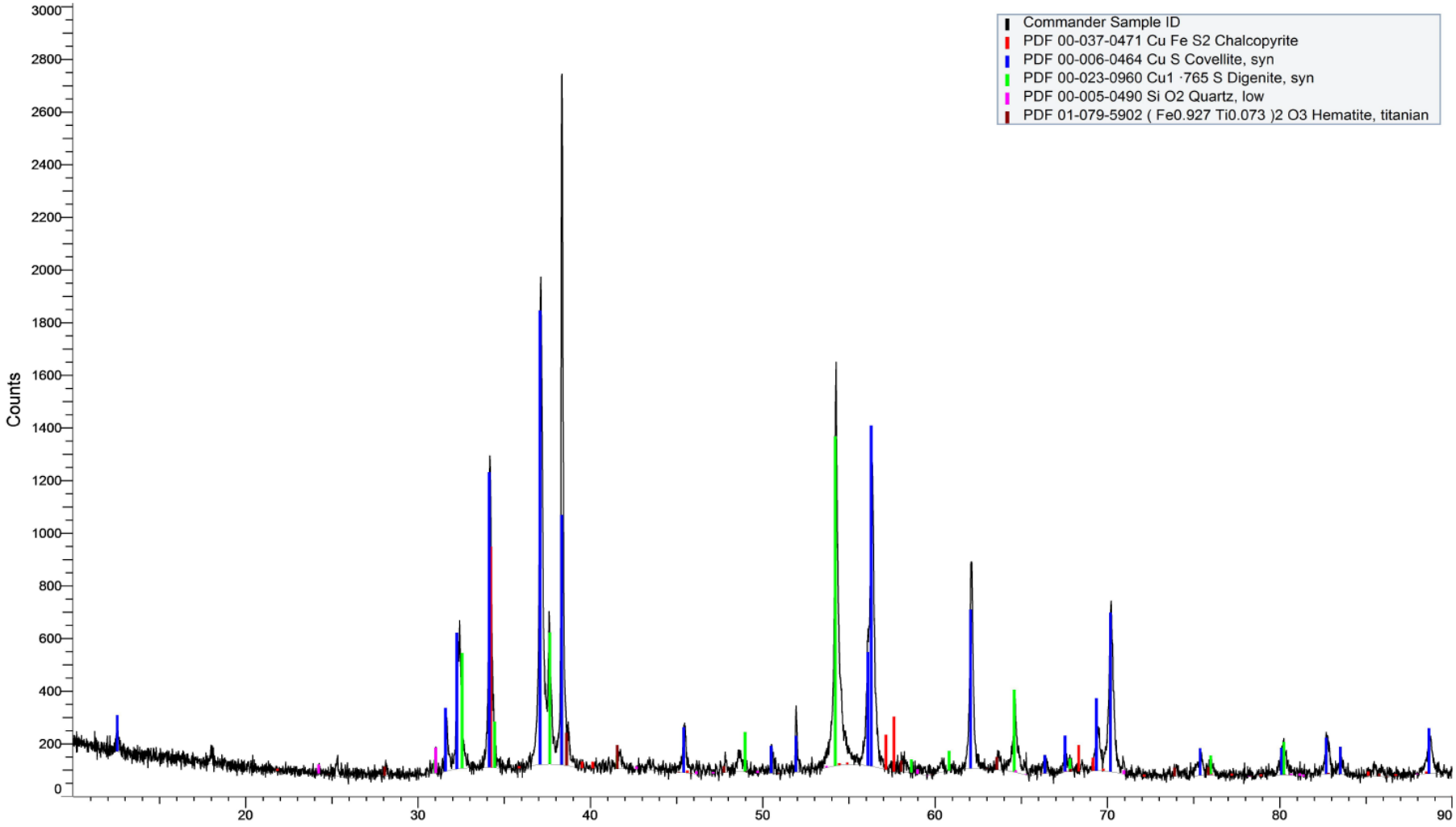

Figure 55 Powder X-ray diffraction data of the solid residue collected by the replacement reaction of chalcopyrite at pH 2 and 180 °C with 0.22 mmol $CuCl_2$ and 0.44 mmol H_2O_2 after 10 days.

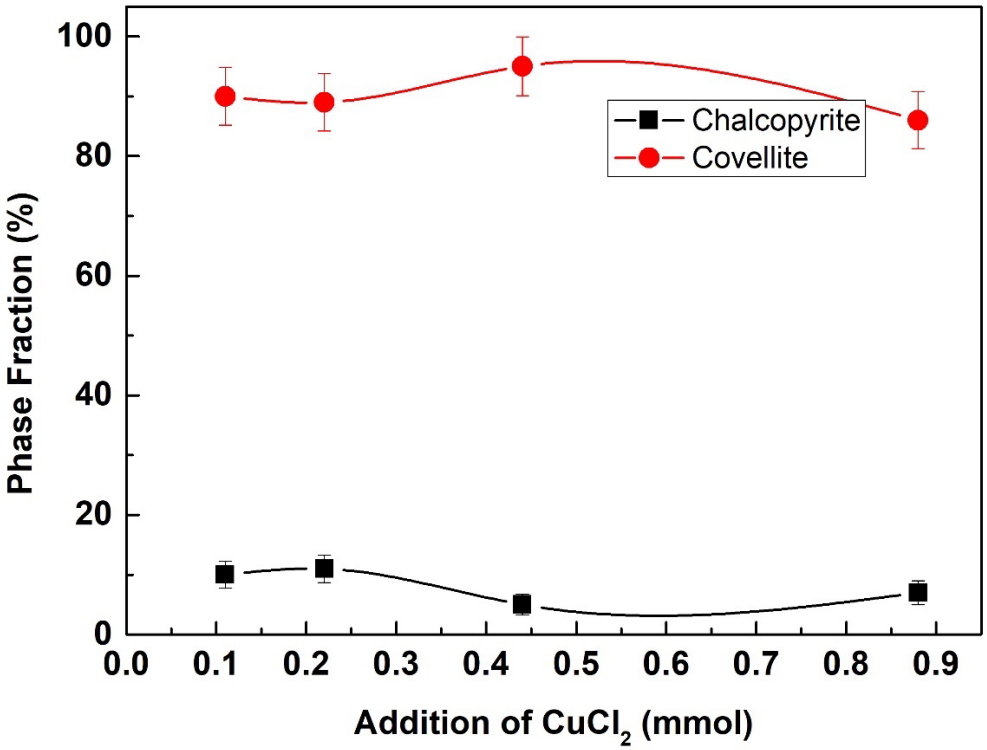

Figure 56 Reaction extent of chalcopyrite and covellite at pH 1 and 180 °C with 0.44 mmol H_2O_2 and different amount of $CuCl_2$ after 24 h.

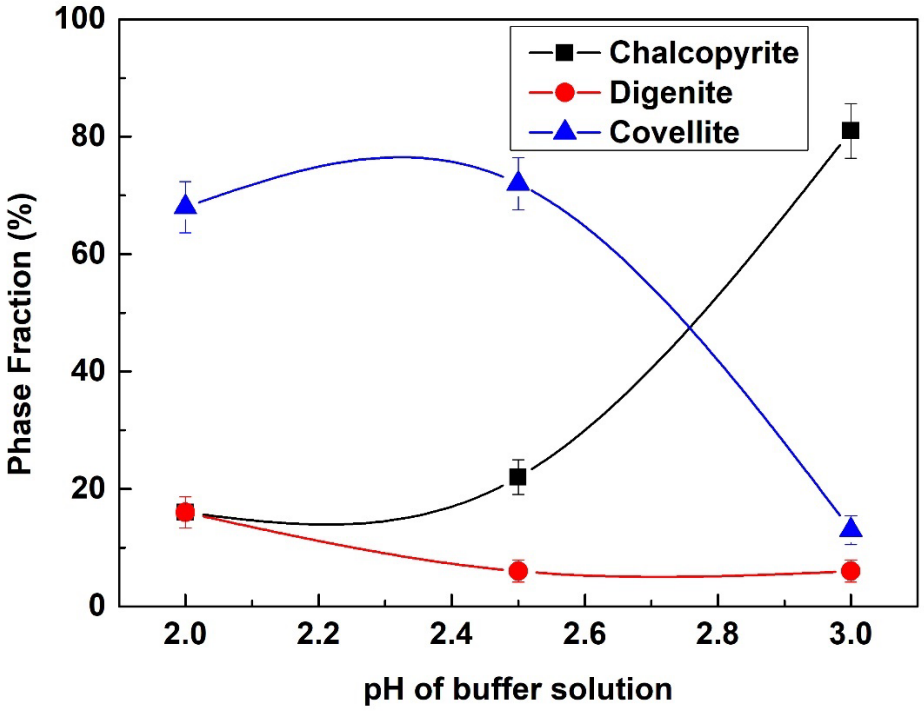

Figure 57 Reaction extent of each mineral phase in the solid residues collected by the replacement reaction experiment of chalcopyrite with 0.22 mmol $CuCl_2$ and 0.44 mmol H_2O_2 at different buffer solution after 24 h.

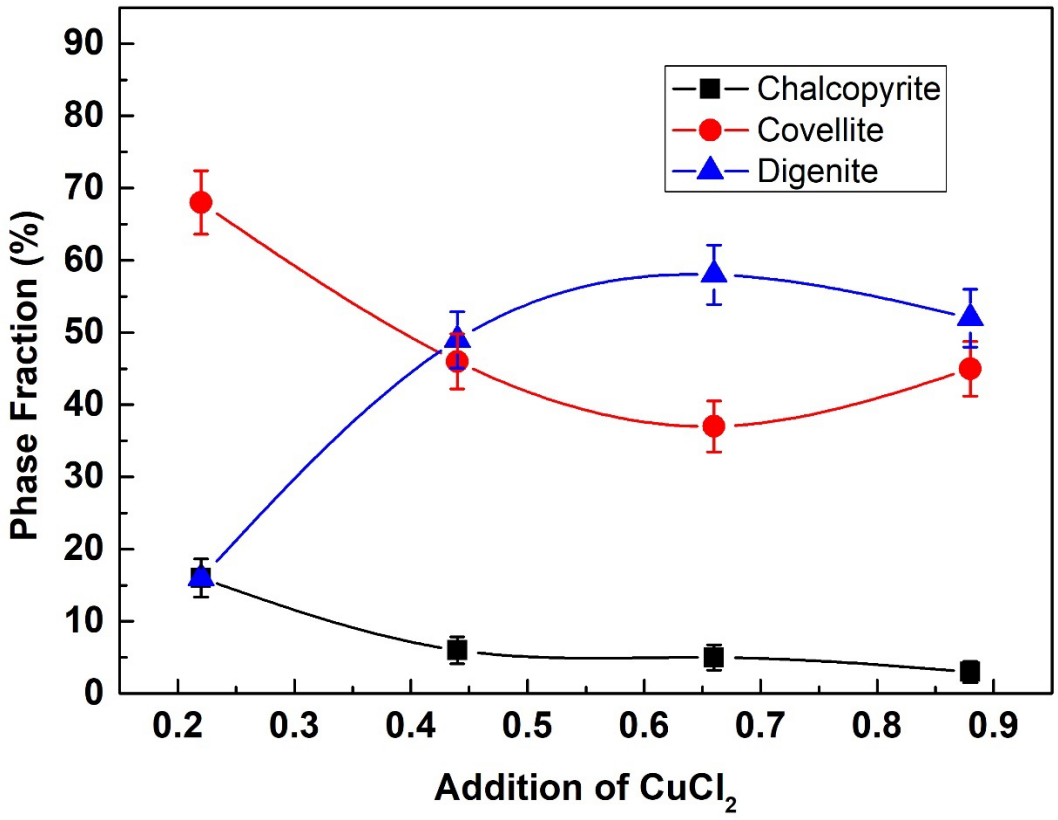

Figure 58 Reaction extent of chalcopyrite and covellite at pH 2 and 180 °C with 0.44 mmol H_2O_2 and different amount of $CuCl_2$ after 70 h.

Four particle sizes (38-75 µm, 75-150 µm, 150-425 µm and 425-1020 µm) were selected to investigate the effect of surface area of chalcopyrite grains on the replacement reaction rate. All starting chalcopyrite grains were assumed to be spherical, and the specific surface areas were then calculated using equation (64). A_{geo} is the total surface area of specific particle size fraction for a given sample mass; where ρ is the density of chalcopyrite d_e is the effective grain diameter of chalcopyrite particles in a given sieved size fraction (cm), d_{max} is the maximum particle size and d_{min} is the minimum particle size. The calculated specific surface areas are 21.1 cm^2/g for 425-1020 µm, 54.2 cm^2/g for 150-425 µm, 132.3 cm^2/g for 75-150 µm and 295.0 cm^2/g for 38-75 µm. The covellite fraction in the precipitates increased with increasing specific surface area of the starting chalcopyrite. 20±3% of solid residues collected from both sized fractions of 425-1020 µm and 150-425 µm was identified as digenite, 18±3% from 75-150 µm and 16±3% from 38-75 µm.

$$A_{geo} = \frac{6}{\rho_{chalcopyrite} \times d_e} \quad (64)$$

$$d_e = \frac{d_{max} - d_{min}}{\ln(\frac{d_{max}}{d_{min}})} \quad (65)$$

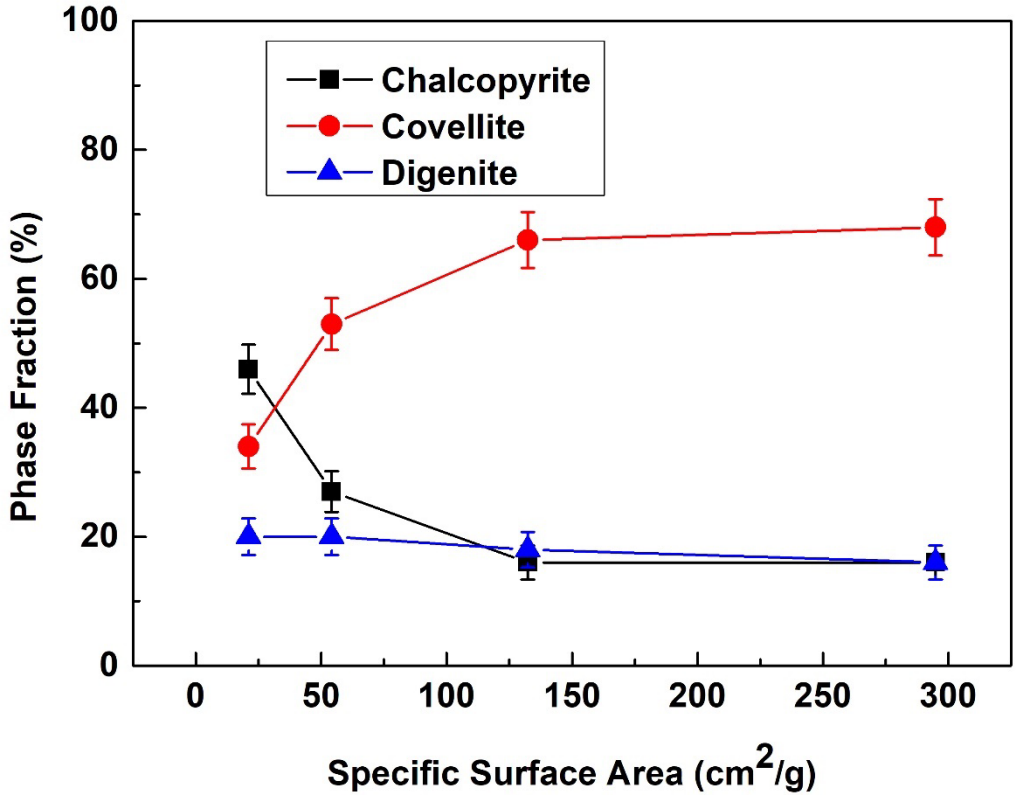

Figure 59 The reaction extent of each mineral in the solid residues collected at pH 2 and 180 °C with 0.22 mmol $CuCl_2$ and 0.44 mmol H_2O_2 after 70 h against specific surface area of starting chalcopyrite.

$CuCl_2$ crystals (eriochalcite) were formed at pH 1 and 2 in the presence of 0.88 mmol $CuCl_2$ added. The added Cu was not completely involved in copper sulphides precipitation. Sulphuric acid (0.1, 0.2 and 0.3 M of H_2SO_4) was used together with the addition of $CuSO_4$ to investigate the mechanism and kinetics of the replacement reaction of chalcopyrite to digenite. Copper sulphate (0.22-0.88 mmol of $CuSO_4$) was separately added to each sulfuric acid solution in different experiment run. All experiments were controlled at 200 °C with 0.44 mmol added H_2O_2 and run for 16 h. Both digenite and covellite precipitated in 0.1 M and 0.2 M H_2SO_4 solutions with different amounts of added $CuSO_4$. Covellite was found as the dominant copper sulphide in the precipitates. At both 0.1 M and 0.2 M H_2SO_4 solutions, the reaction extent of covellite increased with increasing amount of $CuSO_4$

added after reaction for 16 h (Figure 60 and 61). 17±3% of digenite formed in the 0.1 M H_2SO_4 with 0.22 mmol $CuSO_4$ added, 23±3% with 0.44 mmol, 19% with 0.66 mmol and 14±3% with 0.88 mmol $CuSO_4$ added (Figure 60). 12±2% of digenite was found in the 0.2 M H_2SO_4 with 0.22 mmol $CuSO_4$ added, 11±2% with both 0.44 mmol and 0.66 mmol, 16±3% with 0.88 mmol (Figure 61). No digenite was found in the 0.3 M H_2SO_4, but another copper sulphate precipitate (Chalcanthite) was identified by PXRD analysis (Figure 62).

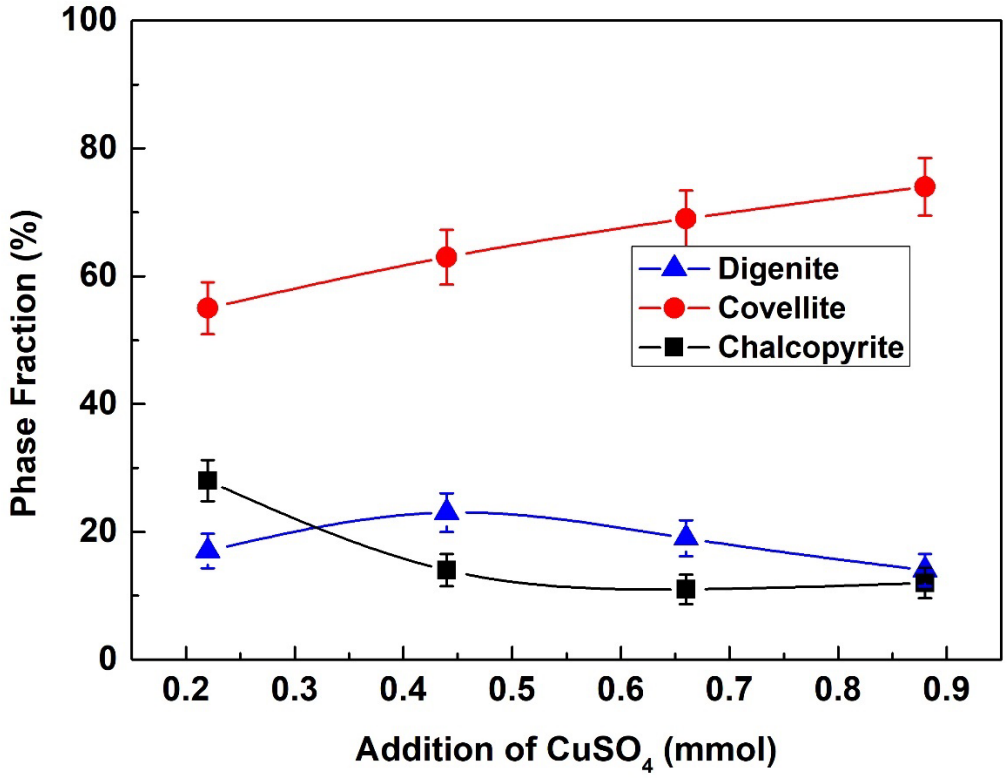

Figure 60 The reaction extent of each mineral in the solid residues collected at 180°C in 0.1M H_2SO_4 with 0.44mmol H_2O_2 after 16 hours against four different amounts of $CuSO_4$ addition.

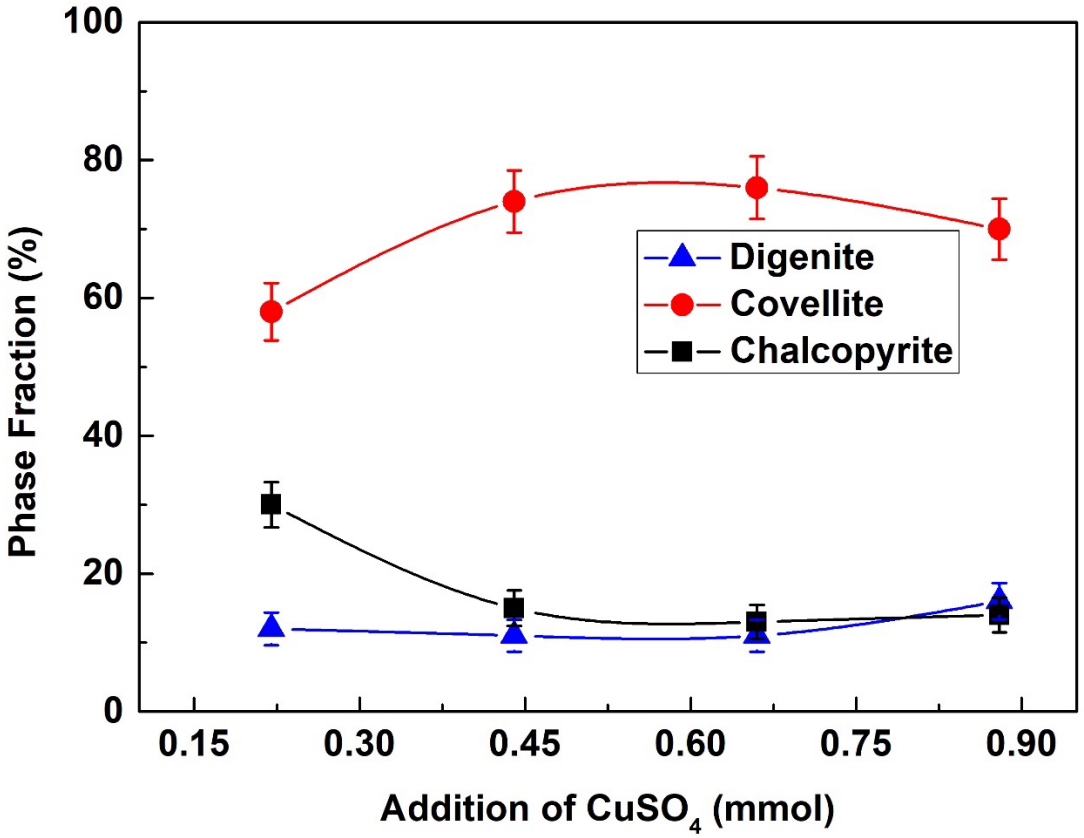

Figure 61 The reaction extent of each mineral in the solid residues collected at 180 °C in 0.2 M H_2SO_4 with 0.44 mmol H_2O_2 after 16 h against four different amounts of $CuSO_4$ addition.

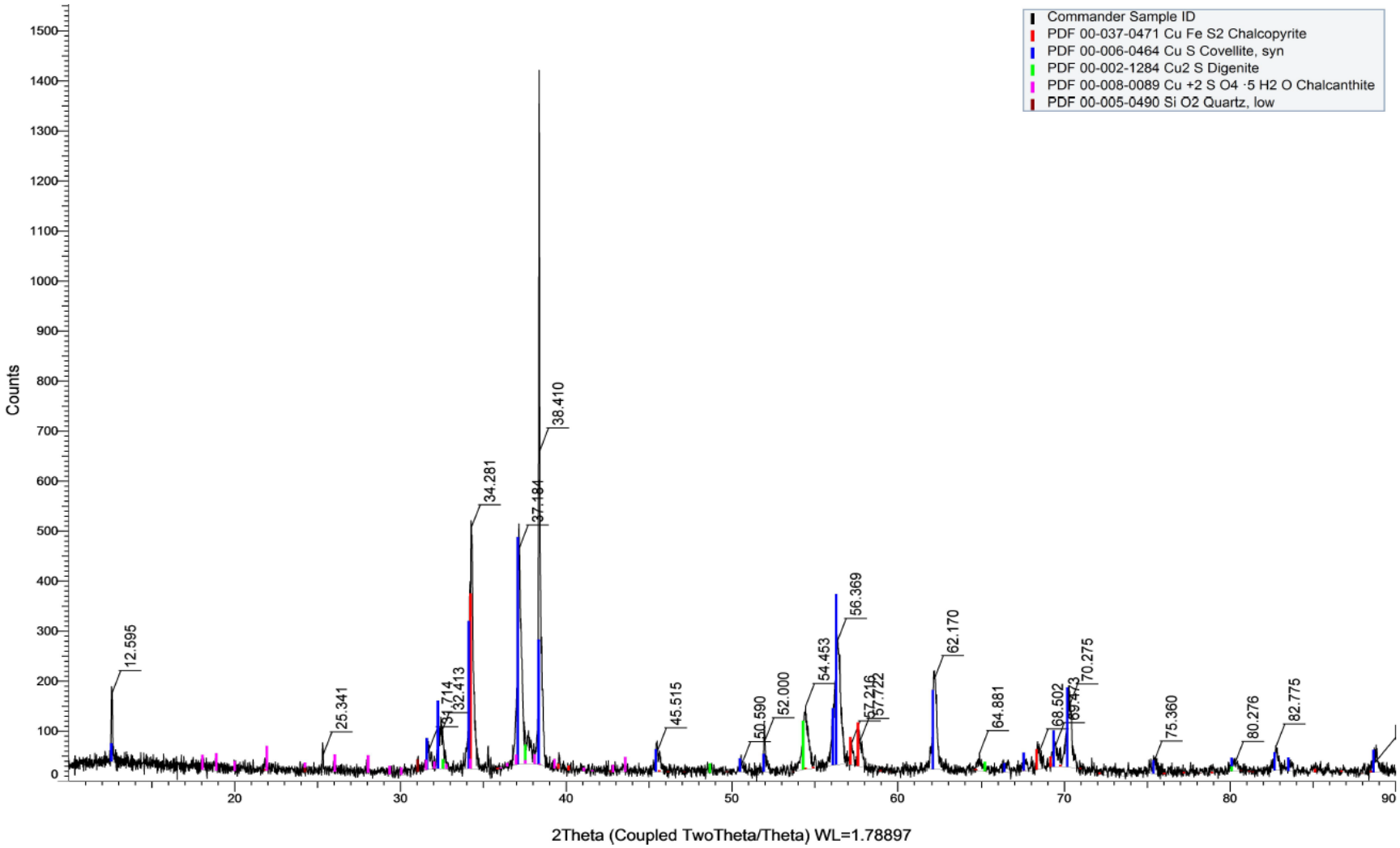

Figure 62 Powder X-ray diffraction data of the solid residue collected by the replacement reaction of chalcopyrite in 0.3 M H_2SO_4 and 180 °C with 0.88 mmol $CuCl_2$ and 0.44 mmol H_2O_2 after 16 h.

4.3.3 Quantitative Kinetic Study

The kinetics of chalcopyrite replacement reactions were studied under the conditions of pH 2 and pH 2.5, 140-200 °C, 0.22 mmol $CuCl_2$ and 0.44 mmol H_2O_2. At 160 °C and 140 °C, covellite was formed as the only copper sulphide precipitate by replacing chalcopyrite. The reaction extent of chalcopyrite in solid residues decreased with increasing temperature. Digenite was found to partially replace chalcopyrite at 180 °C and 200 °C only. The fraction of digenite increased with increasing reaction time at both temperatures. At 180 °C, 3±1% of digenite was initially found at pH 2 after 10 h which increased to 15±3% after 192 h. At pH 2.5 and 180 °C, digenite was initially precipitated after 24 h (10±2%) and increased to 19±3% of reaction product after 120 h. At 200°C, 40±4% of digenite was formed at both pH 2 and pH 2.5 after 16 hours.

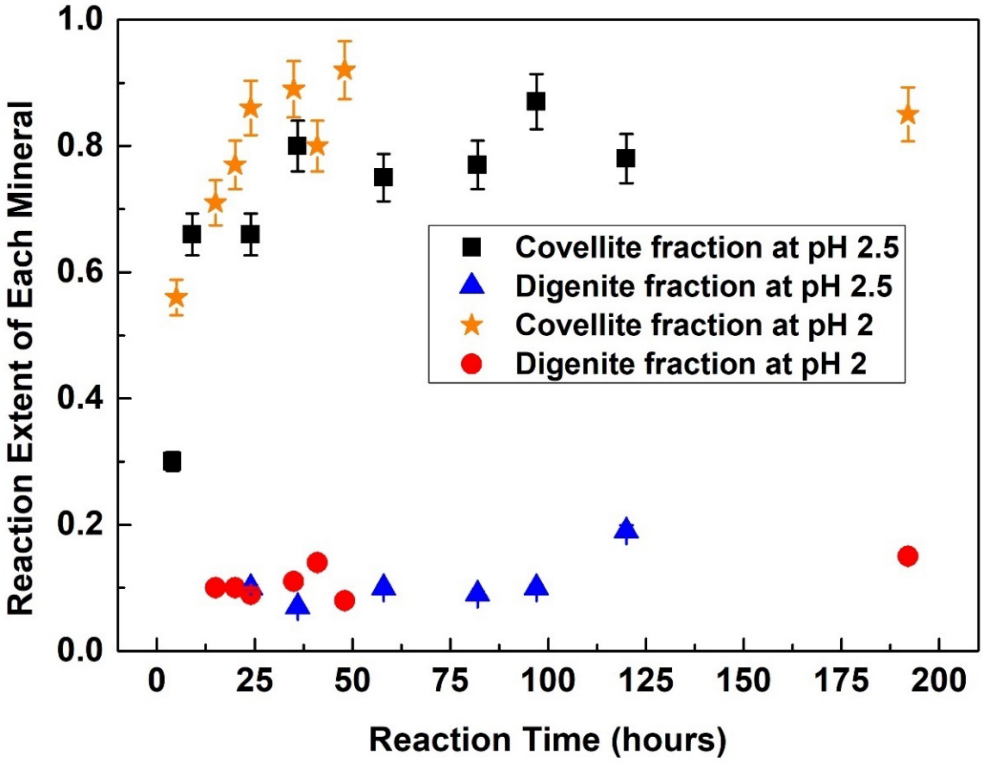

Figure 63 The reaction extent of covellite and digenite in solid residues against reaction time of experiments at pH 2 and pH 2.5 and 180 °C with 0.22 mmol $CuCl_2$ and 0.44 mmol H_2O_2.

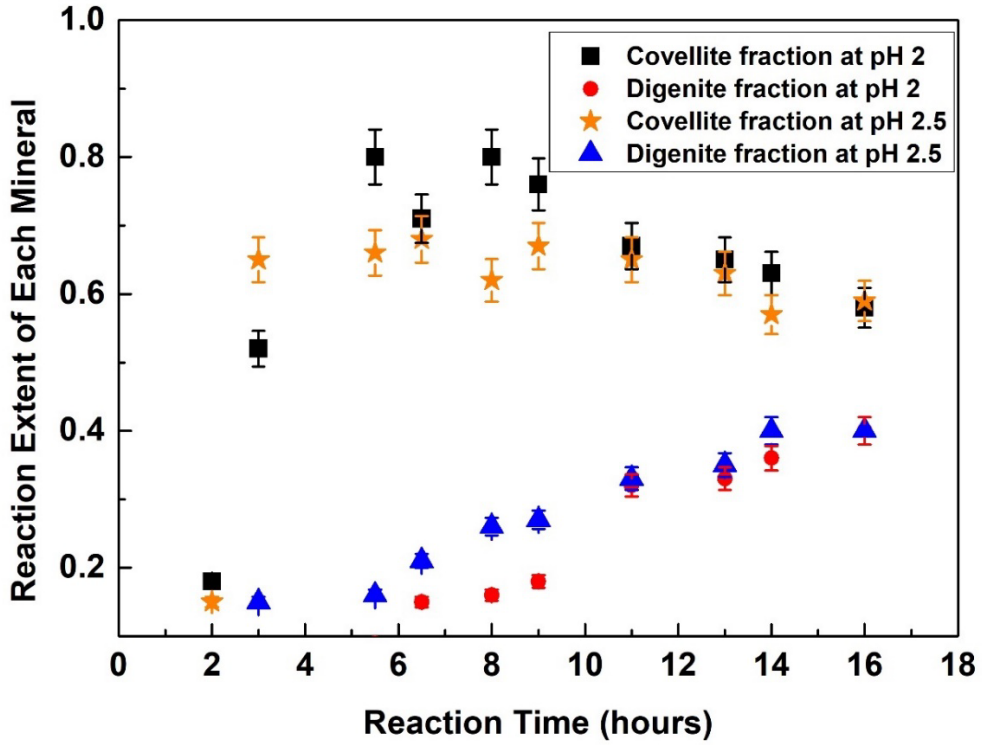

Figure 64 The reaction extent of covellite and digenite in solid residues against reaction time of experiments at pH 2 and pH 2.5 and 200 °C with 0.22 mmol $CuCl_2$ and 0.44 mmol H_2O_2.

A series of experiments were conducted to investigate the overall reaction rate for the replacement of chalcopyrite by covellite. All experimental conditions were at pH 2, with 0.22 mmol $CuCl_2$ and 0.44 mmol H_2O_2, *S/F* = 2 g/L. At 140 °C, the rate constant *k* is 0.053±0.004 h^{-1}, at 160 °C, 0.077±0.001 h^{-1}, at 180 °C, 0.177±0.032 h^{-1} and at 200 °C, *k* is 0.243±0.016 h^{-1}. The values of *n* for the four temperatures are 0.82±0.09, 1.13±0.03, 0.63±0.13 and 1.63±0.23, respectively. The rate constant, *k*, increases with increasing temperature, suggesting the transformation reaction rate is faster at higher temperature. The weight percentage of reacted chalcopyrite against time at all four temperatures were plotted in Figure 65. All *k* and *n* values at each temperature were calculated using the *Avrami* equation and summarised in Table 24.

Another set of experiments were conducted at pH 2.5 with the same amount of added $CuCl_2$ and oxidants. The replacement rate was found to be dependent on the temperature. The plots of reacted chalcopyrite fraction versus time at all four temperatures are shown in Figure 66. *Avrami* equation was used to fit the plots and obtain the rate constant. The rate constant *k* is calculated to be 0.034±0.002 h^{-1} at 140 °C, 0.083±0.006 h^{-1} at 160 °C,

0.074±0.013 h^{-1} at 180 °C and 0.229±0.017 h^{-1} at 200 °C. The values of *n* for the four temperatures are 0.98±0.09, 1.37±0.17, 0.57±0.09 and 1.55±0.25, respectively.

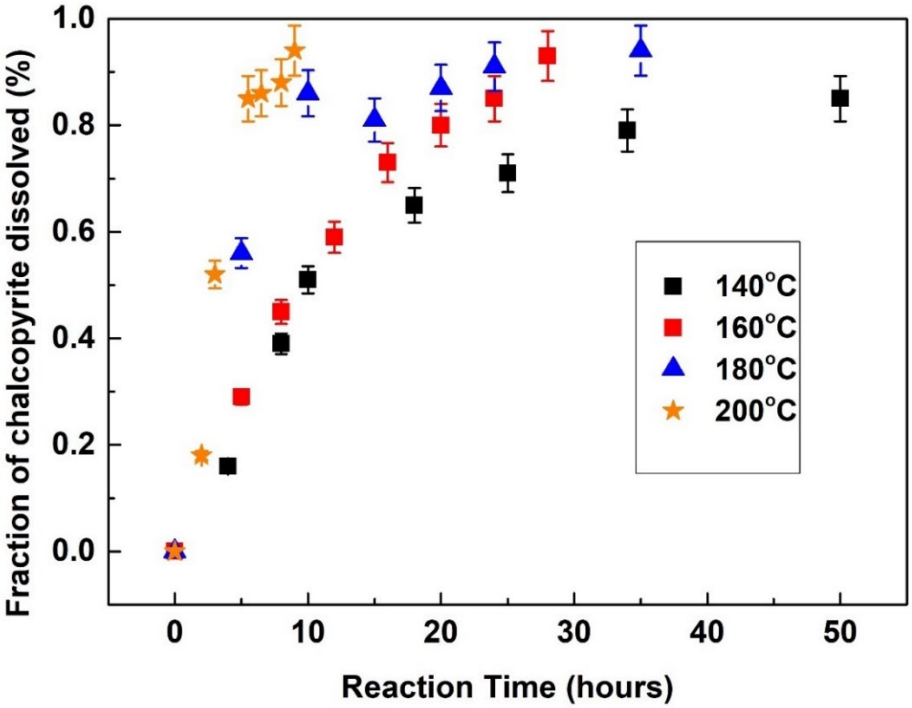

Figure 65 The fraction of chalcopyrite dissolved in the mineral replacement reaction against reaction time of experiments at pH 2 with 0.44 mmol H_2O_2 and 0.22 mmol $CuCl_2$.

Table 24 Summary of kinetic data and fitted *Avrami* curve parameters (*k* and *n*) for the replacement reaction of chalcopyrite by digenite or covellite at pH 2.

pH 2, 140°C		pH 2, 160°C		pH 2, 180°C		pH 2, 200°C	
Time (h)	CPY[1] (wt%)	Time (h)	CPY[1] (wt%)	Time (h)	CPY[1] (wt%)	Time (h)	CPY[1] (wt%)
0	0	0	0	0	0	0	0
4	16	5	29	5	54	2	18
8	39	8	45	10	86	3	52
10	51	12	59	15	81	5.5	85
18	65	16	73	20	87	6.5	86
25	71	20	80	24	91	8	88
34	79	24	85	35	94	9	94
50	85	28	93				
R^2 = 0.98		R^2 = 0.99		R^2 = 0.98		R^2 = 0.97	
k = 0.053±0.004 h^{-1}		k = 0.077±0.001 h^{-1}		k = 0.177±0.032 h^{-1}		k = 0.243±0.016 h^{-1}	
n = 0.82±0.09		n = 1.13±0.03		n = 0.63±0.13		n = 1.63±0.23	

[1] CPY stands for the weight percentage of chalcopyrite reacted.

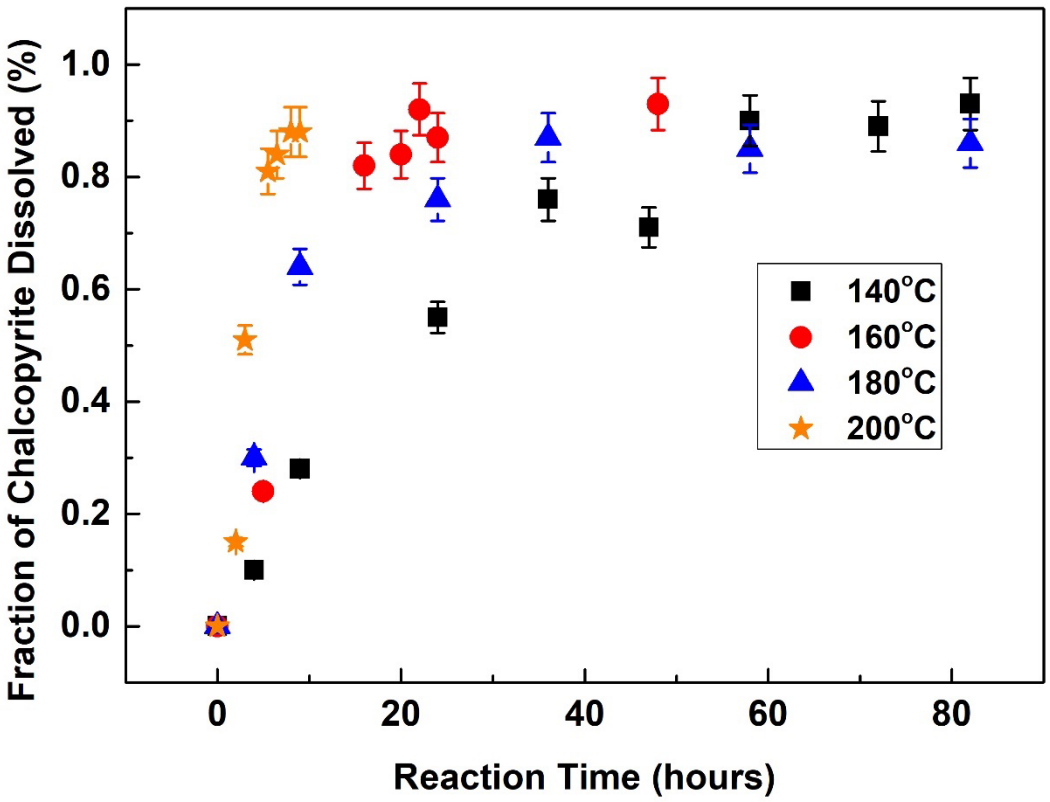

Figure 66 The fraction of chalcopyrite dissolved in the mineral replacement reaction against reaction time of experiments at pH 2.5 with 0.44 mmol H_2O_2 and 0.22 mmol $CuCl_2$.

Table 25 Summary of kinetic data and fitted *Avrami* curve parameters (*k* and *n*) for the replacement reaction of chalcopyrite by digenite or covellite at pH 2.5.

pH 2, 140°C		pH 2, 160°C		pH 2, 180°C		pH 2, 200°C	
Time (h)	CPY[1] (wt%)	Time (h)	CPY[1] (wt%)	Time (h)	CPY[1] (wt%)	Time (h)	CPY[1] (wt%)
0	0	0	0	0	0	0	0
4	10	5	24	4	30	2	15
9	28	16	82	9	64	3	51
24	55	20	84	24	76	5.5	81
36	76	22	92	36	87	6.5	84
47	71	24	87	58	85	8	88
58	90	48	93	82	86	9	88
72	89			97	97		
82	93						
R^2 = 0.98		R^2 = 0.98		R^2 = 0.96		R^2 = 0.96	
k = 0.034±0.002 h^{-1}		k = 0.083±0.006 h^{-1}		k = 0.074±0.013 h^{-1}		k = 0.229±0.017 h^{-1}	
n = 0.98±0.09		n = 1.37±0.17		n = 0.57±0.09		n = 1.55±0.25	

[1] CPY stands for the weight percentage of chalcopyrite reacted.

The experiments of kinetic study at pH 3 were conducted under otherwise identical conditions. The fraction of reacted chalcopyrite versus time at all four temperatures were plotted in Figure 67. *Avrami* equation was used to fit the plots at 140 °C, 160 °C and 180 °C. The rate constant *k* is calculated to be 0.007±0.001 h^{-1} at 140 °C, 0.006±0.002 h^{-1} at 160 °C and 0.003±0.001 h^{-1} at 180 °C. The values of *n* for all three temperatures are 0.78±0.17, 0.34±0.11 and 0.49±0.06, respectively. The transformation rate at pH 3 is slightly decrease with increasing temperature between the range of 140-180 °C. At 200 °C, 28% of chalcopyrite was converted to covellite after 24 h of reaction and only 30% after 216 h. Covellite was the only copper sulphide product formed, with no digenite observed.

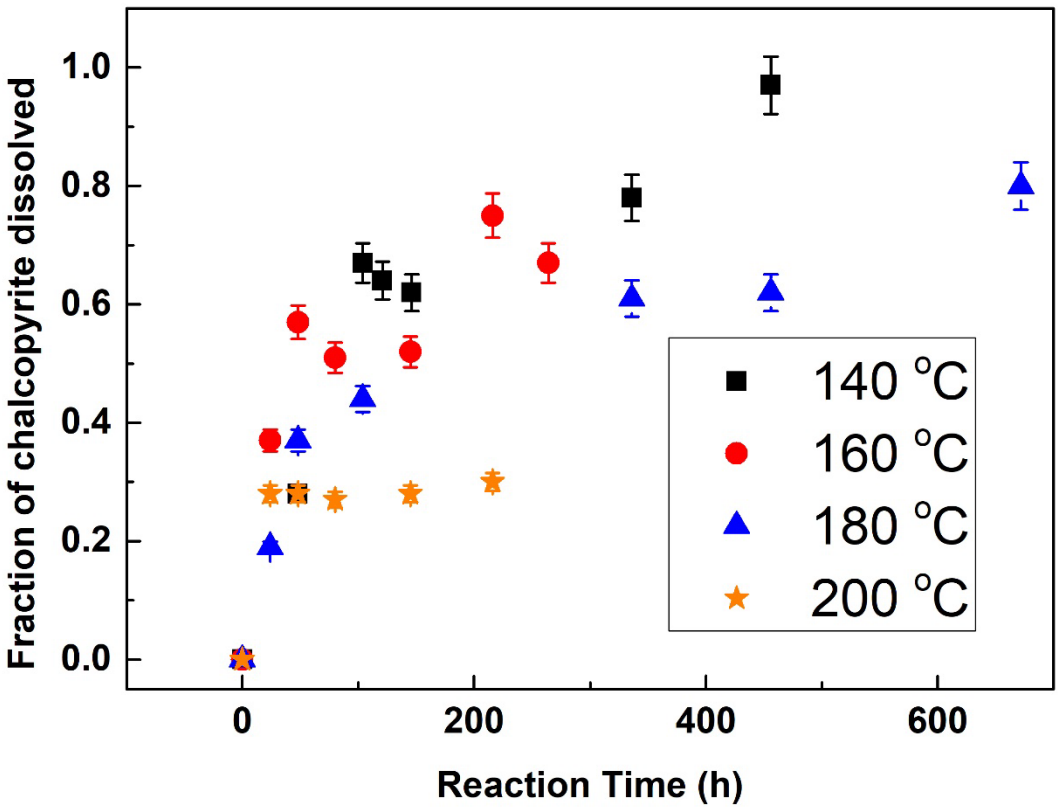

Figure 67 The fraction of chalcopyrite dissolved in the mineral replacement reaction against reaction time of experiments at pH 3 with 0.44 mmol H_2O_2 and 0.22 mmol $CuCl_2$.

Table 26 Summary of kinetic data and fitted *Avrami* curve parameters (*k* and *n*) for the replacement reaction of chalcopyrite by digenite or covellite at pH 3.

pH 3, 140°C		pH 3, 160°C		pH 3, 180°C		pH 3, 200°C	
Time (h)	**CPY[1] (wt%)**	**Time (h)**	**CPY[1] (wt%)**	**Time (h)**	**CPY[1] (wt%)**	**Time (h)**	**CPY[1] (wt%)**
0	0	0	0	0	0	0	0
48	28	24	37	24	19	24	28
104	67	48	57	48	37	48	28
121	64	80	51	104	44	80	27
146	62	145	52	336	61	145	28
336	78	216	75	456	62	216	30
456	97	264	67	672	80		
R^2 = 0.94		R^2 = 0.91		R^2 = 0.97			
k = 0.007±0.001 h^{-1}		k = 0.006±0.002 h^{-1}		k = 0.003±0.001 h^{-1}			
n = 0.78±0.17		n = 0.34±0.11		n = 0.49±0.06			

[1] CPY stands for the weight percentage of chalcopyrite reacted.

4.4 Discussion

4.4.1 Proposed Reaction Pathway

Under acidic conditions, chalcopyrite dissolution follows equation (66) and releases Cu^{2+} and Fe^{2+} into the solution. The oxidation state of Cu, Fe and S in chalcopyrite are +1, +3 and –2 (sulphide S^{2-}) (Pearce et al., 2006, Vaughan, 2006, Kimball et al., 2010). Sulphide species are readily exposed to H^+ upon chalcopyrite dissolved without dissolving oxygen, resulting in the formation of H_2S, Fe^{2+} and Cu^{2+} (Hidalgo et al., 2018, Lu et al., 2016). After adding hydrogen peroxide into the system, chalcopyrite can also be dissolved in the presence of oxygen and release Cu^{2+} and Fe^{2+} into the solution and forming elemental sulphur (Figure 68) (Holliday and Richmond, 1990, Hiroyoshi et al., 2001, Hiroyoshi et al., 1997, Hiroyoshi et al., 2000). Elemental sulphur was reacted with water under high temperature (140 °C or above) and forming H_2S as the replacement of chalcopyrite by covellite in Chapter 3 (Fang et al., 2011; Randall and Bichowsky, 1918). Covellite was precipitated by the reaction of H_2S and Cu^{2+} ions from added $CuCl_2$ or chalcopyrite dissolution (Figure 68) (Rickard, 1972).

$$CuFeS_{2(s)} + 4H^+_{(aq)} \rightarrow Cu^{2+}_{(aq)} + Fe^{2+}_{(aq)} + 2H_2S_{(aq)} \quad (66)$$

$$Cu^{2+}_{(aq)} + HS^-_{(aq)} \rightarrow CuS_{(s)} + H^+_{(aq)} \quad (67)$$

$$CuFeS_{2(s)} + O_{2(g)} + 4H^+_{(aq)} \rightarrow Cu^{2+}_{(aq)} + Fe^{2+}_{(aq)} + 2S^0_{(s)} + 2H_2O_{(aq)} \quad (68)$$

$$3S_{(s)} + 2H_2O_{(g)} \rightarrow 2H_2S_{(aq)} + SO_{2(g)} \quad (69)$$

After adding 0.22 mM $CuCl_2$ (chalcopyrite: $CuCl_2$ = 1:1), chalcopyrite is only replaced by covellite, resulting in release of Fe^{2+} in the solution at pH 1 and 180 °C. Covellite consists of both Cu^{2+} and lesser amounts of Cu^+ in its hexagonal crystal structure (Liang and Whangbo, 1993, Mazin, 2012). Also, the precipitation of covellite can proceed at low temperatures (e.g. 25°C) in the solution containing HS^- and Cu^{2+} ions (Rickard, 1972). Therefore, covellite precipitation is favoured after chalcopyrite dissolution with Cu^{2+} ions (Pejjai et al., 2020). Covellite nucleation occurred on the surface of chalcopyrite when H_2S was produced during chalcopyrite dissolution reacted with added $CuCl_2$ and formed a nest-like structure (Figure 50 C and D).

At pH 2 and 140-200 °C, covellite is also the dominant reaction product rather than digenite at temperature range of 140-200°C. The formation of digenite is competing with precipitation of covellite, but covellite is the dominant replacement product at or below 180°C. At 180-200°C, digenite replaced chalcopyrite only following initial covellite formation. Digenite was observed in the middle of chalcopyrite core and covellite outer rim, suggesting digenite was only precipitated in the presence of high Cu^{2+} concentrations (Chaudhari et al., 2021). On the chalcopyrite surface, the total Cu^{2+} concentration is relatively high due to the Cu^{2+} from chalcopyrite dissolution and the added $CuCl_2$ can also be transported through the pores and cracks of the covellite layer (Figure 68). Chaudhari et al. (2021) has found that chalcopyrite is replaced by covellite in the first stage and by digenite in the second stage in an *in-situ* study. The kinetic data of the present study at 200 °C showed an increase and a decrease in phase abundance for digenite and covellite, respectively, with longer reaction time (up to 16 h) at pH 2 and 2.5.

$$CuFeS_{2(s)} + Cu^{2+}{}_{(aq)} \rightarrow 2CuS_{(s)} + Fe^{2+}{}_{(aq)} \ (\Delta V_{solid} = -6.6\%) \quad (70)$$

$$5CuFeS_{2(s)} + 13Cu^{2+}{}_{(aq)} \rightarrow 10Cu_{1.8}S_{(s)} + 5Fe^{2+}{}_{(aq)} \ (\Delta V_{solid} = 19.1\%) \quad (71)$$

$$4Fe^{2+}_{(aq)} + 3O_{2(aq)} \rightarrow 2Fe_2O_{3(s)} \quad (72)$$

At pH 3, digenite was formed in the temperature range of 140 °C to 200 °C with very low phase abundance (less than 10%). At 200 °C, chalcopyrite fraction only slightly changed between 24 h (72%) and 384 h (70%). A cross-sectional backscattered SEM image with large chalcopyrite grains shows similar results after 216 h of reaction (Figure 52). A previous study suggested that the decomposition rate of acetic acid significantly increases after 230 °C and becomes faster as the pressure increases (Li et al., 2017). pH 3 buffer solution consists of acetic acid and sodium acetate, and it can be (partially) decomposed at 200 °C with increasing pressure in the sealed PTFE cells. At pH 2-3, Fe^{2+} was precipitated with dissolved oxygen in solution and form hematite via equation (72).

4.4.2 Reaction Mechanism

The textures of chalcopyrite sample collected from the run at pH 2 and 200 °C suggest that the replacement reaction involves coupled chalcopyrite dissolution and re-precipitation of both digenite and covellite. The presence of sharp reaction fronts at the adjacent sites of chalcopyrite, covellite and digenite phases are typical characteristics of interfacial

dissolution-reprecipitation reactions (Putnis, 2002, Putnis, 2009, Xia et al., 2009, Zhao et al., 2014b, Zhao et al., 2019). There is no obvious gap found between chalcopyrite, covellite and digenite at the micro-meter scale, but a gap was observed within the covellite phase, indicative of not tightly coupled chalcopyrite dissolution and covellite reprecipitation mechanism (Figure 51) (Xia et al., 2009). On the other hand, a tightly coupled chalcopyrite dissolution and digenite precipitation mechanism was found as no gap was formed at the adjacent sites between digenite and chalcopyrite (Xia et al., 2009). Similar interfacial coupled dissolution and reprecipitation (ICDR) mechanism were found in the replacement reaction of chalcopyrite by bornite within the range of temperature 200-320 °C (Zhao et al., 2014b). They reported pseudo-morphic replacement of chalcopyrite by bornite with significant increase in molar volume due to the overgrowth of bornite.

The change of molar volume for the parent and product minerals also plays a significant role in the reactions. In the case of transformation of pentlandite to violarite, the molar volume change is small and the dissolution of pentlandite and precipitation of violarite are tightly coupled. It has been found as a pseudo-morphic mineral replacement reaction and the product mineral preserved the grain shape and textural features of parent mineral (Xia et al., 2009, Tenailleau et al., 2006). Large positive volume change has been reported in the replacement reaction of hematite by chalcopyrite via sulfidation (290%) with overgrowth (Zhao et al., 2014a). In this study, the volume change was calculated with the consideration of reaction stoichiometries and same equation as section 3.4.1. In the replacement reaction of chalcopyrite by digenite increased by 19.1% (equation 72) and decreased by 6.6% when chalcopyrite transformed to covellite (equation 71).

The formation of pores and cracks in all chalcopyrite, covellite and digenite phases were also one of the characteristics, a result of molar volume change between parent and product phases, which allows the fluids to constantly interact with mineral assemblages (Altree-Williams et al., 2015, Ruiz-Agudo et al., 2014, Pollok et al., 2011, Putnis, 2009, Altree-Williams et al., 2017, Altree-Williams et al., 2019, Pina, 2019, Pöml et al., 2007, Jonas et al., 2014). It has been found that the formation of pores and cracks were required to sustain the replacement reaction (Nakamura and Watson, 2001, Putnis and Mezger, 2004). Therefore, the replacement reaction of chalcopyrite by digenite or covellite is a typical example of interfacial coupled dissolution-reprecipitation reaction.

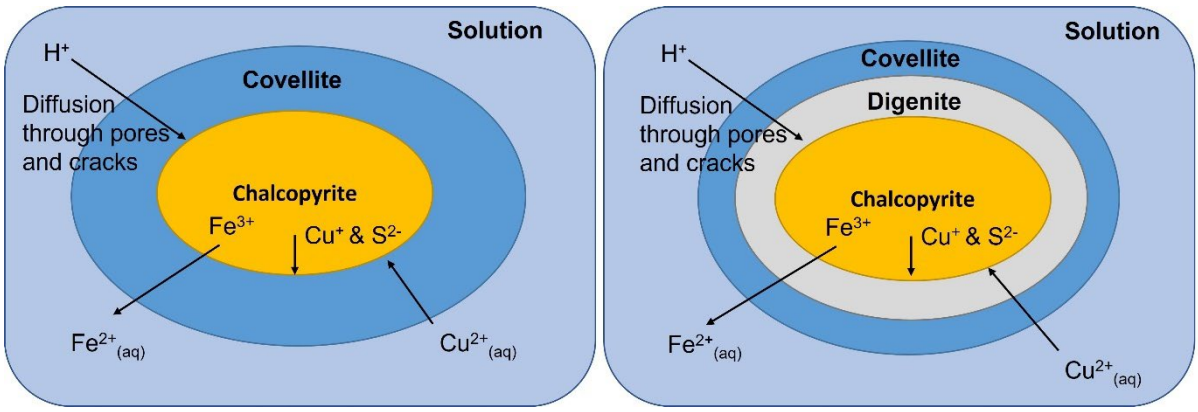

Figure 68 Schematic diagram of chalcopyrite dissolution and re-precipitation of covellite and digenite.

At pH 3 under other identical conditions, chalcopyrite was replaced by covellite with a thin layer of hematite formed on the surface of the covellite. The replacement reaction also proceeded via an interfacial coupled dissolution and reprecipitation mechanism with characteristic textures, including 1) sharp reaction front between chalcopyrite and covellite phases; 2) pores and cracks formed at covellite layer; 3) formation of covellite outer rim; 4) molar volume change between chalcopyrite and covellite (Putnis, 2002, Putnis, 2009, Xia et al., 2009, Adegoke et al., 2022, Zhao et al., 2014b). The reaction rates of chalcopyrite dissolution and covellite reprecipitation were tightly coupled as no gap was observed between chalcopyrite and covellite phases (Xia et al., 2009, Zhao et al., 2014b, Zhao et al., 2014a).

4.4.3 Replacement Reaction in Sulphuric Acid

In sulfuric acid solutions, covellite is the major product at 200 °C independent of the concentration of $CuSO_4$ examined. Digenite has been found in the 0.1 to 0.3 M sulfuric acid solution and the reaction extent decreased as the acidity increased (Figure 60 and 61). The amount of $CuSO_4$ addition has no significant impact on the precipitation of digenite in 0.2 and 0.3 M sulfuric acid at 200 °C. The results are consistent with the in-situ XRD study of chalcopyrite replaced by digenite and covellite at 200 °C in 0.16 M sulphuric acid solution (Chaudhari et al., 2021). The chalcopyrite dissolution rate was found to increase with increasing concentration of sulphuric acid (Aydogan et al., 2006). The chalcopyrite reaction extent was not significantly influenced by the concentration of sulphuric acid, suggesting the chalcopyrite dissolution rate is largely independent of acid concentration between 0.1 M and 0.2 M. This is because the chalcopyrite dissolution rate

was maximized by high specific surface area (particle size of chalcopyrite: 38-75 μm), addition of oxidants (0.44 mmol H_2O_2) and high temperature (200 °C).

4.4.4 Rate-determining Step

Torres et al. (2019) have reported that copper extraction from chalcopyrite is enhanced by addition of Cl^- ions with high concentration of Cu^{2+} ions. When the addition of $CuCl_2$ increased, the chalcopyrite phase decreased, and the dissolution rate might be increased. This indicates that the replacement reaction of chalcopyrite is faster with increasing amount of $CuCl_2$. Copper chloride crystals (eriochalcite) were formed at 180 °C and pH 1 and 2 in the presence of 0.88 mmol $CuCl_2$. The initial concentration of Cu^{2+} and Cl^- in the solution was 2.25 g/L and 2.5 g/L, respectively, indicating that at high concentrations of Cu^{2+} and Cl^- are favourable to the precipitation of $CuCl_2$ crystals.

At pH 2 and 180 °C, the fraction of digenite in the solid residue significantly increased with increasing amount of $CuCl_2$ addition, indicating digenite precipitation is favoured at the high $CuCl_2$ concentration (17.6 mM). The reaction extent of digenite is doubled (19±3% to 40±4%) when the reaction temperature increased from 180 °C to 200 °C at both pH 2 and pH 2.5. The results indicating that the formation of digenite is more complicated than covellite precipitation and only occurs under high temperatures conditions (180 °C or above) with high Cu^{2+} concentration. Chaudhari et al. (2021) reported that no digenite formed at 180 °C in 0.16 M H_2SO_4 and 0.22 M $CuCl_2$, but 30±3% of digenite was found after reaction for 200 mins at 200 °C under otherwise identical conditions. They found the reaction extent of digenite increased with increasing temperature (200-240 °C). Zhao et al. (2014b) found that a large amount of digenite precipitated during the replacement of chalcopyrite by bornite at 200-260 °C under neutral conditions. The fraction of digenite in the solid residues decreased as pH decreased from 7 to 3.

In summary, the precipitation of digenite only takes occurs at or above 180 °C and at or below pH 2.5 in the replacement reaction of chalcopyrite with $CuCl_2$ added. The initial Cu^{2+} concentration needs to reach 0.56 g/L at pH 2 and 3, 2.25 g/L at pH 1 and 180 °C. More digenite can be precipitated when the reaction temperature increased from 180 °C to 200 °C. The mineral replacement reaction requires H^+ ions and oxidants to dissolve chalcopyrite, giving predominantly covellite under very acidic condition (0.01M H^+ or more)

and partially digenite under weaker acidic condition (0.01M H^+ or less). This suggests that the precipitations of digenite are the rate-limiting step and control the overall replacement reactions under acidic conditions with oxidants.

4.4.5 Activation Energy

The kinetic study of the mineral replacement reaction of chalcopyrite by covellite or digenite was determined by the fraction of chalcopyrite dissolved. This is because digenite was only observed at or above 180°C. Kinetic experimental data collected at 140-200°C were fitted using the *Avrami* equation. Activation energies of chalcopyrite dissolution at pH 2 and 2.5 were calculated by plotting natural logarithm rate constant obtained from the *Avrami* fittings against 1000/T. The slope of linear best-fit equation of pH 2 is -5.28±0.68 with an R^2 value of 0.95. At pH 2.5, the slope is -5.46±1.64 with an R^2 value of of 0.77. The average activation energies of chalcopyrite dissolution at pH 2 and pH 2.5 determined using the *Avarmi-Arrhenius* method were 44±6 kJ/mol and 46±14 kJ/mol respectively. Brantley (2008) proposed that the reaction mechanism is phase boundary-controlled with *Ea* above 60kJ/mol and diffusion-controlled with *Ea* about 20 kJ/mol. The *Ea* obtained from *Avrami-Arrhenius* method suggesting the replacement reaction of chalcopyrite mechanism is phase boundary-controlled reaction at pH 2 and pH 2.5. Chaudhari et al. (2021) conducted *in-situ* XRD analysis to examine the replacement reaction of chalcopyrite at different temperatures ranging from 180 °C – 220 °C. They used *Avrami* method and obtained *Ea* values of 42.9±7.4 kJ/mol at first stage and 39.3±13.1 kJ/mol at second stage using the *Arrhenius* equation. The activation energies at both stages are in close agreement with the present study.

The activation energy of chalcopyrite dissolution against reaction extent were also determined using the modified ‘time to given fraction’ method (Qian et al., 2017). One of advantages of this method is that it can determine the variations of activation energy at different stage of reaction, rather than an average activation of the reaction. At pH 2, the initial activation energy required to dissolve 10% chalcopyrite is 24.4 kJ/mol and almost doubled (39.5 kJ/mol) when the reaction extent increased from 10% to 20%. It is continuously increasing with every addition 10% of chalcopyrite dissolution. The *Ea* for between 80-90% reaction extent is 61 kJ/mol. The *Ea* at different reaction extent suggests the replacement reaction of chalcopyrite at pH 2 was initially diffusion-controlled (0-10%) and then changed to phase boundary-controlled. At pH 2.5, the initial activation energy is 44.8 kJ/mol at 10% chalcopyrite and slightly increased to 49 kJ/mol at 90%, suggesting the

chalcopyrite replacement mechanism is phase boundary-controlled from 0-90% reaction extent.

At the beginning of replacement reactions, solutions and oxidants can constantly reacting with chalcopyrite grains, so the E_a was expected to be lower at initial stage. At later stage, covellite layer and digenite layer were formed and inhibits the contact between fluids and remained chalcopyrite grains. Thus, an increased E_a was found at pH 2. At pH 2.5, the dissolution of chalcopyrite was expected to be slower than at pH 2 due to less H^+ ions. A higher E_a at initial stage of replacement reaction was expected. The E_a did not change much as the replacement reaction progress at pH 2.5 is possibly due to the high errors.

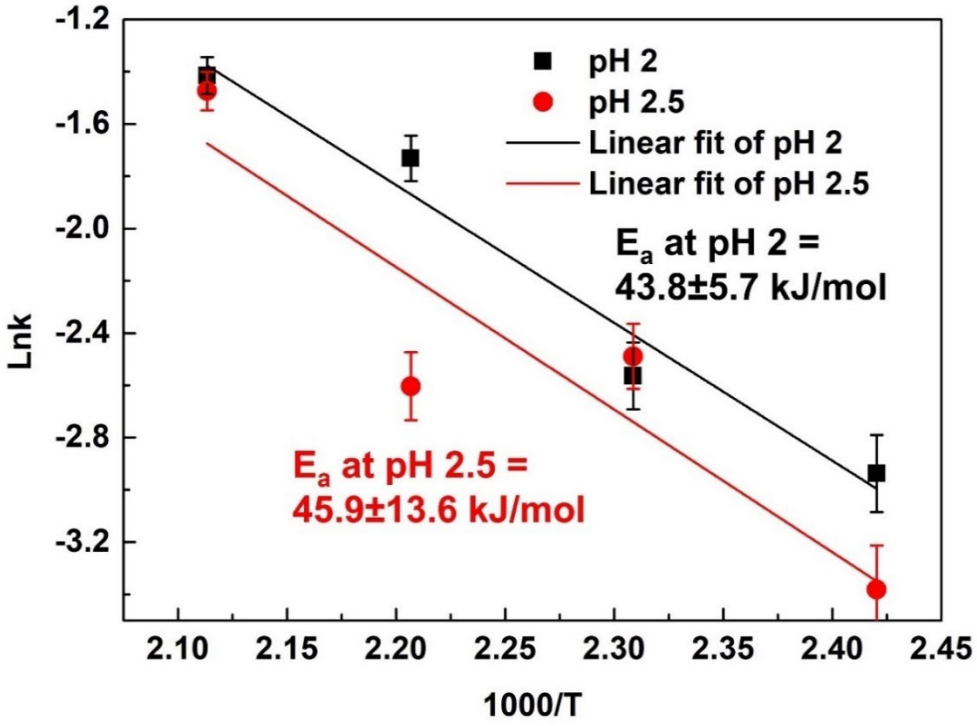

Figure 69 The Arrhenius plot showing the calculated activation energies of chalcopyrite dissolution in the replacement reaction of chalcopyrite by covellite or digenite at pH 2 (black) and pH 2.5 (red) using experimental data collected at 140 °C, 160 °C, 180 °C and 200°C.

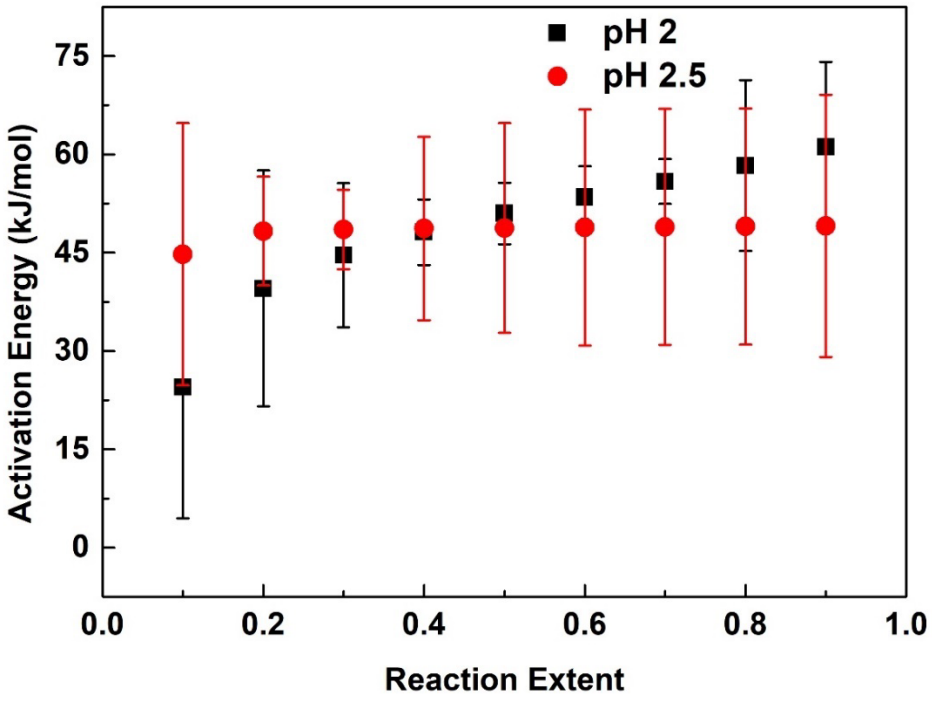

Figure 70 Activation energy as a function of reaction extent (fraction of chalcopyrite dissolved) at pH 2 and 2.5, calculated by using modified time to given fraction method. Experimental data were all collected at temperature 140-200 °C

4.5 Conclusion

In conclusion, chalcopyrite was successfully converted to digenite at pH 2-3 when temperature is at or above 180°C with addition of $CuCl_2$. The mineral replacement reaction observes an interfacial coupled dissolution and reprecipitation mechanism with characteristic features, including 1) sharp reaction front between chalcopyrite, covellite and digenite phases; 2) formation of pores and cracks on the product and parent phases; 3) replacement reaction with molar volume changes between parent phase and product phase. The precipitation of digenite and covellite are the rate-determining steps for the overall chalcopyrite mineral replacement reaction. The dissolution rate of chalcopyrite in the mineral replacement reaction was found to increase with increasing temperature, decreasing pH and increasing specific surface area. The precipitation of covellite and digenite are competing-reactions. Covellite precipitation is the dominant process at pH 1-3 and 140-200 °C as it can be formed by either chalcopyrite dissolution or precipitation from reaction between H_2S and Cu^{2+}. Higher percentage of digenite fraction can be achieved by increasing the added amount of $CuCl_2$ and increasing temperature or by decreasing the concentration of H^+.

Using the *Avrami-Arrhenius* method, the activation energies of overall replacement reaction of chalcopyrite are 44±6 kJ/mol at pH 2 and 46±14 kJ/mol at 2.5, suggesting the reaction is phase boundary-controlled. E_a resulting from the modified 'time to given fraction' method suggests the reaction mechanism was initially diffusion-controlled and then became phase boundary-controlled as the reaction progressed at pH 2.

4.6 Reference List

ADEGOKE, I. A., XIA, F., DEDITIUS, A. P., PEARCE, M. A., ROBERTS, M. P. & BRUGGER, J. 2022. A new mode of mineral replacement reactions involving the synergy between fluid-induced solid-state diffusion and dissolution-reprecipitation: A case study of the replacement of bornite by copper sulfides. Geochimica et Cosmochimica Acta.

ALTREE-WILLIAMS, A., BRUGGER, J., PRING, A. & BEDRIKOVETSKY, P. 2019. Coupled reactive flow and dissolution with changing reactive surface and porosity. Chemical Engineering Science, 206, 289-304.

ALTREE-WILLIAMS, A., PRING, A., NGOTHAI, Y. & BRUGGER, J. 2015. Textural and compositional complexities resulting from coupled dissolution–reprecipitation reactions in geomaterials. Earth-Science Reviews, 150, 628-651.

ALTREE-WILLIAMS, A., PRING, A., NGOTHAI, Y. & BRUGGER, J. 2017. The carbonatation of anhydrite: kinetics and reaction pathways. ACS Earth Space Chemistry, 1, 89-100.

AYDOGAN, S., UCAR, G. & CANBAZOGLU, M. 2006. Dissolution kinetics of chalcopyrite in acidic potassium dichromate solution. Hydrometallurgy, 81, 45-51.

BERRY, L. 1954. The crystal structure of covellite, cuse and klockmannite, cuse. American Mineralogist: Journal of Earth Planetary Materials, 39, 504-509.

BRANTLEY, S. L. 2008. Kinetics of mineral dissolution. Kinetics of water-rock interaction. Springer.

CHAUDHARI, A., WEBSTER, N. A., XIA, F., FRIERDICH, A., RAM, R., ETSCHMANN, B., LIU, W., WYKES, J., BRAND, H. E. & BRUGGER, J. 2021. Anatomy of a complex mineral replacement reaction: role of aqueous redox, mineral nucleation, and ion transport properties revealed by an in-situ study of the replacement of chalcopyrite by copper sulfides. Chemical Geology, 581, 120390.

DUTRIZAC, J. 1989. Elemental sulphur formation during the ferric sulphate leaching of chalcopyrite. Canadian Metallurgical Quarterly, 28, 337-344.

FANG, H., BROWN, B., YOUNG, D. & NEŠIĆ, S. 2011. Investigation of elemental sulfur corrosion mechanisms. CORROSION.

GEELHOED, J. S., MEEUSSEN, J. C., HILLIER, S., LUMSDON, D. G., THOMAS, R. P., FARMER, J. G. & PATERSON, E. 2002. Identification and geochemical modeling of processes controlling leaching of Cr (VI) and other major elements from chromite ore processing residue. Geochimica et Cosmochimica Acta, 66, 3927-3942.

HANCOCK, J. & SHARP, J. 1972. Method of comparing solid-state kinetic data and its application to the decomposition of kaolinite, brucite, and BaCO3. Journal of the American Ceramic Society, 55, 74-77.

HIDALGO, T., KUHAR, L., BEINLICH, A. & PUTNIS, A. 2018. Kinetic study of chalcopyrite dissolution with iron (III) chloride in methanesulfonic acid. Minerals Engineering, 125, 66-74.

HIROYOSHI, N., HIROTA, M., HIRAJIMA, T. & TSUNEKAWA, M. 1997. A case of ferrous sulfate addition enhancing chalcopyrite leaching. Hydrometallurgy, 47, 37-45.

HIROYOSHI, N., MIKI, H., HIRAJIMA, T. & TSUNEKAWA, M. 2000. A model for ferrous-promoted chalcopyrite leaching. Hydrometallurgy, 57, 31-38.

HIROYOSHI, N., MIKI, H., HIRAJIMA, T. & TSUNEKAWA, M. 2001. Enhancement of chalcopyrite leaching by ferrous ions in acidic ferric sulfate solutions. Hydrometallurgy, 60, 185-197.

HOLLIDAY, R. & RICHMOND, W. 1990. An electrochemical study of the oxidation of chalcopyrite in acidic solution. Journal of electroanalytical chemistry interfacial electrochemistry, 288, 83-98.

JANG, J. H. 1992. Hydrothermal Conversion of Chalcopyrite to Copper Sulfide. Doctorate of Philosophy in Metallurgy PhD Thesis, University of Utah.

JONAS, L., JOHN, T., KING, H. E., GEISLER, T. & PUTNIS, A. 2014. The role of grain boundaries and transient porosity in rocks as fluid pathways for reaction front propagation. Earth Planetary Science Letters, 386, 64-74.

KIMBALL, B. E., RIMSTIDT, J. D. & BRANTLEY, S. L. 2010. Chalcopyrite dissolution rate laws. Journal of Applied Geochemistry, 25, 972-983.

KNIGHT, K. S., MARSHALL, W. G. & ZOCHOWSKI, S. W. 2011. The low-temperature and high-pressure thermoelastic and structural properties of chalcopyrite, CuFeS2. The Canadian Mineralogist, 49, 1015-1034.

LASAGA, A. C. 1998. Kinetic theory in the earth sciences, JSTOR.

LI, Y., ZHOU, S., LI, J., MA, Y., CHEN, K., WU, Y. & ZHANG, Y. 2017. Experimental study of the decomposition of acetic acid under conditions relevant to deep reservoirs. Applied Geochemistry, 84, 306-313.

LIANG, W. & WHANGBO, M.-H. 1993. Conductivity anisotropy and structural phase transition in covellite CuS. Solid State Communications, 85, 405-408.

LU, D., WANG, W., CHANG, Y., XIE, F. & JIANG, K. 2016. Thermodynamic analysis of possible chalcopyrite dissolution mechanism in sulfuric acidic aqueous solution. Metals, 6, 303.

MAZIN, I. Structural and Electronic properties of the 2D Superconductor CuS covellite with 113-valent Copper. APS March Meeting Abstracts, 2012. Q21. 008.

MORIMOTO, N. & KULLERUD, G. 1963. Polymorphism in digenite. American Mineralogist: Journal of Earth Planetary Materials, 48, 110-123.

NAKAMURA, M. & WATSON, E. 2001. Experimental study of aqueous fluid infiltration into quartzite: implications for the kinetics of fluid redistribution and grain growth driven by interfacial energy reduction. Geofluids, 1, 73-89.

NICOL, M., MIKI, H. & VELÁSQUEZ-YÉVENES, L. 2010. The dissolution of chalcopyrite in chloride solutions: Part 3. Mechanisms. Hydrometallurgy, 103, 86-95.

NIKKHOU, F., XIA, F. & DEDITIUS, A. P. 2019. Variable surface passivation during direct leaching of sphalerite by ferric sulfate, ferric chloride, and ferric nitrate in a citrate medium. Hydrometallurgy, 188, 201-215.

PARKER, A., PAUL, R. & POWER, G. 1981. Electrochemistry of the oxidative leaching of copper from chalcopyrite. Journal of electroanalytical chemistry interfacial electrochemistry, 118, 305-316.

PEARCE, C., PATTRICK, R., VAUGHAN, D., HENDERSON, C. & VAN DER LAAN 2006. Copper oxidation state in chalcopyrite: Mixed Cu d9 and d10 characteristics. Geochimica et Cosmochimica Acta, 70, 4635-4642.

PEJJAI, B., REDDIVARI, M. & KOTTE, T. R. R. 2020. Phase controllable synthesis of CuS nanoparticles by chemical co-precipitation method: effect of copper precursors on the properties of CuS. Journal of Materials Chemistry and Physics, 239, 122030.

PINA, C. M. 2019. Topotaxial replacement of celestite single crystals by strontianite aggregates: pseudomorphisation and porosity generation. Geochimica et Cosmochimica Acta, 244, 155-162.

POLLOK, K., PUTNIS, C. V. & PUTNIS, A. 2011. Mineral replacement reactions in solid solution-aqueous solution systems: Volume changes, reactions paths and end-points using the example of model salt systems. American Journal of Science, 311, 211-236.

PÖML, P., MENNEKEN, M., STEPHAN, T., NIEDERMEIER, D., GEISLER, T. & PUTNIS, A. 2007. Mechanism of hydrothermal alteration of natural self-irradiated and synthetic crystalline titanate-based pyrochlore. Geochimica et Cosmochimica Acta, 71, 3311-3322.

PUTNIS, A. 1992. An introduction to mineral sciences, Cambridge University Press.

PUTNIS, A. 2002. Mineral replacement reactions: from macroscopic observations to microscopic mechanisms. Mineralogical Magazine, 66, 689-708.

PUTNIS, A. 2009. Mineral replacement reactions. Reviews in mineralogy geochemistry, 70, 87-124.

PUTNIS, C. V. & MEZGER, K. 2004. A mechanism of mineral replacement: isotope tracing in the model system KCl-KBr-H2O. Geochimica et Cosmochimica Acta, 68, 2839-2848.

QIAN, G., LI, Y., LI, J. & GERSON, A. R. 2017. Consideration of enthalpic and entropic energy contributions to the relative rates of chalcopyrite dissolution in the presence of aqueous cationic impurities. International Journal of Mineral Processing, 159, 42-50.

RANDALL, M. & BICHOWSKY, F. R. V. 1918. EQUILIBRIUM IN THE REACTION BETWEEN WATER AND SULFUR AT HIGH TEMPERATURES. THE DISSOCIATION OF HYDROGEN SULFIDE. Journal of the American Chemical Society, 40, 368-375.

RAKOVAN, J. 2003. A Word to the Wise: Hypogene & Supergene. Rocks & Minerals, 78, 419.

REICH, M. & VASCONCELOS, P. M. 2015. Geological and economic significance of supergene metal deposits. Elements, 11, 305-310.

RICKARD, D. 1972. Covellite formation in low temperature aqueous solutions. Mineralium Deposita, 7, 180-188.

ROSEBOOM, E. H. 1966. An investigation of the system Cu-S and some natural copper sulfides between 25 degrees and 700 degrees C. Economic Geology, 61, 641-672.

RUIZ-AGUDO, E., PUTNIS, C. & PUTNIS, A. 2014. Coupled dissolution and precipitation at mineral–fluid interfaces. Chemical Geology, 383, 132-146.

TENAILLEAU, C., PRING, A., ETSCHMANN, B., BRUGGER, J., GRGURIC, B. & PUTNIS, A. 2006. Transformation of pentlandite to violarite under mild hydrothermal conditions. American Mineralogist, 91, 706-709.

TORRES, C. M., GHORBANI, Y., HERNÁNDEZ, P. C., JUSTEL, F. J., ARAVENA, M. I. & HERREROS, O. O. 2019. Cupric and chloride ions: Leaching of chalcopyrite concentrate with low chloride concentration media. Minerals, 9, 639.

VAUGHAN, D. J. 2006. Sulfide mineralogy and geochemistry, Mineralogical Society of America.

WILL, G., HINZE, E. & ABDELRAHMAN, A. R. M. 2002. Crystal structure analysis and refinement of digenite, Cu1. 8S, in the temperature range 20 to 500 C under controlled sulfur partial pressure. European Journal of Mineralogy, 14, 591-598.

XIA, F., BRUGGER, J., CHEN, G., NGOTHAI, Y., O'NEILL, B., PUTNIS, A. & PRING, A. 2009. Mechanism and kinetics of pseudomorphic mineral replacement reactions: A case study of the replacement of pentlandite by violarite. Geochimica et Cosmochimica Acta, 73, 1945-1969.

ZHAO, J., BRUGGER, J., CHEN, G., NGOTHAI, Y. & PRING, A. 2014a. Experimental study of the formation of chalcopyrite and bornite via the sulfidation of hematite: Mineral replacements with a large volume increase. American Mineralogist, 99, 343-354.

ZHAO, J., BRUGGER, J., NGOTHAI, Y. & PRING, A. 2014b. The replacement of chalcopyrite by bornite under hydrothermal conditions. American Mineralogist, 99, 2389-2397.

ZHAO, J., BRUGGER, J. & PRING, A. 2019. Mechanism and kinetics of hydrothermal replacement of magnetite by hematite. Geoscience Frontiers, 10, 29-41.

CHAPTER 5: THE COVELLITE DISSOLUTION UNDER ALKALINE CONDITION WITH GLYCINE SOLUTION

5.1 Introduction

The subject of covellite dissolution under acidic conditions has been extensively studied (see for examples Thomas and Ingraham, 1967, Dutrizac and MacDonald, 1974, Cheng and Lawson, 1991) and was briefly reviewed in Chapter 1 of the thesis. Ammonia- and EDTA-assisted covellite dissolution were investigated under alkaline conditions in some studies (Tomásek and Neumann, 1982, Baba et al., 2017). Both ammonia and EDTA are well-known complexing agents, however, they are not considered a economically viable options if used on an industry scale. Glycine has been widely used as a complexing agent in the dissolution of copper-bearing or gold-bearing minerals (O'Connor et al., 2018, Oraby and Eksteen, 2014, Tanda et al., 2017, Eksteen et al., 2017, Tanda et al., 2018, Tanda et al., 2019). However, glycine has only been used on the laboratory-scale, and none of these previous studies was focused on the kinetics and mechanisms of covellite dissolution.

5.1.1 Glycine

Glycine is an amino acid and consists of an amine group and a carboxyl group, with a neutral zwitterion form. When reacting with hydroxide ions, glycine can transfer to the glycinate anionic form by losing a proton or the glycinium cation form by gaining a proton under acidic condition (Streitwieser et al., 1992). Glycinate anions dominate at pH > 9.8. Only the zwitterion and glycinate anions of glycine will be considered in this study.

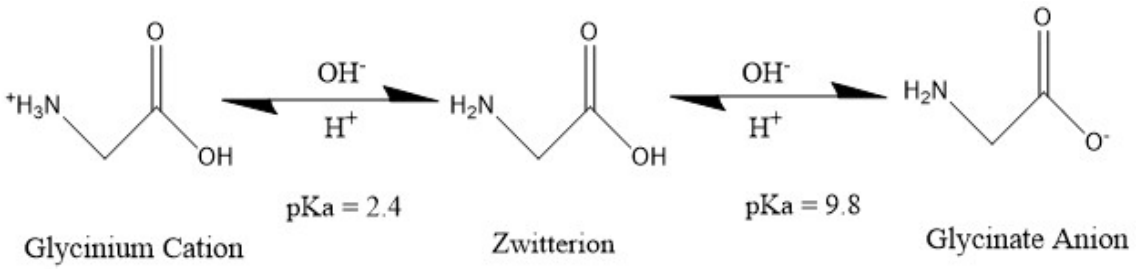

Figure 71 Equilibrium of glycine to glycinium cation and glycinate anion with different pKa (Aksu and Doyle 2001).

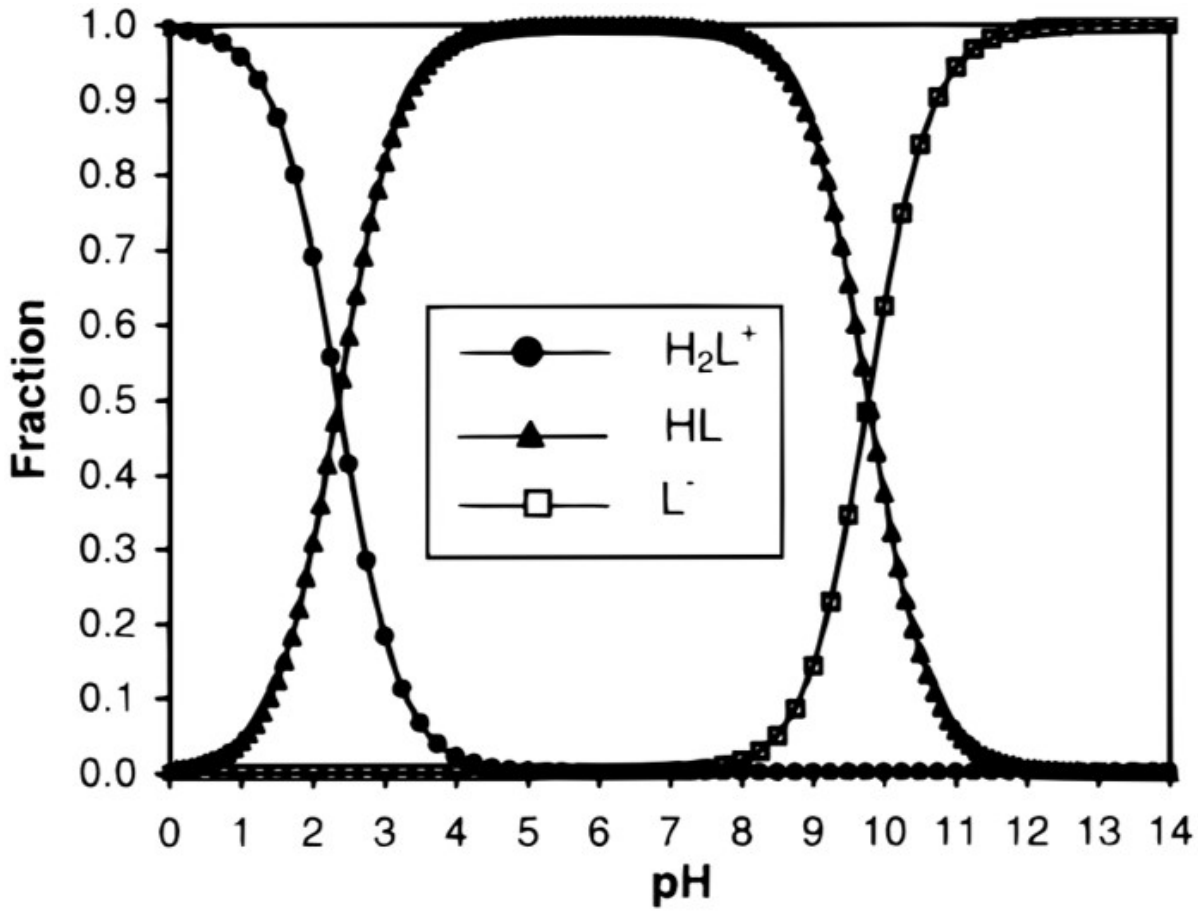

Figure 72 The proportion of glycine species at different pH in the glycine-water system. H_2L^+ is the glycinium cation form, HL is the zwitterion form and L^- is the glycinate anion form. Data are sourced from Aksu and Doyle (2001).

Chalcopyrite and chalcocite are dissolved with glycine under alkaline condition by forming stable Cu-glycinate complexes (Tanda et al., 2018, Tanda et al., 2019). It has been found the copper dissolution is strongly dependent on the glycinate anion concentration under alkaline conditions (Aksu and Doyle, 2001, Halpern et al., 1959, Pearlmutter and Stuehr, 1968). After dissolving glycine under alkaline conditions, the concentration of the glycinate anion can be determined using the Handerson-Hasselbalch equation with pKa constant and measured pH values.

$$pH = pKa + log\frac{[Gly^-]}{[HGly]} \quad (73)$$

Where *[Gly⁻]* is the concentration of glycinate ions, *[HGly]* is the concentration of glycine zwitterion form. Izatt et al. (1992) investigated the relationship between the temperature and the protonation of glycine in water in the temperature range of 25-75 °C. Their

experimental data showed that the pKa value of glycine zwitterion to glycinate anion decreases linearly with increasing temperatures. The pKa changes from 9.8 at 25 °C to 9.0 at 60 °C, suggesting that the higher temperatures are favourable for the formation of glycinate ions.

5.1.2 Formation of Copper Glycinate Complexes

Under alkaline conditions (pH>10), glycine can readily transfer from its zwitterion form to glycinate anions. It can form strong soluble glycinate complexes with Cu(II) ions, but Cu(I)-glycinate complexes only forms when the total glycine activity is much greater than the dissolved Cu activity in the copper-glycine-water system (Aksu and Doyle, 2001).

$$H_2NCH_2COOH + NaOH \rightarrow H_2NCH_2COO^- + Na^+ + H_2O \quad (74)$$

$$Cu^{2+} + H_2NCH_2COO^- \rightarrow Cu(H_2NCH_2COO)^+ \quad (75)$$

$$Cu^{2+} + 2H_2NCH_2COO^- \rightarrow Cu(H_2NCH_2COO)_2 \quad (76)$$

$$Cu^{+} + 2H_2NCH_2COO^- \rightarrow Cu(H_2NCH_2COO)_2^- \quad (77)$$

The zwitterion glycine concentration under alkaline condition is very low (Figure 72), limiting its buffering capability. Copper oxides are likely to form via equilibrium reactions of copper glycinate complexes as shown in Eqs. (78) and (79). These copper oxides form on the surface of copper or copper-bearing minerals, block active surface sites and inhibit the dissolution reaction. These species are insoluble in water and form a duplex layer to passivating on the surface of copper or copper minerals (O'Connor et al., 2018, De Chialvo et al., 1984, Kunze et al., 2004, Speckmann et al., 1985).

$$Cu(H_2NCH_2COO)_2 + H_2O \rightarrow CuO + 2H^+ + 2H_2NCH_2COO^- \quad (78)$$

$$2Cu(H_2NCH_2COO)_2 + 2H_2O + 2e^- \rightarrow Cu_2O + 2H^+ + 4H_2NCH_2COO^- \quad (79)$$

As described in Section 1.7, glycine has been in chalcopyrite and chalcocite leaching studies under alkaline conditions (Tanda et al., 2018, Tanda et al., 2019, Khezri et al., 2021, Shin et al., 2019a). Covellite was found as an intermediate product in the chalcocite dissolution study. Tanda et al. (2018) proposed a two-stages chalcocite dissolution mechanism as in Eqs. (80) and (81). However, the dissolution of covellite in alkaline

glycine solutions has yet to be examined. The aim of Chapter 5 was to investigate the mechanisms and kinetics of covellite dissolution, using alkaline glycine solutions, by investigating the roles of dissolved oxygen concentrations, stirring speed rates, pH values, glycine concentrations and temperatures of the reactions.

$$Cu_2S + 2NH_2CH_2COOH + 0.5O_2 \rightarrow Cu(NH_2CH_2COOH)_2 + CuS + H_2O \quad (80)$$

$$CuS + 2NH_2CH_2COOH + 2OH^- + 2O_2 \rightarrow Cu(NH_2CH_2COOH)_2 + SO_4^{2-} + 2H_2O \quad (81)$$

5.2 Methodology

5.2.1 Dissolution Experiments

The covellite dissolution experiments with alkaline glycine solution were carried out as described in Sections 2.2 and 2.3. Covellite sample (38-75 μm) was detailed described in Section 2.1 with Cu content of 67% based on the ICP-MS results after acid digestion of covellite sample. The general conditions of the covellite dissolution experiments are: 40 °C, pH 11, 250 rpm stirring speed and 0.5 M glycine in an air atmosphere. Based on previous studies on the dissolution of other copper sulphides, the dissolution rate is dependent on temperature, stirring speed, concentration of glycine and the concentration of dissolved oxygen in solution. One of these parameters varied in covellite dissolution experiment, while all other parameters remained constant. All conditions described in Table 27 were investigated to understand the covellite dissolution mechanism by glycine, and how the reaction rate is influenced by those key factors. The solid weight to liquid volume ratio was kept at 4 g/L (2 g covellite in 500 mL solutions), 5 mL of the solution collected at designed time intervals within 5 days while minimalizing the loss of mineral particles by using Millipore syringe filters (0.45 μm) for ICP-OES analysis. 5 mL of the fresh solutions were added to the reactor to keep the solid weight to liquid volume ratio constant. Solid residues were collected at the end of dissolution and stored under vacuum for XRD, SEM imaging and EDAX.

Table 27 Experimental conditions investigated in covellite dissolution experiments.

Factors	Conditions
Dissolving Oxygen Concentrations	Purged N_2, Purged Compressed Air, 0.02mol H_2O_2 and Air
pH	9, 10 and 11

Stirring Speed Rates	100, 250 and 500 rpm
Glycine Concentrations	0 M, 0.5 M, 0.75 M, 1 M and 1.5 M
Temperatures	25 °C, 35 °C,45 °C and 55 °C

5.2.2 Kinetic Models

It is important to note that the solid phase might be changed during the reactions between a solid and a fluid phase. The solid particles are likely to shrink during the reaction if no precipitate formed. Assuming the solid reactant is spherical and not porous, the fluid covers the surface of solid particle initially, with a mass transfer occurring between the solid and fluid. A product layer forms and surround the unreacted core of solid reactant as the reaction progressing. Equation 82 described the general reaction occurring in a shrinking core model (SCM) (Levenspiel, 1999, Li et al., 2013, Konishi et al., 1991, Tanda et al., 2019).

$$A(Fluid) + bB(solid) \rightarrow fF(fluid) + sS(solid) \quad (82)$$

The solid-fluid reaction would be under a pseudo-steady state when the reacting fluid concentration is in excess. The mineral dissolution rate is determined by one of following mechanisms: 1) diffusion though the fluid film on the surface of solid reactant, 2) diffusion through the ash or inert product layer, 3) chemical reaction between the fluid and the surface of the unreacted solid reactant. Equations (83), (84) and (85) described each of the reaction mechanism of shrinking core model. Each equation was used to fit the experimental data against time to determine the controlling step of the reaction mechanism. The controlling step of the covellite leaching process is expected to have a correlation coefficient closest to one (Tanda et al., 2018, Tanda et al., 2019). The SCM (Levenspiel, 1999) has been widely used in covellite leaching studies (Cheng and Lawson, 1991, Baba et al., 2017), and chalcopyrite and chalcocite leaching with glycine under alkaline condition (Tanda et al., 2018, Tanda et al., 2019).

Fluid film diffusion controlled: $k_l t = x$ (83)

Product layer diffusion controlled: $k_d t = 1 - 3(1-x)^{2/3} + 2(1-x)$ (84)

Chemical reaction controlled: $k_r t = 1 - (1-x)^{1/3}$ (85)

Where *x* is the volume fraction converted from solid particles, k_l, k_d and k_r are the apparent reaction rate constants for different controlling steps, and *t* is the time of reaction.

However, it also been found that the rate controlling step is very difficult to determine when the correlation coefficients obtained from each model equation are very similar (Feng et al., 2015, Sultana et al., 2014, Nazemi et al., 2011, Ekmekyapar et al., 2003). In the special case of the reaction rate controlled by multiple steps, Levenspiel (1999) suggesting that a combined equation of all possible controlled model equations can be used to determine the rate-limiting step. Sultana et al. (2014) used this method in the study of iron oxide leaching reaction in oxalic acid, which was initially found to be controlled by both diffusion through the product layer and chemical reaction on the surface of unreacted core. The combined model equation suggested that the diffusion-controlled process is the more dominant reaction step than another.

The activation energy of the covellite dissolution reaction can be estimated by the Arrhenius equation (Equation 86 and 87) by plotting the rate constant against temperature. *A* is a pre-exponential factor, *R* is the gas constant (equivalent to 8.314 $Jmol^{-1}K^{-1}$), *T* is temperature in kelvin, Ea is the activation energy (kJ/mol) (Levenspiel, 1999, Tanda et al., 2018, Tanda et al., 2019, Hidalgo et al., 2019). The enthalpy and entropy of the reaction were obtained from the Eyring equation (Equation 88 and 89) by plotting $T \times ln(k/T)$ against *T*, with calculation of ΔH++ from the intercept and ΔS++ from the slope (Lente et al., 2005, Hidalgo et al., 2019).

$$k = Ae^{(-\frac{E_a}{RT})} \quad (86)$$

$$lnk = lnA - \frac{Ea}{RT} \quad (87)$$

$$k = \frac{k_1 T}{h} e^{(-\frac{\Delta G^{++}}{RT})} \quad (88)$$

$$T \times \ln\left(\frac{k}{T}\right) = T \times \left[\ln\left(\frac{k_1}{h}\right) + \frac{\Delta S^{++}}{R}\right] - \frac{\Delta H^{++}}{R} \quad (89)$$

5.3 Results

5.3.1 SEM Imaging

The unreacted covellite surface, shown in Figure 73A, appeared to have a layered structure. It was rinsed and sonicated to minimise the presence of fine particles on the surface prior to dissolution experiments. Sharp-edged, finer mineral particles were formed and adhered to covellite surface after dissolution in alkaline glycinate solutions (Figure 73B, C and D). Khezri et al. (2021) also found the chalcopyrite particle sizes decreased significantly after leaching in a glycine medium.

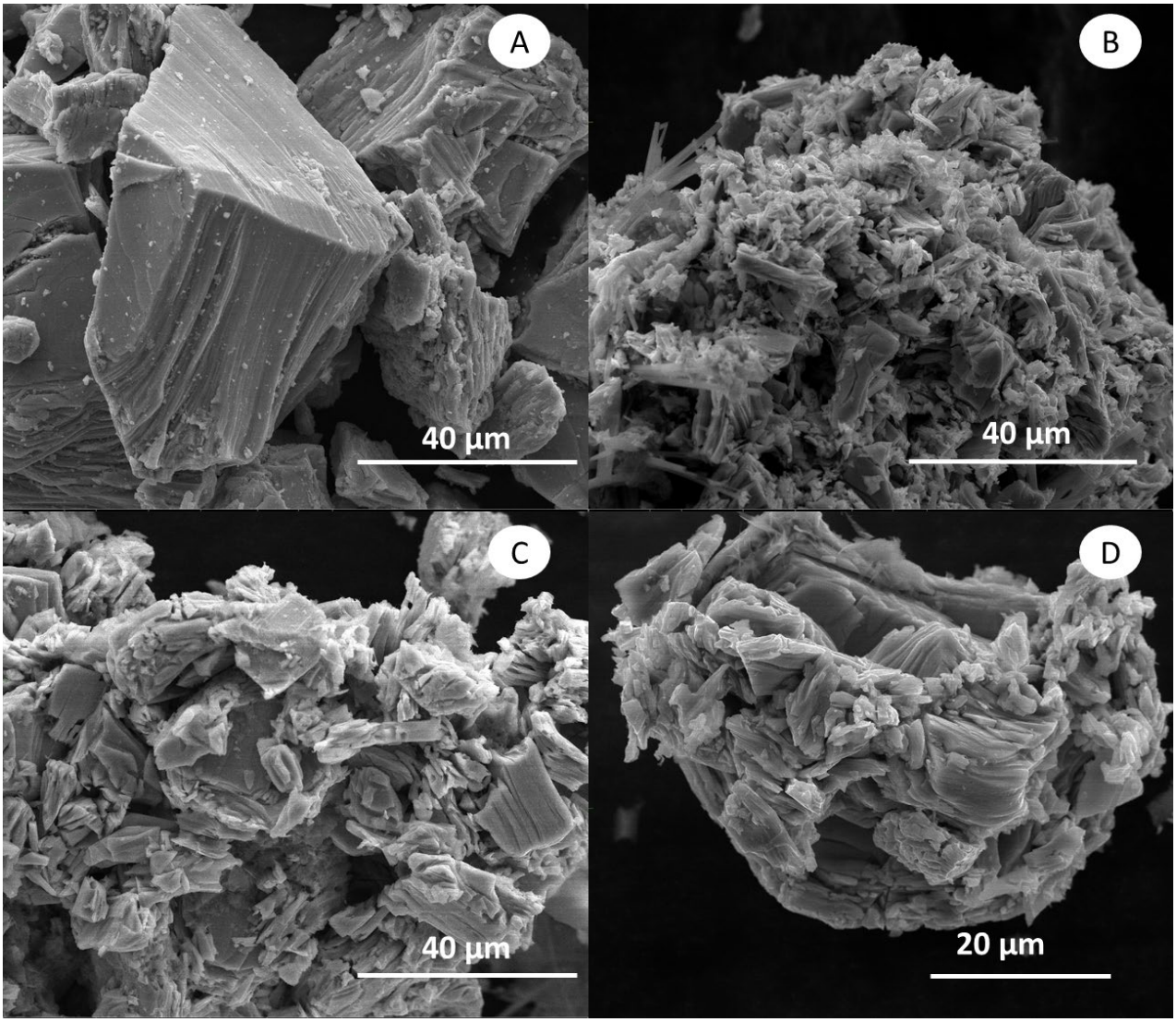

Figure 73 The SEM images of A) unreacted covellite; B) dissolution residues collected at pH 10, 40 °C with 0.5 M glycine after 128 h; C) dissolution residues collected at pH 11, 40 °C with 0.75 M glycine after 128 h and D) dissolution residues collected at pH 11, 40°C with 1 M glycine after 121 h.

5.3.2 Cu Extraction in Alkaline Glycine Solution

High Cu extraction from covellite results were obtained from dissolution in 0.5 M glycine under air atmosphere at pH 11. The covellite dissolution at 55 °C resulted in 19±2% of Cu extraction after 24 h; 29±3% after 48 h; and 57±5% after 120 h. This dissolution rate is comparable to those presented in two previous copper sulphide dissolution studies under similar conditions of temperature, particle size and glycine concentration, but faster than chalcopyrite (20% after 48 h at 50 °C) (Tanda et al., 2019) and slower than chalcocite dissolutions (50% after 48 h at 55 °C) (Tanda et al., 2018). Miki et al., (2011) showed the slow dissolution rate of synthetic covellite in HCl solution with Fe and Cu ions relative to chalcocite. The pH value of the dissolution solution decreased slightly as the reaction progressed, indicating that the concentration of hydroxide ions in the solution decreased with time.

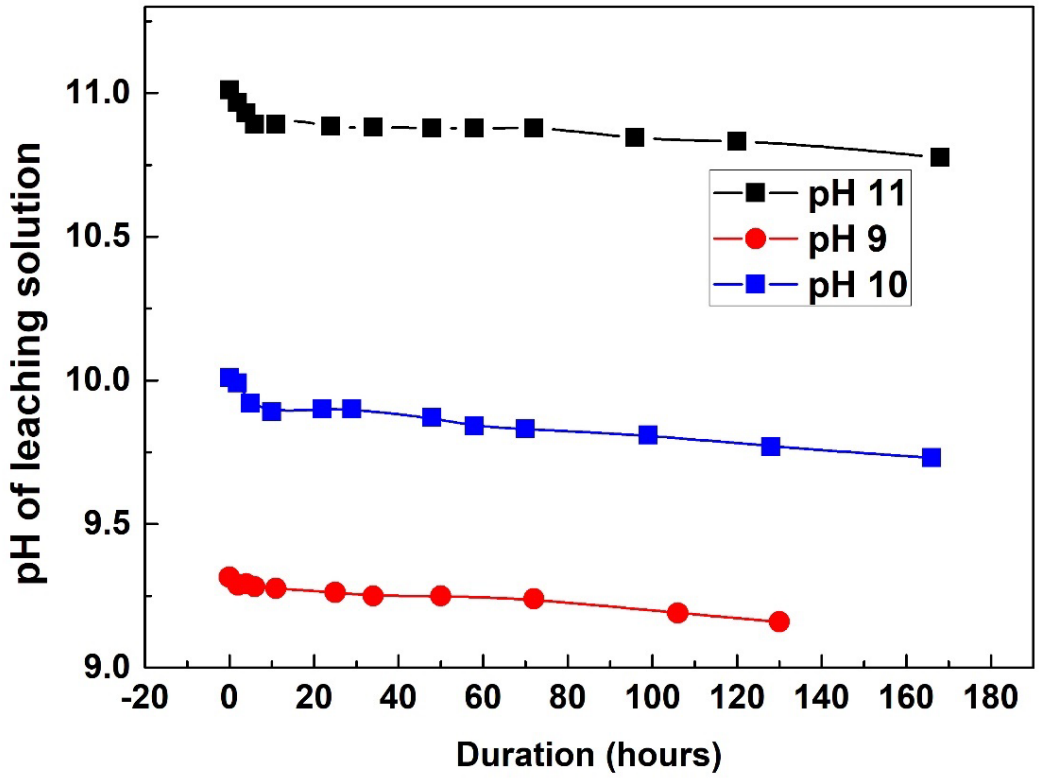

Figure 74 The pH value of the dissolution solution against reaction time. Solutions collected from pH 9, 10 and 11 0.5M glycine in atmospheric conditions.

5.3.3 Identification of Dissolution Residue

The XRD analysis indicated that the dissolution residues contained covellite, quartz, goethite, chalcopyrite and pyrite. Quartz, chalcopyrite and pyrite were from the impurities of the natural covellite sample as per Section 2.1. Goethite was formed by precipitation of the Fe (III) released from the dissolution of chalcopyrite. The formation of iron hydroxide during chalcopyrite dissolution has been previously reported (Tanda et al., 2019, Ghahremaninezhad Gharelar, 2012). SEM analysis found rod-like crystalline particles on the surface of residue collected at pH 10 (with 0.5 M glycine after 128 h). EDAX mapping data showed three areas with different elemental compositions represented by yellow, blue and red pixels. Each yellow pixel containing atomic percentage of 25% O, 10% S, 23% Fe and 42% Cu, suggesting the presence of Fe oxides or hydroxides on the surface. In areas indicated by the blue and red pixels, the elemental compositions were 16% O, 26% S, 1% Fe and 57% Cu (for the blue pixels), and 4.4% O, 13% S, 0.04% Fe and 84% Cu, suggesting that copper sulphides were the dominant mineral phase on the surface of residues. A very small amount of copper oxides might be formed in covellite surface but was not detected by XRD. No copper-glycinate complexes were observed as precipitates formed on the surface of covellite as no nitrogen was detected by EDX.

Table 28 Elemental compositions of species formed on the surface of residues collected from dissolution reaction.

	O (wt. %)	**S (wt. %)**	**Fe (wt. %)**	**Cu (wt. %)**
Yellow pixels	25	10	23	42
Blue pixels	16	26	1	57
Red pixels	4	13	0	83

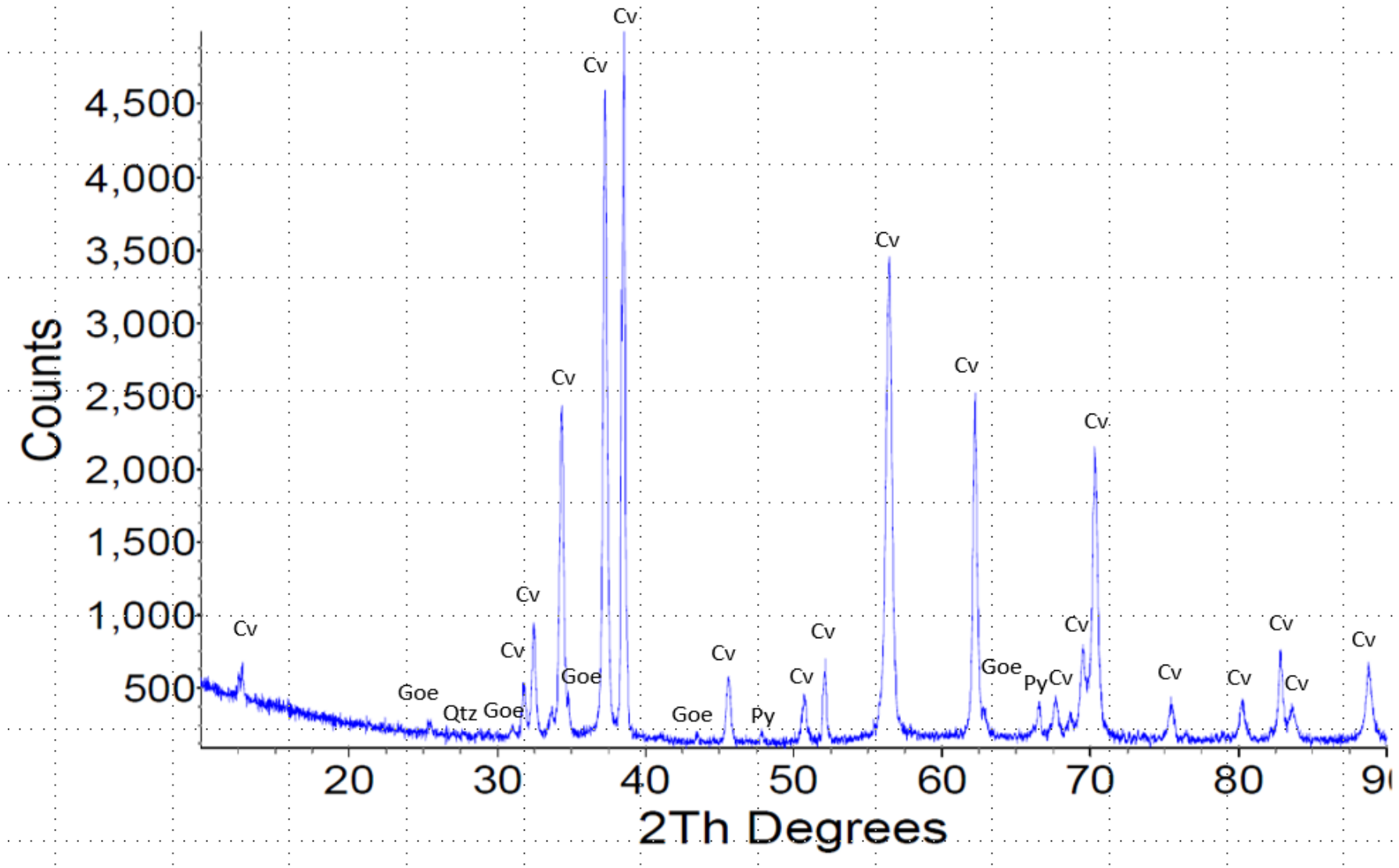

Figure 75 The XRD pattern of covellite dissolution residue collected at 128 h from dissolution experiment at pH 11 in the presence of 0.75 M glycine

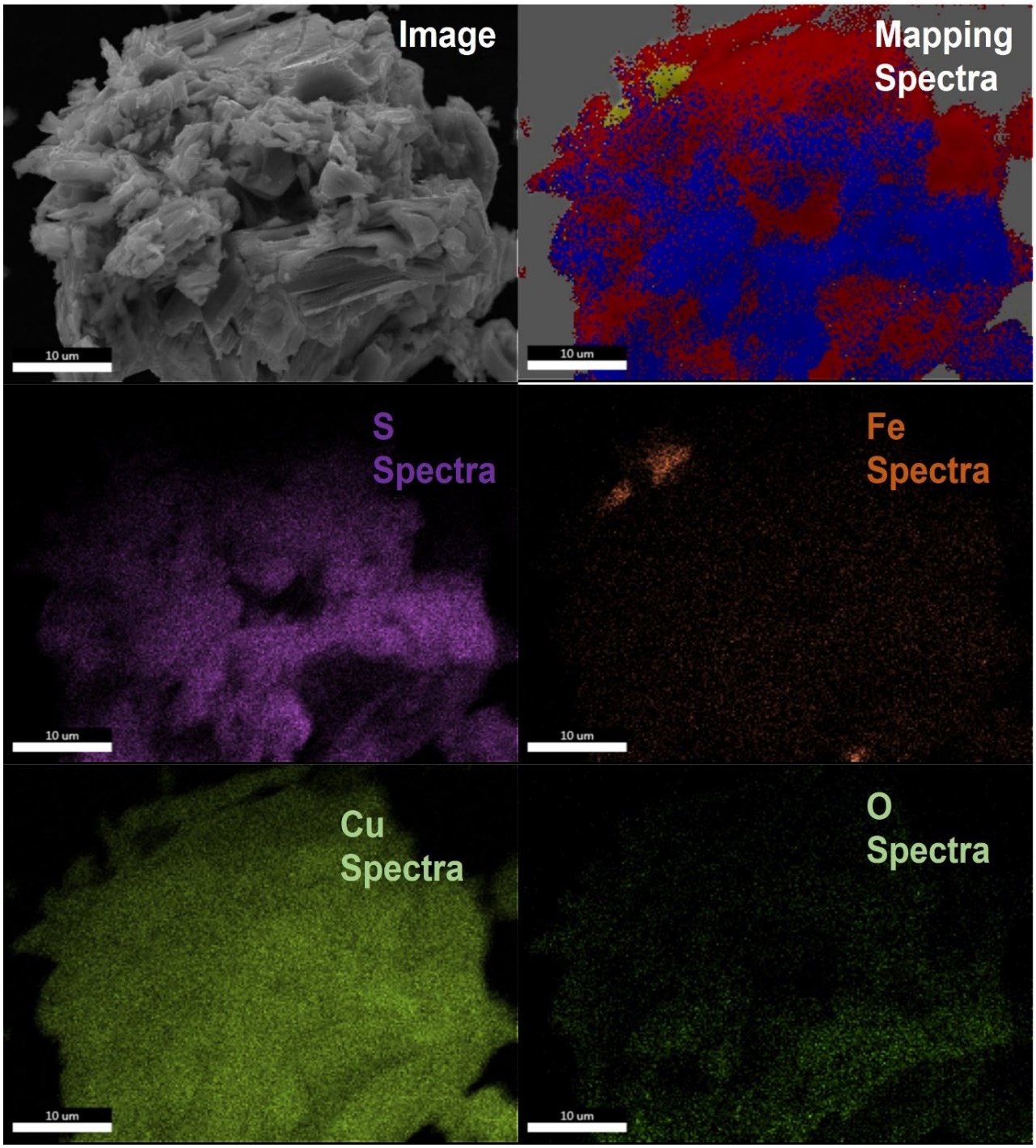

Figure 76 The EDAX elemental mapping of SEM image collected on residue collected from experiments at pH 10, 0.5 M glycine after 128 h of reaction.

5.3.4 Effect of Temperature

The effect of temperature on covellite dissolution was investigated under the conditions of 25 to 55 °C, with 0.5 M glycine and pH 11. Figure 77 shows that the rate of covellite dissolution in alkaline glycine solutions increases with increasing temperature. After 24 h of reaction, the Cu extracted from covellite at 55 °C dramatically increased (19±2%), about

2.5 times more than those at 35 °C (6±1%) and 45 °C (7±1%) and 4 times more than that at 25 °C (3.5±1%). Only 17±2% of covellite was dissolved after 129 h of dissolution reaction at 25 °C. After 131 h of reaction, 27±3% of covellite dissolved in an alkaline glycinate solution at 35 °C and 32±3% at 45 °C. When the temperature was elevated to 55 °C, 29±3% of covellite was dissolved within 48 h in solution, and 57±5% of reaction extent was achieved after 124 h of reaction.

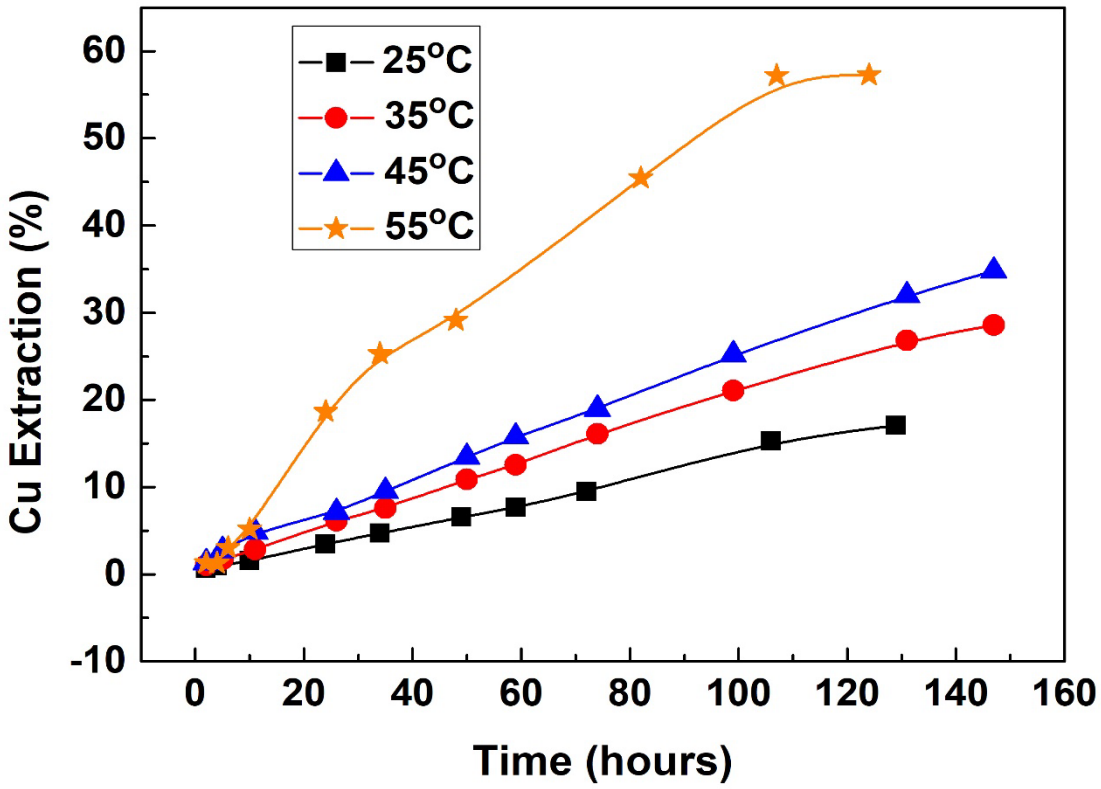

Figure 77 The effect of temperature on covellite dissolution: pH 11, 0.5 M glycine, 250 rpm, air atmosphere, 38-75 µm, 4 g/L solid weight to liquid volume ratio. Estimated errors are ±10%.

5.3.5 Effect of Glycine Concentration

The effect of glycine concentration on the covellite dissolution kinetics was studied at the different glycine concentrations of 0 (i.e. no glycine) to 1.5 M. 38-75 µm covellite grains were used for all dissolution experiments. The conditions of experiment were fixed at the stirring speed of 250 rpm, 40 °C, pH 11 and in air (Figure 73). Without glycine, almost no Cu (only 0.05%) was extracted from covellite after 130 h, suggesting covellite cannot be dissolved in alkaline solution without glycine. In comparison, the dissolution rate at all glycine concentrations were very similar within 48 h, with approximately 11±1% of Cu

extracted from covellite after 48 h. After 58 h, the dissolution rate is decreased as the glycine concentration increased. 0.5 M glycine concentration was selected for other covellite dissolution experiments to investigation the effects of other parameters, including solution pH, temperature and concentration of dissolved oxygen.

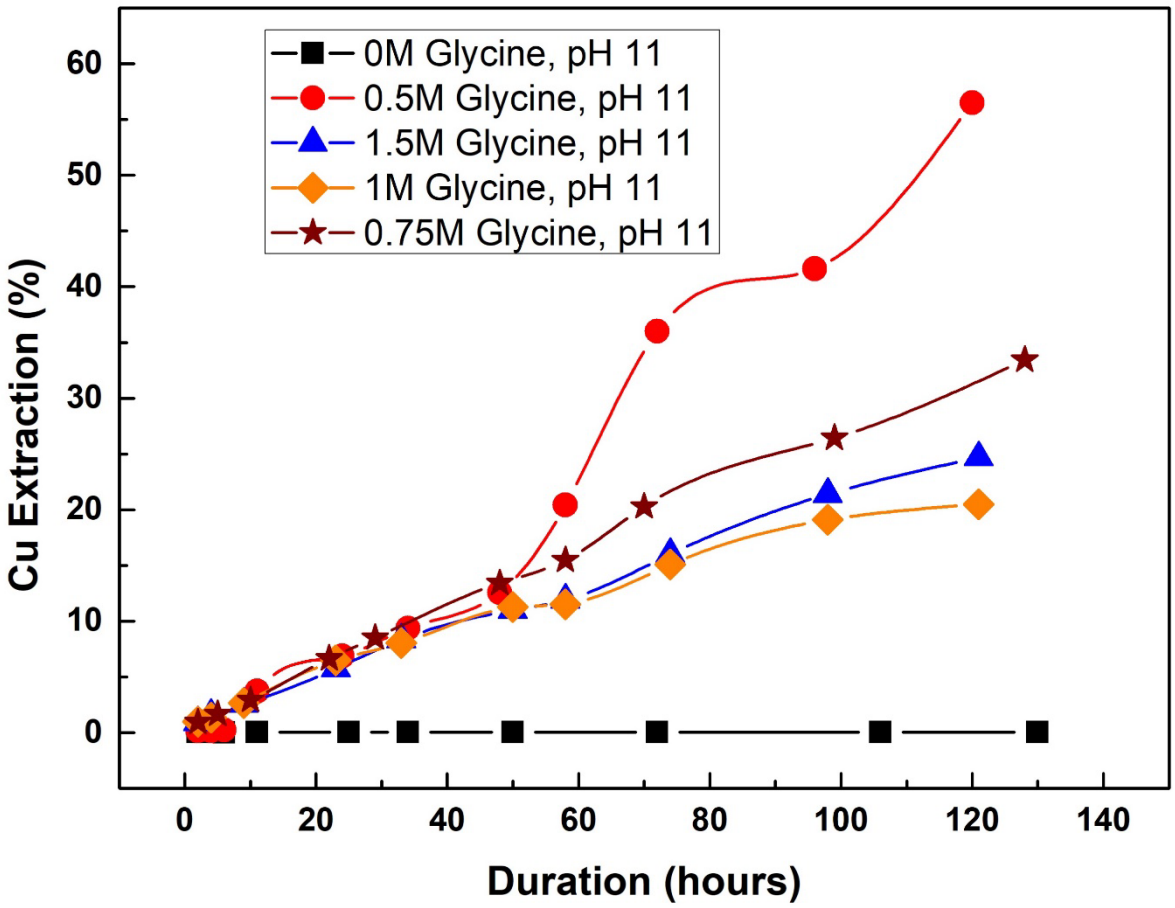

Figure 78 The effect of glycine concentration on covellite dissolution: pH 11, 40 °C, 250 rpm, air atmosphere, 38-75 μm, 4 g/L solid weight to liquid volume ratio. Estimated errors is ±10%.

5.3.6 Effect of pH

The effect of pH on the covellite dissolution rates was investigated at pH 9-11. Cu was successfully extracted from covellite with 0.5 M glycine from the pH range of 9 to 11. The dissolution rate at pH 9 is the slowest, only 10±1% of Cu was dissolved into solution from covellite after 130 h. At pH 10 and pH 11, dissolution rates were very similar before 48 h, but dissolution rate at pH 11 increased rapidly after 58 h. After 120 h, 57±5% of Cu were extracted from covellite dissolution at pH 11, approximately 1.7 times and 4.4 times more

than those at pH 10 and pH 9. The results indicates that covellite dissolution with glycine solutions is faster under more alkaline conditions.

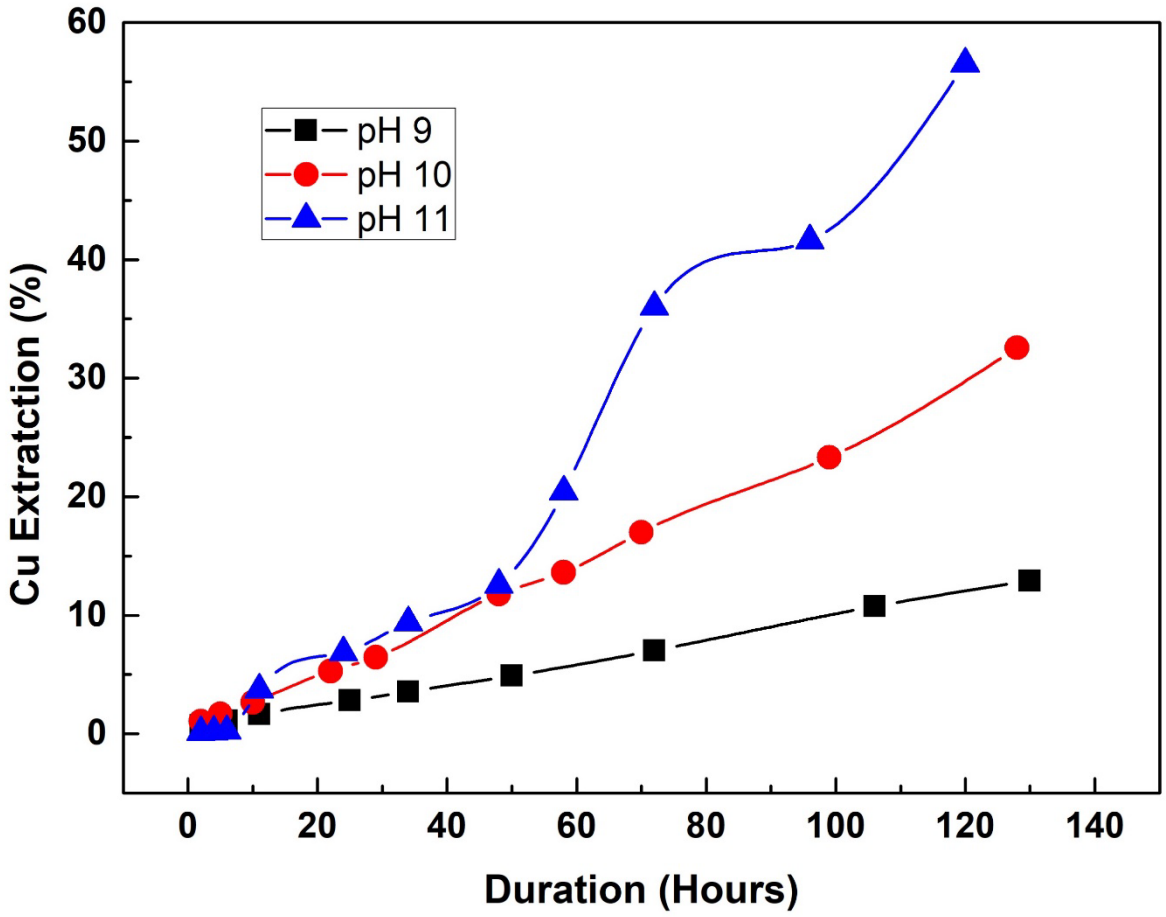

Figure 79 The effect of pH on covellite dissolution: 40°C, 0.5 M glycine, 250 rpm, air atmosphere, 38-75 μm, 4 g/L solid weight to liquid volume ratio. Estimated errors are ±10%.

5.3.7 Effect of Dissolved Oxygen

The effect of dissolved oxygen in solution was studied by purging compressed air or N_2 or adding hydrogen peroxide. The other parameters for the experiment were maintained at 40 °C, 0.5 M glycine, pH 11, 250 rpm stirring speed. The dissolution rate in the solution purged with N_2 gas is the slowest, only 7% of Cu recovered from covellite after 129 h. It indicates that the covellite dissolution in alkaline glycine solution is inhibited due to the lack of oxygen. With the addition of 0.02 mol of H_2O_2, the Cu extraction was rapidly increased after 2 h dissolution and remained constant for 24 h. The dissolution rate is slower than

those for the experiments purged with compressed air and without addition of H_2O_2 after 24 h.

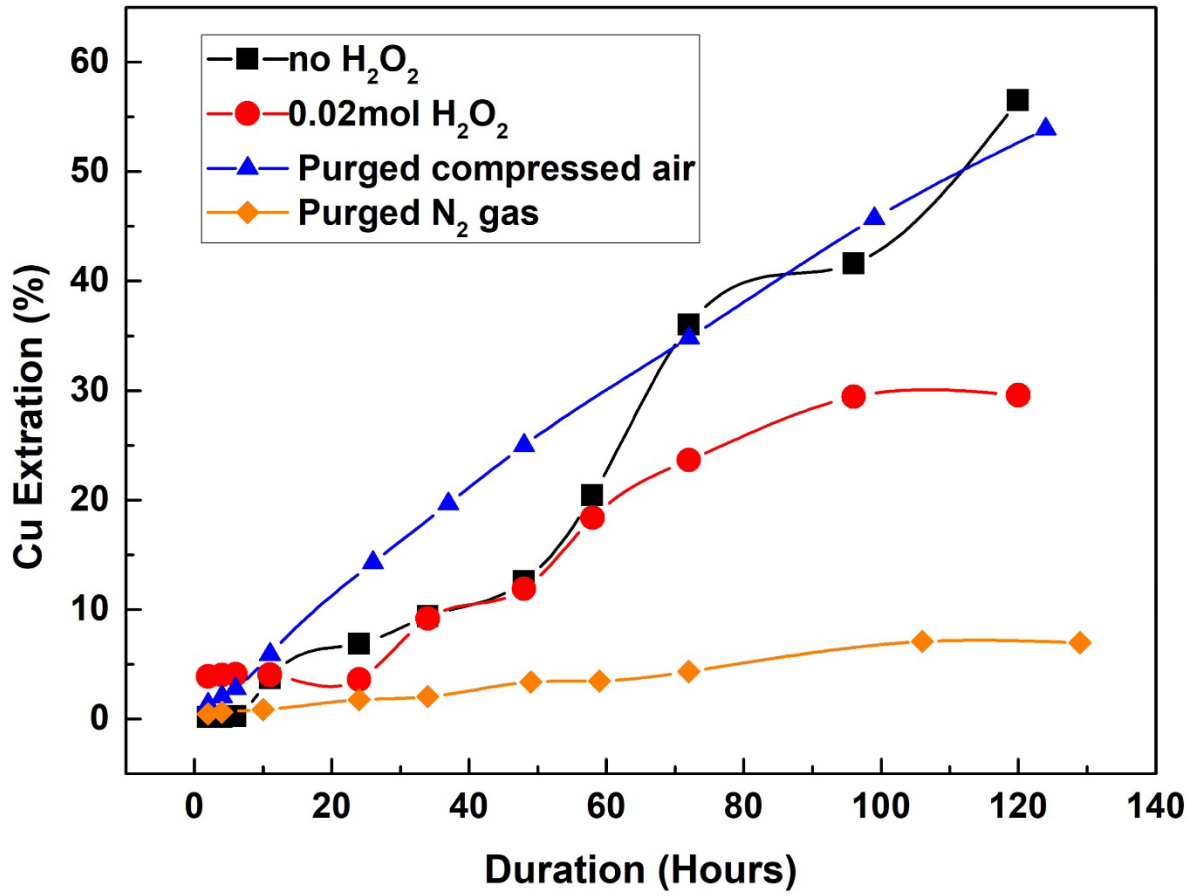

Figure 80 The effect of dissolving oxygen in solution on covellite dissolution: pH 11, 40 °C, 0.5 M glycine, 250 rpm, 38-75 µm, 4 g/L solid weight to liquid volume ratio. Estimated errors are ±10%.

5.4 Discussion

5.4.1 Proposed Mechanism

The effects of glycine concentration and pH indicates the covellite dissolution requires glycine and hydroxide ions. Glycine was dissociated with hydroxide ions, which forms glycinate (I) ions and water as equation (90). The dissociation between glycine and hydroxide ions is under equilibrium state, and it favours to the production of glycinate ions at pH above the pKa value (pKa value = 9.8) as illustrated in Figure 72 (Aksu and Doyle, 2001). Covellite was dissolved by the glycinate ions with oxidants (dissolving oxygen) and forms a water-soluble, stable copper-glycinate complex as per equation (92) (Aksu and Doyle, 2001, Shin et al., 2019b, Eksteen et al., 2017, Tanda et al., 2018, Tanda et al., 2017, Tanda et al., 2019).

$$NH_2CH_2COOH_{(aq)} + OH^-{}_{(aq)} \leftrightarrow NH_2CH_2COO^-{}_{(aq)} + H_2O_{(aq)} \quad (90)$$

$$NH_2CH_2COO^-{}_{(aq)} + Cu^{2+}{}_{(aq)} \leftrightarrow Cu(NH_2CH_2COO)_{2(aq)} \quad (91)$$

$$CuS_{(s)} + 2NH_2CH_2COO^-{}_{(aq)} + 2O_{2(aq)} \rightarrow Cu(NH_2CH_2COO)_{2(aq)} + SO_{4(aq)}^{2-} \quad (92)$$

The change of the solution pH indicates the covellite dissolution is consuming hydroxide ions as the reaction proceeds. This is because the formation of copper-glycinate complexes from covellite dissolution (equation 92) reduces the amount of glycinate ions in the solution. Hydroxide ions reacted with glycine, forming more glycinate ions in order to re-establish the equilibrium state and maintain the dissolution reaction as equation (90) (Aksu and Doyle, 2001), and decreases the pH of the solution during the reaction, as shown in Figure 74.

The experimental results of oxygen availability suggest the increasing dissolving oxygen concentration increases the rate of covellite dissolution. The alkaline glycinate solution was purged with N_2 gas for 30 mins prior to dissolution experiment, resulting less dissolved oxygen concentration (approximately 0 ppm) than under an air atmosphere. Covellite dissolution rate was significantly reduced with less dissolved oxygen in solution. Dissolution experiments with N_2 purging indicated that covellite might be dissolved under anaerobic condition in alkaline glycine solution. The experimental setups were not completely sealed and could not be ensure all dissolved oxygen in solution completely removed. Improved experimental settings would be required to ascertain whether covellite

dissolved by alkaline glycinate solution under anaerobic condition. The covellite dissolution without purging of compressed air is fluctuate, rather than a steady increasing trend as experiments with compressed air (Figure 80). This is because covellite dissolution consumed the dissolved oxygen from the solution and needs time to re-dissolve the oxygen from air atmosphere in solution (Figure 80). On the contrary, the dissolution rate is very steady with continuing purged with compressed air, indicating that sufficient new oxygen is dissolving into the solution and allows the reaction to continue (Figure 80). The overall covellite dissolution equation under alkaline glycine solutions is described by equation (93). Tanda (2018) found covellite formed as an intermediate product from the chalcocite dissolution under alkaline glycine solution, and they proposed the same 2nd stage covellite dissolution reaction equation.

$$CuS_{(s)} + 2NH_2CH_2COOH_{(aq)} + 2OH^-{}_{(aq)} + 2O_{2(aq)} \rightarrow Cu(NH_2CH_2COO)_{2(aq)} + SO^{2-}_{4(aq)} + 2H_2O_{(aq)} \quad (93)$$

5.4.2 Kinetic Model

Assuming the covellite grains are spherical, the rate limiting steps during the dissolution reaction can be determined using the shrinking core model. The experimental results of each variable were used to fit each equation. The rate limiting step is the kinetic model with best fit (R^2 closest to 1). The correlation coefficients (R^2) values of fitted data of the covellite dissolution are included in Table 29. According to the R^2 values in Table 29, the covellite dissolution in alkaline glycine solutions is most likely to be controlled by diffusion through fluid film as the R^2 values are closest to 1.

The Arrhenius plots were made by plotting by *lnk* against 1/T using the reaction rate constant from the kinetic equation for diffusion through fluid film. The activation energy of covellite dissolution in alkaline glycine solution is estimated to be 33±7 kJ/mol. It is well known that systems with activation energy greater than 40 kJ/mol are chemical controlled reaction while with activation energy smaller than 40 kJ/mol are transport-controlled (Levenspiel, 1999). The activation energy suggests the covellite dissolution with glycine is transport-controlled reaction, which is similar to the controlling step from SCM. Similar covellite dissolution studies conducted with different reagents are also found to be transported-controlled reaction, such as Baba et al. (2017) with an E_a of 37 kJ/mol, Tomásek and Neumann (1982) with an E_a values of 18 and 19 kJ/mol. Chalcopyrite (<10 μm) dissolution in alkaline glycine solutions reported similar activation energy of 30 kJ/mol

(Tanda et al., 2019). The activation enthalpy and entropy of the covellite dissolution were obtained from the Eyring equation (Lente et al., 2005, Hidalgo et al., 2019) using the rate constant from diffusion through fluid film-controlled model. The calculated enthalpy and entropy values are 31 kJ/mol and -284 $Jmol^{-1}K^{-1}$, respectively.

Table 29 The correlation coefficient resulting from the shrinking core model.

Variables	**The correlation coefficient, R^2**		
	Diffusion through film control	**Diffusion through product layer control**	**Chemical reaction control**
	$kt = x$	$kt = 1 - 3(1-x)^{\frac{2}{3}} + 2(1-x)$	$kt = 1 - (1-x)^{\frac{1}{3}}$
Air	0.9636	0.7861	0.9517
0.02mol H2O2	0.971	0.9166	0.9728
Purged with compressed air	0.9949	0.9305	0.9998
Purged with N_2	0.9871	0.9118	0.9875
Solution pH			
pH 9	0.9981	0.9096	0.9967
pH 10	0.9957	0.995	0.8467
pH 11	0.9636	0.7861	0.9517
Temperature (°C)			
25	0.9947	0.8945	0.9934
35	0.9970	0.9346	0.9984
45	0.9976	0.9297	0.9831
55	0.9653	0.9608	0.9917
Glycine concentration			
1.5M	0.9958	0.9195	0.9977
1M	0.9767	0.9648	0.9876
0.75M	0.9972	0.9053	0.9993
0.5M	0.9636	0.7861	0.9517

Reaction rate constants used to determine empirical rate law were obtained from experimental data fitted the kinetic equation for diffusion through fluid film controlled. K_d value obtained from different experimental variables including glycine concentration [*Gly*]

and hydroxide ions concentration [OH^-] (or pH) for covellite dissolution were used to determine an empirical rate law model in air atmosphere using the plots of *lnKd* versus *ln[Gly]* and *ln[OH^-]*. *A* is derived from the intercept from the *Arrhenius* equation (Figure 82). The slope of each linear equation represents the estimated reaction order of each experiment variable respectively. The reaction order of *[Gly]* and *[OH^+]* were -0.82 and -0.35 respectively. The empirical model of dissolution of covellite dissolution in the presence of glycine under air atmosphere can be represented by Eq. (94).

$$x = k_d t = \{757[Gly]^{-0.82}[OH^-]^{-0.35} exp^{\frac{33}{RT}}\}t \quad (94)$$

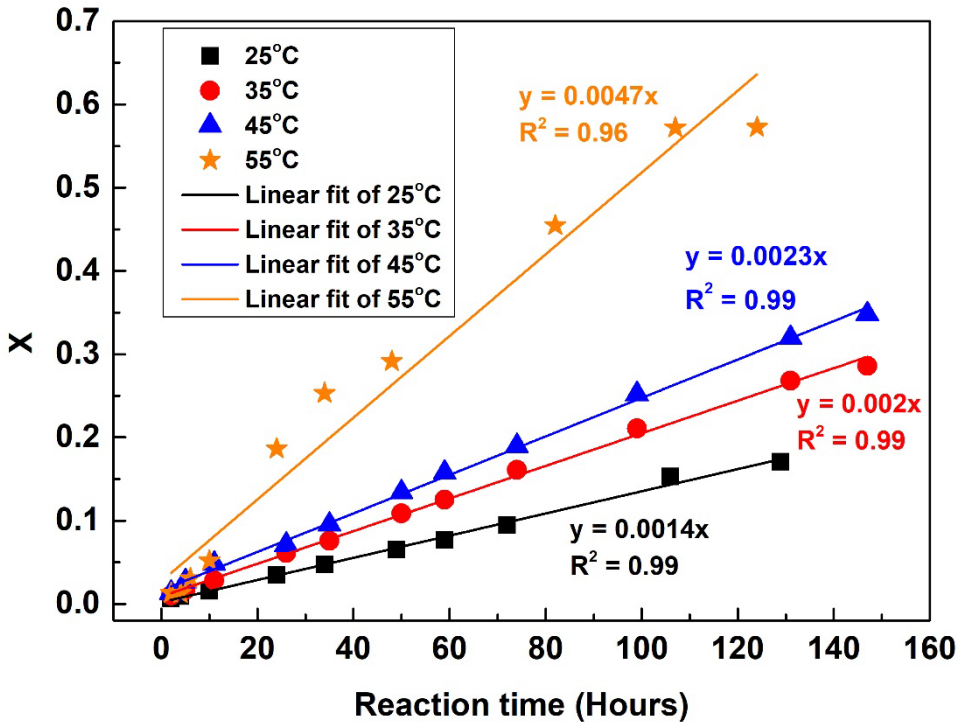

Figure 81 Plot of X vs. dissolution time at different temperatures, where X is the fraction of covellite dissolved. (0.5 M glycine, stirring speed 250 rpm and pH 11).

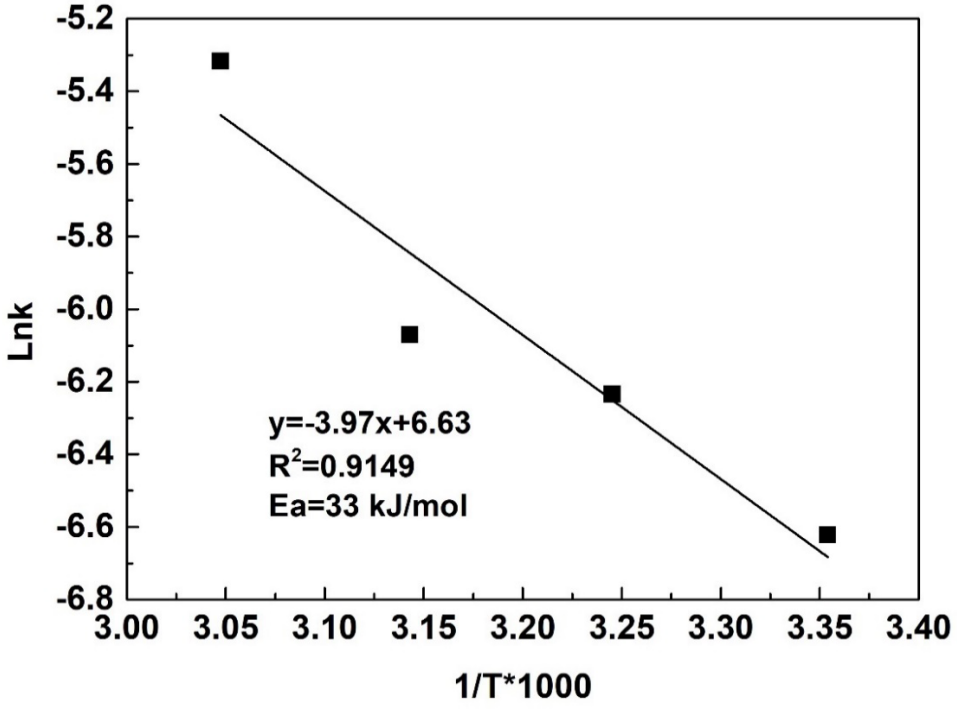

Figure 82 Arrhenius plot for diffusion through fluid film-controlled dissolution of covellite in alkaline glycine solution.

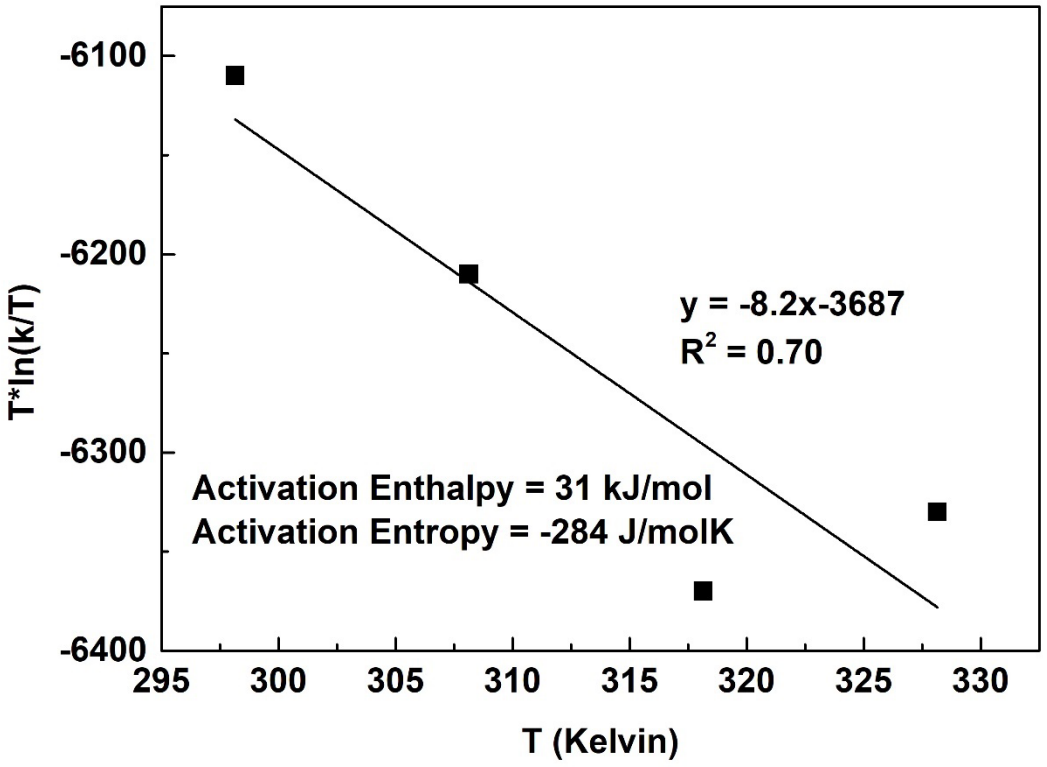

Figure 83 Activation enthalpy and entropy of covellite dissolution determined by Eyring plot using reaction rate constant from kinetic equation for diffusion through fluid film.

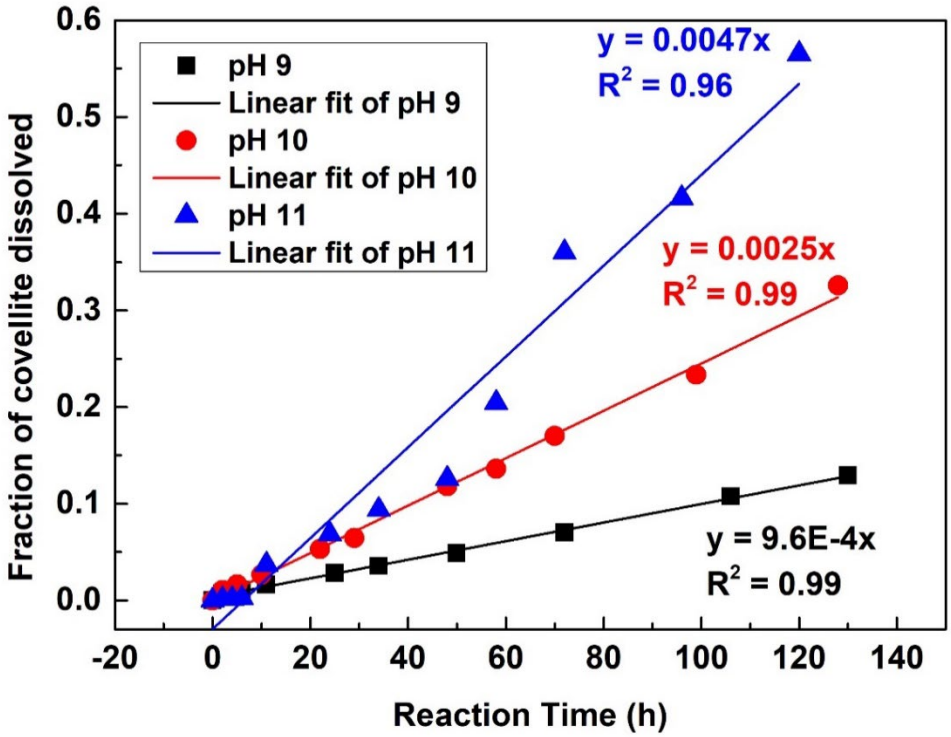

Figure 84 Plot of X vs. dissolution time at different solution pH, where X is the fraction of covellite dissolved. (0.5 M glycine, stirring speed 250 rpm and 40 °C)

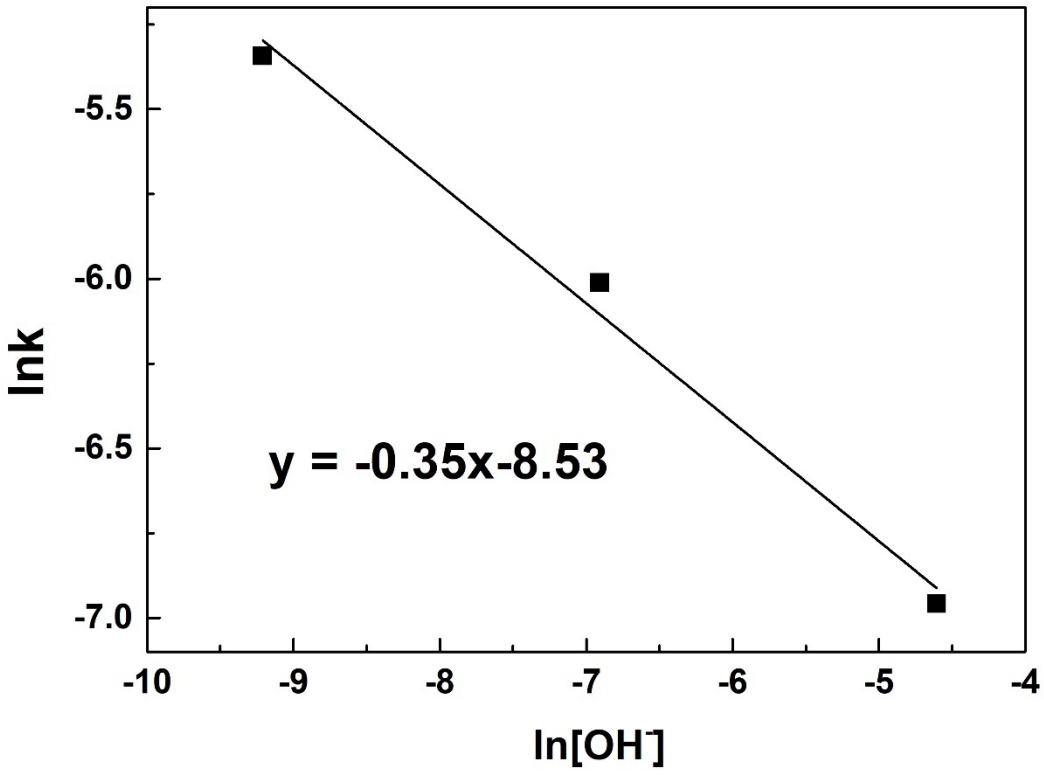

Figure 85 Plot of dissolution rate constant as a function of hydroxide ion concentration.

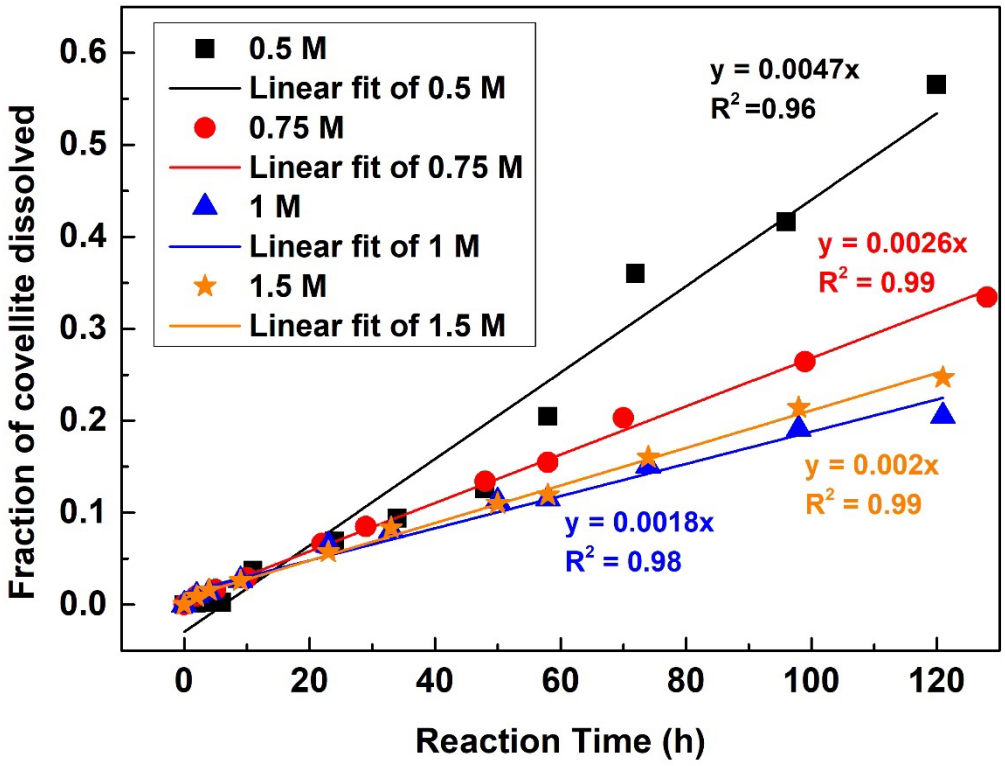

Figure 86 Plot of the fraction of covellite dissolved vs. dissolution time at different concentration of glycine. (pH 11, stirring speed 250 rpm and 40 °C)

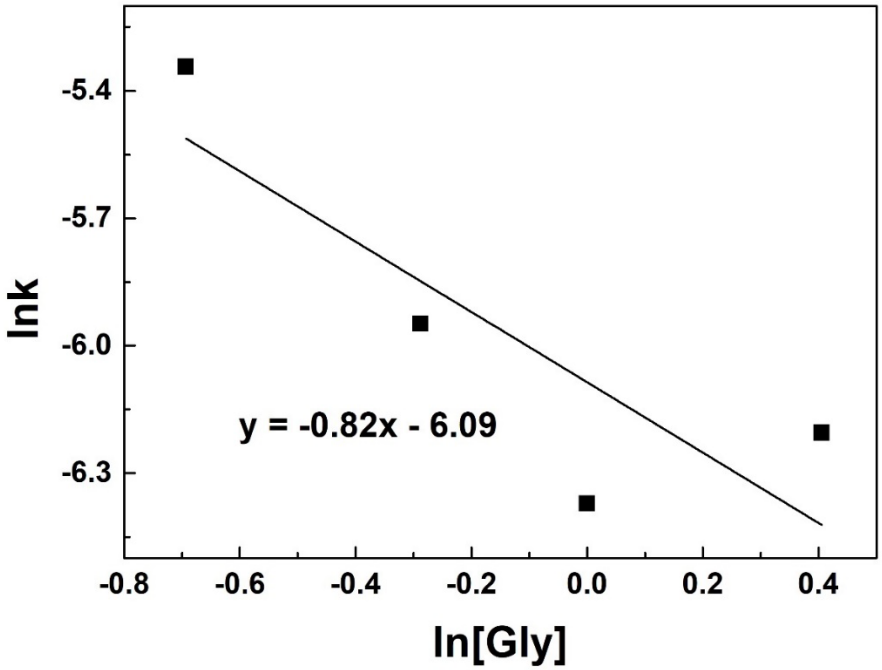

Figure 87 Plot of dissolution rate constant as a function of glycine concentration.

Table 30 Summary of copper sulphides dissolution under alkaline condition.

Material	Reagents	Temperature range, °C	Ea (kJ/mol)	Author
Covellite	Glycine	25-55	33	Present study
Chalcocite	Glycine	25-55	25 1st stage 108 2nd stage	(Tanda et al., 2018)
Chalcopyrite (20-38 µm)	Glycine	40-70	72	(Tanda et al., 2019)
Chalcopyrite (<10 µm)	Glycine	30-60	30	(Tanda et al., 2019)
Covellite	Ammonia Sulphate	25-75	37	(Baba et al., 2017)
Chalcocite	Na_4EDTA	65-94	38	(Konishi et al., 1991)
Covellite	EDA	20-60	19	(Tomásek and Neumann, 1982)
Covellite	EDTA	20-60	18	(Tomásek and Neumann, 1982)
Chalcocite	EDTA	20-60	30	(Tomášek and Neumann, 1982)

The modified ‘time to given fraction method’ was used to determine the activation energy at different reaction extents. As the final solution collected at 25 °C only dissolved 17% of covellite, the results collected from all dissolution temperatures were used to determine the activation energy in the reaction extent range of 0-5%, 5-10% and 10-15%. Data collected at 35-55 °C were used to calculate the activation energy of 15-20% and 20-25% reaction progresses. The activation energies at different reaction extent are shown in Figure 87. The activation energy increased from 40 to 63 kJ/mol when the reaction extent increased from 0 to 20%, and then decreased to 50 kJ/mol at the reaction extent of 20-25%. It is slightly higher than the activation energy calculated using the shrinking core model. It suggests that the covellite dissolution reaction is a transport-controlled reaction between 0-25% reaction extent. However, the R^2 value of the linear regression of natural logarithm of reaction extent is very low and the fitting is poor. Therefore, the change of E_a at different reaction extent may be not true.

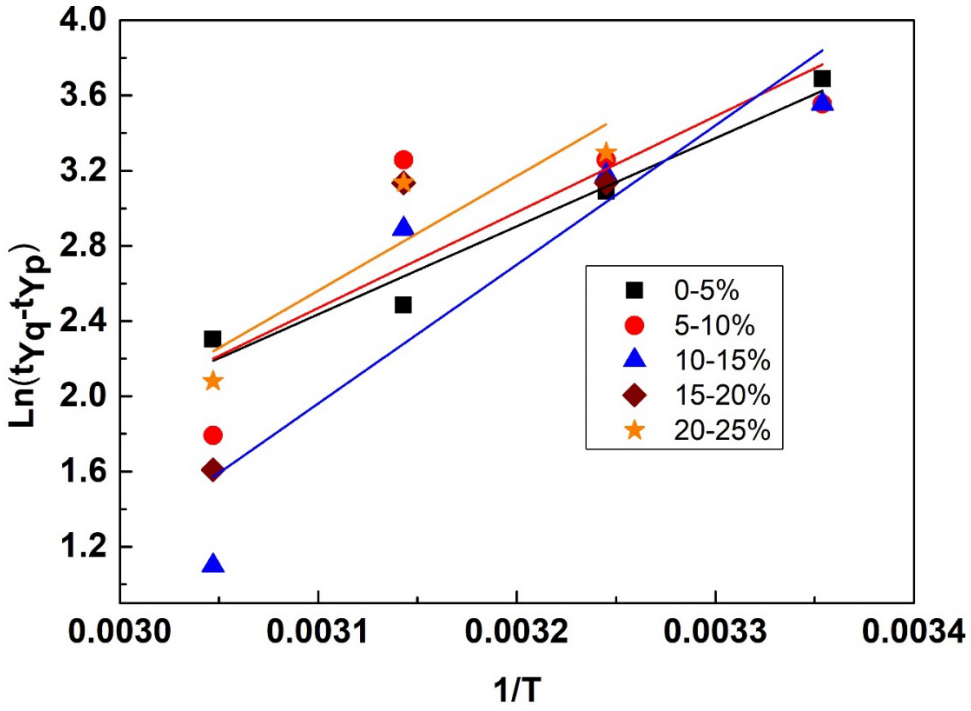

Figure 88 The linear relationship of natural logarithm of different reaction extent against 1/T.

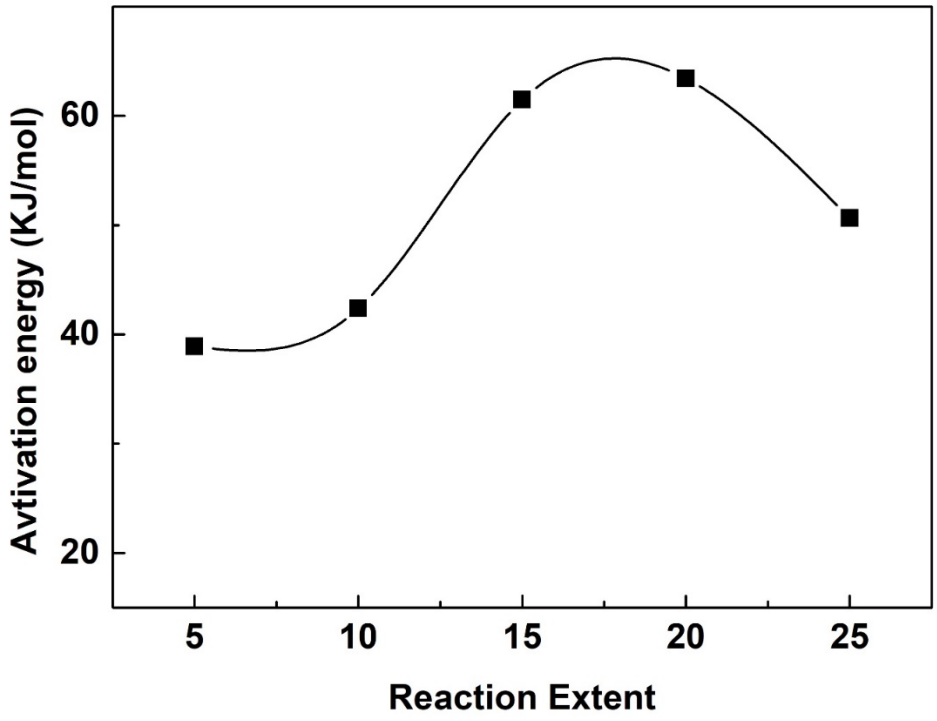

Figure 89 The change of activation energy at different reaction extent of covellite dissolution.

5.5 Conclusion

Covellite dissolution in the presence of glycinate anions at low temperatures (25-55 °C) was systematically studied under various conditions. The parameters include temperature, glycine concentration, solution pH and the concentration of dissolved oxygen. The covellite dissolution is accelerated in the presence of glycine under alkaline condition, forming water soluble Cu-glycinate complexes. 57±5% of covellite was dissolved at pH 11 and 55 °C with 0.5 M glycine after 107 h. At room temperature (25°C), 17±2% of covellite was dissolved after reaction of 129 h at pH 11 with 0.5 M glycine. The covellite dissolution rate increased as increasing temperature (25-55 °C), increasing concentration of dissolving oxygen, and increasing solution pH (pH 9-11). Experimental results show constantly increasing Cu concentrations and close to a linear relationship as the covellite dissolution processing.

Shrinking core models were used to determine the kinetics of covellite dissolution. Results indicates that the reaction is controlled by diffusion. *Arrhenius* equation gave an activation energy of 33±7 kJ/mol for the dissolution process. *Eyring* plot suggests that the activation enthalpy and entropy of the dissolution reaction were 31 kJ/mol and -284 $Jmol^{-1}K^{-1}$, respectively. The reaction order for glycine concentration and hydroxide ion concentration were -0.82 and -0.35, respectively. The modified 'time to a given fraction method' showed an increasing activation energy from 40 kJ/mol (0-5% covellite dissolved) to 63 kJ/mol (10-15% covellite dissolved), then decreased to 50 kJ/mol at 20-25% reaction extent.

5.5 Reference List

AKSU, S. & DOYLE, F. M. 2001. Electrochemistry of copper in aqueous glycine solutions. Journal of the Electrochemical Society, 148, B51.

BABA, A. A., BALOGUN, A. F., BALE, R. B., ADEKOLA, F. A. & ALABI, A. G. 2017. Treatment of a Nigerian covellite ore. Part I: Dissolution kinetics study by ammonia solution. Russian Journal of Non-Ferrous Metals, 58, 1-7.

CHENG, C. Y. & LAWSON, F. 1991. The kinetics of leaching covellite in acidic oxygenated sulphate-chloride solutions. Hydrometallurgy, 27, 269-284.

DE CHIALVO, M. G., MARCHIANO, S. & ARVIA, A. 1984. The mechanism of oxidation of copper in alkaline solutions. Journal of applied electrochemistry, 14, 165-175.

DUTRIZAC, J. & MACDONALD, R. 1974. The kinetics of dissolution of covellite in acidified ferric sulphate solutions. Canadian metallurgical quarterly, 13, 423-433.

EKMEKYAPAR, A., OYA, R. & KUNKUL, A. 2003. Dissolution kinetics of an oxidized copper ore in ammonium chloride solution.

EKSTEEN, J., ORABY, E. & TANDA, B. 2017. A conceptual process for copper extraction from chalcopyrite in alkaline glycinate solutions. Minerals Engineering, 108, 53-66.

FENG, Q., WEN, S., ZHAO, W., LV, C., BAI, X. J. S. E. R. & DEVELOPMENT, J. 2015. Leaching of copper from malachite with methane-sulfonic acid. Solvent Extraction Research Development, Japan 22, 159-168.

GHAHREMANINEZHAD GHARELAR, A. 2012. The surface chemistry of chalcopyrite during electrochemical dissolution. University of British Columbia.

HALPERN, J., MILANTS, H. & WILES, D. 1959. Kinetics of the Dissolution of Copper in Oxygen-Containing Solutions of Various Chelating Agents. Journal of the Electrochemical Society, 106, 647.

HIDALGO, T., KUHAR, L., BEINLICH, A. & PUTNIS, A. 2019. Kinetics and mineralogical analysis of copper dissolution from a bornite/chalcopyrite composite sample in ferric-chloride and methanesulfonic-acid solutions. Hydrometallurgy, 188, 140-156.

IZATT, R., OSCARSON, J., GILLESPIE, S., GRIMSRUD, H., RENUNCIO, J. & PANDO, C. 1992. Effect of temperature and pressure on the protonation of glycine. Biophysical journal, 61, 1394-1401.

KHEZRI, M., REZAI, B., ABDOLLAHZADEH, A. A., WILSON, B. P., MOLAEINASAB, M. & LUNDSTRÖM, M. 2021. Investigation into the effect of mechanical activation on the leaching of chalcopyrite in a glycine medium. Hydrometallurgy, 203, 105492.

KONISHI, Y., KATOH, M. & ASAI, S. 1991. Leaching kinetics of copper from natural chalcocite in alkaline Na4EDTA solutions. Metallurgical Transactions B, 22, 295-303.

KUNZE, J., MAURICE, V., KLEIN, L. H., STREHBLOW, H.-H. & MARCUS, P. 2004. In situ STM study of the duplex passive films formed on Cu (1 1 1) and Cu (0 0 1) in 0.1 M NaOH. Corrosion science, 46, 245-264.

LENTE, G., FÁBIÁN, I. & POË, A. J. 2005. A common misconception about the Eyring equation. New Journal of Chemistry, 29, 759-760.

LEVENSPIEL, O. 1999. Chemical reaction engineering, John Wiley & Sons.

LI, N., ZHANG, Y., KONG, D., ZHOU, Q., CHEN, X. & HUI, S. 2013. Fluid particle group reaction model and experimental verification. Advanced Powder Technology, 24, 200-206.

LIU, Z.-X., YIN, Z.-L., HU, H.-P. & CHEN, Q.-Y. 2012. Dissolution kinetics of malachite in ammonia/ammonium sulphate solution. Journal of Central South University, 19, 903-910.

NAZEMI, M., RASHCHI, F. & MOSTOUFI, N. 2011. A new approach for identifying the rate controlling step applied to the leaching of nickel from spent catalyst. International Journal of Mineral Processing, 100, 21-26.

MIKI, H., NICOL, M. & VELÁSQUEZ-YÉVENES, L. 2011. The kinetics of dissolution of synthetic covellite, chalcocite and digenite in dilute chloride solutions at ambient temperatures. Hydrometallurgy, 105, 321-327.

O'CONNOR, G., LEPKOVA, K., EKSTEEN, J. & ORABY, E. 2018. Electrochemical behaviour of copper in alkaline glycine solutions. Hydrometallurgy, 181, 221-229.

ORABY, E. & EKSTEEN, J. 2014. The selective leaching of copper from a gold–copper concentrate in glycine solutions. Hydrometallurgy, 150, 14-19.

PEARLMUTTER, A. F. & STUEHR, J. 1968. Kinetics of copper (II)-glycine interactions in aqueous solution. Journal of the American Chemical Society, 90, 858-862.

QIAN, G., LI, J., LI, Y. & GERSON, A. R. 2014. Probing the effect of aqueous impurities on the leaching of chalcopyrite under controlled conditions. Hydrometallurgy, 149, 195-209.

SAXENA, N. & MANDRE, N. 1992. Mixed control kinetics of copper dissolution for copper ore using ferric chloride. Hydrometallurgy, 28, 111-117.

SHIN, D., AHN, J. & LEE, J. 2019. Kinetic study of copper leaching from chalcopyrite concentrate in alkaline glycine solution. Hydrometallurgy, 183, 71-78.

SPECKMANN, H. D., LOHRENGEL, M., SCHULTZE, J. & STREHBLOW, H. H. 1985. The growth and reduction of duplex oxide films on copper. Berichte der Bunsengesellschaft für physikalische Chemie, 89, 392-402.

STREITWIESER, A., HEATHCOCK, C. H., KOSOWER, E. M. & CORFIELD, P. J. 1992. Introduction to organic chemistry, Macmillan New York.

SULTANA, U., GULSHAN, F. & KURNY, A. 2014. Kinetics of leaching of iron oxide in clay in oxalic acid and in hydrochloric acid solutions. Materials Science Metallurgy Engineering, 2, 5-10.

TANDA, B., EKSTEEN, J. & ORABY, E. 2017. An investigation into the leaching behaviour of copper oxide minerals in aqueous alkaline glycine solutions. Hydrometallurgy, 167, 153-162.

TANDA, B., EKSTEEN, J. & ORABY, E. 2018. Kinetics of chalcocite leaching in oxygenated alkaline glycine solutions. Hydrometallurgy, 178, 264-273.

TANDA, B., EKSTEEN, J., ORABY, E. & O'CONNOR, G. 2019. The kinetics of chalcopyrite leaching in alkaline glycine/glycinate solutions. Minerals Engineering, 135, 118-128.

THOMAS, G. & INGRAHAM, T. 1967. Kinetics of dissolution of synthetic covellite in aqueous acidic ferric sulphate solutions. Canadian Metallurgical Quarterly, 6, 153-165.

TOMÁSEK, J. & NEUMANN, L. 1982. Dissolution of secondary copper sulphides using complex-forming agents (EDTA, EDA). Part I: Covellite dissolution in EDTA and EDA. International Journal of Mineral Processing, 9, 23-40.

CHAPTER 6: CONCLUSION AND FUTURE WORK

This thesis provides an advanced understanding of the mechanism of the replacement of chalcopyrite by covellite and digenite under hydrothermal conditions. Chapter 3 and Chapter 4 reported that both mineral replacement reaction proceeds via the interfacial coupled dissolution-reprecipitation mechanism. Kinetic analysis was conducted in both Chapter 3 and Chapter 4 using the *Avrami-Arrhenius* method and the modified 'time to given fraction' method. In Chapter 5, the outcome filled the gap of knowledge in the mechanisms and kinetics of covellite dissolution in alkaline glycinate solutions and its potential implications in the Cu mining industry. Covellite dissolution mechanism was investigated as a function of temperature, the concentration of dissolved oxygen, solution pH and glycine concentration. Kinetics of dissolution reaction was analysed using the shrinking core model.

6.1 Replacement Reaction of Chalcopyrite by Covellite under Hydrothermal Conditions

In this chapter, it has been found that the replacement of chalcopyrite by covellite proceeds via interfacial coupled dissolution-reprecipitation reaction (ICDR), which is characterized by the formation of pores and cracks in the product layer, a sharp reaction front between chalcopyrite and covellite with visible gaps and the reaction preferential progress along the fractures and boundaries of chalcopyrite grains. The replacement reaction was found to start from chalcopyrite dissolution, releasing Cu(II), Fe(II) and elemental sulphur as shown in equation (44). At or above 140°C, the elemental sulphur reacts with water and forming H_2S as shown in equation (51), then covellite precipitated via reaction between Cu(II) and HS^- (from H_2S equilibrium, equation 52) as represented in equation (53). The overall replacement reaction of chalcopyrite by covellite was proposed to occur via equation (54). The replacement reaction rate increased with increasing temperature, increasing oxidant concentration (H_2O_2 or Fe^{3+}), increasing concentration of H^+ (or decreasing pH) and greater specific surface area. Thus, the dissolution of chalcopyrite is the rate-limiting step, rather than covellite precipitation. Analysis using the *Avrami-Arrhenius* method gave an activation energy of 90±21 kJ/mol, 86±17 kJ/mol and 27±7 kJ/mol at pH 0.5, 1 and 1.5 respectively, suggesting that the replacement reaction is interface-controlled at pH 0.5 and 1 and transport-controlled at pH 1.5.

XPS survey scan found an increase S/(Cu + Fe) ratio of on the chalcopyrite surface after reaction at pH 0.7-1.5 and 180 °C for 2 h, indicating metal-deficient surface formed. Sulphur *2p* spectra showed five different four species, including bulk monosulphide (161.2 eV), surface disulphide (162.2 eV), polysulphide (163.3 eV) and elemental sulphur (164.0 eV). A significant increase of elemental sulphur observed on the chalcopyrite surface after reaction as shown in equation (94).

$$CuFeS_{2(s)} + O_{2(g)} + 4H^{+}_{(aq)} \rightarrow Cu^{2+}_{(aq)} + Fe^{2+}_{(aq)} + 2S^{0}_{(s)} + 2H_2O_{(aq)} \quad (44)$$

$$3S_{(s)} + 2H_2O_{(g)} \rightarrow 2H_2S_{(aq)} + SO_{2(g)} \quad (51)$$

$$H_2S_{(aq)} \leftrightarrow H^{+}_{(aq)} + HS^{-}_{(aq)} \quad (52)$$

$$Cu^{2+}_{(aq)} + HS^{-}_{(aq)} \rightarrow CuS_{(s)} + H^{+}_{(aq)} \quad (53)$$

$$2CuFeS_{2(s)} + 3O_2 + 6H^{+} \rightarrow 2CuS_{(s)} + 2Fe^{2+} + H_2S_{(g)} + 2H_2O + SO_4^{2-} \ (\Delta V_{solid} = -53.3\%) \quad (54)$$

The reaction time of each 10% of replacement of chalcopyrite by covellite at 25°C was estimated by extrapolation of kinetic data. The results suggested that approximately 2.8 years are required for precipitation of 10% covellite at pH 0.5 or 500 years at pH 1 at 25 °C. At 120°C, chalcopyrite was dissolved into Cu^{2+}, Fe^{2+} and elemental sulphur, but no covellite precipitation occurs due to the lack of H_2S (effectively no reaction between sulphur and water at this temperature) (Fang et al., 2011; Randall and Bichowsky, 1918). It is also explained one part of Cu-S system, which is a complex process limited by various variables (e.g. temperature, oxidants, solution pH etc.).The investigation of replacement reaction mechanism of chalcopyrite by covellite matches the supergene metal deposits formation model proposed by Vasconcelos et al., (2015). Chalcopyrite is expected to dissolve in leaching zone by water and oxygen and release Cu^{2+} ions into water table; covellite will then precipitate in the H_2S-containing zone), rather than an *in-situ* replacement reaction. It is not a suitable approach for an *in-situ* mineral replacement reaction of chalcopyrite as it will takes hundreds of years.

6.2 Replacement Reaction of Chalcopyrite by Copper Sulphides with Addition of Cu^{2+} Ions under Hydrothermal Conditions

Chapter 4 demonstrates the replacement of chalcopyrite by covellite and digenite with addition of Cu^{2+} ions at temperatures between 140-200°C. The cross-sections of the reaction products showed three layers consisting of covellite outer rim, digenite middle layer and (unreacted) chalcopyrite core, with the characteristic features of ICDR such as sharp reaction front between chalcopyrite, digenite and covellite layer, pores and cracks formed within products. The replacement reaction of chalcopyrite with added Cu^{2+} also initiated with chalcopyrite dissolution as equations (66).At pH 1, nest-like covellite was formed on the chalcopyrite surface as equation (70) using SEM, but no digenite was found in XRD result. Porous digenite is found at or above 180°C or at pH 2 and pH 2.5 by replacing chalcopyrite (equation 71), identified using SEM and XRD. In the replacement of chalcopyrite by covellite in acidic $CuCl_2$ solutions, chalcopyrite dissolution is the rate-limited step. On the contrary, digenite precipitation is the rate limited step in chalcopyrite replacing by digenite.

$$CuFeS_{2(s)} + 4H^+ \rightarrow Cu^{2+} + Fe^{2+} + 2H_2S \quad (66)$$

$$CuFeS_{2(s)} + Cu^{2+} \rightarrow 2CuS_{(s)} + Fe^{2+} \ (\Delta V_{solid} = -6.6\%) \quad (70)$$

$$5CuFeS_{2(s)} + 13Cu^{2+} \rightarrow 10Cu_{1.8}S_{(s)} + 5Fe^{2+} \ (\Delta V_{solid} = 19.1\%) \quad (71)$$

The fraction of digenite increased with increasing concentration of Cu^{2+} ions or temperature. Activation energies calculated using *Avrami-Arrhenius* method for the replacement of chalcopyrite by mixed copper sulphides (covellite and digenite), were 44±6 kJ/mol at pH 2 and 46±14 kJ/mol at pH 2.5, suggesting that the replacement of chalcopyrite by covellite and digenite is interface-controlled replacement reactions.

This Chapter also described a complex Cu-S system in the replacement reaction of chalcopyrite. The replacement reaction rate is affected by various variables, such as temperature, solution pH, oxidants, concentration of Cu^{2+} and the formed copper sulphide layers. The precipitation of digenite is very critical, which need to perform at 180 °C or higher with Cu^{2+} ions addition. In Nature, the formation of digenite needs to be further investigated as it is unlikely to formed at low temperature. It is also helping geologists understand the formation of copper-bearing ore in Nature. The results indicate the formation of digenite needs higher temperature and copper-rich fluids, while covellite can be formed at low temperature with copper-deficient fluids.

6.3 Covellite Dissolution under Alkaline Condition with Glycine Solution

The dissolution of covellite was systematically studied in Chapter 5 to understand the mechanism and kinetics of the reaction as a function of different pH (pH 9-11), glycine concentrations (0-1.5 M), dissolved oxygen concentration and temperature (25-55 °C). Covellite was dissolved in alkaline glycinate solutions with oxygen, resulting in the formation of Cu-glycinate complexes (equation 90-93). The dissolution rate was found to increase with increasing temperature, increasing OH^- concentration, increasing concentration of dissolved oxygen in solutions, and with decreasing glycine concentration. The shrinking core model was used to determine the rate constant in kinetic analysis and suggested that the covellite dissolution is controlled by diffusion through a fluid film, which is surrounding covellite particle. Activation energy was calculated by *Arrhenius* equation, giving an activation energy of 33±7 kJ/mol, suggesting that the covellite dissolution is a transport-controlled reaction. Activation enthalpy and entropy calculated using *Eyring* equation for covellite dissolution in alkaline glycinate solutions were 31 kJ/mol and -284 $Jmol^{-1}K^{-1}$. An empirical rate law was developed to show the correlation between fraction of covellite dissolved x and concentration of glycine and OH^-, and temperature as shown in equation (94).

$$NH_2CH_2COOH_{(aq)} + OH^-{}_{(aq)} \leftrightarrow NH_2CH_2COO^-{}_{(aq)} + H_2O_{(aq)} \quad (90)$$

$$NH_2CH_2COO^-{}_{(aq)} + Cu^{2+}{}_{(aq)} \leftrightarrow Cu(NH_2CH_2COO)_{2(aq)} \quad (91)$$

$$CuS_{(s)} + 2NH_2CH_2COO^-{}_{(aq)} + 2O_{2(aq)} \rightarrow Cu(NH_2CH_2COO)_{2(aq)} + SO_{4(aq)}^{2-} \quad (92)$$

$$CuS + 2NH_2CH_2COOH + 2OH^- + 2O_2 \rightarrow Cu(NH_2CH_2COO)_2 + SO_4^{2-} + 2H_2O \quad (93)$$

$$x = k_a t = \{757[Gly]^{-0.82}[OH^-]^{-0.35} exp^{\frac{33}{RT}}\}t \quad (94)$$

This study filled the gap of knowledge in copper sulphide dissolution in alkaline glycine solutions and advanced our understanding of the mechanism and kinetics. The results indicate glycine is a suitable chemical reagent for *in-situ* covellite leaching under alkaline condition. The average E_a is same as the ammonia sulphate and higher then EDTA. However, glycine is very environmentally friendly and the dissolution rate at pH 9 and room temperature is acceptable.

6.5 Future Work

This Ph.D. project investigated the mechanisms and kinetics of the replacement of chalcopyrite by covellite and digenite under mild hydrothermal conditions. There are several further research may be interesting to others.

Cu-S system is a very complicated system as there are many other copper sulphides between covellite (CuS) and chalcocite (Cu_2S), such as geerite ($Cu_{1.6}S$), anilite ($Cu_{1.75}S$), digenite ($Cu_{1.8}S$) and djurleite ($Cu_{1.96}S$). Covellite was only found at for above 140°C, digenite is only formed at or above 180°C in this study. Geerite was found in one of experiment conducted at 250°C. The precipitation of copper sulphides might be related to reaction temperatures. A further study of the replacement reaction as a function of temperature (200-300 °C), Cu^{2+} and Cu^{+} concentration in the mineral replacement reaction of chalcopyrite may be potentially interesting to the mining industry. The textural characteristics of chalcopyrite replacing by covellite and digenite may be different under a relative dry system (much lower S/F ratio) as it undergoes a solid-state reaction mechanism. A further investigation on solid-state replacement of chalcopyrite by covellite can be used to understand the differences of reaction mechanism and kinetic between fluid-mediated ICDR and solid-state mechanisms.

All experiments performed in this project were in optimal conditions with pure solutions and mineral sample with high purity. In Nature, chalcopyrite is generally associated with other impurities including pyrite, sphalerite or other minerals. The reaction mechanisms and kinetics of chalcopyrite replacement might be affected by those impurities. A study investigates the effects of those impurities on mineral replacement reaction can provides a comprehensive insight into how the secondary copper mineral deposits have been formed in Nature.

In the covellite dissolution chapter, no glycinate species were found on the covellite surface using EDAX. The identification of glycinate species formed in covellite dissolution might be helpful to the understanding of mechanism. The formation of glycinate species might be change the covellite dissolution rate. Tanda et al. (2019) used XPS for a surface analysis reported an increase of nitrogen of the chalcopyrite surface after exposed in alkaline glycinate solutions, but not able to identified the species of nitrogen. XPS, Photoemission Electron Microscopy (PEEM) and Time of Flight Secondary Ion Mass Spectrocscopy are all surface sensitive techniques for further covellite surface analysis.

PEEM is a technique which is able to analysed the sample surface using photoelectron spectroscopy with a small scalce of the sample surface and produce images with both topograph information and spatial distribution of each atoms with different chemical states. A soft X-ray absoption spectra is used in this technique to determine the chemical states of each elemental on the sample surface. ToF-SIMS is another highly surface sensitive techinique, which can determine the elemental composition of the outmost atomic layers of a sample surface. A further analysis on covellite surface using these techiques can understand the glycinate species formed on the surface when covellite dissolved with glyine at alkaline solution.

6.6 Reference List

RICKARD, D. 1972. Covellite formation in low temperature aqueous solutions. Mineralium Deposita, 7, 180-188.

TANDA, B., EKSTEEN, J., ORABY, E. & O'CONNOR, G. 2019. The kinetics of chalcopyrite leaching in alkaline glycine/glycinate solutions. Minerals Engineering, 135, 118-128.

VASCONCELOS, P. M., REICH, M. & SHUSTER, D. L. J. E. 2015. The paleoclimatic signatures of supergene metal deposits. Elements, 11, 317-322.

APPENDIX 1: SUPPLEMETARY MATERIALS FOR CHAPTER 3

Table 31 Measured pH and Eh values of the solutions collected from hydrothermal reactions.

Experimental conditions	Measured pH	Measured Eh vs. SHE (mV)
A73: pH 0.7, 180 °C, 0.44 mmol H_2O_2, 24 h	0.70	538.5
A53: pH 1, 180 °C, 0.44 mmol H_2O_2, 24 h	1.02	648.5
A93: pH 1.5, 180 °C, 0.44 mmol H_2O_2, 24 h	1.58	606.8
D1: pH 2, 180 °C, 0.44 mmol H_2O_2, 24 h	2.09	521.8
A11: pH 3, 180 °C, 0.44 mmol H_2O_2, 61 days	2.79	538.4
A12: pH 4, 180 °C, 0.44 mmol H_2O_2, 61 days	4.68	436.6
A13: pH 5, 180 °C, 0.44 mmol H_2O_2, 61 days	5.76	383.6
A14: pH 6, 180 °C, 0.44 mmol H_2O_2, 61 days	3.96	346.2
A15: pH 7, 180 °C, 0.44 mmol H_2O_2, 61 days	6.77	231.3
A16: pH 9, 180 °C, 0.44 mmol H_2O_2, 61 days	8.58	201.3
A17: pH 11, 180 °C, 0.44 mmol H_2O_2, 61 days	7.85	119.4
A28: pH 1, 180 °C, 0, 24 h, N_2 atm	1.15	-
A30: pH 1, 180 °C, 0.88 mmol H_2O_2, 24 h	1.04	501.9
A31: pH 1, 180 °C, 1.76 mmol H_2O_2, 24 h	1.03	616.5
A18: pH 1, 120 °C, 0.44 mmol H_2O_2, 18 days	1.27	714.5
A70: pH 0.7, 180 °C, 0.44 mmol H_2O_2, 2 h	0.67	742.0
A50: pH 1, 180 °C, 0.44 mmol H_2O_2, 2 h	1.05	751.2
A90: pH 1.5, 180 °C, 0.44 mmol H_2O_2, 2 h	1.63	727.4
A108: pH 1, 180 °C, N_2 atm, 0.22 mmol $CuCl_2$, 24 h	1.19	-
A109: pH 1, 180 °C, N_2 atm, 0.44 mmol $CuCl_2$, 24 h	1.15	-
A110: pH 1, 180 °C, N_2 atm, 0.88 mmol $CuCl_2$, 24 h	1.15	-
A111: pH 1, 180 °C, N_2 atm, 0.22 mmol $FeCl_3$, 24 h	1.18	393.5
A112: pH 1, 180 °C, N_2 atm, 0.44 mmol $FeCl_3$, 24 h	1.13	400.4
A113: pH 1, 180 °C, N_2 atm, 0.88 mmol $FeCl_3$, 24 h	1.08	394.1
A114: pH 1, 180 °C, N_2 atm, 0.22 mmol $FeSO_4$, 24 h	1.23	356.4
A115: pH 1, 180 °C, N_2 atm, 0.44 mmol $FeSO_4$, 24 h	1.23	351.5
A116: pH 1, 180 °C, N_2 atm, 0.88 mmol $FeSO_4$, 24 h	1.27	345.9
A117: pH 1, 180 °C, N_2 atm, 0.22 mmol H_2S, 24 h	1.21	283.7
A118: pH 1, 180 °C, N_2 atm, 0.44 mmol H_2S, 24 h	1.29	274.6
A119: pH 1, 180 °C, N_2 atm, 0.88 mmol H_2S, 24 h	1.42	228.3

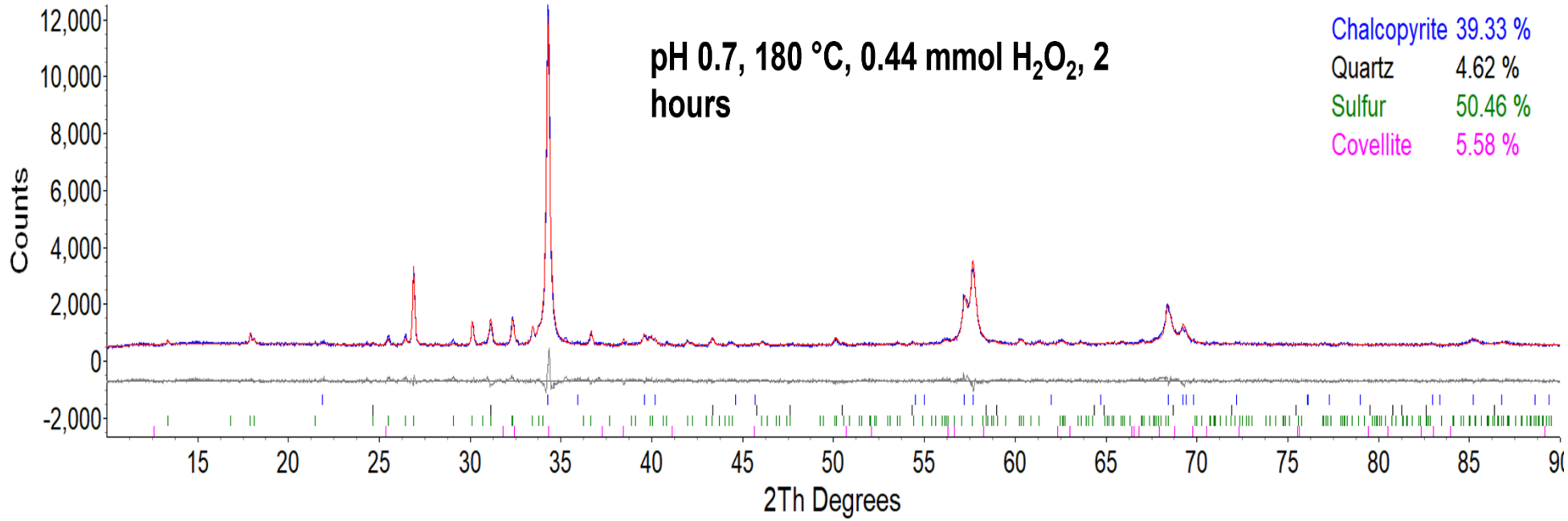

Figure 90 XRD results of chalcopyrite reacted at 180 °C, pH 0.7, with 0.44 mmol H_2O_2 after 2 h. This is the samples used for XPS analysis in Chapter 3.

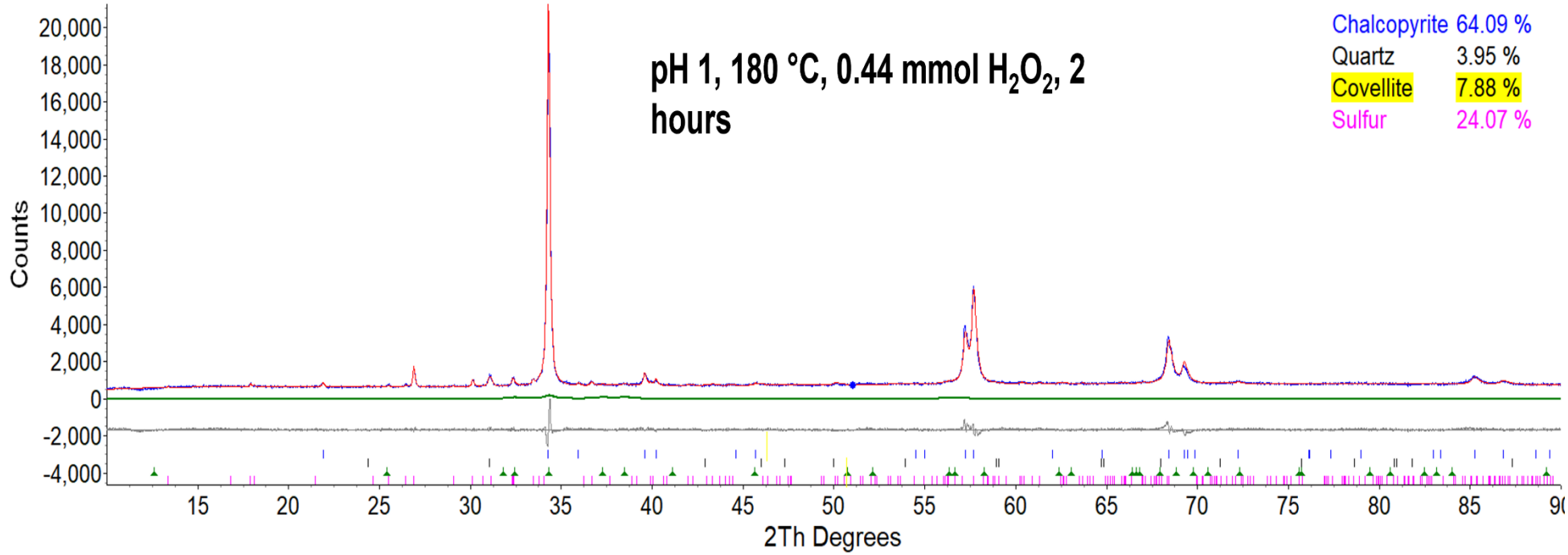

Figure 91 XRD results of chalcopyrite reacted at 180 °C, pH 1, with 0.44 mmol H_2O_2 after 2 h. This is the samples used for XPS analysis in Chapter 3.

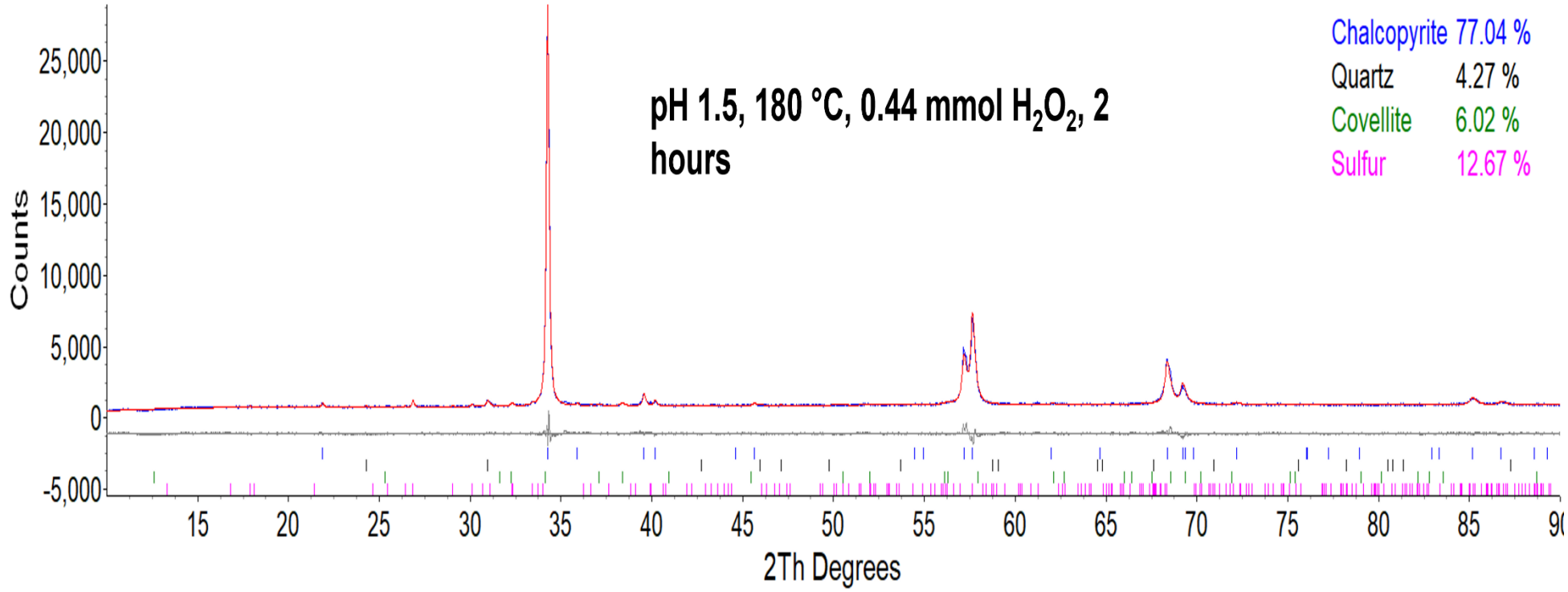

Figure 92 XRD results of chalcopyrite reacted at 180 °C, pH 1.5, with 0.44 mmol H_2O_2 after 2 h. This is the samples used for XPS analysis in Chapter 3.

APPENDIX II: SUPPLEMENTARY MATERIALS FOR CHAPTER 4

Table 32 Measured pH and Eh values of the solutions collected from hydrothermal reactions in Chapter 4.

Experimental conditions	Measured pH	Measured Eh vs. SHE (mV)
T1: pH 1, 180 °C, 0.44 mmol H_2O_2, 0.22 mmol $CuCl_2$, 48 h	1.10	372.6
T4: pH 1, 180 °C, 0.44 mmol H_2O_2, 0.44 mmol $CuCl_2$, 48 h	1.06	346.9
T21: pH 1, 200 °C, 0.44 mmol H_2O_2, 0.22 mmol $CuCl_2$, 24 h	1.03	373.3
T24: pH 1, 200 °C, 0.44 mmol H_2O_2, 0.44 mmol $CuCl_2$, 48 h	1.05	333.8
T7: pH 1, 180 °C, no H_2O_2, 0.22 mmol $CuCl_2$, 16 days	1.04	551.8
T10: pH 1, 180 °C, no H_2O_2, 0.44 mmol $CuCl_2$, 16 days	0.98	387.1
T13: pH 0.7, 180 °C, no H_2O_2, 0.22 mmol $CuCl_2$, 16 days	0.70	392.0
T16: pH 0.7, 180 °C, no H_2O_2, 0.44 mmol $CuCl_2$, 16 days	0.75	380.5
D1: pH 1, 180 °C, 0.44 mmol H_2O_2, 0.11 mmol $CuCl_2$, 24 h	1.10	433.1
D2: pH 1, 180 °C, 0.44 mmol H_2O_2, 0.22 mmol $CuCl_2$, 24 h	1.08	347.4
D3: pH 1, 180 °C, 0.44 mmol H_2O_2, 0.44 mmol $CuCl_2$, 24 h	1.12	334.1
D4: pH 1, 180 °C, 0.44 mmol H_2O_2, 0.88 mmol $CuCl_2$, 24 h	1.15	355.8
D5: pH 1, 180 °C, 0.44 mmol H_2O_2, no $CuCl_2$, 24 h	1.02	648.5
D6: pH 1, 180 °C, no H_2O_2, 0.22 mmol $CuCl_2$, 24 h	1.06	483.1
D7: pH 1, 180 °C, 0.88 mmol H_2O_2, 0.22 mmol $CuCl_2$, 24 h	1.08	379.2
D8: pH 1, 180 °C, 1.76 mmol H_2O_2, 0.22 mmol $CuCl_2$, 24 h	1.09	390.4
D9: pH 2, 180 °C, 0.44 mmol H_2O_2, 0.22 mmol $CuCl_2$, 26 days	1.64	372.4

D10: pH 3, 180 °C, 0.44 mmol H_2O_2, 0.22 mmol $CuCl_2$, 26 days	1.95	145.7

APPENDIX III: SUPPLEMENTARY MATERIALS FOR CHAPTER 5

Table 33 ICP-OES results of solution collected from covellite dissolution experiment conducted at pH 11, 40 °C, with 0.5 M glycine and 0.02 mol H_2O_2.

Experimental number	Reaction time	Cu Concentration (ppm)	Measured pH
Cv1	2	103.4	10.71
Cv2	4	107.1	10.76
Cv3	6	108.7	10.75
Cv4	11	107.4	10.73
Cv5	24	96.3	10.72
Cv6	34	244.8	10.70
Cv7	48	316.8	10.69
Cv8	58	490	10.69
Cv9	72	630.5	10.67
Cv10	96	784.7	10.64
Cv10A	120	788.7	10.62

Table 34 ICP-OES results of solution collected from covellite dissolution experiment conducted at pH 11, 40 °C, with 0.5 M glycine.

Experimental number	Reaction time	Cu Concentration (ppm)	Measured pH
Cv11	2	3.995	10.87
Cv12	4	4.722	10.93
Cv13	6	6.134	10.89
Cv14	11	98.98	10.89
Cv15	24	183.05	10.88
Cv16	34	250	10.88
Cv17	48	335.1	10.88
Cv18	58	544.6	10.90

Cv19	72	960.1	10.88
Cv20	96	1109.5	10.85
Cv20A	120	1506.9	10.83

Table 35 ICP-OES results of solution collected from covellite dissolution experiment conducted at pH 11, 40 °C, with 0.5 M glycine and purging of compressed air.

Experimental number	**Reaction time**	**Cu Concentration (ppm)**	**Measured pH**
Cv21	2	36.41	11.05
Cv22	4	54.7	11.02
Cv23	6	73.83	11.01
Cv24	11	157.22	10.96
Cv25	26	381	10.88
Cv26	37	524.36	10.80
Cv27	48	666.38	10.73
Cv28	72	928.11	10.64
Cv29	99	1218.92	10.50
Cv30	124	1436.89	10.43

Table 36 ICP-OES results of solution collected from covellite dissolution experiment conducted at pH 11, 40 °C, with 0.5 M glycine and purging of N_2 gas.

Experimental number	**Reaction time**	**Cu Concentration (ppm)**	**Measured pH**
Cv31	2	12.28	11.04
Cv32	4	16.40	11.05
Cv33	10	22.84	11.04
Cv34	24	46.88	11.03
Cv35	34	54.13	11.02
Cv36	49	89.95	11.02
Cv37	59	92.59	11.01
Cv38	72	115.56	10.99
Cv39	106	188.56	10.99
Cv40	129	185.69	10.99

Table 37 ICP-OES results of solution collected from covellite dissolution experiment conducted at pH 11, 25 °C, with 0.5 M glycine.

Experimental number	Reaction time	Cu Concentration (ppm)	Measured pH
Cv41	2	16.99	11.04
Cv42	4	24.47	11.03
Cv43	10	40.92	11.03
Cv44	24	92.64	11.03
Cv45	34	124.85	11.02
Cv46	49	174.01	11.02
Cv47	59	204.02	11.02
Cv48	72	252.52	11.02
Cv49	106	407.37	10.98
Cv50	129	454.77	10.98

Table 38 ICP-OES results of solution collected from covellite dissolution experiment conducted at pH 11, 35 °C, with 0.5 M glycine.

Experimental number	Reaction time	Cu Concentration (ppm)	Measured pH
Cv51	2	27.16	11.19
Cv52	5	44.81	11.18
Cv53	11	75.22	11.18
Cv54	26	163.09	11.16
Cv55	35	202.07	11.16
Cv56	50	289.27	11.16
Cv57	59	334.06	11.15
Cv58	74	428.67	11.15
Cv59	99	561.90	11.14
Cv60	131	715.20	11.11

Table 39 ICP-OES results of solution collected from covellite dissolution experiment conducted at pH 11, 45 °C, with 0.5 M glycine.

Experimental number	Reaction time	Cu Concentration (ppm)	Measured pH

Cv61	2	35.23	11.18
Cv62	5	72.64	11.17
Cv63	11	128.82	11.17
Cv64	26	189.20	11.17
Cv65	35	254.01	11.16
Cv66	50	357.75	11.16
Cv67	59	420.21	11.15
Cv68	74	505.08	11.15
Cv69	99	672.00	11.13
Cv70	131	852.71	11.10

Table 40 ICP-OES results of solution collected from covellite dissolution experiment conducted at pH 11, 55 °C, with 0.5 M glycine.

Experimental number	**Reaction time**	**Cu Concentration (ppm)**	**Measured pH**
Cv71	2	34.33	11.10
Cv72	4	33.95	11.08
Cv73	6	80.74	11.09
Cv74	10	137.5	11.06
Cv75	24	496.61	11.01
Cv76	34	674.8	10.97
Cv77	48	776.8	10.90
Cv78	82	1211.8	10.59
Cv79	107	1525	10.39
Cv80	124	1526.8	10.24

Table 41 ICP-OES results of solution collected from covellite dissolution experiment conducted at pH 11, 40 °C, with no glycine.

Experimental number	**Reaction time**	**Cu Concentration (ppm)**	**Measured pH**
Cv81	2	0.60	10.93
Cv82	4	0.61	10.89
Cv83	6	0.48	10.88
Cv84	11	0.71	10.81

Cv85	25	1.01	10.70
Cv86	34	0.90	10.53
Cv87	50	0.99	10.38
Cv88	72	1.09	10.16
Cv89	106	1.34	9.78
Cv90	130	1.39	9.50

Table 42 ICP-OES results of solution collected from covellite dissolution experiment conducted at pH 11, 40 °C, with 0.75 M glycine.

Experimental number	**Reaction time**	**Cu Concentration (ppm)**	**Measured pH**
Cv91	2	24.86	11.10
Cv92	5	44.41	11.08
Cv93	10	78.10	11.09
Cv94	22	177.12	11.06
Cv95	29	226.79	11.01
Cv96	48	357.55	10.97
Cv97	58	412.53	10.90
Cv98	70	540.85	10.59
Cv99	99	705.03	10.39
Cv100	128	891.93	10.24

Table 43 ICP-OES results of solution collected from covellite dissolution experiment conducted at pH 11, 40 °C, with 1 M glycine.

Experimental number	**Reaction time**	**Cu Concentration (ppm)**	**Measured pH**
Cv101	2	26.01	-
Cv102	4	35.85	-
Cv103	9	71.20	-
Cv104	23	172.85	-
Cv105	33	214.14	-
Cv106	50	300.19	-
Cv107	58	307.36	-
Cv108	74	402.14	-

Cv109	98	509.13	-
Cv110	121	546.18	-

Table 44 ICP-OES results of solution collected from covellite dissolution experiment conducted at pH 11, 40 °C, with 1.5 M glycine.

Experimental number	**Reaction time**	**Cu Concentration (ppm)**	**Measured pH**
Cv111	2	24.29	-
Cv112	4	41.95	-
Cv113	9	69.08	-
Cv114	23	153.25	-
Cv115	33	222.50	-
Cv116	50	292.91	-
Cv117	58	317.29	-
Cv118	74	426.98	-
Cv119	98	570.49	-
Cv120	121	658.00	-

Table 45 ICP-OES results of solution collected from covellite dissolution experiment conducted at pH 9, 40 °C, with 0.5 M glycine.

Experimental number	**Reaction time**	**Cu Concentration (ppm)**	**Measured pH**
Cv121	2	18.35	9.29
Cv122	4	25.51	9.29
Cv123	6	29.21	9.28
Cv124	11	43.84	9.28
Cv125	25	75.13	9.26
Cv126	34	94.84	9.25
Cv127	50	130.62	9.25
Cv128	72	187.46	9.24
Cv129	106	286.51	9.19
Cv130	130	344.63	9.16

Table 46 ICP-OES results of solution collected from covellite dissolution experiment conducted at pH 10, 40 °C, with 0.5 M glycine.

Experimental number	Reaction time	Cu Concentration (ppm)	Measured pH
Cv131	2	28.38	9.99
Cv132	5	44.53	9.92
Cv133	10	71.14	9.89
Cv134	22	141.27	9.90
Cv135	29	172.27	9.90
Cv136	48	314.29	9.87
Cv137	58	363.18	9.84
Cv138	70	453.24	9.83
Cv139	99	622.07	9.81
Cv140	128	868.45	9.77